Design, Syntheses and Study of Photo Physical Properties of 'Aggregation Induced Emission' active Compounds: Applications in Bio-imaging and Mechanoluminescence

THESIS

Submitted in partial fulfillment of the requirements for the degree

of

DOCTOR OF PHILOSOPHY

by

Sheik Saleem Pasha

Under the supervision of

Prof. Inamur Rahaman Laskar

BIRLA INSTITUTE OF TECHNOLOGY AND SCIENCE
PILANI (RAJASTHAN) INDIA

2018

BIRLA INSTITUTE OF TECHNOLOGY AND SCIENCE,
PILANI (RAJASTHAN)

CERTIFICATE

This is to certify that the thesis **"Design, Syntheses and Study of Photo Physical Properties of 'Aggregation Induced Emission' active Compounds: Applications in Bio-imaging and Mechanoluminescence"** submitted by **Mr. Sheik Saleem Pasha,** ID No. **2012PHXF0024P** for the award of Ph. D. Degree of the Institute embodies the original work done by him under my supervision.

Signature in full of the Supervisor

Prof. Inamur Rahaman Laskar
Designation: Associate Professor

Date:

Dedicated to

My beloved parents

and my most precious

daughter

Acknowledgement

I take this opportunity to put my gratitude and thanks on record to all those who were of great help and support to me in their own special ways during the journey of my doctoral studies.

Firstly, I would like to thank my supervisor, Professor Inamur Rahaman Laskar, who gave me the opportunity to join his group in the BITS Pilani, and directed me through nearly six years of thesis work. His supportive discussions and enthusiasm for chemistry always replenished my energy to work. His inspiring hard work and constant motivation have helped me to understand better and remain optimistic during the course of my study. His forensic scrutiny of my technical writing has been invaluable.

I am immensely thankful to the Vice-Chancellor, Directors, Deputy Directors and Deans of Birla Institute of Technology and Science (BITS) Pilani for providing me the opportunity to pursue my doctoral studies by providing necessary facilities and financial support.

My whole-hearted gratitude to Prof. Sanjay Kumar Verma, Dean, Academic Research Division (ARD), BITS Pilani, Pilani Campus and Prof. I owe my sincere thanks Dr. Hemanth Jadav, Dr. Navin Singh, nucleus members of ARD, other members of DRC, Department of Chemistry, BITS Pilani, Pilani Campus for their cooperation and constant support. I, overwhelmingly acknowledge the office staff of ARD, whose secretarial assistance helped me in submitting the various evaluation documents in time. Ram Kinkar Roy (earlier DRC Convener), Prof. Ajay Kumar Sah, Prof. Saumi Ray (present DRC Convener), Departmental Research Committee (DRC), Department of Chemistry, BITS Pilani, Pilani Campus for his official support and encouragement.

I am grateful to the members of my Doctoral Advisory Committee, Prof. Subit Kumar Saha and Dr. Saumi Ray for their great cooperation in refining my thesis.

I am thankful to my research collaborators, Dr. Angshuman Roy Choudhury, IISER Mohali and Prof. Nigam Rath, Department of Chemistry and Biochemistry, University of Missouri-St Louis, University Blvd, St Louis, MO 63121, USA for Single X-Ray facility and valuable suggestions. I would like to thank Prof. Nikhil Ranjan Jana

(IACS, Kolkata), Dr. Aniruddha Roy (BITS Pilani) and Dr. Rajdeep Choudhury (BITS Pilani) for biological studies.

Also, I am thankful to Dr. Debashree Bandyopadhyay (BITS Pilani, Hyderabad Campus), Prof. Ram Kinkar Roy (BITS Pilani, Pilani Campus) and Dr. Pere Alemany (University at de Barcelona, Spain) for validating some of the experimental data through computational calculations.

I am thankful to all the respectable faculty members and office staffs of the Department of Chemistry, BITS Pilani for their generous help and support along with fruitful discussions during the different stages of my doctoral study. Thanks are also to all the office staff of the other Departments for their help during my work. My sincere thanks to the Librarians, BITS Pilani and other staff of library for their support and help rendered while utilizing the library facilities.

My sincere thanks to Prof. Jamil Akthar, Dr. Mirnmoyee Basu, Dr. Manoj Muthyala, Dr. Amit Tiwari, Dr. Sonu, Mr. Narendra Mishra, Dr. Arun, Dr. Abdul Shakoor, Dr. Nisar Mir, Dr. Ganesh, Dr. Chandra Shekar, Sunita Poonia, Sunita Chaudhury, Sushila, Mr. Fayaz Baig, Mr. Pallavi Rao, Mr. P. Venkata Ramana Reddy, Mr. Anoop Sing, Dr. Pragati fageria, Ms. Leena fageria, Dr. Hare ram Yadav, Dr. Satheeshvarma, Mr. Abid Hamid, Mr. Sreenu Naik, Mr. Jani Pasha, Mr. Khadar Pasha, Mr. Roshan Nazir and Dr. Noorullah Baig for helpful discussions. Thanks to my group members Dr. Parvej Alam, Dr. Dinesh Kumar Sengotuvelu, Mr. Vishal Kachwal, and Ms. Jagrity Chaudhury with whom I have worked.

I extend my heartfelt thanks to my friends Mr. Sohail, Mr. Dugge Venkanna, Mr. P. Edukondalu, Cheennaboina Sreenu, Ramanjaneyulu, Dr. Shakoor, Dr. Nisar, Dr. Panduga Ramaraju, Dr. Kaashi Pericherla, Sheik. Jani Pasha, Sheik Kadhar pasha, Sheik Rahmath Ali, Sheik Rasheed, Mr. Ravi Pratap Singh, Dr. Bhupendra Mishra, Dr. Amrith, Mr. Mukund, Mr. Hitesh, Dr. Pinku, Ms. Santosh, Nitesh, Mr. Prasant, Mr. Arpit, Mrs. Prameela Jha, Mrs. Pushp Lata, Dr. Navin Jain, Mr. Gagandeep Singh, Jharna pala, Amar Chaudhury, Monika Poonia, Surendra Pratap, Tej Verma, Pramod Saini and Mr. Phool Hasan. I would like to thank my Grandpa Sheik Mahaboob Ali, Grandmother Saida and Rasoolbee, My uncle Sheik janimiya, my aunty Sheik Fathima, brother-in-law Sheik Chotu (Mahaboob Ali) .

I would like to thank my parents Sheik Janimiya and Jameela, who always pushed me to succeed over the years. Their vision, ethical principles, moral support, endless patience and eternal inspiration, to face any situation in life have guided to the successful completion of this work. They sacrificed a lot for my education and I truly do appreciate it. I would also like to acknowledge my Sisters Ms. Asha Begum and Khairunbee, my nieces Sameera and Samreen, brother in laws Sheik Moulana and Sheik Naheem Pasha for their love and support. I would also like to thank my wife Rafiya and my precious daughter Sheik Zainab.

Finally, I want to acknowledge CSIR and BITS Pilani for financially support in the form of Project Fellow during my research tenure.

Sheik Saleem Pasha

Abstract

The thesis entitled "Design, Syntheses and Study of Photo Physical Properties of 'Aggregation Induced Emission' active Compounds: Applications in Bio-imaging and Mechanoluminescence" deals with the synthesis of new organic and platinum(II) based metal complexes which is structurally characterized and exhibited a unique 'Aggregation Induced Emission (AIE)' property. The synthesized complexes were used in different applications such as Mechanouminescence and Bioimaging. The thesis is divided in five chapters.

The Chapter 1 of the thesis describes a literature overview about the fundamentals of fluorescence and phosphorescence, various types of transitions such as MLCT, LLCT etc. Additionally the chapter describes the history of AIE active compounds and their probable mechanistic pathways. The general features of AIE active platinum(II) complexes are described in this chapter. The background of applications of luminescent materials in bioimaging and mechanoluminescence has been described in this chapter.

The Chapter 2 of the thesis describes the materials and instruments have been used to complete the whole thesis work.

The Chapter 3 The chapter consists of three parts.

Chapter 3A, describes the simple methodology of synthesis of a water soluble platinum(II) based complex. The solid state emission of the complex is different from its solution state which arises due to the formation of a new electronic state, ^{3}MLLCT. This complex spontaneously enters into cell cytoplasm and then localize preferably into cell nucleus. The cellular uptake of Pt(II) complex by cancerous cells was observed higher as compared to the normal cells. Low cyto-toxicity of this complex facilitates for the possible application as bio-imaging probe.

In Chapter 3B**,** we have reported the syntheses of three AIE active cyclometalated complexes, [Pt(C^N)(CH^N)Cl] (**1**), [Pt(C^N)P^P]Cl where [C^N = 2-phenylpyridine; P^P is bis(diphenylephasphino)ethane (**2**) and *cis*- 1,2-Bis (diphenylephasphino)ethene (**3**)] and study of their photophyscial properties. The computational studies of one of the complexes was performed and correlated with its spectroscopic observations. All these complexes are found to exhibit AIE activity and show very strong emission in the solid state. It is determined the cytotoxicity of **2** by MTT based study against non-resistant and *cis*-platin-resistant cell line which showing very good results. Utilizing its AIE and rich photophysical

properties, we have used complex **2** in bio-imaging applications such as in staining ability of cancer cells, human hepatocellular carcinoma cells, Hep3B etc.

In Chapter 3C, it is reported that the advanced biomedical research which has established the cancer is a multifactorial disorder which is highly heterogeneous in nature and responds differently to different treatment modalities, due to which constant monitoring of the therapy response is becoming extremely important. To accomplish this, different theranostic formulations has been evaluated, however, most of them was found to suffer from several limitations extending from poor resolution, radiation damage, high costs. In order to develop a better theranostic modality, we have designed and synthesized a novel platinum(II)-based AIE molecule (BMPP-Pt) which showed strong intra-cellular fluorescence and also simultaneously exhibited potent cytotoxic activity. Due to this duel functionality, we wanted to explore the possibility of using this compound as a single molecule based theranostic modality. The compound was found to exhibit strong AIE property with emission maxima at 497 nm. For more efficient cancer cell targeting, BMPP-Pt was encapsulated into mesoporous silica nanoparticles (Pt-MSNPs) and the MSNPs were further surface modified with anti-EpCAM aptamar (Pt-MSNP-E). Pt-MSNP exhibited higher intracellular fluorescence as compared to free BMPP-Pt. Anti-EpCAM aptamar modification was found to increase both cytotoxicity and intracellular fluorescence compared to the unmodified MSNPs. Our study showed that the EpCAM functionalized BMPP-Pt loaded MSNPs can efficiently internalize. This study provides cues towards development of a potential single compound based theranostic modality in future.

The Chapter 4 of the thesis describes the syntheses of mono cyclometalated diamine platinum(II) complexes with a series of 'Aggregation Induced Emission (AIE)' active, eximeric and non excimeric platinum(II) complexes, [Pt(C^N)(L_n)(Cl)], [C^N = 2-phenylpyridine]; **1** [L_1 = 2-phenylpyridine], **2** [L2 = N-Tritylpyridine-2-amine], **3** [L3 = N^1-tritylethane-1,2-diamine], **4** [L4 = N^1-tritylpropane-1,3-diamine] and **5** [L5 = N^1-tritylhexane-1,6-diamine]. The complexes, **3**, **4** and **5** exhibited mechanoluminesence (ML) and thereby transformed into an orange emitting complex, **3a**, **4a** and **5a** upon grinding. Crushing of **3**, **4** and **5** (or **3a**, **4a** and **5a**) with meso-structured silica produced a luminescent composite material, **3b**, **4b** and **5b** were formed with a drastic change of emission color (yellow → green). The solid-state luminescent behavior and computational based calculations have been carried out.

The Chapter 5 consists of two parts.

In Chapter 5A**,** we have reported the syntheses of multi-functional 'Aggregation Induced Emission (AIE)' active molecules in a simple manner. These molecules are drawing a great attention in current luminescent material research. In this perspective, a simple diamine molecule (N1-tritylethane-1,2-diamine (**1**)) is reacted with salicylaldehyde by Schiff-base technique giving a new AIE active organic molecule [2-((2-(tritylamino)ethylideneamino)methyl)phenol (**2**)]. Computational calculations shows that the nature of transition is intra-molecular charge transfer/twisted intramolecular charge transfer (ICT/TICT). The mechanism of AIE has been attributed to restricted intramolecular rotation (RIR). Packing diagram supports the nature of aggregation which corresponds to J-aggregation. The compound, **2** exhibits an irreversible mechanoluminescent (ML) property with a drastic colour change from blue to green (λ_{max}, 445 nm → 512 nm) upon grinding. But it undergoes a reversible transition with the same colour change (blue → green) through applying pressure axially (using a hydraulic press). Again, the reversible transition is observed by lowering the temperature of **2** to liquid nitrogen. The causes of such transitions showing emission color upon varying triggers have been investigated. In addition, the compound, **2** has been successfully tested in sensing Zn(II) which shows a rare turn-on luminescent change and the mechanism behind it has been explored. The detection limit of Zn(II) is determined to 0.064 ppm.

In Chapter 5B**,** we have reported the synthesis of 2-((E)-(4-tritylphenylimino)methyl)phenol (**1**) and characterized by NMR and HRMS. **1** exhibits AIE activity and showing turn on mechanoluminescent (ML) property(**1**). We have investigated the mechanism of AIE property and found that it occurs *via* 'Excited State Intramolecular Proton Transfer' (ESIPT). It has been explored the mechanism of molecular level ML property.

List of abbreviations and symbols

Abbreviation/Symbol	Description
α	Alpha
Å	Angstrom
ACN	Acetonitrile
n-BuLi	*n*-Butyl lithium
β	Beta
Bu	n-Butyl
Calcd.	Calculated
COD	1,5- cyclooctadiene
^{13}C	Carbon-13
Conc	Concentration
^{0}C	Degree centigrade
c	velocity of light
δ	Delta
$CDCl_3$	Deuterated chloroform
cd	candela
d	Doublet
dd	Doublet of doublet
DCM	Dichloromethane
DMF	*N,N*-Dimethylformamide
DMSO-d_6	Deuterated dimethylsulfoxide
DFT	Density Functional Theory
ESI	Electron spray ionization
EtOAc	Ethyl acetate
Equiv	Equivalent

ε	dielectric constant
ε	molar extinction coefficient
ξ	spin–orbit coupling constant
f_w	Water fractions
f_H	Hexane fractions
g	Gram
h	Hours
Hz	Hertz
IR	Infrared
Ir	Iridium
IC_{50}	half maximal inhibitory concentration
ILCT	Intraligand charge transfer
J	Coupling constant
k_T	Rate of energy transfer
K_{sv}	Stern–Volmer quenching constant
LLCT	Ligand -to- ligand charge transfer
LMCT	Ligand -to- metal charge transfer
λ	Wavelength
lm	Lumens
MS	Mass spectrometry
M.p.	Melting point
m	Multiplet
mg	Milligram
MHz	Mega hertz
MLCT	Metal -to- Ligand charge transfer
min	Minutes
mL	Milliliter

μM	Micro molar
M	Molar
mmol	Millimole
ML	Mechano Luminescence
$\bar{\upsilon}$	Wave number
N_2	Nitrogen gas
η_{ex}	external quantum efficiency
NMR	Nuclear magnetic resonance
nM	Nano molar
nm	Nanometer
PEG	Polyethylene glycol
Pt	platinum
^{31}P	Phosphorous-31
Φ	Quantum efficiency
PZL	Piezoluminescence
%	Percentage
Rt	Room temperature
S	Singlet
Σ	standard deviation
TFA	Trifluoroacetic acid
THF	Tetrahydrofuran
TLC	Thin layer chromatography
THT	Tetrahydrothiophene
TMS	Tetramethylsilane
OTf	Triflouromethanesulfonate
μL	Microliter

µM	Micromolar
v	Volume
W	Watt
EI	Electron ionization

Table of Contents

List of Tables

List of Figures

List of Figures

Chapter I

Introduction

1.1 General overview: Light is very essential for surviving and sustaining life in the universe. It can be generated from variable sources - directly it can be obtained from sun, stars etc, while indirectly it can be obtained from fossil fuel, electrical energy etc. In 1879, the pioneer scientist Thomas Alva Edison discovered a bulb with carbon filament. This discovery became a milestone of modern lighting. Emission of light by a substance which is not resulting from heat is called as luminescence (Latin: Lumen = light). It is a form of cold body radiation which can be caused by chemical reaction [1] etc. There are many types of luminescence as shown in the Table 1.

Table.1 Types of luminescence:

Types of Luminescence	**Definition**
Chemiluminescence	The emission of light results from chemical reactions.
Bioluminescence	Light result of biochemical reactions in an organism.
Electrochemiluminescence	The emission of light due to an electrochemical reactions.
Crystalloluminescence	Light is resulted during crystallization.
Electroluminescence	Light is resulted when an electric current passed through a substance.
Cathodoluminescence	Light is resulted when a luminescent material being struck by electrons.
Triboluminescence .	Produced when bonds in a material are broken when that material is scratched, crushed or rubbed.
Fractoluminescence	Light is emitted due to bonds in certain crystals are broken by fractures
Sonoluminescence	Light is produced of imploding bubbles in a liquid when excited by sound.
Radio luminescence	Light is generated with bombardment by ionizing radiation.
Cryoluminescence	The emission of light due to an object is cooled (an example of this is wulfenite).

Photoluminescence	The emission of light from materials during the decay from excited state to ground state by the irradiation of any electromagnetic radiation (EMR).

The emission of light from the compounds by the irradiation of electromagnetic radiation (EMR) was explained by the polish physicist Alexander Joblonski (Figure 1) [2]. Molecules irradiated with EMR lead to transition to the excited state ($S_0 \rightarrow S_1$). Excited state molecule is not stable, hence it returns to the ground state by emitting excess absorbed energy. The decay of emission is primarily of two types.

1.1.1 Non radiative decay: The absorbed energy is radiated as heat.

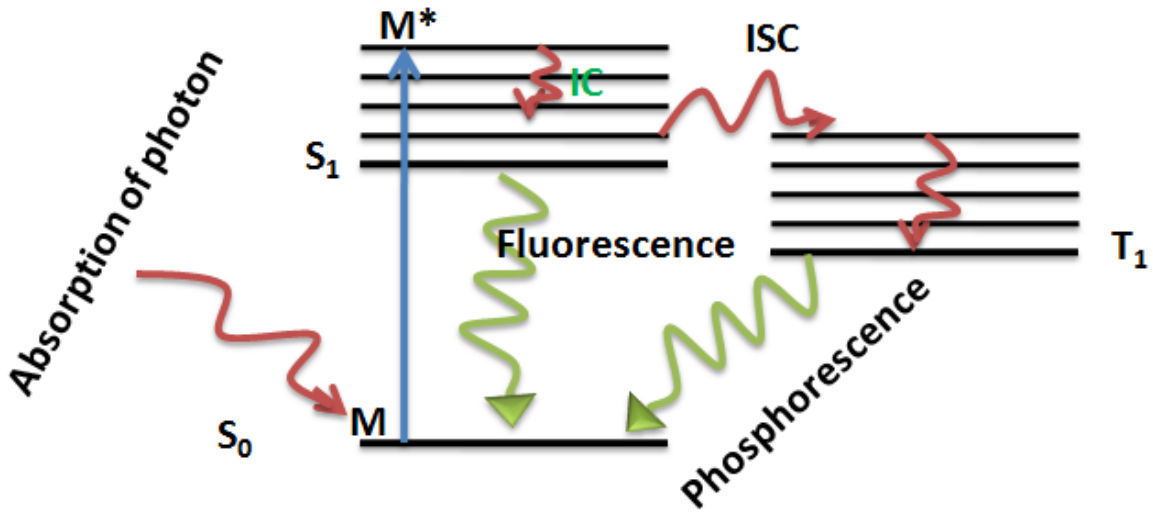

Figure. 1 Simplified Joblonski Diagram

1.1.1.1 Internal Conversion (IC)

The internal conversion (IC) is inter-electronic state process where the molecule has a transition from higher electronic state to lower electronic state without any emission of light [3]. It happens within the same multiplicity states e.g., singlet-to-singlet or triplet-to-triplet states. With increasing energy of the electronic state, the difference in energy becomes gradually less which increases the overlap of vibronic energy levels. It enhances the probability of internal

conversion. These type of transitions mostly observed in aliphatic compounds where the deactivation rate is too fast.

1.1.1.2 Inter System Crossing (ISC)

A spin crossover between electronic states of different multiplicity singlet state to a triplet state (S_1 to T_1) is known as intersystem crossing (ISC) [4]. The intersystem crossing process is more facile in presence of heavy atoms *e.g.*, Ir(III), Pt(II), Os(IV), iodine (I) or bromine (Br) etc. The presence of heavy atom will increase the probability of spin and orbital interaction *i.e.*, spin-orbit coupling (SOC) [5-6] that facilitates the intersystem crossing (ISC) process.

1.1.2. **Radiative decay**: The absorbed energy can be emitted as light.

Based on the nature of the excited state, the emission of light is divided into two types: (i) Fluorescence; (ii) Phosphorescence

1.1.2.1 Fluorescence

The emission of light from the singlet excited state to singlet ground state is called fluorescence. Fluorescence is a very fast process (excited state lifetime, ~10^{-9} s). Majority of organic luminescent molecules emit light through fluorescence [4].

1.1.2.2 Phosphorescence

The emission of light which make the transition from triplet excited state to singlet ground state is known as phosphorescence. Phosphorescence is a delayed process. In general, the excited state lifetime of phosphorescent compounds is extended from micro seconds to milli seconds, but it can be extended even for hours. Most of the heavy metal based organometallic complexes emit light through phosphorescence and the lifetime falls in the micro to millisecond range [4].

1.2 Synthesis of platinum(II) based luminescent compounds:

Platinum is one of the rarer elements in Earth's crust. The most common oxidation states of platinum are +2 and +4. The +1 and +3 oxidation states are less commonly observed. The platinum(II) forms the square planar geometry.

Cyclometalated Pt(II) complexes are playing an important role in the field of wide range of applications like, OLEDs, sensors, bioimaging, anticancer activity etc. The internal quantum efficiency of Pt(II) complexes can be reached theoretically 100% (triplet emitter), high stability, high photoluminescence (PL) efficiency and relatively short excited state lifetime as well as facile synthetic route make them promising for these applications. There are six different structural types of Pt(II) complexes have been used for these applications. These are C^C^N, C^N^N, C^N^C, N^N^N, N^N and C^N types co-ordinated complexes (**1-5**) of platinum(II) (Figure 2).

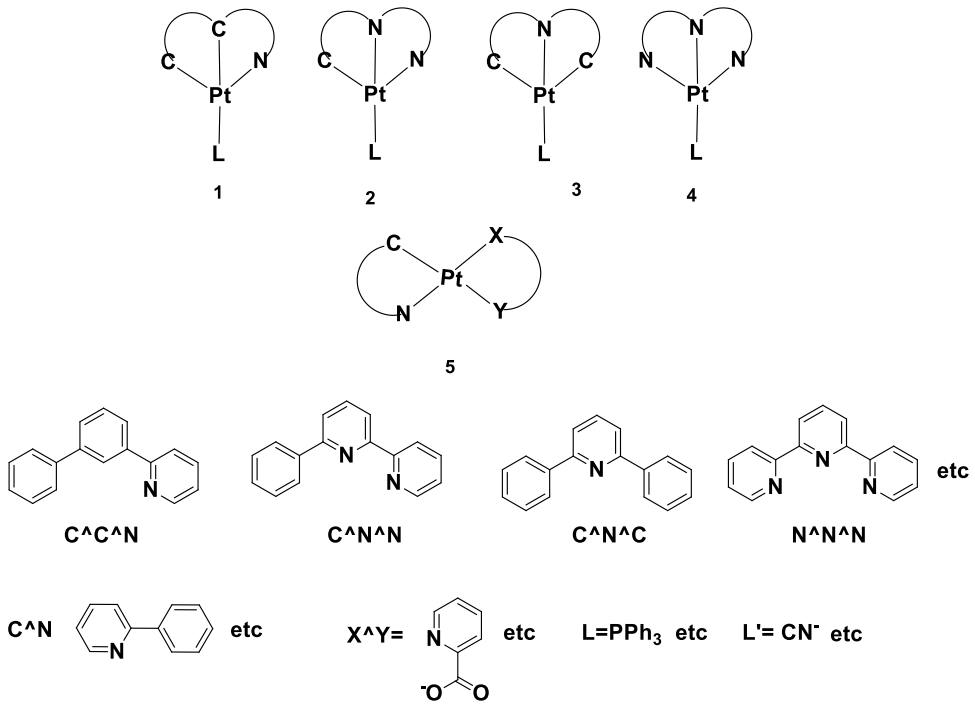

Figure 2. Structures of different types of cyclometalated Pt(II) complexes 1-4.

For the preparation of Pt(II) complexes with coordination of C^N type of ligands (**6-7**), usually the "bridge-splitting" strategy is a well-known approach. In this synthetic strategy, a cyclometalating ligand (*e.g.*, 2-phenylpyridine, 2-phenylbenzothiazole, etc.) is allowed to react with K_2PtCl_4 (Figure 3) in 2-ethoxyethanol under inert atmosphere producing the corresponding air-stable μ-chloro bridged precursor material as reported by Zelewsky [7]. On literature survey, few alternative reports have been found.

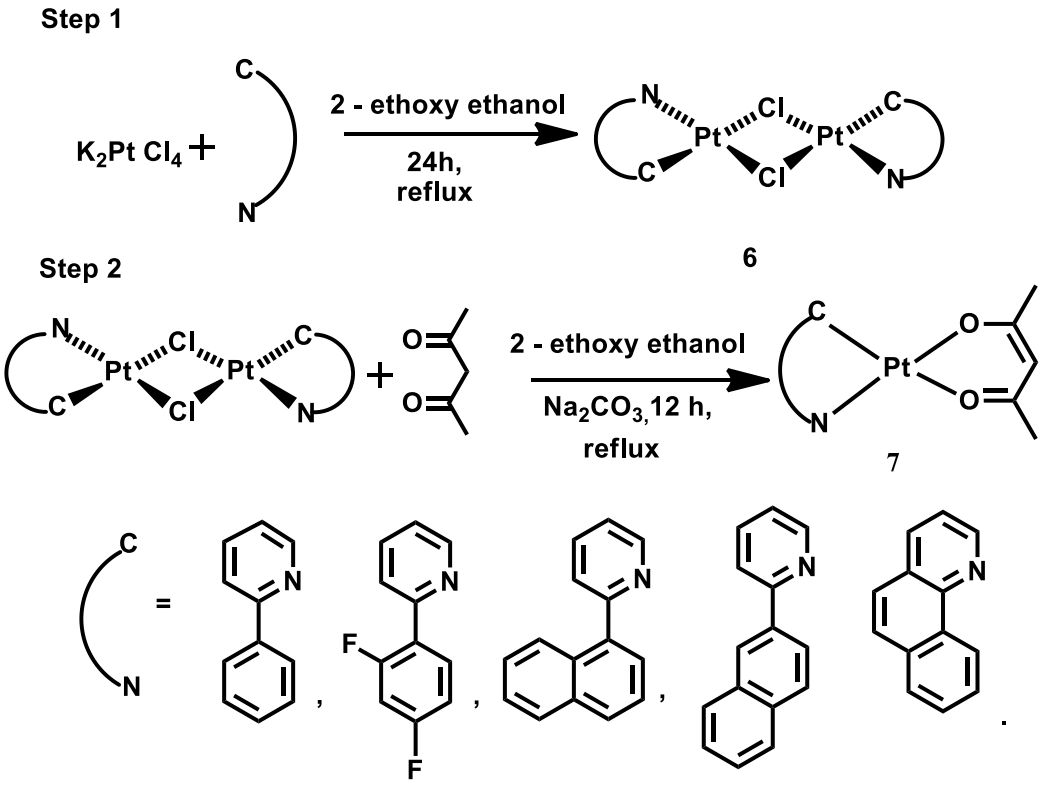

Figure. 3 Synthetic protocol of C^N type of ligands coordinated Pt(II) complexes 6-7.

For the preparation of Pt(II) complexes with C^C^N, C^N^N, C^N^C, N^N^N type of ligands, the cyclometalated ligand is allowed to react with K_2PtCl_4 (Figure 4) in acetic acid /or ACN/Water /or 2-ethoxyethanol under inert atmosphere producing the corresponding cyclometalated complexes [8] (*e.g*, complex **8**).

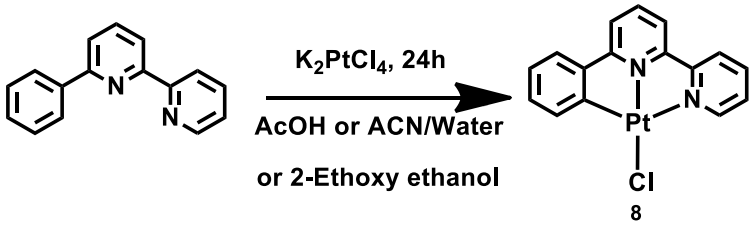

Figure. 4 Synthesis of N^C^N coordinated Pt(II) complexes

1.3 'Aggregation Induced Emission' (AIE) active compounds

1.3.1 Impetus for the synthesis of AIE active compounds: Most of the luminescent materials exhibit strong luminescence in their diluted solutions, but the emission intensity become quenched at their high concentrations, a phenomenon which is known as 'Aggregation-Caused Quenching (ACQ)' [9] effect.

N,N-dicyclohexyl-1,7-dibromo-3,4,9,10-perylenetetracarboxylic di-imide (DDPD) **9** (Figure 5) is the best example for ACQ effect. This molecule shows very bright emission in THF solution, but the emission intensity is gradually decreased when water concentration increased from 0% to 90% in the solution of DDPD in THF (in THF the compound is highly soluble and in water, the compound is completely insoluble, by the progress of addition of water to the THF solution, the degree of aggregation of compound will be increased). The molecule contains a disc-like perylene core. In the DDPD aggregates [9], the perylene rings may experience strong π–π stacking interactions. This prompts the formation of such detrimental species as excimers, thus it leads to the observed ACQ effect.

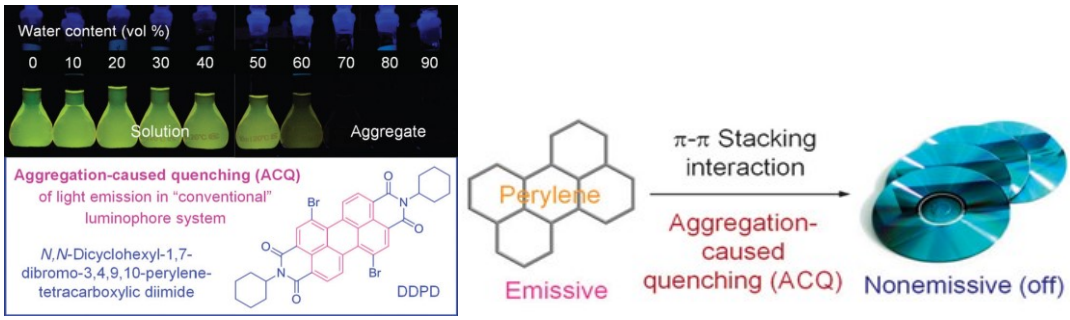

a **b**

Figure. 5 Fluorescence image of solutions/suspensions of DDPD (10 mM) in THF/water mixtures with different water contents. b) Planar luminophoric molecules such as perylene tend to aggregate as discs pile up, due to the strong π–π stacking interactions between the aromatic rings, which commonly turns ''off'' light emission. Adapted from Ref. 9 with permission from 'The Royal Society of Chemistry'.

1.3.2 Discovery and mechanism study behind of AIE activity of luminescent compounds:

To avoid the ACQ problem, a common phenomenon of luminescent materials, in 2001 Tang and his co-workers [9 - 10] discovered 'Aggregation Induced Emission' compounds in

hexaphenylsilole which is an exactly opposite phenomenon to ACQ. The aggregate formation increased their fluorescence quantum yields by more than 300 fold in comparison to their solution [7], hence these can be treated as a strong solid state emitters (Figure 6). Hexaphenylsilole (HPS) (**10**) is typical example of AIE luminogen [9]. The mechanism behind the AIE molecule is often found as the 'Restriction of Intra-molecular Rotation' (RIR) [9]. An isolated excited AIE molecule undergoes non-radiative decay by rotation of rotating units (e.g., phenyl etc), allowing the energy to decay without any emission. In contrast, the AIE molecules in their solid state/ or aggregated states, the intramolecular rotations of the rotating units gets restricted (RIR = intramolecular restricted rotations) that causes the molecules to block the non-radiative channels and open up a new radiative channels and thus showing a strong luminescence upon excitation. Apart from RIR, some other mechanisms have been proposed such as intramolecular charge transfer (ICT) [11-14], twisted intramolecular charge transfer (TICT) [11-14], *cis–trans* isomerisation [11-14], planarization [11-14], J-type aggregates [11-14] etc., to investigate the AIE activity of various compounds.

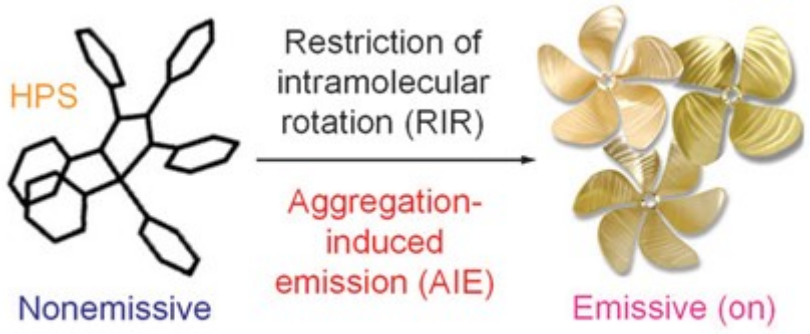

Figure. 6 The light emission of non-planar luminogenic molecule, hexaphenylsilole (HPS) is turned ''on'' by aggregate formation, due to the restriction of the intramolecular rotation (RIR) of the multiple phenyl rotors against the silole stator in the aggregate state. Adapted from Ref. 9 with permission from 'The Royal Society of Chemistry'

1.3.3 Heavy metal based AIE active compounds:

In general organic molecules are fluorescent in nature (PL lifetime ~10^{-9} s) and hence emit light from the singlet excited state. As a result, on a probability point of view, 25% singlet excitons will recombine that lead to a maximum 25% quantum yield. On the other hand, heavy

metal based compounds show phosphorescence along with fluorescence because of a strong spin-orbit coupling (SOC) leading to a 100% quantum yield theoretically.

1.3.3.1 Pt(II) based AIE active compounds:

Pt(II) complexes being a square planar structure, it has a tendency to stack one molecule to the other that lead to the formation of excimer. Hence these compounds result a rich electronic excited states, such as metal-metal to ligand charge transfer (MMLCT) (Figure 7), ligand-ligand to metal charge transfer (LLMCT) etc [15-20].

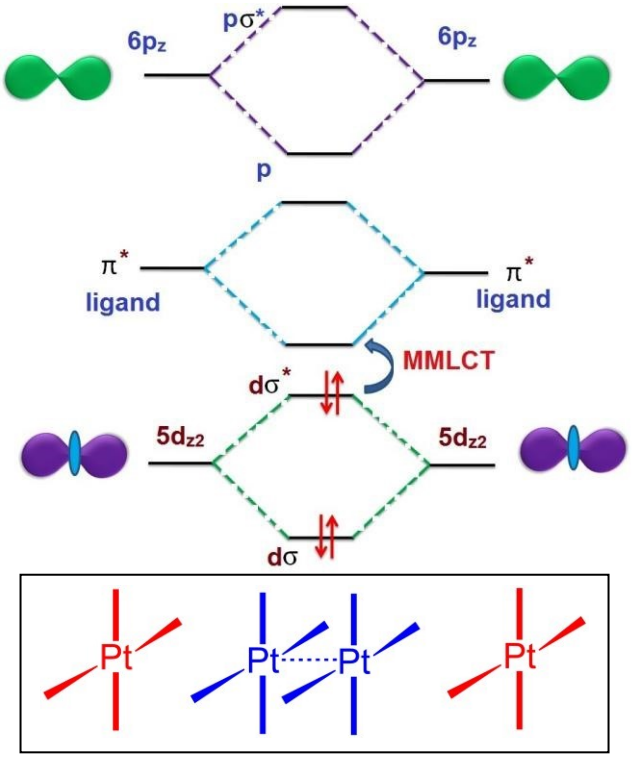

Figure. 7 Molecular energy diagram of Pt-Pt interaction (formation of MMLCT state) [15-20].

Che et al. reported [21] AIE active Pt(II) complex **11** (Figure 8) which shows virtually a non-phosphorescent in an acetonitrile solution. With addition of a large amount of water into an acetonitrile solution of Pt(II) complex results the enhancement of emission intensity of 37 times.

In the aqueous mixtures, the molecules of the Pt(II) complex form aggregates, which sets off the RIR process and boosts the phosphorescence.

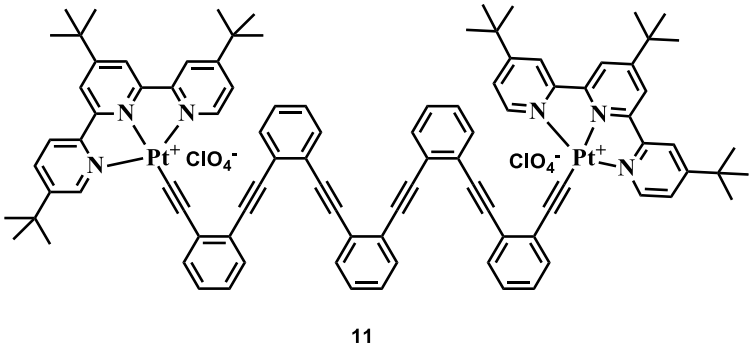

Figure. 8 Chemical structure **11**

Liu *et al*. reported [22] 'Aggregation Induced Enhanced Emission' (AIEE) active complexes (Figure 9) [Pt(ppy)(LX), Pt(dfppy)(LX) and Pt(fiq)(LX) (**12–17**), where ppy = 2-phenylpyridine, dfppy = 2-(2,4-difluoro-phenyl)pyridine, fiq = 1-(9,9-dioctylfluoren-2-yl)isoquinoline, LX = 2-(phenyliminomethyl)-phenol (L1), 2-(naphthyliminomethyl)-phenol (L2) and 2-(propyliminomethyl)-phenol (L3)]. By simply changing the N^O ligands, the emission property of the aggregated Pt(II) complexes have been tuned. From the experimental results and theoretical calculations, AIE mechanism of complexes is proposed to through ''restricted distortion of excited-state structure (RDES)''. These results provide a rational design principle for AIE-active metallophosphors.

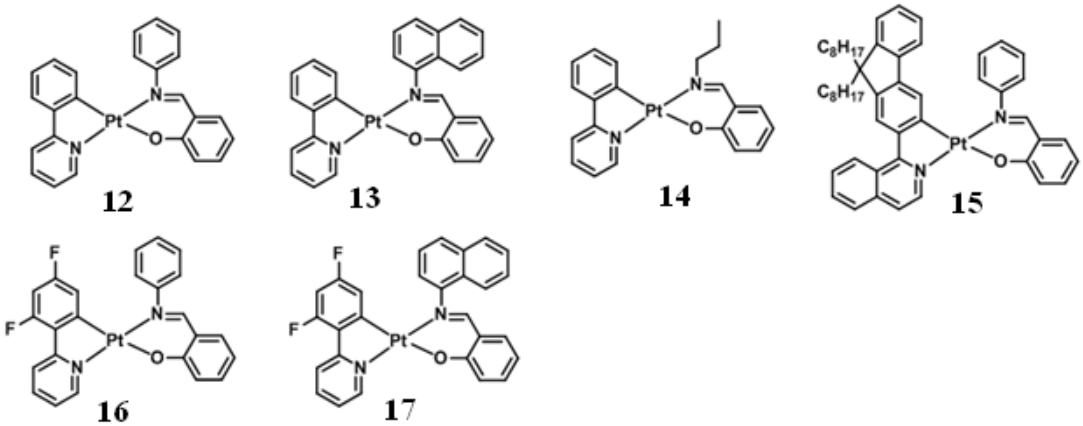

Figure. 9 Chemical structures of Pt(II) complexes **12-17**

Zhu *et al.* reported [23] a series of AIE active Pt(II) complexes (Figure 10) bearing difluoro-boron-dipyrromethene (Bodipy) acetylide ligands and different alkyl/aryl substituted 2,2'-bipyridyl ligands (**18-20**).

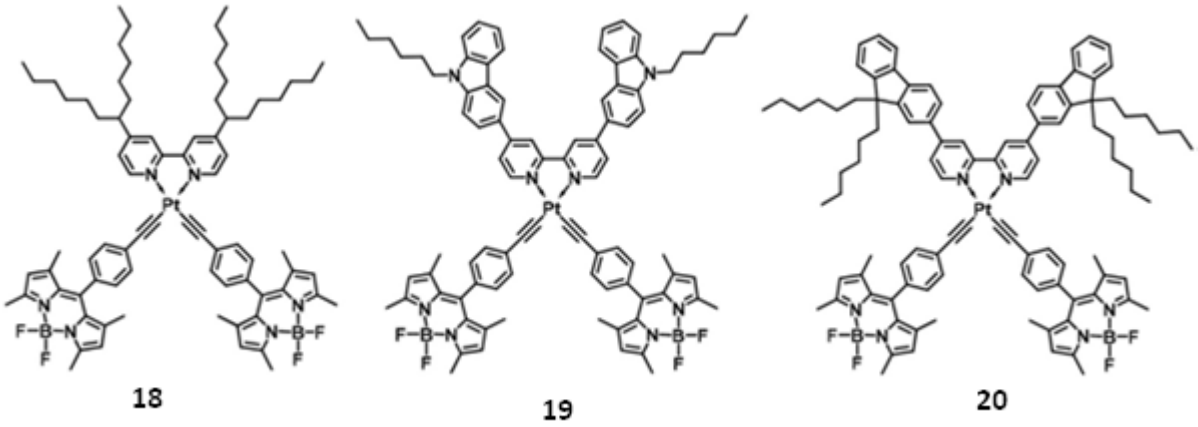

Figure. 10 Chemical structures of **18-20**.

T. Kanbara and his co-workers reported [24] cationic platinum(II) complexes **21-23** (Figure 11) containing secondary thioamide units showing aggregation-induced emission (AIE) activity in the mixed solvent (methanol/water) mixtures. The reason for the AIE activity is hydrogen bonding within the thioamide units and interionic interactions with counter anions.

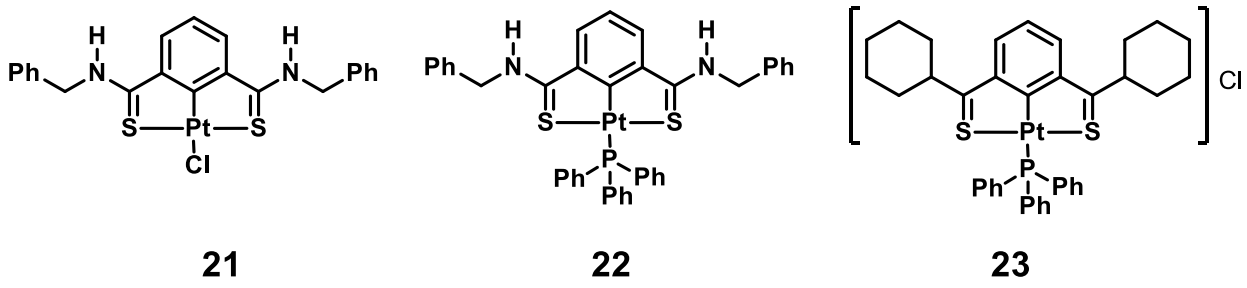

Figure. 11 Chemical structures of **21-23**.

Honda *et al*. reported [25] an amphiphilic pincer platinum(II) complex **24** (Figure 12) bearing a poly(ethylene oxide) (PEO) chain exhibiting AIE activity because of micelle formation in water. Hydrogen-bonding interactions between the PEO chain and an additive (trimesic acid)

enhance the AIE activity. Authors reported triphenyl part acting as hydrophobic and PEO as hydrophilic.

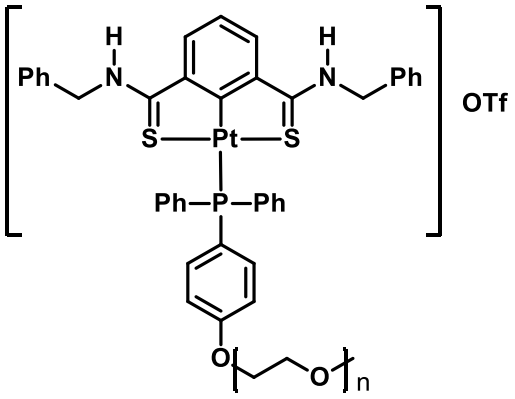

24

Figure. 12 Chemical structure of **24**

1.3.3.2 Small organic molecule based AIE compounds:

Panda et al. reported [26] AIE active fluorenyl-diformyl phenol Schiff base based compound **25** (Figure 13). The restricted intra-molecular rotation (RIR) process is operated in fluorenyl moiety.

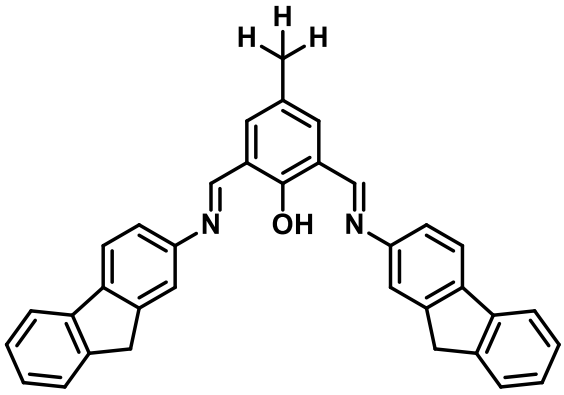

25

Figure. 13 Chemical structure of **25**

Lucia et. al reported [27] AIE active thiophene derivatives (TTE and TTB) **26-27** (Figure 14). AIE property is explained through the mechanistic understanding of the restriction of intramolecular rotation (RIR).

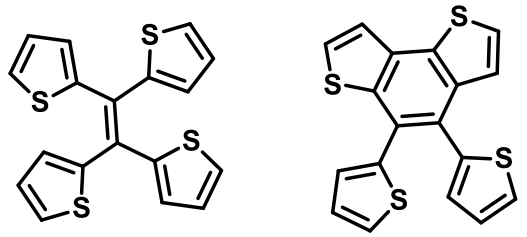

26 **27**

Figure. 14 Chemical structures of **26-27**

Three new AIE active cyanostilbene with tetraphenyl imidazole derivative (**28-30**) were synthesized [28] by J. Yang and co-workers (Figure15). The mechanism of AIE was proposed as restriction of phenyl rings present in the molecule.

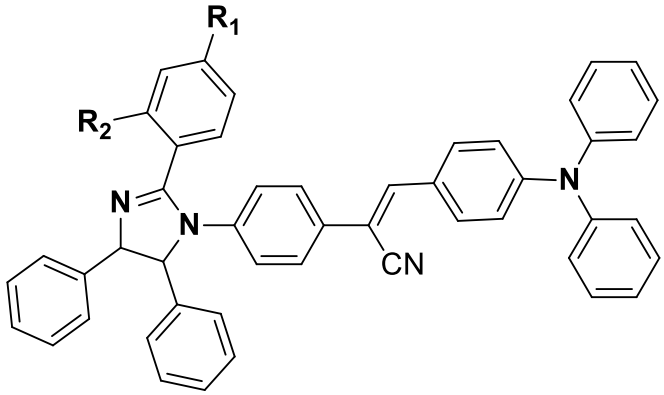

28 : R_1= -N(CH_2CH_3)$_2$, R_2=H
29 : R_1= H R_2=-OH
30 : R_1= -N(CH_2CH_3)$_2$, R_2=OH

Figure. 15 Chemical structures of **28-30**

Ohshita and his group reported [29] a water soluble AIE active compound of tetraphenylethene (WS-TPE) bearing with four sulfonate salt **31** (Figure 16). AIE activity was investigated by the gradual addition of an organic solvent into the WS-TPE aqueous solution.

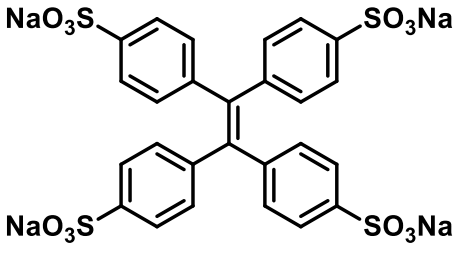

31

Figure. 16 Chemical structure of **31**

1.4 Mechanoluminescence

1.4.1 General overview of mechanoluminescence compounds (ML)

Mechanoluminescent materials are widely known as 'smart materials' which change their emission properties in presence of external stimuli such as pressure, grinding, stress, shearing, rubbing, milling and crushing [30-33]. If the change in emission of a compound occurs by applying a direct pressure (e.g., by pressing with hydraulic press) then it is called piezoluminescence. The mechanoluminescence (ML) falls in the category of fourth generation of materials after natural materials, synthetic polymer materials and artificial design materials [34]. This materials have been achieved a considerable attention by the scientific community because of their potential applications in mechanosensors, security papers, and optical storage. It is obvious that the development of such kind of materials will lead the world to the development of next generation technologies [35].

Upon exerting the mechanical stimuli, the change in intermolecular interactions such as π–π interaction, dipole-dipole interaction or hydrogen bonding can lead to different morphological changes such as crystalline to amorphous states, from stable to metastable liquid crystalline phase, or between two different crystalline phases [36-37]. With respect to molecular level mechanism, the observation of ML properties is resulted from the subtle/major change in

the structure of molecular packing upon grinding/pressing. Most of the materials exhibiting ML property are irreversible in nature, but these can be reverted easily by solvent fuming [36-37]. However, efficient mechanism of ML was still not clear. The first report of organic compounds exhibiting ML was published by Weder et al. [38]. In this case, two cyano groups substituted oligo(p-phenylenevinylene) was blended with low density poly(ethylene) as a matrix. The similar observation was not obtained with changing the matrix from oligo(poly(ethylene)) to polyethylene tetrathalate (PET) because of the higher solubility of dyes in PET. But the incorporation of long chain alkyl group in the dye molecule resulted microphase separation that led to the formation of excimer. ML property is observed because of the transformation of H-aggregated species to the metastable species. However, the study of ML property with the metal-complexes are limited as compared to the organic dyes, though the coordination/organometallic complexes combining with metal ions and ligands would result more interesting ML properties.

1.4.2 AIE based ML compounds: As per our earlier discussion, the emission of most of the luminescent materials were found to be quenched in aggregated state or solid state (ACQ) [39-40] which poses a serious obstacle in the development of efficient mechanoluminescent materials. There are several advantages for ML materials on replacing ACQ materials by AIE active materials. Firstly, the strong emission in the solid state improves the quantum efficiency. Secondly, the RIR based AIEgens have a propeller type twisted geometry which resulted a weak interaction in the crystal packing. The loosely packed molecules can transform themselves in different morphologies (crystalline and amorphous) by means of grinding/pressing. Many AIE mechanoluminescent materials were discovered by Tang [41], Park [42], Chi [43], Weder [44], Xu [45], Tian [46] and their co-workers. The mechanism of ML materials were attempted to explain by these groups but often the proposed mechanism is not completely clear [37]. The design and syntheses with high spectral shift, multicolor and reversibility in solid phase ML materials still poses a great challenge to the scientists.

1.4.2.1 AIE based ML organic/polymeric compounds

1.4.2.1.1 Cyanostilbene: In 2010, S. Y. Park and co-worker synthesized a multi-stimuli responsive cyanostilbene-based highly luminescent molecular sheet (2Z,2′Z)-2,2′-(1,4-phenylene)bis(3-(4-butoxyphenyl) acrylonitrile) (DBDCS) (32) which exhibits two-color fluorescence (Figure17) [42]. The switching of color was highly sensitive towards pressure,

temperature, and solvent vapor. The emission color gets changed from green to blue after heating the sample to 125 °C for an hour.

The author claimed that the cause for the multi stimuli response was the change in the intermolecular multiple C-H---N and C-H---O hydrogen bonding formed between two-directional molecular sheets with shear-sliding capability. The two states were recognized based on the structural, optical, photo physical, and computational studies *i.e.* metastable green emitting phase (G-phase) with λ_{max} = 533 nm and thermodynamically stable blue emitting phase (B-phase) with λ_{max} = 458 nm. The mechanism of phase change was elucidated based on molecular packing where G-phase crystal are arranged in slip stacks along the long molecular axis with a pitch angle of 26.6° and distance between the adjacent molecular sheets was 3.7 Å, consistent with the reported π-π stacking distance. The driving force for this specific slip-stack formation is the antiparallel coupling between the local dipoles in adjacent molecular sheets. After thermal annealing of the G-phase crystal the obtained B-phase showed a head to tail arrangement and they have proposed slip stacks pitch angle of 26.6° based on d-spacing (27.9 Å) with the molecular Van der Waals length (31.4 Å) where the formation of π-π stacking was diminished.

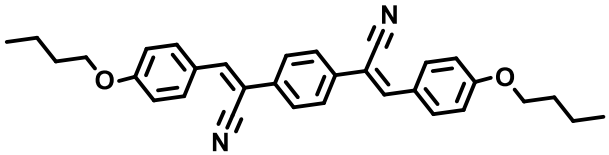

DBDCS (32)

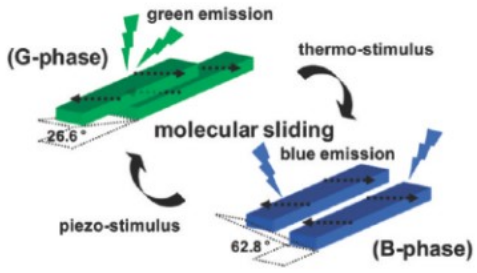

Figure. **17** Molecular structure of DBDCS and single crystal state Illustration of two different modes of slip-stacking in DBDCS molecular sheets, dictated by different ways of antiparallel/head-to-tail coupling of local dipole. Reprinted from ref 42. Copyright 2018 American Chemical Society.

Based on the previous structural framework, Park and co-workers had synthesized a new dicyanodistyrylbenzene-based compound with unique polymorphism and ML behavior (Figure 18). The authors had found many secondary interactions such as local dipole interaction, C–H---π interaction, and C–H---N hydrogen bond which were responsible for molecular stacking

assembly, as well as in polymorphic, AIEE and mechanoluminescence behaviors of (2Z, Z)-2-(1,4-phenylene)bis(3-(naphthalen-2-yl)acrylonitrile) (NDCS) (**33**) [47]. The polymorphs of NDCS showed two emission *i.e.* phase I (λ_{max} = 508 nm) and phase II ($\lambda_{ma\ x}$= 554 nm). The recrystallization of NDCS (**33**) done by using THF and MeOH. NDCS showed a yellow emission ($\lambda_{ma\ x}$ = 554 nm, phase II) which was changed to green emission (λ_{max} = 508 nm, phase I) after melting and solidification of pristine NDCS (**33**) powder. Further grinding the melt-solidified (phase I) was changed to greenish yellow emission (λ_{max} = 531 nm). The change in the solid state emission was investigated using PXRD and life time data. The phase I of the NDCS showed long emission lifetime (τ = 15.2 ns) and small tilt angle of 46 ^{o} measured from the PXRD patterns. These data revealed the slip-stacking along the molecular axis was originated by antiparallel coupling of the local dipoles resulted a strong π-π interaction. However, In case of phase I, the life time was found to be τ_1 = 1.1 ns (82%) and τ_2 = 3.5 ns (18%) with large tilt angle of 61^0 revealed the less π-π interaction. The after grinding sample showed totally different life time (τ_1 = 0.9 ns (45%), τ_2 = 4.5 ns (35%), and τ_3 = 15.6 ns (20%) and PXRD pattern suspecting the formation of different species. Finally other concluded that the emission color of phase I and phase II was originated from different coupling situations such as ground state dimeric coupling, or excitonic coupling (for phase I) and excited state dimeric coupling (for phase II).

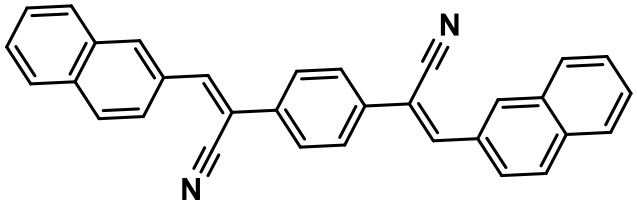

NDCS (33)

Figure.**18** Molecular Structure of NDCS (**33**).

A piezoluminescence AIE active fluorescent compounds (Figure 19) were synthesized by J. Huo and co-workers by introducing thiomethyl substituent to the peripheral positions cyano oligo (p-phenylene vinylenes) (CN-OPV), namely, 1,4-bis(1-cyano-2-(4-thiomethylphenyl)ethenyl) benzene (TOPV2) (**34**). As discussed earlier, the cyano-stilbene derivatives were well known for their piezoluminescence properties [48]. After applying the

pressure the emission color change which was attributed to change in the molecular packing revealed from PXRD data.

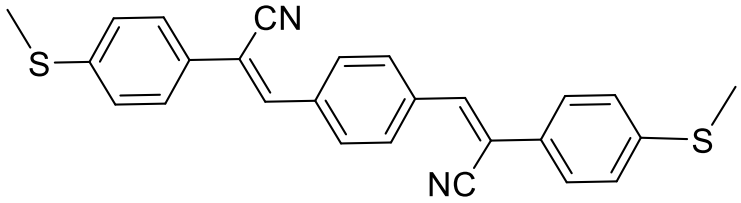

TOPV2 (34)

Figure. 19 Molecular structure of TOPV2 (**34**).

A cyanostilbene-based derivative (α-CN-TPA) (**35**) with ML property was synthesized by C. Zhang which shows the different emission colour under external stimuli (Figure 20) [49]. A turn on emission (dark no emission to green emission) was obtained with emission maxima 498 nm ($\phi < 0.1\%$) to 512 nm ($\phi = 24.1\%$). A sky blue emission ($\lambda_{max} = 490$ nm, $\phi = 13.3\%$) was obtained after heating the sample at 130^0C for 2 minutes. The solidified powder was obtained after melting and air dried (Melted-S) showing a green emission ($\lambda_{max} = 515$ nm, $\phi = 26.8$ %). The change in the emission property with varying external stimuli has been explained based on PXRD data. The sharp and intense reflection peaks obtained in PXRD is observed to match well with simulated XRD from single crystals however the ground sample showing the broad peak revealing the transformation from crystalline to amorphous. But the PXRD data of Melted-S was showing a new diffraction peak indicating the transformation from one crystalline phase to another crystalline phase. It is concluded that the phase transformation was responsible for different emission.

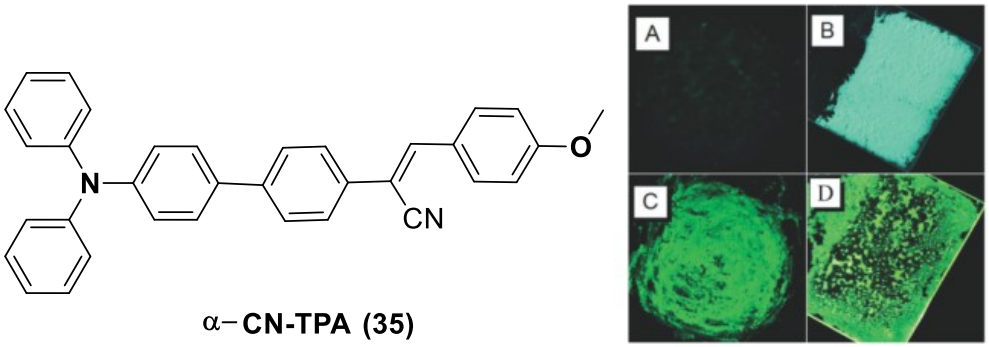

Figure. 20 Photographs of the α-CN-TPA (**35**) powder under 365 nm UV light: (A) pristine powders, (B) the original powders annealed at 130 °C for 1 min, (C) after grinding pristine powder and (D) after heating powders to melt and solidification at room temperature(Melted-S). Reproduced from from Ref. 49 with permission from The Royal Society of Chemistry

Y. Ma and co-workers synthesized the two cyanostilbene isomers with triphenylamine; (Z)-2-(4-(diphenylamino)phenyl)-3-(4-methoxyphenyl)-acrylo nitrile (TPA-Can) (**36**) (blue emission) and (Z)-3-(4-(diphenylamino) phenyl)-2-(4-methoxyphenyl) acrylonitrile (TPA-CNb) (**37**) (green emission) [50]. The solid state efficiency of the compound was recorded and found to be 44.9% and 7.7% TPA-CNb (**37**) (twisted geometry) (Figure 21). The TPA-CNa is AIE active and showing reversible ML and thermofluorochromic behaviors. The emission color changes from sky blue (λ_{max} = 470 nm) to green (λ_{max} = 502 nm, ϕ = 21.2%) after grinding by spatula. The green emission easily reverts back to its original sky blue emission after heating at 60 °C or fuming. The PXRD data revealed that the emission change after grinding was attributed to conversion of a well-ordered phase (crystalline phase) to a poorly organized phase (amorphous phase).

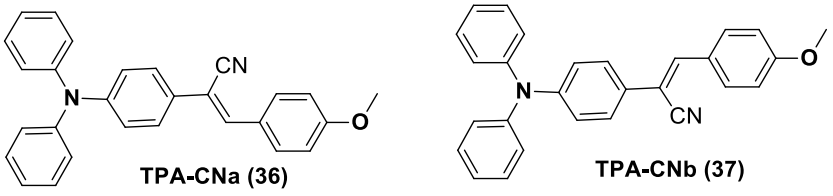

Figure. 21 Molecular structures of two isomers of **36** and **37**

1.4.2.1.2 Distyrylanthracene derivatives:

Many ML materials have been synthesized using long flexible alkyl or alkyloxy side chains which made them less thermally stable with high glass transition temperature and high decomposition temperature.

According to the earlier reports, the 9,10-distyrylanthracene derivatives were renowned for their strong solid state emission as well as many of them exhibited PZLAIE (Piezio luminescence aggregation induced emission) property. It has been proved that the restriction of intramolecular rotation between the 9,10-anthylene core and the vinylene segment were responsible for AIE phenomenon.

In 2011, J. Xu and co-workers designed and synthesized a 9, 10-distyrylanthracene derivative with TPE core (TPE-An) (**38**) (Figure 22) [51]. It was hypothesized that the twisted geometry and weak π-π interaction of the compound might lead to loose packing. The effect of pressure may lead to planarization of molecular conformation or slip deformation which results the red shifted emission. The authors found that the compound change its emission from green (506 nm) to yellow (574 nm) after grinding and reverted into its original form after annealing. Based on the UV-Vis spectra, the red shift in the emission spectra was attributed to planarization of molecular conformation. Further, the study of WAXD (Wide-Angle X-ray Diffraction) supports the mechanism of PZL is occurring due to the transformation from crystalline phase to amorphous phase. Furthermore, the obtained cold-crystallization peak ~336 °C in DSC data, confirmed that the existence of meta stable phase in ground sample.

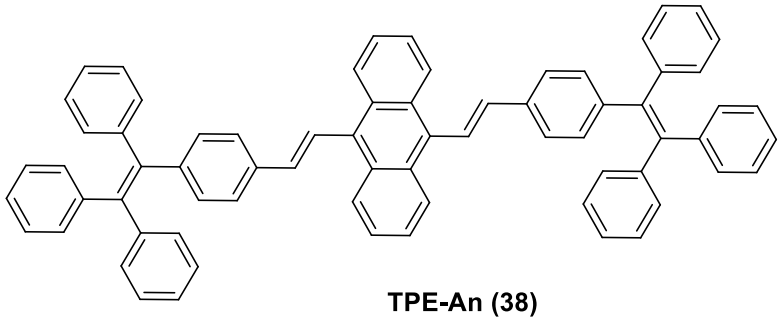

Figure. **22** Molecular structure of TPE-An (**38**).

In 2012, a series of AIEE compounds (**39-42**) with tetraphenylethylene and triphenylethylene end group were strategically synthesized by J. Xu and co-workers where two of them exhibited the piezoluminescence (PZL) property along with AIEE property (Figure 23) [45]. The authors claimed that the presence of tetraphenylethylene as end group may be more bulkier than triphenylethylene end group. This steric effect may play an interesting role in PZL. In case of tetraphenylethylene end group, the degree of order of molecular aggregation gets decreased in presence of pressure and it was very difficult for the aggregates to revert into the unpressed state. In presence of heating, the aggregate at pressed state may be reverted to the unpressed state.

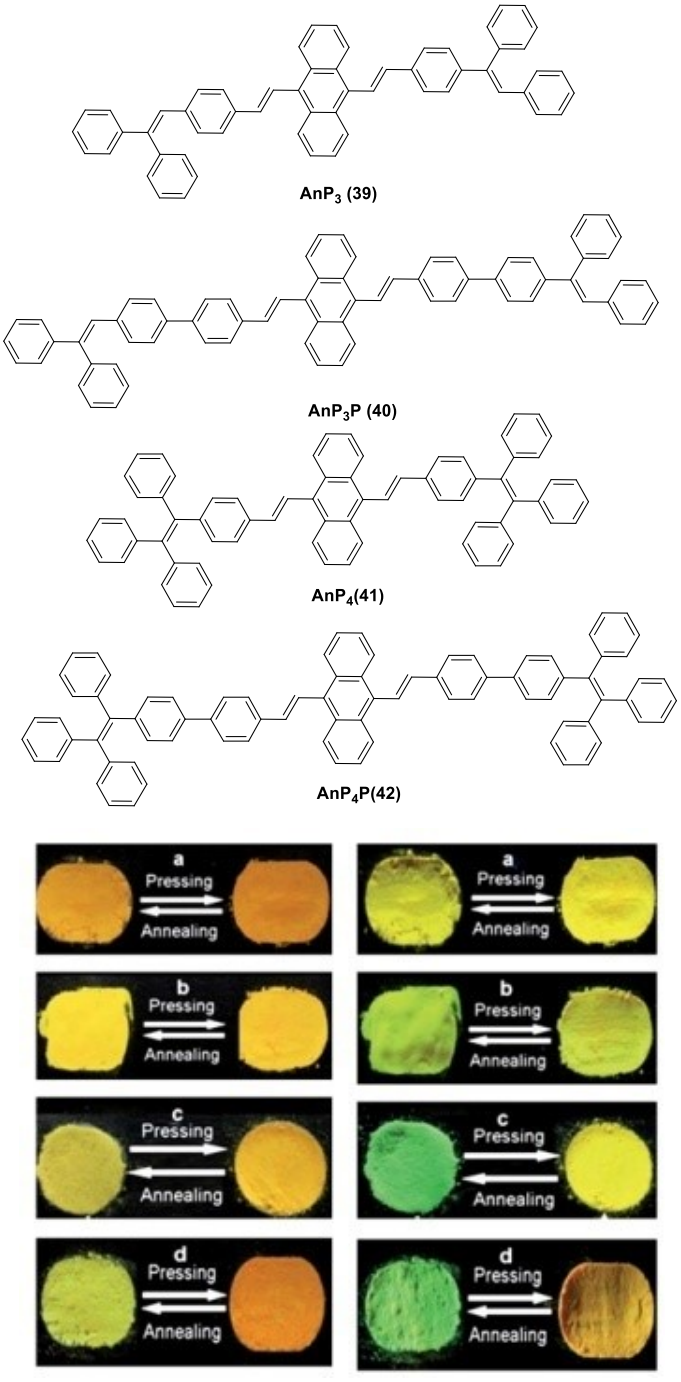

Figure. **23** The images of AnP3 (**39**) (a), AnP3P (**40**) (b), AnP4 (**41**) (c) and AnP4P (**42**) (d) takenat room temperature under (left column) natural light and (right column) UV light after pressing and annealing. Reproduced from Ref. 49 with permission from The Royal Society of Chemistry.

In this sequence, one new compound (**43**) with tetraphenylethene units connected in the core with tetra-substitution was synthesized by same group (Figure 24) [52]. The emission color was changed from orange (561 nm) to red (583 nm) with ΔML = 22 nm after grinding revealed its ML property. According to the reports, it is the third mechanoluminescence AIE active compound. The mechanism of ML property was explained based on WAXD data. The ungrounded sample showed a sharp and reflected peak (at 2θ = 6.4, 9.6, 10.3, 11.1, 13.7, 17.8 and 20.5°) which transformed into a broad and diffused peak after grinding indicating the phase transformation (crystalline to amorphous).

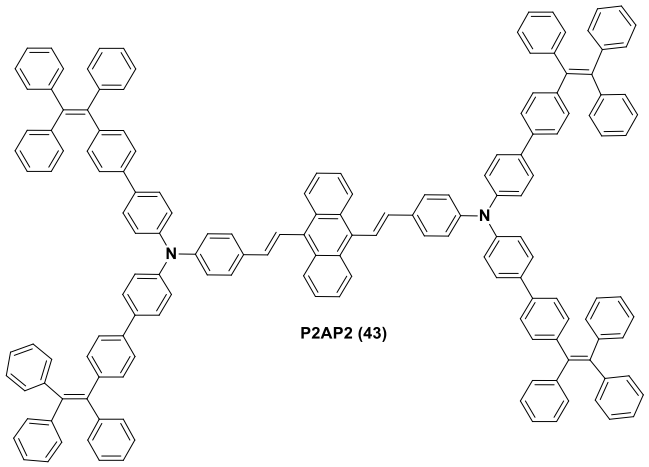

Figure. **24** Chemical structure of the compound, **43**.

W. Yang and co-workers synthesized 9,10-Bis(N-alkylphenothiazin-3-yl-vinyl-2)anthracenes (PT-Cn) with different carbon number of alkyl chain (**44-51**) (n= 2, 3, 5, 6, 7, 9, 12, 18) (Figure 25) [53]. The author found good relationship between PZLAIE property and the length of the carbon chain where the increasing number of carbon chain resulted a larger piezoluminescence shift (ΔPZL = 71 nm). The piezoluminescence behavior of these compounds were checked by using IR pellet press (30s at 1500 psi) where they changed their emission maxima from C2 = 577 nm, C3 = 568 nm, C5 = 563 nm, C6 = 554 nm, C7 = 546 nm , C9 = 547 nm , C12 = 537 nm, C18 = 517 nm to C2 = 620 nm, C3 = 608 nm, C5 = 607 nm, C6 = 605 nm, C7 = 600 nm, C9 = 5 99 nm, C12 = 595 nm, C18 = 588 nm respectively. The reversibility of the

compounds has been checked by repressing and fuming and found to be highly reversible in nature.

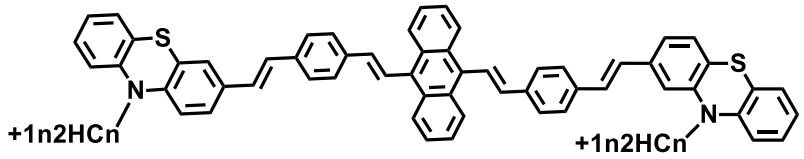

44-51

PT-Cn (n=2, 3, 5, 6, 7, 9, 12, 18)

Figure. 25 Chemical structure of the compounds **44-51**

1.4.2.2 Several other AIE molecular systems with mechanoluminescence properties

Till date, most of the AIE molecules have been synthesized by using silole, tetraphenylethene and cyanostilbene frameworks. Apart from these, the AIE compounds have been synthesized with using the other frameworks.

1.4.2.2.1 Oxadiazole derivatives

A V-shaped organic fluorescent compound bis(2-aryl-1,3,4-oxadiazol-5-yl)diphenyl sulfone (OZA-SO) (**52**) based on D-A system was synthesized by J.-M. Lu and co-workers. It exhibited AIEE and ML behavior (Figure 26) [54]. The crystal emission of the compound was found to be green emissive (λ = 510 nm) which was converted to strong yellow light (λ = 570 nm) after grinding. Additionally, the compound showed the thermofluorochromic property where the pristine powder changes its emission from green to yellow after heating at different temperature (125, 195, or 245°C) followed by cooling. The recorded WXRD data of the crystals (obtained after slow evaporation) exhibited sharp peaks and the broad peak from amorphous sample (obtained after fast evaporation). The red shifted emission was observed because of the formation of dimer after grinding.

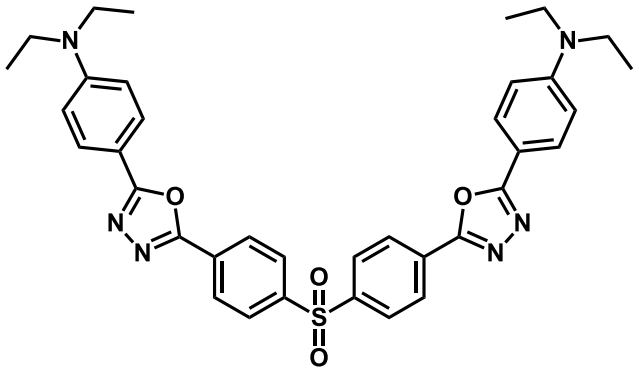

OZA-SO (52)

Figure. 26 Chemical structure of the compound **52**.

1.4.2.2.2 Schiff-base Derivatives:

Recently, a salen type salicylaldehyde based Schiff base linking with methylene bridges $(CH_2)_6$ was reported by J. Liu and co-workers (Figure 27). The compound (**53**) was found to be non-emissive in the crystalline form but resulted bright emission after grinding (turn-on fluorescence) [55]. The same emission was observed after fast evaporation of the dissolved crystals in DCM solution. The ML mechanism was proposed to be lamellar packing which favors molecular movement under external mechanical pressure. According to the author, by the effect of external stimuli (grinding), the π–π interactions may be damaged, and resulted the turn on fluorescence. In case of fast evaporation, the crystals may not fully dissolve and not getting much time to arrange themselves in the regular manners (stack closely and regularly by π–π interactions). This irregular arrangement creates crystal defects and resulting in a crystal-defect-induced emission.

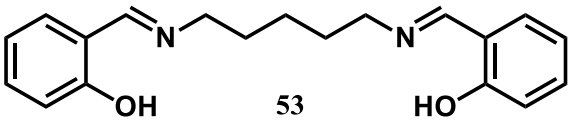

53

Figure. **27** Chemical structure of **53**.

1.4.2.2.3 Pyran derivatives:

A strong red emissive quinoline malononitrile derivative (denoted as ED) (**54**) was designed and synthesized via alteration of the conventional ACQ dicyanomethylene-4H-pyran

(DCM) derivative (denoted as BD) through crystal engineering (Figure 28) [56]. The synthesized compound showed an extraordinary self-assembly property in different solvents which formed a "waving ribbons" with a length of 6 mm and a diameter of 10 μm. The crystal packing of the BD showed a head to tail J- type aggregation *via* different interaction like CH···π and CH···N supramolecular interactions. According to the author, these types of morphology or stacking arrangement of the aggregate can be easily destroyed by external stimuli. The ED exhibited emission color change from orange (λ = 605 nm) to red (λ = 645 nm) after grinding. The observed red shifted emission spectrum was ascribed to the strong π-π interaction. The mechanism of the ML was explained with the help of WAXD and DSC data, revealing that the ML was originated due to morphology change from crystalline to amorphous.

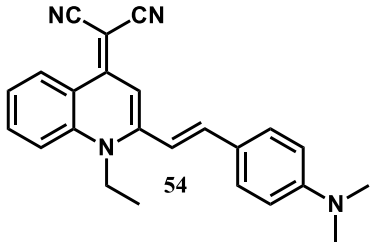

Figure. **28** Chemical structure of the compound **54.**

1.4.2.2.4 Butadiene derivatives:

A new 4, 4′- ((Z,Z)-1,4-diphenylbuta-1,3-diene-1,4-diyl)dibenzoic acid (TABD-COOH) (**55**) exhibited the MLAIE (Mechanoluminescence Aggregation Induced Emission) property was reported by Y. Dong (Figure 29) [57]. The emission of compound was changed from blue (F-form) to yellow-green (G-form) upon grinding of TABD-COOH using a spatula or mortar, and found to be fully reversible after fuming by solvent vapor (*e.g.*, MeOH, EtOH, THF). The methylester (TABD-$COOCH_3$) exhibited AIE activity but it was not ML active. The recorded IR data of F-form showed a broad peak near 3430 cm^{-1} indicating the existence of H-bonding interactions where the G-form exhibited relatively sharp peak at 3423 cm^{-1} resulting from ''free'' O–H bands. The strong bonding was further supported by the C–O stretching which changed from 1205cm^{-1} (F-form) to 1267 cm^{-1} (G-form). According to author, these weak interactions were easily destroyed in presence of pressure. Finally the change in the emission from blue to green was further supported by PXRD and DSC data. The PXRD data of F-form showed

crystalline nature while G-form displayed two exothermic peaks at 133 and 151°C (DSC data). Hence, the mechanoluminescence behavior of this compound was attributed to the phase change from crystalline nature (with strong hydrogen bonding interactions) to amorphous nature (no hydrogen bonding interactions).

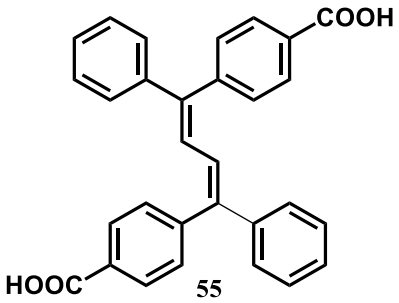

55

Figure. **29** Chemical structure of the compound **55**.

A similar types of 1,3-butadiene derivatives (**56-58**) were synthesized (Figure 30) [58] with different types of substituent such as $COOCH_3$, CF_3 and NPh_2. The compound with NPh_2 groups showed maximum spectral shift after grinding (ΔML = 20 nm). The emission maxima of TABDE-NPh_2 (dimethyl 4,4'-((1Z ,3 Z)-1,4-bis(4-(diphe-nylamino)phenyl)buta-1,3-diene-1,4-diyl)dibenzoate) derivative was changed from green (520 nm) to yellow (540 nm) however the other derivatives, TABDE (dimethyl 4,4'-((1Z,3Z)-1,4-diphenylbu-ta-1,3-diene-1,4-diyl)dibenzoate) and TABDE-CF3 (dimethyl 4,4'-((1Z,3Z)-1,4-bis(4-(trifluoromethyl)phenyl)buta-1,3-diene-1,4-diyl)diben-zoate) were not shown any significant change after grinding. These compounds were reversible ML in presence of polar solvents dissolving or by the presence of (MeOH, EtOH, and THF) vapour. The PXRD data of the ground sample showed broad and featureless peaks whereas ungrounded sample exhibited sharp and intense peaks. The authors proposed that the ML of these compounds were highly dependent on their electronic structures. In comparison to TABDE and TABDE-CF_3, TABDE-NPh_2 was a good D-A system being capable of forming ICT interactions. Hence, the more push-pull interaction and the molecular polarity of TABDE-NPh_2 have generated more dipole-moment which was favorable to the occurrence of sharp mechanoluminescence change.

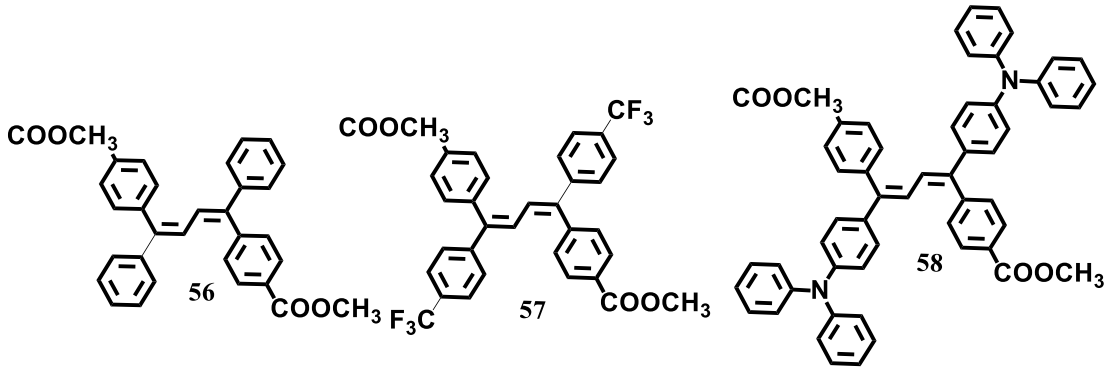

Figure. **30** Chemical structures of the compounds **56-58.**

1.4.2.2.5 Lactone, anthracene and pyrene derivatives

A new rigid, planar, and well-conjugated endo-cyclic alkenyl lactone framework (**59-61**) with thienodipyrandione (TDP) was designed and synthesized by S.-S. Sun and co-workers (Figure 31) [59]. Strategically, the author designed the framework in such a way where the TDP moiety was introduced in between the anthracene or pyrene groups. The synthesized compounds exhibited higher order of conformational twisting and unique supramolecular stacking architectures in comparison to 9,10-distyrylanthracene vinylene moiety. The emission of TDAn and TDAnPh were changed from green (507 nm) and bluish green (491 nm) to yellow (548 nm and 540 nm), respectively. The authors concluded that both the compounds exhibited a highly twisted conformation in solid state and become planer to some extent in amorphous state after applying the pressure. Hence, the piezoluminescence of these compounds are attributed to phase change from crystalline nature to amorphous nature.

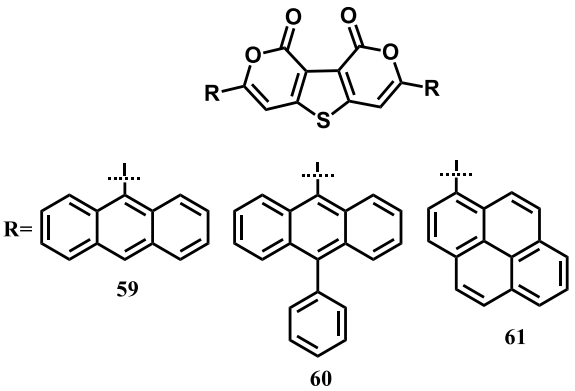

Figure. **31** Chemical structures of the compounds **59-61**.

1.4.2.3 ML with hypsochromic Shift: Crystallization Induced Emission Enhancement (CIEE)

Tang and co-workers investigated the solid state emission property of many silole derivatives (**62-64**) [60-62] which shows a blue shifted emission as compared to ground powder. In the first report, the hexaphenylsilole (HPS) [63] recognized as a very good green emitter (~495 nm) but the same compound shows a blue emission (~462 nm) from its crystalline state (Figure 32). In general, the emission spectra of the organic compounds with regular packing results in the red shifted emission (because of delocalized excitons), but the HPS showed the opposite behavior [64]. To investigate this property, the inner wall of a quartz cell was coated by HPS which showed green emission but the emission tuned to blue in presence of acetone fume. Finally, the authors concluded that the HPS turned from amorphous to crystalline after acetone fuming. Thus, the change in the emission of HPS from green to blue was ascribed to CIEE property.

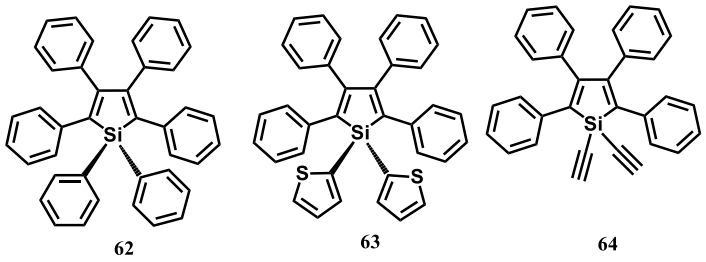

Figure. **32** Chemical structures of the compounds, **62- 64.**

One more CIEE active compound 2-diphenyl-3,4-bis(diphenylmethylene)-1-cyclobutene (HPDMCb) (**65**) was synthesized by Tang and co-workers which formed different types of aggregations in different water fractions (Figure 33) [65]. The AIE property of HPDMCb was investigated, which showed blue emission at f_w= 70% and green emission at f_w = 90%. According to the authors, the blue and green emission at different water fractions (f_w = 70% and 90%) were attributed to the formation of crystalline and amorphous aggregates, respectively. Further investigation of CIEE, the thin film of HPDMCb was prepared that exhibited green emission (508 nm) which turned into a blue emission (474 nm) with three fold higher intensity after annealing at 100 °C for 5h. The calculated full width at half maximum suggested the

compound after annealing changed into crystalline state which was confirmed by TEM image of as-prepared and annealed film.

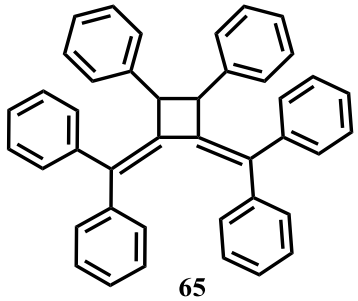

65

Figure. 33 Chemical structure of the compound **65**.

To investigate the mechanism of CIEE [66], one has to explore the structure property relationship, with the help of their crystal packing. In most of the cases, the CIEE active molecules having a propeller-type structure, resulted twisted geometries which were responsible for blue shift in the emission under grinding. The twisted geometry is resulted in a weak packing pattern where the possibility for formation of strong interaction such as π-π or H/J types of aggregate is neglected in the solid state. The loose packing in amorphous state helping the rotors to rotate or vibrate at some extend which lead to quenching in amorphous state. However, in the crystal structure the molecules experienced many intermolecular short contacts such as C−H···π and C−H···O which helped to rigidify the molecular motion. The red shifted emission spectra of CIEE compounds after grinding may attribute to geometry planarization after applying pressure. A series of diaryldibenzofulvenes (DPDBs) (**66-70**) were investigated for CIEE property (Figure 34) [67a]. The aggregate of **67** at higher water contents showed non-emissive nature but the emission changed to bright emission with a λ_{em} of 462 nm after one hour. The process showed its fast crystallization property which made this compound as virtually CIEE active. The (4-biphenylyl)phenyl dibenzofulvene (BpPDBF) (**67**) was found to be CIEE active [68], which showed 32 fold solid state quantum yield enhancement in the crystalline state as compared to amorphous state. The crystalline compound exhibited blue emission whereas the amorphous powder became non emissive. The presence of one more phenyl on the BpPDBF made the geometry more twisted and showed blue shifted emission as compared to DPDB.

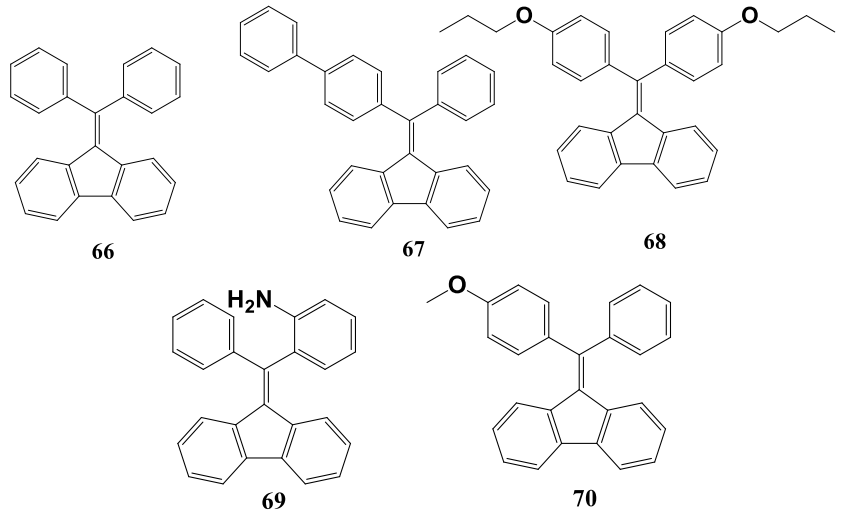

66 67 68 69 70

Figure. 34 Chemical structures of the compounds **69-70**.

A series of fluorenyl-containing tetrasubstituted ethylenes (BBFT (**71**), BFT1 (**72**), and BFT2 (**73**)) are reported with blue emission in their crystalline (Figure 35) [67b]. The compounds are changed emission from blue (459 to 470 nm) to greenish-yellow (507 to 517 nm) after grinding due to morphology change from crystalline to amorphous. The quantum efficiency of the crystals was found to be more superior to their amorphous powder.

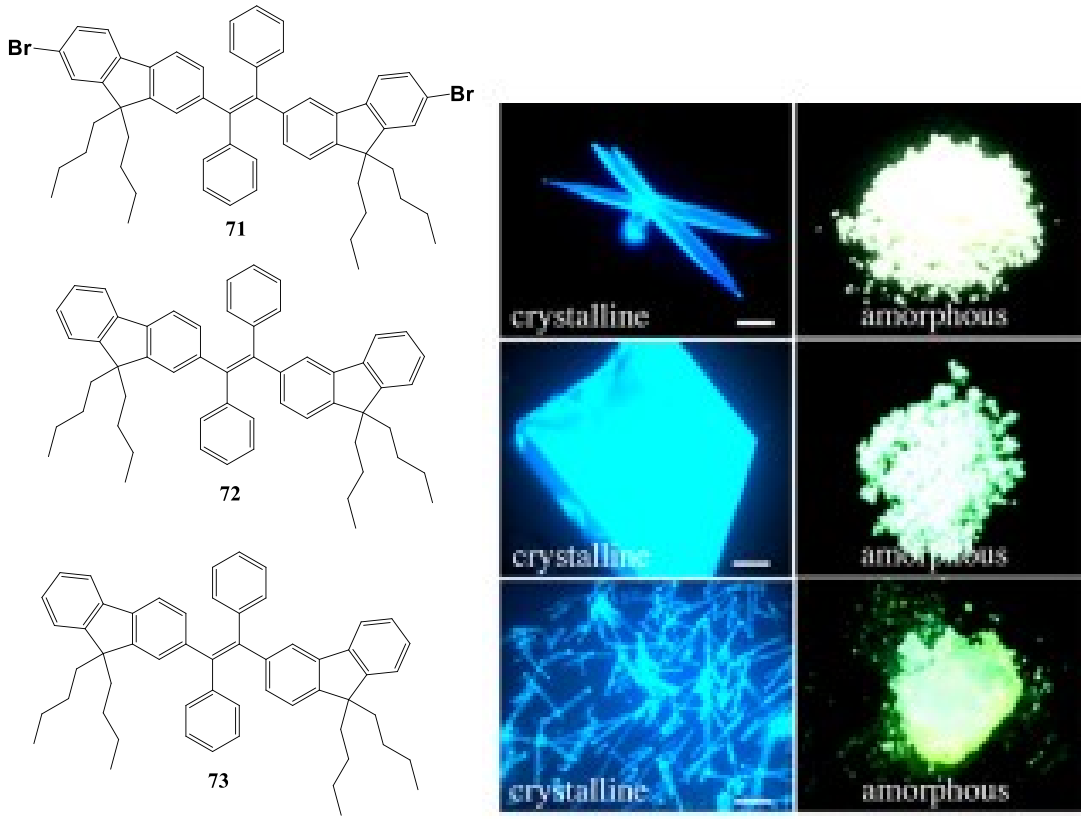

Figure. 35 Chemical structures of BBFT (**71**), BFT1(**72**), and BFT2(**73**), and the corresponding fluorescent images of crystalline and as-prepared powders. Scale bars, 100 mm. Reproduced from Ref. 67b with permission from The Royal Society of Chemistry.

1.4.2.4. Mechanoluminescence of AIE active metal complexes

1.4.2.4.1 Zn(II) complexes:

In 2011, a terpyridine system (a type of tridentate ligand) linked with tetraphenyl ethylene was synthesized [69] by Chi and Xu et al (Figure 36). This ligand was found to be AIE active. Further, a zinc(II) complex (**74**) was synthesized using the synthesized AIE active ligand which was the first mechanoluminescent AIE complex. The emission color of the complex was highly dependent on external stimuli such as grinding, heating, solvent-fuming as well as exposure to acid and base. A drastic change in the emission spectra was observed after grinding the Zn(II) complex from 474 nm (light green powder) to 555 nm (strong brilliant yellow) *i.e.*, a large shift of 81nm was observed. The change in emission color was completely reversible and

can be obtained easily after solvent fuming and annealing. The mechanoluminescence of Zn(II) complex was explained based on powder X-ray diffraction (PXRD).

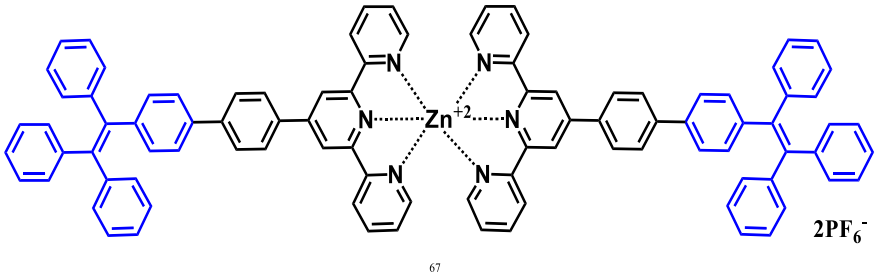

67

74

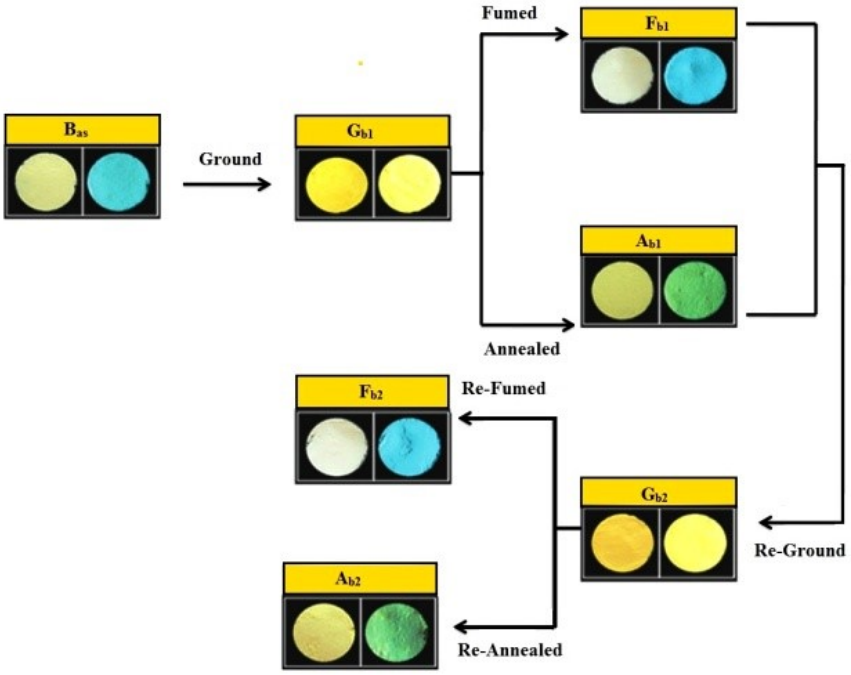

Figure. 36 (a) Chemical Structure of complex **74** (b) The photograph of complex **75** was taken at room temperature under ambient light (left) and UV light (right). Samples: b_{as}, original sample; G_{b1}, ground sample; F_{b1}, fumed sample (ground sample exposed by methanol vapour for five minutes); A_{b1}, annealed sample (the ground sample was annealed at 300 ^{0}C for 1 hour and cooled down at room temperature); G_{b2}, re-ground sample; F_{b2}, re-fumed sample; A_{b2}, re-annealed sample. Reproduced from Ref. 69 with permission from The Royal Society of Chemistry.

The recorded PXRD spectrum showed a sharp and intense peak in case of as-synthesized, fumed and annealed samples which revealed the crystalline nature of the complex. However, the PXRD spectra of ground samples exhibited broad peaks, indicating the amorphous nature. Hence, the authors concluded the change in the emission color (from greenish blue to bright yellow) after grinding attributed to a morphological change *i.e.* a change from crystalline nature to amorphous state.

1.4.2.4.2 Iridium(III) complexes: A novel cationic Iridium(III) complex (**75**) with dendritic ancillary ligand was synthesized by Z.-M. Su and co-workers [70]. The recrystallized complex originally exhibited bright yellow emission which changed into orange after grinding. According to the literature survey, this was the first example of mechanoluminescence of AIE iridium(III) complex (Figure 37). The orange emitting form was fully reverted to its original form through recrystallization in DCM, petroleum ether or by heating it at 325°C for 5 min. To investigate the origin of PAIE, the crystal packing of the complex was investigated. The crystal packing showed many short contacts like C-H---π interaction which was easily destroyed after grinding and playing a crucial role in changing the packing rearrangement or phase transitions. This hypothesis was supported by NMR spectroscopy, Differential Scanning Calorimetry (DSC) and powder X-ray diffraction (PXRD).

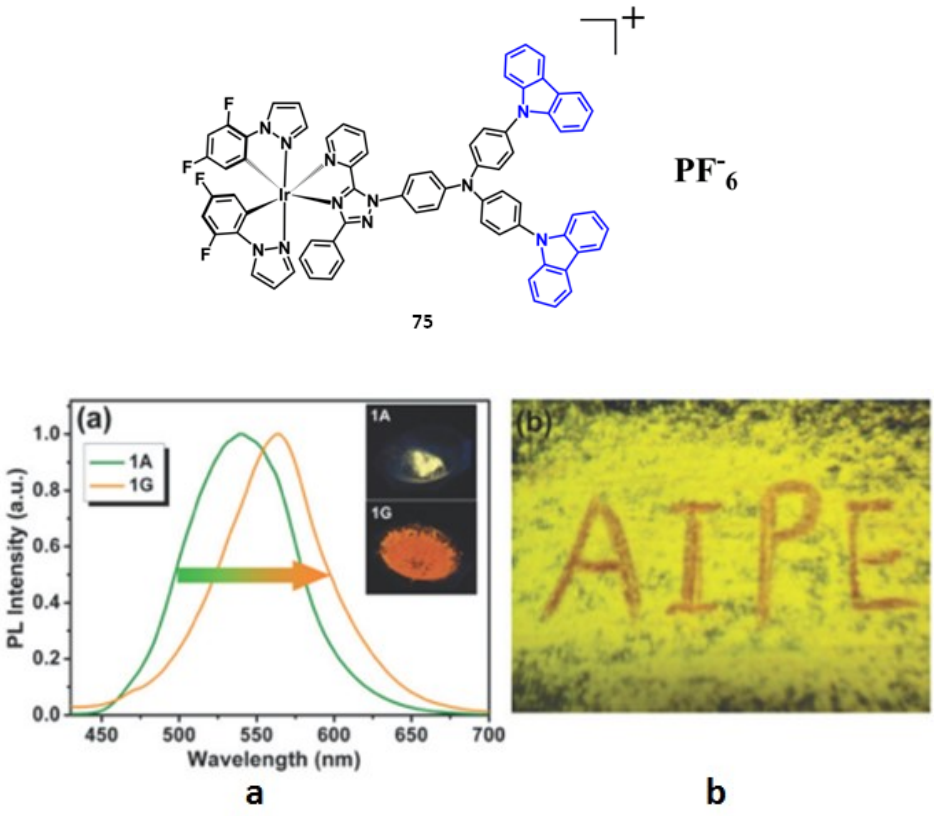

Figure. **37** (a) Emission spectra of the samples 75A and 75G. (b) The powder 75A was cast on the filter paper and the letters "AIE" were written with a spatula under UV light at room temperature. Reproduced from Ref. 70 with permission from The Royal Society of Chemistry.

The studied PXRD pattern of ground sample showed broad peaks whereas the recrystallized product exhibited sharp reflection peaks. The obtained PXRD data revealed that the phase change from crystalline to amorphous after grinding is the origin of mechanoluminescence. This fact was further supported by DSC experiment which showed a clear endothermic melting peak in case of ungrounded sample while broad exothermic recrystallization peak at ca. 320 °C was observed in the case of ground sample. The successful synthesis of a MLAIE iridium (III) complex motivated the Z.-M. Su and coworkers [71], to synthesis of new MLAIE iridium(III) complexes. In this consequence, they have designed three new complexes (**76-78**) where the ancillary ligand was changed strategically. 1-(2,4-difluorophenyl)-1H-pyrazole was kept as usual chromophoric ligand but the triazole-pyridine ligand, 2-(5-methyl-2H-1,2,4-triazol-3-yl) pyridine (an ancillary) was linked with new substituents such as butyl (complex 77), 9-(4-butyl)-9H-carbazole (complex 78) and 9-(4-butyl)-

3,6-di-tert-butyl-9H-carbazole (complex **78)** (Figure 38). All three complexes exhibited the AIE property where the transmission electron microscopy (TEM) and electron diffraction (ED) measurements of 90% acetone-water mixture confirmed that the formation of nano aggregates which were amorphous in nature.

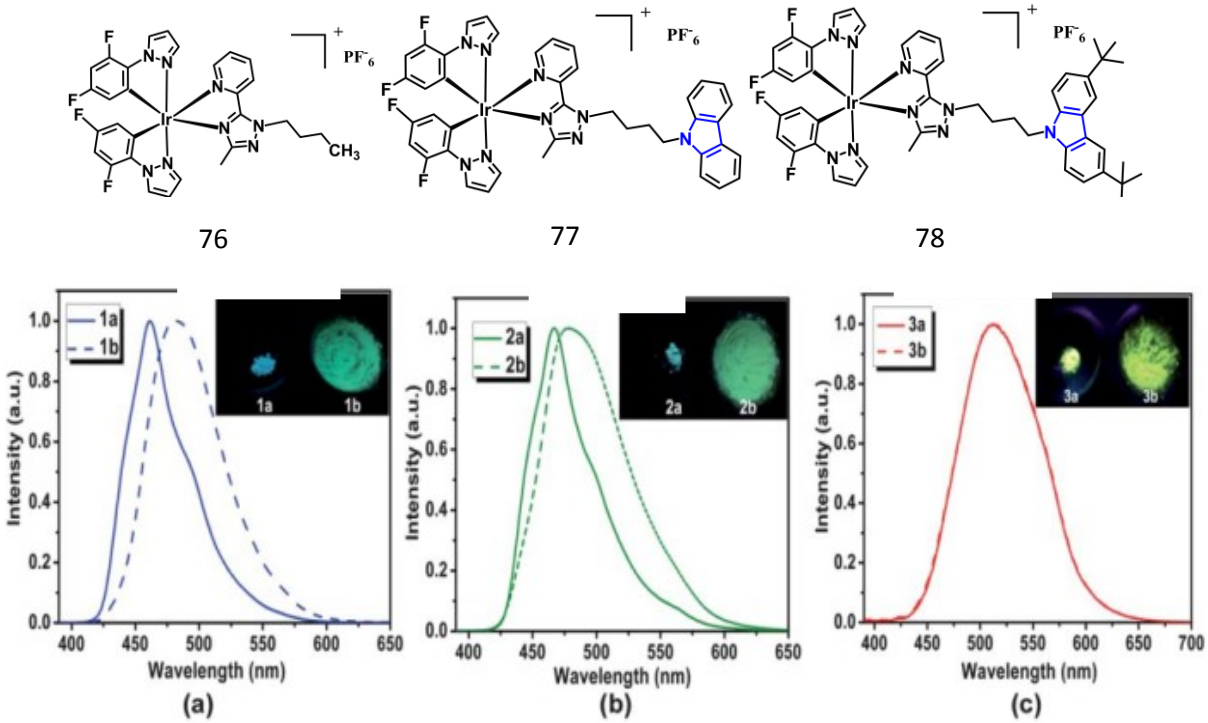

Figure. **38** Emission spectra of complexes **76–78** in solid state before (solid line) and after (dotted line) grinding at room temperature. Reproduced from Ref. 71 with permission from The Royal Society of Chemistry.

The PXRD data of these three complexes revealed that **76** and **77** were crystalline and **78** was amorphous in nature. The emission spectra of the solid complexes were recorded and the emission maxima were found at 461, 467 and 512 nm for the complexes, **76, 77** and **78**, respectively. After grinding, the emission maxima of the complexes **76** and **77** were changed from 461 nm and 467 nm to 482 nm and 478 nm, respectively. The ML emission of these complexes was highly reversible in nature in presence upon heat. Coincidentally, the emission spectra of **77** and **78** after grinding produced the same emission maxima which was obtained at f_w = 90%. This result indicating the alteration of aggregation may responsible for ML. The mechanism of ML was investigated with the help of PXRD and DSC analysis. The PXRD of **76**

and **77** have showed broader and weaker reflection peaks that supported its amorphous nature. Additionally, DSC analysis showed exothermic peaks for recrystallization temperatures at ~149 °C and ~156 °C for **76** and **77**, respectively. These data again supported that the transformation from a crystalline to an amorphous phase upon grinding was the origin of ML behavior. The complex **77** was found to be a multi-channel responsive material. Complex **77** was changed its emission color from sky blue to green in presence of external stimuli such as heating and fuming.

Till date, ionic mono iridium(III) complexes with dendrimer-like or flexible alkyl chain substituent have been explored for ML.

In 2015, two new dinuclear iridium(III) complexes (**79-80**) were synthesized by M. R. Bryce and co-workers where a Schiff base ligand was used as ancillary ligand (Figure 39) [72]. Apart from the simplicity for the synthesis of Schiff-base ligand, the flexibility and the presence of hetero atoms in imine may be introduced to generate several short contacts such as intermolecular π–π or C–H---π interactions in the aggregated or crystalline state. And these short contacts can be destroyed in presence of external stimuli that results a change in emission property.

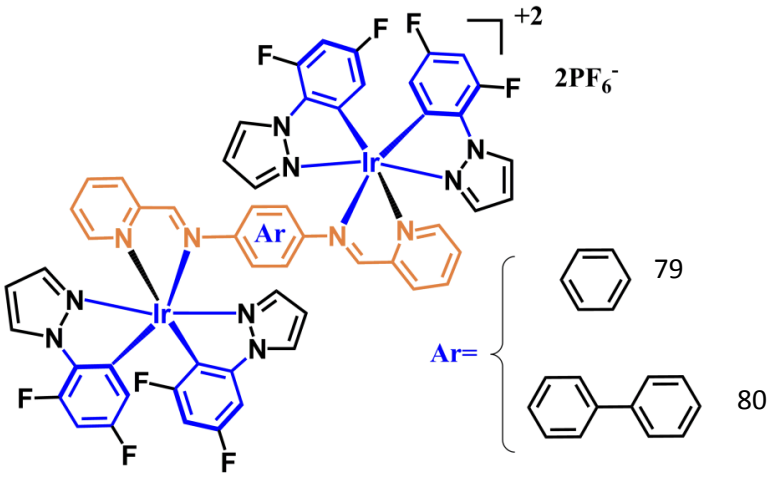

a

Figure. 39 Chemical structures of the complexes **79-80**.

The TEM image and electron diffraction (ED) experiments proved the formation of amorphous molecular aggregates at f_w= 60% for the complexes, 79-80. The solid state emission

showed the maximum emission at 612 nm (yellow) and 627 nm (orange) which was mainly originated from the major contribution of Metal-to-Ligand Charge Transfer (MLCT) and Ligand-to-Ligand Charge Transfer (LLCT) transitions. The emission maxima of these complexes were shifted from 612 nm and 627 nm to 635 nm and 648 nm, respectively after grinding. Interestingly, these ground samples were highly reversible in presence of DCM. To investigate the ML behavior, a close examination of crystal packing was done which showed π–π interaction between the neighbouring pyrazole rings. The PXRD data of ground samples were found to be weak and broad indicating the amorphous nature. However, the PXRD data of un-ground samples matched well with PXRD data recorded after heating and fuming of ground sample. The above results indicate the origin of ML behavior in these complexes was due to crystallization and amorphization upon the grinding–heating (or vapour exposure) process. Some recent interesting contributions showing more possible uses for Ir(III) based complexes in the fields of data protection [73].

1.4.2.4.3 Pt(II) complexes:

X.-P. Zhang *et al* reported [74] couple of enantiomeric chiral alkynylplatinum (II) bipyridine complexes **(Figure 40)**, Pt((-)-L1)(C≡CPh)$_2$((-)-1) (L1 = (-)-4,5-pinene-2, 2'-bipyridine and Pt((+)-L1)(C≡CPh)$_2$((+)-1)(L1= (+)-4,5-pinene-2, 2'-bipyridine). complexes **81** and **82** exhibiting ML property. Mechanical force would induce a sharp color change from yellow to orange and a distinct luminescence variation from orange to red. Crystal-to-amorphous and ordered-to-disorder transformation is the cause for the ML property.

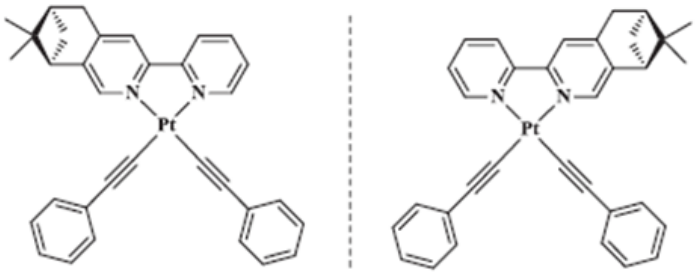

81 82

Figure. **40** Chemical structures of **81-82**.

C-J Lin et al reported [75] ML active organometallic Pt(II) complexes **83-87 (**Figure 41**)** with the N^C^N coordinated ligand [X-NCNPtY], where X = Br or Pa, the substituent on the terdentate dipyridylbenzene N^C^N ligand, and Y = Cl or Pa, the ancillary ligand, in which Pa = pentiptycene acetylene. The ML mechanism was reported due to alteration of metallophilic interaction between the Pt···Pt changes the emissive state from MMLCT and LC monomer that accounts for the ML properties of the cyclometalated Pt(II) complexes [Pa-NCNPtCl], [Br-NCNPtPa], and [Pa- NCNPtPa].

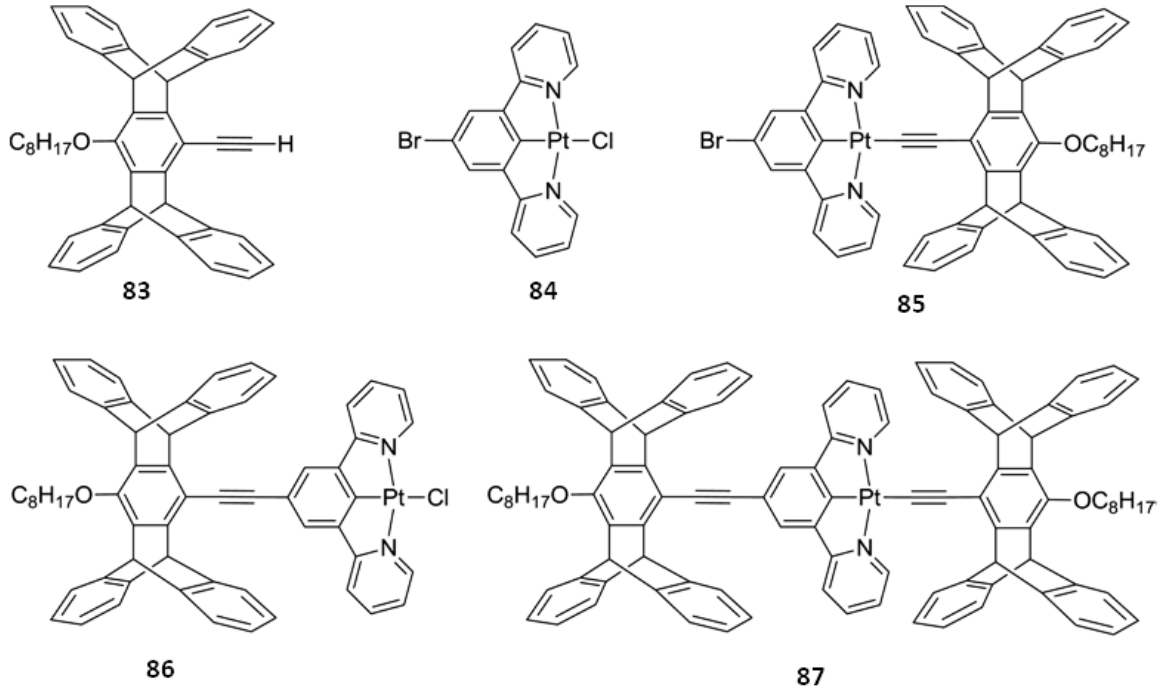

Figure. **41** Chemical structures of **83-87**

1.5 Applications of luminescent compounds in Bioimaging

1.5.1 General overview of bioimaging: Bio-imaging is a technique in which a luminescent compound is targeted to label the cells (HeLa, CHO-KI, Hep3A, etc.), cell organelles (mitochondria, cytoplasm, nucleus, nucleolus etc.), tissues etc., for biological or clinical analysis and medical intervention [76]. Traditionally, the following imaging techniques magnetic resonance imaging (MRI), ultrasound imaging, X-ray radiography, positron emission tomography etc., have been used for body-internal imaging purpose [41]. In comparison, florescence imaging would be more attracting because of high contrast intense output signal,

high spatial resolution, low cost and less complexity etc., [77-79]. In fluoroscence bioimaging technique, the most crucial issue is the development of highly sensitive and selective bioimaging probe. On literature survey, most of the works on bioimaging have been performed using inorganic quantum dots (QDs), organic dyes and metal-complexes as bioimaging probes. QDs have been extensively used in bioimaging due to their high photostability, large quantum yield, broad band absorption and narrow and tunable emission spectra. There have been some disadvantages for using QDs in bioimaging [41]. Firstly, it is commonly observed surface defects which affect the recombination of holes and electron. These defects create temporary traps, which results in blinking. Secondly, quantum dots also suffer from high amount of nonspecific adsorption *via* electrostatic interactions, even this was found to be true for PEG (Poly ethylene glycol)-containing nanoparticles making them undesirable for selective targeting. Finally, CdSe, CdTe, CdS quantum dots are carcinogenic for using in bioimaging [41].

Conventional organic/ metal-complex based fluorophores have been suffering from many problems such as low quantum yield, low stoke shift, high photobleaching effect, poor water solubility, less selectivity to cell-organelles etc [41]. The most desirable criteria for an ideal bio-imaging probe should have a good thermal stability, water solubility, low cyto-toxicity, high cellular uptake, selectivity for specific organelles, high quantum yield etc. In addition to the problems for QDs and traditional fluorophores, the inherent ACQ effect severely interrupted the use of these probes in biological environments. As AIE materials emit strong light in the aggregated state, it overcomes the ACQ effect and hence the quality ensures their suitability in bioimaging application. In addition, their high absortivity, free from random blinkness and strong photobleaching effect make them to use in fluorescent imaging at the subcellular, cellular and/or tissue levels in a noninvasive and high contrast manner [78].

In addition, heavy metal based AIE fluorophore has the advantage to show higher quantum yield as compared to their organic/light-metal based complexes due to the strong spin-orbit coupling. On literature survey, many heavy metal ions [Pt(II), Ir(III), Os(II), Re(I), Rh(III)] based luminescent complexes have been used in bioimaging as luminophoric probe molecules [80].

Among the heavy metals used in bioimaing, Pt(II) complexes are widely known phosphorescent emitters at room temperature. Being the square planar geometry, Pt(II)

complexes generates many excited states depending upon the nature and structure of coordinated ligands and metal centers. Because of rich electronic excited state of planar platinum(II) complexes, people are using these in different kinds of applications (*e.g.*, OLED, chemosensor and bioimaging etc) [81].

1.5.2 Non AIE organic compound based bio-imaging probes:

Maji *et al*. reported [82] a turn-on fluorescence with attaching rhodamine in Schiff base (**88**) **(**Figure 42). This non-toxic probe has been used to identify the distribution of Cu^{2+} ions in living cells.

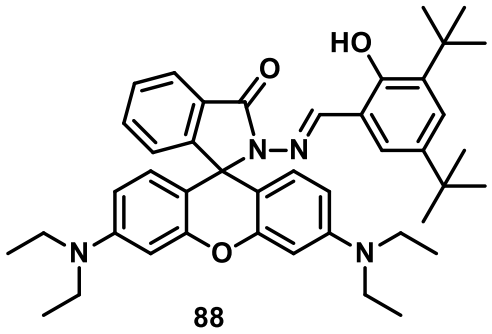

88

Figure. 42 Chemical structure of **88**.

Wang et al. reported [83] a naphthaldehyde based compound, **89 (**Figure 43) which has a tendency to sense the Al^{+3} cations. It is shown that **89** has a good cell membrane permeability and successfully employed to detect Al^{3+} within the living cells

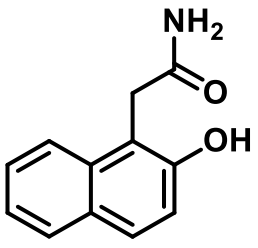

89

Figure. 43 Chemical structure of **89**.

Rani *et al.* reported [84] a fluorogenic pyrene-amino mercapto thiadiazole, **90 (**Figure 44) for live cell imaging, but the disadvantage of the compound that it is not water soluble and it is required to excite at UV range excitation.

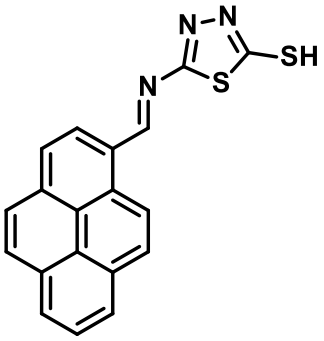

90

a

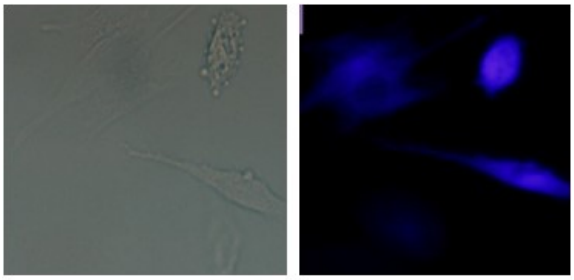

b

Figure. 44 a) Chemical structure of the compound **90**; b) Fluorescence images of Live HeLa cells bright field image of cells loaded with 5M PYAMT and the corresponding fluorescent image.

1.5.3 Non AIE Bioimaging Probes by Pt(II) complexes

In 2008, Williams et al. reported [85] the first example of time-resolved imaging using Pt(II) complex **(**Figure 45) as luminescent probes. The Pt(II) complex (**91**) successfully stained the CHO cell lines and overcome the problem of short-lived background fluorescence.

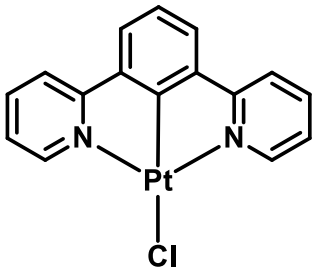

91

Figure. 45 Chemical structures of complex **91**.

After these impressive results, the heavy metal complexes were recognized as a potential candidate for bioimaging. Since then many other heavy metal complexes have been synthesized and employed for bioimaging [**85-86**].

Several Pt(II) complexes with N^N^C, N^C^N and porphyrin ligands have been used as bioimaging materials [87]. The Pt(II) complex **92 (**Figure 46) containing a deprotonated carboxylate shows as cytoplasm marker in 24h incubation at conc. 5μM with HeLa cells. The Pt(II) complex **93 (**Figure 46) is also reported to label cytoplasm .

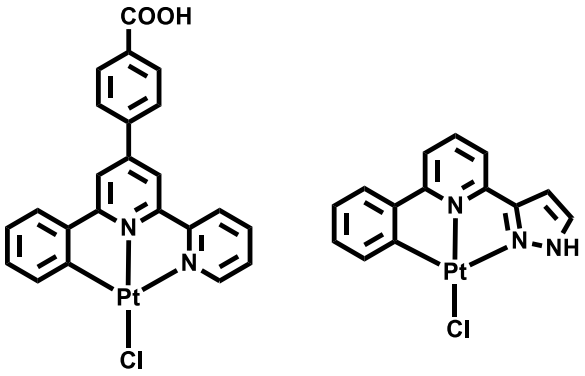

92 93

Figure. 46 Chemical structures of **92-93**.

In order to increase stability of complexes to stop the biological reactions and ligand exchange reactions, Sun and his co-workers synthesized [88] C^N^N coordinated platinum(II) complexes **(**Figure 47) containing N-heterocyclic carbene (NHC), as the ancillary ligands **(94-96**). In comparison to other closely related Pt(II) complexes [85], **94–96** show high cytotoxicity

and selectivity towards cancerous cells. They are stable in water and, more importantly, resistant towards reduction/substitution by glutathione (GSH). The complexes **94a–c** (green) and **95a–b** (red) are emissive in the solution and solid state with similar emission maxima λ_{max} (~545 nm) with moderate emission quantum yields. The binuclear Pt(II) complex **94d** shows red shifted emission with λ_{max} at 619 nm. Complex **94a** used for HeLa cell internalization and as well as anti-cancer agent towards several cancer cell lines (IC_{50} = 0.057–0.77 mM). More importantly, this complex was less cytotoxic towards the normal human cell lines (CCD-19Lu) with an IC_{50} value of 11.6 mM, which is 232-fold higher than that for HeLa cells. Complex **94a** also co-localized at mitochondria.

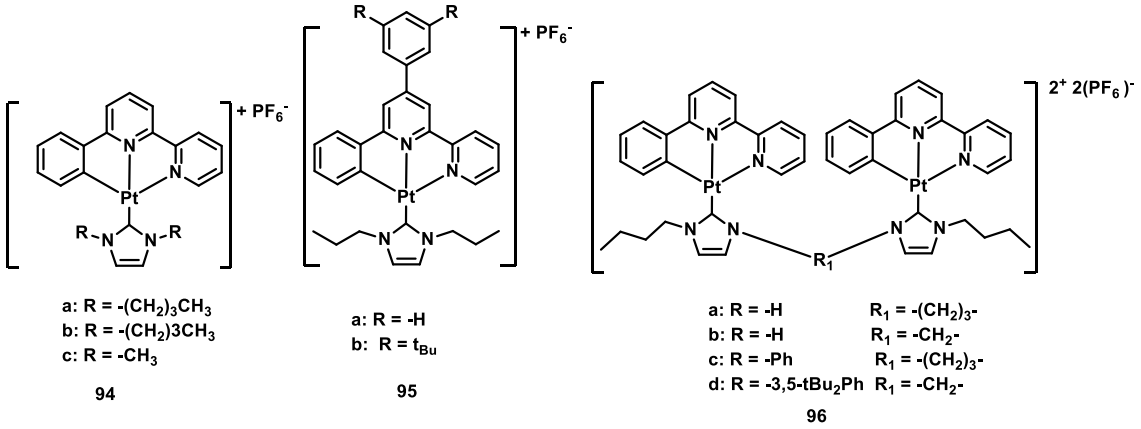

Figure. **47** Chemical structure of **94-96**.

Out of all the bidentate ligands coordinated to Pt(II), the cyclometallated chelating ligands are the interesting ones because of their high thermal stability and strong emission. Till date the hundreds of complexes have been synthesized with these types of ligands, but only few complexes have been found to show good water solubility which is required for bio-applications. Lai et al. [89] reported $[Pt(thpy)(Hthpy)pyridine]^+$ (thpy = 2-(20 thienyl)pyridine **97)) (**Figure 48)**,** which was used for cell labeling and showing photo-induced cytotoxicity. Complex **97** also exhibits room temperature orange emission with reasonable emission quantum yield. The complex **97** was used to label the nucleolus and mitochondria of HeLa cells. Complex **97** showed visible toxicity under broad band visible light irradiation. Indeed, this complex, as many other

metal compounds, can sensitize oxygen by energy transfer, leading to the generation of toxic singlet oxygen.

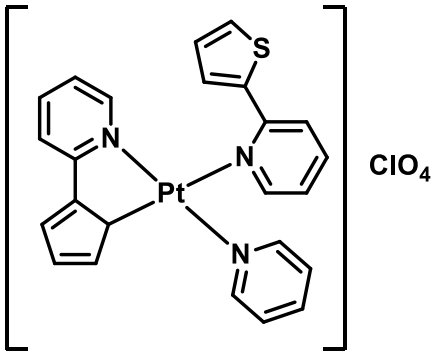

97

Figure. **48** Chemical structure of **97**.

Che and coworkers reported [90] cyclometalated platinum (II) compounds, namely [Pt(ppy)(bisNHC$_2$C$_6$)]OTf, **98** (ppy = 2-phenylpyridine and bis-NHC = bis-N-heterocyclic carbene), and [Pt(II)(thpy)- (bisNHC2C6)]OTf, **99** which have been used for theranostic applications.

Platinum(II) complexes **98** and **99 (**Figure 49) are internalized into HeLa cells which selectively stained endoplasmic reticulum (ER). Moreover, the results of MTT assay experiments revealed very high toxic activity for both complexes towards several cancer cell lines such as breast cancer (MCF-7), nasopharyngeal carcinoma (HONE1, SUNE1), lung carcinoma (HCC827, H1975), a non-tumorigenic liver cell line (MIHA) and hepatocellular carcinoma (HepG2). In particular, the toxicity of platinum(II) complex **99** was 5.3 - to 60-fold stronger than cisplatin. Furthermore, they also reported that the toxicity activity was governed by the ER stress, inducing cell apoptosis.

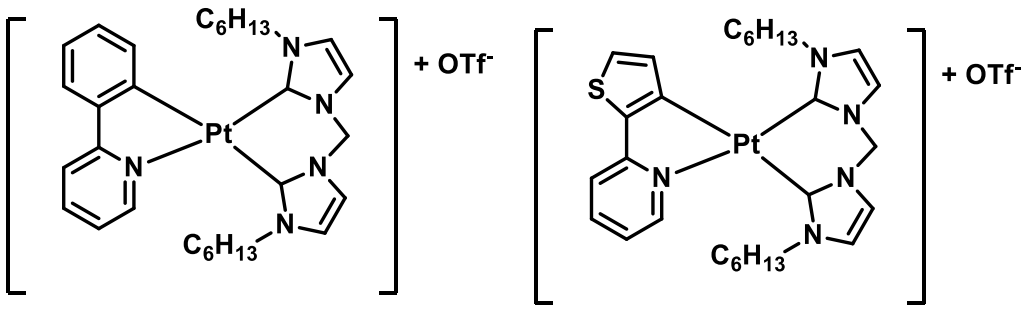

98 **99**

Figure. 49 Chemical structure of the complexes, **98** and **99**

Huang and coworkers reported [91] a series of four Pt(II) complexes, bearing beta-diketonate ligands, namely **100–103** , are shown in Figure 50. The complexes were stained into the cytoplasm of the HeLa cells. Interestingly, the results of MTT experiment showed more than 80% cell viability. The findings obtained from this experiments lead them to conclude that the complexes did not show any toxicity, as compared with previous examples.

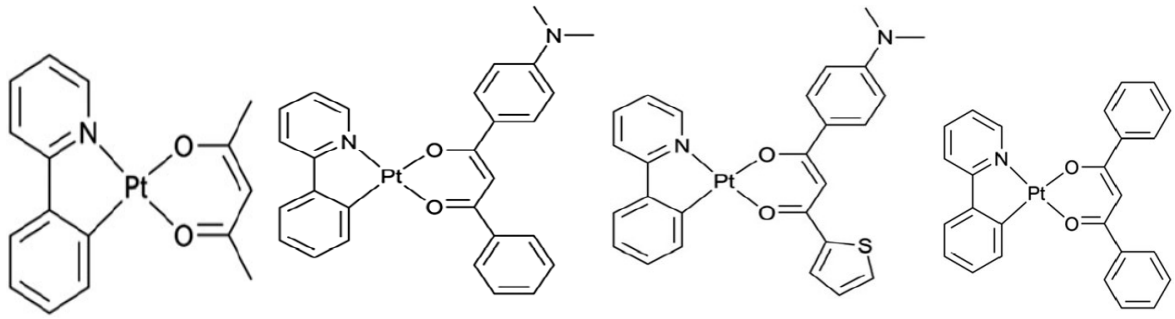

Figure. **50** Chemical structures of **100-103**.

1.5.4 Non AIE Iridium(III) complexes as bioimaging probes

Li *et al*. reported [92] water soluble, PEG functionalized Ir(III) complexes **104-108 (**Figure 51) which have exceptionally low cytotoxicity, with their IC_{50} values significantly higher as compared to the complexes without modification with PEG. A possible reason is that the long PEG chains protecting the complexes from interacting non-specifically with the extracellular proteins and triggering immunogenicity and antigenicity inside the cells.

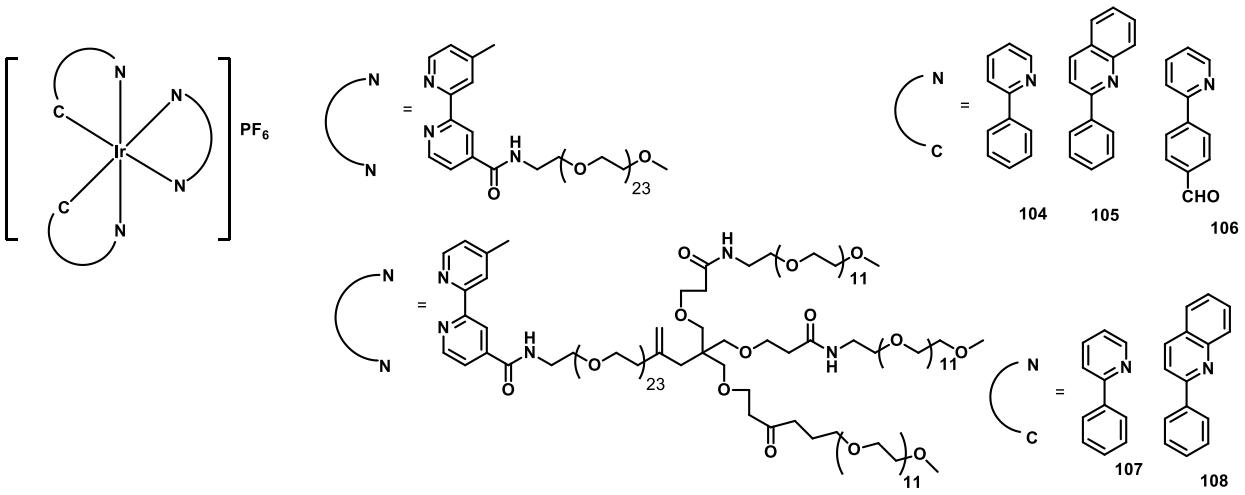

Figure. **51** Chemical structures of **104-108**

The charge of complexes significantly affects their cell penetration. Due to the nature of negative surface charge on living cells, metal complexes with positive charge facilitate in penetrating the cell membrane. In this contest, Zhao et al. reported [93] cationic Ir(III) complexes 109–112 **(**Figure 52) after incubation of HeLa cells with 20 mM cationic Ir(III) complexes, **109**–**112** in DMSO/phosphate buffered solution (PBS) (pH 7, 1 : 49, v/v) for 10 min at 25°C. An intense intracellular luminescence with high signal-to-noise ratio was observed in the cytoplasm using confocal luminescence microscopy, indicating that these cationic Ir(III) complexes enters into the living HeLa cells.

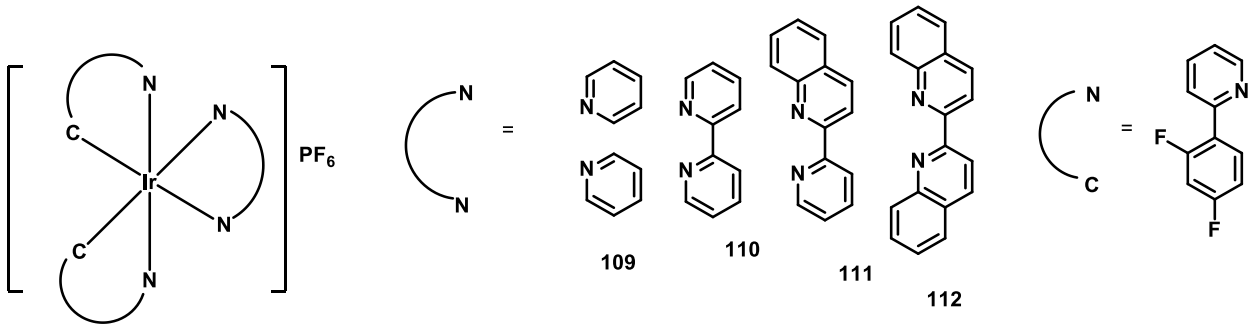

Figure. **52** Chemical structures of **109-112**

1.6 AIE active bio imaging probes

1.6.1 Organic based AIE active compounds for bioimaging

Ji Yang *et al.* reported [94] turn-on AIE active dibenzophenazine based NIR fluorescence probe **113 (**Figure 53) for superoxide anion detection. The fluorescent sensor BDP has a high selectivity for superoxide anions over some other intracellular reactive oxygen species (ROS). When HepG2 cells undergo apoptosis and inflammation, 113 is a good probe to keep track of the endogenous superoxide anion level.

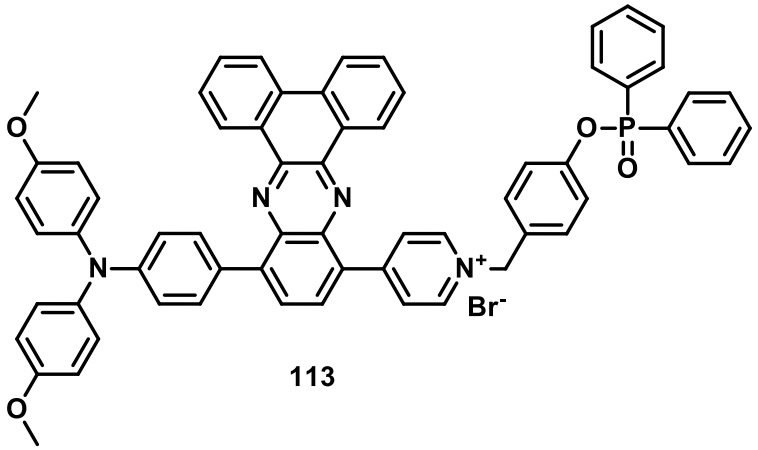

113

Figure. **53** Chemical structure of **113**

Wen *et al.* reported [95] dual-sensing fluorescence probe L (**114) (**Figure 54) which was designed and synthesized for highly selective and sensitive detection of Zn(II) metal ion and DNA. Significant stoke shifts were observed (~100 nm). The probe L-Zn(II) displayed significantly enhanced fluorescence upon binding with DNA because of the metal coordination interaction of Zn(II) with DNA.

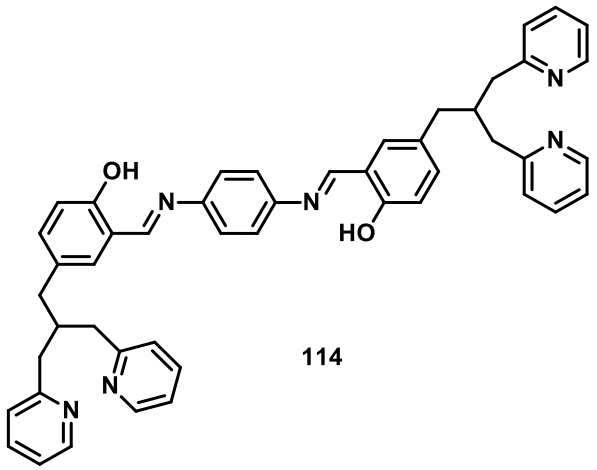

Figure. **54** Chemical structure of **114**

Y. Miao and coworkers reported [96] a silica coated AIE-active dye **115** (Figure 55) which was prepared to fabricate the composite nanomaterial 115@SiO_2. The **115** showed strong emission in aggregated state. Then, the fabricated composite core-shell structure 115@SiO_2 exhibited remarkable photostability and biocompatibility. After incubating 115@SiO_2 with KB cells, this material could go through the cell membrane and specifically light up the mitochondria.

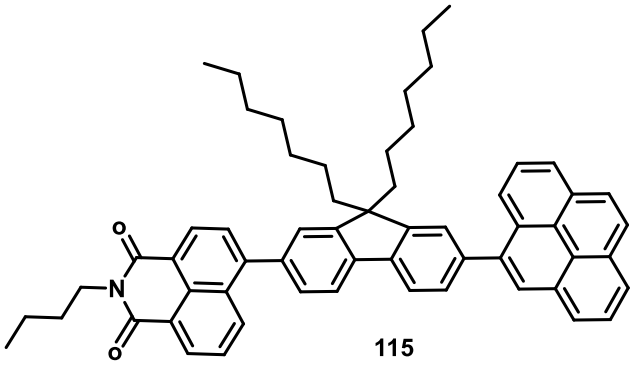

Figure. **55** Chemical structure of **115**

1.6.2 Pt(II) and Ir(III) complexes based AIE active compounds for bioimaging

After invention of AIE phenomenon by Tang group one major problem was resolved in luminescent materials *i.e*. ACQ. Presently, scientists mainly focused on AIE based bio imaging probes. Still very few AIE moieties are reported as bioimaging probe

Hermida and his group reported [97] cycloplatinated Pt(II) complexes based on 2-(4-substituted)benzothiazole ligands of type [Pt(R-PBT-kC,N)Cl(L)] (PBT = 2-phenylbenzothiazole; R = Br (**116**), Me_2N (**117**); L = dimethyl sulfoxide (DMSO; a), 1,3,5-triaza-7-phosphaadamantane (PTA; b), triphenylphosphine 3,3',3''-trisulfonate (TPPTS; c)) (Figure 56). The biological activities of **116** and **117** toward the human-cell lines A549 and HeLa suggests that there is no clear correlation between the substituent Me_2N or Br in the phenyl ring of the cyclometalated PBT group and the cytotoxic activity. Moreover, fluorescence cell imaging indicated a similar biodistribution of both types of complex (**116** and **117**); that is, in general cytoplasmic staining was observed in both cell lines, with exclusion from the nucleus and greater visibility in the perinuclear areas.

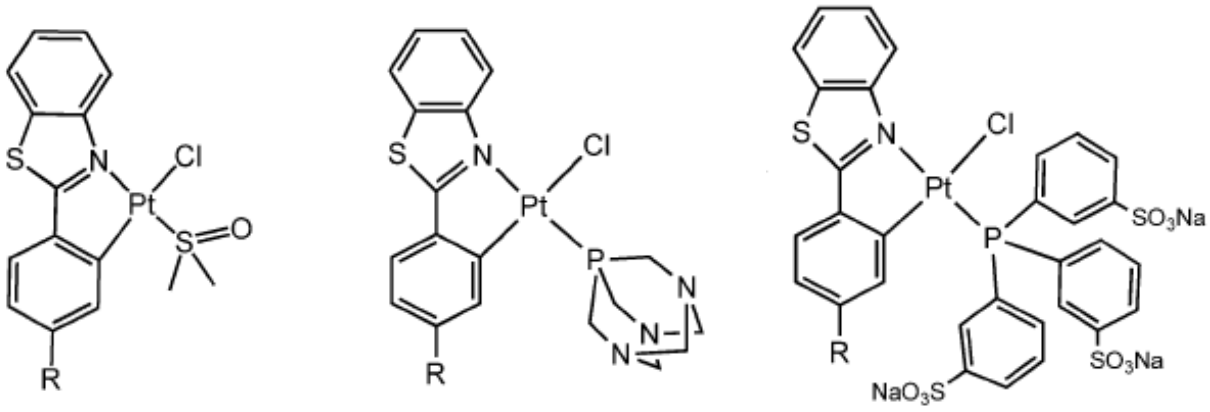

R = Br 116a

NMe_2 117a

R = Br 116b

NMe_2 117b

R = Br 116c

NMe_2 117c

Figure. 56 Chemical structures of **116-117**.

Platinum(II) complexes bearing triphenyl phosphine **118** (Figure 57) has been used for staining cell nucleolus. Colocation confirmed by fibrillarin and noncolocation with FUS (a DNA and RNA binding protein known to be localized exclusively in the nucleoplasm) [98].

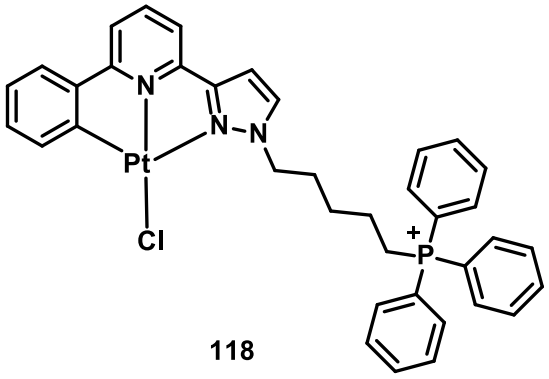

118

Figure. 57 Chemical structure of **118**.

Liu and the coworkers developed [99] a fluorescent light-up platinum(II) complex **119** (Figure 58) incorporated with an AIE for real-time monitoring of drug activation as well as for combinatorial photodynamic and chemotherapy against *cis*-platin-resistant cancer cells. The prodrug is almost non-emissive in aqueous media but lights up upon reduction by intracellular GSH. The fluorescence ‘‘turn-on’’ can also selectively label avb3 integrin overexpressed cancer cells for image-guided photodynamic therapy. Cell viability studies showed that combined treatment could result in enhanced cell inhibition of *cis*-platin-resistant cancer cells using MDA-MB-231 cells as an example.

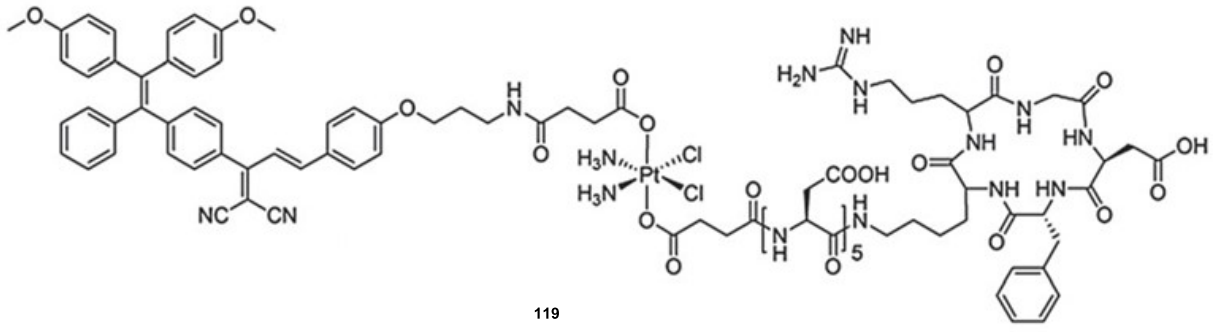

119

Figure. 58 Chemical structure of **119**.

Laskar *et al* reported [100], the AIE-active iridium(III) complex **120** (Figure 59) which was encapsulated inside the hydrophobic core of PEG–PLA nanoparticles *via* a simple oil-in-water based emulsion–evaporation method. The aggregation of Ir(III) complex molecules in the hydrophobic core

of the PEG–PLA particles leads to an important increase in their emission intensity. The colloidal form of these luminescent PEG–PLA particles is shown to behave as potential cell imaging probe.

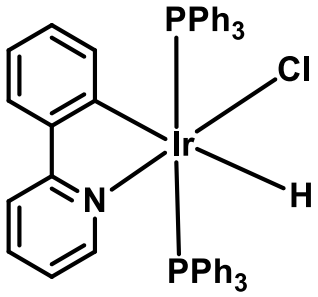

120

Figure. 59 Chemical structure of **120**.

Alam *et al.* reported [101] a new bis-cyclometalated iridium(III) complex, $[Ir(ppy)_2(L)]$, where ppy = 2-phenylpyridine and L = 1,2-((pyridin-2-ylimino)methyl)phenol, **121** (Figure 60). It was shown to have a potential application as a non-toxic bio-imaging probe for mitochondrial staining.

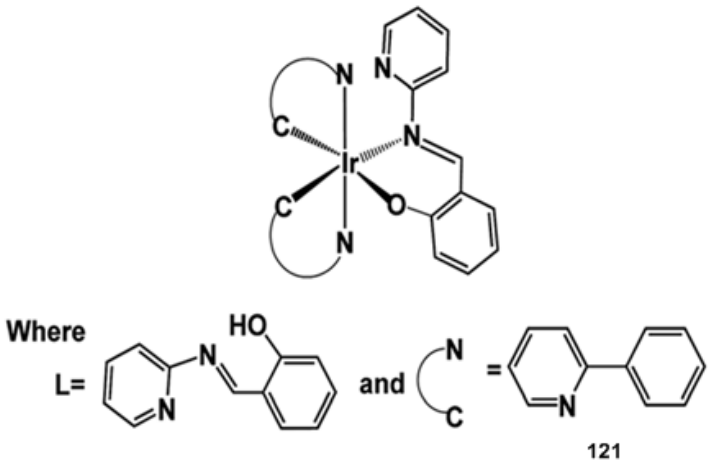

Figure. 60 Chemical structure of **121**.

In the present dissertation, we have reported the strategic synthesis of AIE based organic and Pt(II) compounds, photophysical property study and their applications in bioimaging and

mechanoluminescence. On literature survey, it is observed that most of the Pt(II) based luminogens have been synthesized by multi-steps and hence a lengthy procedure was required to obtain the desired product [21, 23, 25, 28]. In addition, the report of AIE based Pt(II) compounds are very less. The reported organic based AIEgens are mostly limited to tetra-phenyl ethylene (TPE) compounds. Most of the substituted TPE compounds have been synthesized in a lengthy process [51]. These facts reveal that there has enough scope to develop synthetic strategies of Pt(II) and organic based AIEgens in simplified routes.

ML compounds can be used for various applications such as data storage devices, tamper proof packaging technology etc. These compounds should be strongly emissive in the solid state for successfully using them in solid state applications. Most of the traditional ML compounds are weakly emissive in solid state because of ACQ effect. Hence, there has a high demand to syntheses of AIE active ML compounds for solid state applications. Moreover, most of the reported ML active compounds are irreversible in solid state which has limited applications. There has an opportunity to develop AIE active reversible ML materials. Most of the ML compounds are reversible in nature when the pressed sample (the compound after grinding) is dissolved in some solvent. Hence, growing of single crystals is not possible for the pressed sample to know their authenticated structure. This fact creates limitations in exploring the mechanism of ML, hence creating problem to justify the real cause of ML property.

Bioimaging would be a good technique, as compared to the conventional MRI technique to understand the dynamic property of cellular organelles and it can help to provide prior indication of various diseases. One of the dire requirements for using the luminogens in bioimaging – the fluorophores should be soluble / dispersible in water medium. Most of the luminescent heavy-metal / organic based complexes used for bioimaging are insoluble / not dispersible in water [41]. The other challenge in this area is targeting selectively to the desired cell organelles with appropriately designing the luminogens. Two distinct functionally different molecules – imaging for diagnostic purposes and drug for therapeutic purposes have been used for theranostic applications [102]. It is not convenient to target the same cell organelle by two functionally different types of molecules. This problem can be rectified with integrating the two properties – bioimaging and drug action into a single entity. After the revolutionary discovery of *cis*-platin [103], only few reports are found for theranostic applications [102, 104-105]. It

provides an avenue to focus on the design and synthesize of new AIE active Pt(II) complexes for theranostic applications.

2. References

[1] G. Drummen, *Molecules*, 2017, **17**, 14067.

[2] D. Frackowiak, *J. Photochem. Photobiol. B: Biology*, 1998, **2**, 399.

[3] M. Kasha, *J. Chem.Phys*., 1952, **20,** 71.

[4] M. Karplus, *J. Chem.Phys*., 1959, **30**, 11.

[5] S. Lamansky, P. Djurovich, D. Murphy, F. Abdel-Razzaq, H. -E. Lee, C. Adachi, P.E. Burrows, S. R. Forrest, M.E. Thompson, *J. Am. Chem. Soc*., 2001, **123**, 4304.

[6] M.G. Colombo, T.C. Brunold, T. Riedener, H.U. Guedel, M. Fortsch, H.-B. Buergi, *Inorg. Chem*., 1994, **33**, 545.

[7] O. Deuschel, S. Evans, V. Zelewsky, *J. Chem. Soc*., *Chem. Commun*., 1990, **121,** 1211.

[8] W. Lu, M. C. W. Chan, N. Zhu, C. -M. Che, C. Li, and Z. Hui, *J. Am. Chem. Soc*., 2004, **126**, 7639.

[9] Y. Hong, J. W. Y. Lam and B. Z. Tang, *Chem. Soc. Rev*., 2011, **40**, 5361.

[10] J. Luo, Z. Xie, J. W. Y. Lam, L. Cheng, H. Chen, C. F. Qiu, H. S. Kwok, X. Zhan, Y. Liu, D. Zhuc and B. Z. Tang, *Chem. Commun*., 2001, **0**, 1740.

[11] R. T. K. Kwok, C. W. T. Leung, J. W. Y. Lam, B. Z. Tang, *Chem. Soc. Rev*., 2015, **44**, 4228.

[12] Z. Ning, Z. Chen, Q. Zhang, Y. Yan, S. Qian, Y. Cao, H. Tian, *Adv. Funct. Mater*., 2007, **17**, 3799.

[13] J. Mei, Y. Hong, J. W. Y. Lam, A. Qin, Y. Tang, B. Z. Tang, *Adv. Mater*., 2014, **26**, 5429.

[14] Z. Chi, X. Zhang, B. Xu, X. Zhou, C. Ma, Y. Zhang, S. Liu, J. Xu, *Chem. Soc. Rev*., **2012**, **41**, 3878.

[15] V. W. -W. Yam, K. M. -C. Wong, N. Zhu, *J. Am. Chem. Soc*., 2012, **124**, 6506.

[16] S. Cho, M. W. Mara, X. Wang, J. V. Lockard, A. A. Rachford, F. N. Castellano, L. X. Chen, *J. Phys. Chem. A*, 2011, **115**, 3990.

[17] S. -W. Lai, H. -W. Lam, W. Lu, K.-K. Cheung, C. -M. Che, *Organomet*, 2002, **21**, 226.

[18] Z. A. Siddique, T. Ohno, K. Nozaki, T. Tsubomura, *Inorg. Chem*., 2004, **43**, 663.

[19] J. N. Demas, B. A. D. Graff, *Anal. Chem*., 1991, **63**, 829.

[20] S. Huang, B. Yang, J. Zhong, H. Zhang, Synthetic Metals, 2015, **205**, 222.

[21] M. X. Zhu, W. Lu, N. Y. Zhu and C. M. Che, *Chem.–Eur. J*., 2008, **14**, 9736.

[22] S. Liu, H. Sun, Yun Ma, Shanghui Ye, X. Liu, X.i Zhou, X Mou, L. Wang, Q. Zhao and W. Huang, *J. Mater. Chem.*, 2012, **22**, 22167.

[23] Rui Liu, Senqiang Zhu, Jiapeng Lu, Hong Shi, Hongjun Zhu, *Dyes Pigm.,* 2017, **147**, 291.

[24] H. Honda, Y. Ogawa, J. Kuwabara, and T. Kanbara, *Eur. J. Inorg. Chem*., 2014, 1865.

[25] H. Hiroya, K. Junpei, K. Takaki, *J. Organomet. Chem*., 2014, **772**, 139.

[26] U. Panda, S. Roy , D. Mallick, A. Layek, P. P. Ray, C. Sinha, *J. Lumin*, 2017, **181**, 56.

[27] L. Viglianti, L. C. N. Leung, N. Xie, X. Gu, Herman, H. Y. Sung, Q. Miao, I. D. Williams, E. Licandroand, B. Z. Tang, *Chem. Sci*., 2017, **8**, 2629.

[28] Y. Zhang, H. Li, G. Zhang, X. Xu, L. Kong, X. Tao, Y. Tian and J. Yang, *J. Mater. Chem. C*, 2016, **4**, 2971.

[29] Y. Oyama, M. Sugino, T. EnoKi, K. Yamamoto, Nao Tsunoji and J. Ohshita, *New J. Chem*., 2017,41, 4747.

[30] X. Zhang, J. -Y. Wang, J. Ni, L. Y. Zhang and Z. -N. Chen, *Inorg. Chem.*, 2012, **51**, 5569.

[31] X. Zhang, Z. Chi, Y. Zhang, S. Liu and J. Xu, *J. Mater. Chem. C*, 2013, **1**, 3376.

[32] Y. Sagara and T. Kato, *Angew. Chem., Int. Ed.*, 2008, **47**, 5175-5178.

[33] D. R. T. Roberts and S. J. Holder, *J. Mater. Chem.*, 2011, **21**, 8256-8268.

[34] *Mechanochromic Fluorescent Materials: Phenomena, Materials and Applications*, The Royal Society of Chemistry, 2014, DOI: 10.1039/9781782623229-FP001, P001.

[35] J. Ni, X. Zhang, N. Qiu, Y. -H. Wu, L. -Y. Zhang, J. Zhang and Z. -N. Chen, *Inorg. Chem.*, 2011, **50**, 9090.

[36] H. Sun, S. Liu, W. Lin, K. Y. Zhang, W. Lv, X. Huang, F. Huo, H. Yang, G. Jenkins, Q. Zhao and W. Huang, *Nat. Commun.*, 2014, **5,** 23.

[37] Y. Sagara and T. Kato, *Nat. Chem.*, 2009, **1**, 605.

[38] J. Kunzelman, M. Kinami, B. R. Crenshaw, J. D. Protasiewicz and C. Weder, *Adv. Mater.*, 2008, **20**, 119.

[39] M. Noh, T. Kim, H. Lee, C.-K. Kim, S.-W. Joo and K. Lee, *Colloids Surf., A*, 2010, **359**, 39.

[40] G. v. Bünau, *Berichte der Bunsengesellschaft für physikalische Chemie*, 1970, **74**, 1294.

[41] J. Mei, N. L. C. Leung, R. T. K. Kwok, J. W. Y. Lam and B. Z. Tang, *Chem. Rev.*, 2015, **115**, 11718.

[42] S. J. Yoon, J. W. Chung, J. Gierschner, K. S. Kim, M. -G. Choi, D. Kim and S. Y. Park, *J. Am. Chem. Soc.*, 2010, **132**, 13675.

[43] Z. Chi, X. Zhang, B. Xu, X. Zhou, C. Ma, Y. Zhang, S. Liu and J. Xu, *Chem. Soc. Rev.*, 2012, **41**, 3878.

[44] C. Lowe and C. Weder, *Adv. Mater.*, 2002, **14**, 1625.

[45] X. Zhang, Z. Chi, B. Xu, C. Chen, X. Zhou, Y. Zhang, S. Liu and J. Xu, *J. Mater. Chem.*, 2012, **22**, 18505.

[46] Y. Dong, J. Zhang, X. Tan, L. Wang, J. Chen, B. Li, L. Ye, B. Xu, B. Zou and W. Tian, *J. Mater. Chem. C*, 2013, **1**, 7554.

[47] S. -J. Yoon and S. Park, *J. Mater. Chem.*, 2011, **21**, 8338.

[48] X. Hou, J. Ling, N. Arulsamy and J. Huo, 2013.

[49] Y. Zhang, J. Sun, X. Lv, M. Ouyang, F. Cao, G. Pan, L. Pan, G. Fan, W. Yu, C. He, S. Zheng, F. Zhang, W. Wang and C. Zhang, *CrystEngComm*, 2013, **15**, 8998.

[50] Y. Zhang, G. Zhuang, M. Ouyang, B. Hu, Q. Song, J. Sun, C. Zhang, C. Gu, Y. Xu and Y. Ma, *Dyes Pigm.*, 2013, **98**, 486.

[51] X. Zhang, Z. Chi, H. Li, B. Xu, X. Li, W. Zhou, S. Liu, Y. Zhang and J. Xu, *Chem. Eur. J*, 2011, **6**, 808.

[52] H. Li, Z. Chi, B. Xu, X. Zhang, X. Li, S. Liu, Y. Zhang and J. Xu, *J. Mater. Chem.*, 2011, **21**, 3760.

[53] Q. K. Sun, W. Liu, S. A. Ying, L. L. Wang, S. F. Xue and W. J. Yang, *RSC Adv.*, 2015, **5**, 73046-73050

[54] P. -Y. Gu, Y. -H. Zhang, G. -Y. Liu, J. -F. Ge, Q. -F. Xu, Q. Zhang and J. -M. Lu, *Chem. Asian J.,* 2013, **8**, 2161.

[55] J. Cheng, Y. Li, R. Sun, J. Liu, F. Gou, X. Zhou, H. Xiang and J. Liu, *J. Mater. Chem. C*, 2015, **3**, 11099.

[56] C. Shi, Z. Guo, Y. Yan, S. Zhu, Y. Xie, Y. S. Zhao, W. Zhu and H. Tian, *ACS Appl. Mater. Interfaces*, 2013, **5**, 192.

[57] T. Han, Y. Zhang, X. Feng, Z. Lin, B. Tong, J. Shi, J. Zhi and Y. Dong, *Chem. Commun.*, 2013, **49**, 7049.

[58] Y. Zhang, T. Han, S. Gu, T. Zhou, C. Zhao, Y. Guo, X. Feng, B. Tong, J. Bing, J. Shi, J. Zhi and Y. Dong, *Chem. Eur. J.*, 2014, **20**, 8856.

[59]. R. Rao M, C.-W. Liao and S.-S. Sun, *J. Mater. Chem. C*, 2013, **1**, 6386.

[60] Y. Dong, J. W. Y. Lam, Z. Li, A. Qin, H. Tong, Y. Dong, X. Feng and B. Z. Tang, *J Inorg Organomet Polym*, 2005, **15**, 287.

[61] W. -C. Wu, C .-Y. Chen, Y. Tian, S. -H. Jang, Y. Hong, Y. Liu, R. Hu, B. Z. Tang, Y. -T. Lee, C .-T. Chen, W. -C. Chen and A. K. Y. Jen, *Adv. Fun. Mater*, 2010, **20**, 1413.

[62] H. Wang, E. Zhao, J. W. Y. Lam and B. Z. Tang, *Mater. Today*, 2015, **18**, 365.

[63] T. Zhang, Y. Jiang, Y. Niu, D. Wang, Q. Peng and Z. Shuai, *J. Phys. Chem. A*, 2014, **118**, 9094.

[64] Y. Dong, J. W. Y. Lam, A. Qin, Z. Li, J. Sun, Y. Dong and B. Z. Tang, *J Inorg Organomet Polym*, 2007, **17**, 673-678.

[65] Y. Dong, J. W. Y. Lam, A. Qin, J. Sun, J. Liu, Z. Li, J. Sun, H. H. Y. Sung, I. D. Williams, H. S. Kwok and B. Z. Tang, *Chem. Commun.*, 2007, DOI: 10.1039/B704794K, 3255.

[66] Y. Q. Dong, J. W. Y. Lam and B. Z. Tang, *J. Phys. Chem. Lett.*, 2015, **6**, 3429

[67] a) X. Luo, J. Li, C. Li, L. Heng, Y. Q. Dong, Z. Liu, Z. Bo and B. Z. Tang, Adv. Mater., 2011, 23, 3261; b) Y. Lv, Y. Liu, X.Ye, G. Liu and X. Tao, *CrystEngComm*, 2015, **17**, 526.

[68] Y. Dong, J. W. Y. Lam, A. Qin, Z. Li, J. Sun, H. H. Y. Sung, I. D. Williams and B. Z. Tang, *Chem. Commun.*, 2007, DOI: 10.1039/B613157C, 40.

[69] B. Xu, Z. Chi, X. Zhang, H. Li, C. Chen, S. Liu, Y. Zhang and J. Xu, *Chem. Commun*., 2011, **47**, 11080–11082

[70] G. -G. Shan, H.-B. Li, J.-S. Qin, D.-X. Zhu, Y. Liao and Z.-M. Su, *Dalton Trans.*, 2012, **41**, 9590.

[71] G. G. Shan, H. -B. Li, H. Z. Sun, D. X. Zhu, H. T. Cao and Z. M. Su, *J. Mater. Chem. C*, 2013, **1**, 1440.

[72] G. Li, X. Ren, G. Shan, W. Che, D. Zhu, L. Yan, Z. Su and M. R. Bryce, *Chem. Commun.*, 2015, **51**, 13036.

[73] Z. Song, R. Liu, Y. Li, H. Shi, J. Hu, X. Cai and H. Zhu, *J. Mater. Chem. C*, 2016, **4**, 2553.

[74] X. P. Zhang, D. S. Zhang, X. W. Qi, L. H. Zhu, X. H. Wang, W. Sun, Z. F. Shi, Q. Lin, *Inorg. Chim Acta*, 2017, **467**, 99

[75] C. J. Lin, Y. H. Liu, S. M. Peng, T. Shinmyozu, and J. S. Yang, *Inorg. Chem*. 2017, **56**, 4978.

[76] S. S. Pasha, P. Das, N. P. Rath, D. Bandyopadhyay, N. R. Jana and I. R. Laskar, *Inorg. Chem. Commun.*, 2016, **67**, 107.

[77] J. Mei, Y. Hong, J. W. Y. Lam, Qin, Y. Tang, B. Z. Tang, *Adv. Mater*. 2014, **26**, 5429.

[78] R. Hu, N. Leung, B. Z. Tang, *Chem. Soc. Rev*. 2014, **43**, 4494

[79] D. Ding, D, K. Li, B. Liu, B. Z. Tang, *Acc. Chem. Res*. 2013, **46**, 2441.

[80] Q. Zhao, C. Huang and F. Li, *Chem. Soc. Rev.***,** 2011, **40**, 2508

[81] M. Mauro, A. Aliprandi, D. Septiadi, N. S. Kehr and L. D. Cola, *Chem. Soc. Rev.*, 2014, **43**, 4144.

[82] A. Maji, S. Lohar, S. Pal, P. Chattopadhyay, *J. Chem. Sci*., 2017, **129**, 1423.

[83] Q. Wang, L. Yang, H. Wang, J. Song, H. Ding, X. H. Tang, H. Yao, *Lumin*, 2017, **32**, 779.

[84] B. K. Rani, S. A. John, *J Hazard Mater,* 2018, **343**, 98.

[85] S. W. Botchway, M. Charnley, J. W. Haycock, A. W. Parker, D. L. Rochester, J. A. Weinstein, J. A. G. Williams, *Proc. Natl. Acad. Sci*., 2008, **105**, 16071

[86] Y. You, *Curr. Opin. Chem. Biol*., 2013, **17**, 699

[87] Wu, E. L. -M. Wong, D. -L. Ma, G. S .-M. Tong, K. -M. Ng and C. -M. Che, *Chem. Eur. J.* , 2009, **15**, 3652

[88] W.-Y. Sun, A. L.-F. Chow, X.-H. Li, J. J. Yan, S. S.-Y. Chui and C. -M. Che, Chem. Sci. , 2011, **2**, 728.

[89] S. W. Lai, Y. Liu, D. Zhang, B. Wang, C. N. Lok, C. M. Che and M. Selke, *Photochem. Photobiol*., 2010, **86**, 1414.

[90] T. Zou, C. N. Lok, Y. M. E. Funga and C. M. Che, *Chem. Commun*. , 2013, **49**, 5423.

[91] X. Mou, Y. Wu, S. Liu, M. Shi, X. Liu, C. Wang, S. Sun, Q. Zhao, X. Zhoua and W. Huang, *J. Mater. Chem*., 2011, **21**,13951

[92] S. P. Y. Li, H. W. Liu, K. Y. Zhang and K. K. W. Lo, *Chem. Eur. J*., 2010, **16**, 8329.

[93] Q. Zhao, M. X. Yu, L. X. Shi, S. J. Liu, C. Y. Li, M. Shi, Z. G. Zhou, C. H. Huang and F. Y. Li, *Organomet*, 2010, **29**, 1085.

[94] J. Yang, X. Liu, H. Wang, H. Tan, X. Xie, X. Zhang, C. Liu, X. Qub and J. Hua, *Analyst*, 2018, **143**, 124

[95] X. Wen, Q. Wang, Z. F. Fan, *Anal. Chim. Acta*, 2018, **1013,** 79.

[96] Y. Li, R. Liu, J. Chang, M. Huang, H. Chang, Y. Miao, *Dyes Pigm.*, 2017, **139**, 110.

[97] E. Lalinde, R. Lara, P. Ljpez, M. T. Moreno, E. A. Arnedo, G. Pichel, and S. P. Hermida, *Chem. Eur. J.*, 2018, **24,** 2440 .

[98] C. -K. Koo, L. K. -Y. So, K. -L. Wong, Y. -M. Ho, Y. -W. Lam, M. H. -W. Lam, K. -W. Cheah, C. C. -W. Cheng and W. -M. Kwok, *Chem. Eur. J*., 2010, **16**, 3942

[99] Y. Yuan, C. Jing Zhang and B. Liu, *Chem. Commun.,* 2015, **51**, 8626.

[100] P. Alam, P. Das, C. Climent, M. Karanam, D. Casanova, A. R Choudhury, *J. Mater. Chem. C,* 2015*,* **2**, 5615

[101] P. Alam, S. Dash, C. Climent, G. Kaur, A. R. Choudhury, D. Casanova, P. Alemany, R. Chowdhury and I. R. Laskar, *RSC Adv*., 2017, **7**, 5642

[102] V. F. Moreira, M. C. Gimeno, *Chem. Eur. J*, 2018, **24**, 3345

[103] M. Peyrone, *Ann. Chem. Pharm*., 1984, **51**, 1.

[104] G. Yu, T. R. Cook, Y. Li, X. Yan, D. Wu, L. Shao, J. Shen, G. Tang, F. Huang, X. Chen, and P. J. Stangd, *PNAS*, 2016, **113**, 13721.

[105] A. Chandra, K. Singh, S. Singh, S. Sivakumar and A. K. Patra, *Dalton Trans*., 2016, **45**, 494.

Chapter II

Materials and Methods

2.1 Materials

Used Reagents

Potassiumtetrachloropalatinate(II), 2-Aminopyridine, Tritylechloride, Sodiumhydride, Iridium(III) chloride hydrate, 2-phenyl pyridine, benzaldehyde, Sodiumcarbonate, 1,2-Bis(diphenylphosphino)ethane, *cis*-1,2-Bis(diphenylphosphino)ethylene, Bis(diphenylphosphino)propane, ethylenediamine, mesoporous silica, tritylaniline, salicylaldehyde, p-bromosalicyladehyde, triphenylamine, 2-ethoxyethanol were purchased from Sigma Aldrich Chemical Company. Trifluoroacetic acid, acetic acid, hydrochloric acid, trifluoromethanesulphonic acid and triethylamine were procured from Merck Company.

Ephithelial Cellular Adhesion Molecule (EpCAM) aptamer was synthesized by IDT (Integrated DNA Technologies). The sequence for the same is 5'-CAC TAC AGA GGT TGC GTC TGT CCC ACG TTG TCA TGG GGG GTT GGC CTG-3'. Dulbecco's modified eagle medium (DMEM), penicillin/streptomycin, Triton X-100 and propidium iodide were purchased from Sigma-Aldrich. Fetal bovine serum (FBS) was purchased from invitrogen. 3-(4,5-Dimethylthiazol-2-yl)-2,5-diphenyltetrazolium bromide (MTT) was purchased from Himedia. This work done by the help of Dr. Rajdeep Chaudhury [1] and his group.

The UV-Vis grade solvents (Methanol, DCM, hexane, ethylacetate, toluene, 1, 4-dioxane, chloroform, acetone and acetonitrile, all the names of the solvents) were procured from Merck Company. 2-(naphthalen-2-yl) pyridine and 2-(naphthalen-5-yl) pyridine were synthesized by following the literature [2-3], PEG(1000)-b-PLA(5000) was purchased from Poly sciences Inc.. Benzoic acid, 3,5 dinitro toluene, 1,3 dintro benzene, 2,5 dinitro phenol, 2,4,6-trinitrophenol and metal nitrate salts were procured from Merck Company.

NaOH, triethyl amine, trifluoroacetic acid and acetic Buffer solutions (pH 1- pH 14) have been prepared by using KCl-HCl, KH_2PO_4-HCl, KH_2PO_4-NaOH and NaOH. For selectivity of cations, different metal salts (KI, KBr, KCl, $NaNO_3$ etc) were procured from SD fine.

2.2 Methods

2.2.1 Fabrication of thin-film on thin glass substrate for photoluminescence (PL) measurement

The 10^{-4} M solution of platinum(II) complex in THF/DCM were prepared. 2-3 drops of the solution were placed on thin glass substrate ($2x2cm^2$) and the solvent was allowed to evaporate slowly.

2.2.2 Sample preparation to investigate the 'Aggregation Induced Emission (AIE)' property At the beginning, we have chosen two solvents, in which one of them the AIE compound is soluble and in another solvent the AIE compound is insoluble. Then, it has been prepared a series of AIE solutions with maintaining the final concentration, ~10^{-4} – 10^{-5}M (total volume, 10ml). Then, the other solvent was gradually added with increasing volume so that the total volume of the solvent will be 10ml. As for example, conc. of 0% water: 10^{-6}M of complex in 1 ml THF (rest is 9 mL THF); conc. of 30% water: 10^{-6} M of complex in 1ml (rest is 6 ml THF and 3 ml of Water), conc. of 60% water: 10^{-6} M of complex in 1ml (rest is 3 ml THF and 6 ml water), conc. of 90% water: 10^{-6} M of complex in 1ml (rest is 9 ml of water).

2.2.3 Fluorescence quantum yield calculations

The fluorescence relative quantum yield (ϕ) of the compounds were calculated with reference to quinine sulphate [4] (ϕ = 0.55) in 0.1N H_2SO_4, the commonly used fluorescence standard. Fluorescence spectra were recorded for solutions of absorbance less than 0.1 at the excitation wavelength. Generally, the longest wavelength band maximum was chosen for excitation. In case of a system with an isosbestic point in the absorption spectra, the excitation was carried out at isosbestic wavelength.

Quantum yield of the samples were calculated using the Equation 2.1.

$$\boldsymbol{\phi}_{unknown} = \boldsymbol{\phi}_{standard} \times \frac{\mathbf{F}_{unknown}}{\mathbf{F}_{standard}} \times \frac{\mathbf{A}_{standard}}{\mathbf{A}_{unknown}} \quad \text{--- Equation 2.1}$$

ϕ is fluorescence quantum yield,

F is area under the curve of corrected fluorescence spectra,

A is absorbance at excitation wavelength.

2.2.4 Experimental procedure for detection limit calculations

To determine the Signal/Noise ratio, the emission intensity of organic Schiff base compound in methanol without zinc(II) nitrate was measured by 10 times and the standard deviation of blank measurements was determined. The detection limit is then calculated with the following equation.

Detection limit = 3σ/m; where σ is the standard deviation of blank measurements, m is the slope between the plot of PL intensity versus sample concentration [5-7].

2.3 Instrumentation

2.3.1 UV-Visible spectrophotometer

Absorption spectroscopy is the most widely used spectroscopic tools which provide useful information about the sample under studied. It refers to spectroscopic tool that measures the absorption of radiation, as a function of frequency or wavelength, due to its interaction with a sample. The environmental effects alter the relative energy of ground and excited states, and this alteration causes spectral shifts. The absorbance (A) of an absorber (concentration C) having a molar extinction coefficient ε at wavelength λ is given by the Equation 2.2.

$$\mathbf{A = \log\left(\frac{I_0}{I}\right) = \varepsilon\lambda cl} \qquad \text{--- Equation 2.2}$$

where A is absorbance (optical density), I_0 and I represent the intensity of the incident and transmitted light, respectively, c is the concentration of the light absorbing species and l is the path length of the light absorbing medium in decimeter. A matched pair of 10 cm quartz cuvettes (Hellma, 1 cm light path, capacity 3.5 ml, Model: 100-QS) was used for absorption measurements. UV-Vis absorbance spectra were recorded using a Simadzu Spectrophotometer (model UV-1800 and 2550).

2.3.2 Steady-state spectrofluorimeter

Fluorescence measurements were performed using a Horiba Jobin Yvon Fluoromax-4 scanning spectrofluorimeter and Simadzu (A40195003382SA). The spectrofluorimeter irradiates a sample with excitation light and measures the fluorescence emitted from the irradiated sample to perform a qualitative or quantitative analysis. The block diagram of the instrument is shown in Figure 1. The brief description of its components is given below:

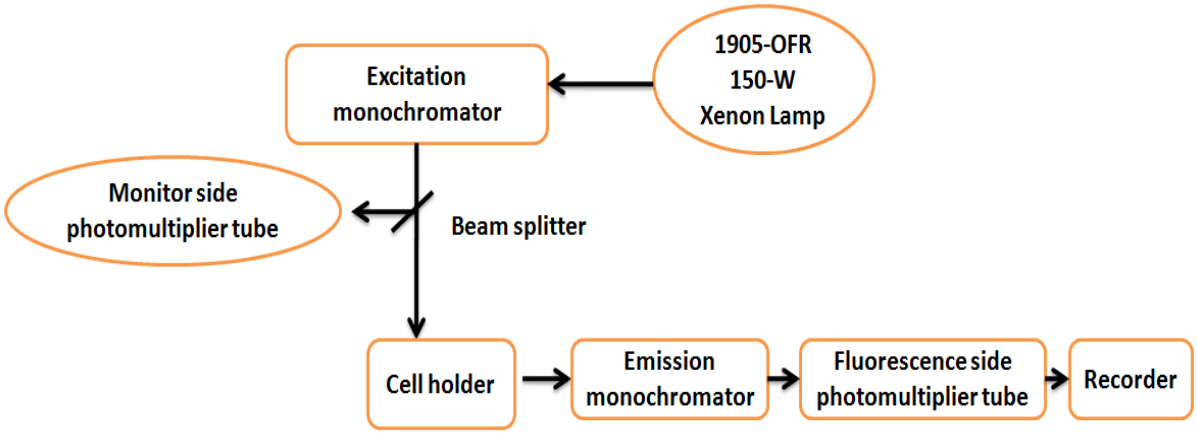

Figure. 1 Block diagram of a steady-state spectrofluorimeter.

This instrument is equipped with the light source of 1905-OFR 150-W Xenon lamp. The lamp housing is provided with ozone self-decomposition. This instrument contains Czerny Turner monochromators for excitation and emission. The important part of monochromator is a reflection grating. A grating disperses the incident light by means of its vertical grooves. The gratings in this instrument contain 1200 grooves mm^{-1}, and are blazed at 330nm (excitation) and 500nm (emission). Blazing is etching the grooves at a particular angle, to optimize the grating's reflectivity in a particular spectral region. This instrument uses a direct drive for each grating, to scan the spectrum at up to 200 nm s^{-1}, with accuracy better than 0.5 nm, and repeatability of 0.3 nm. The scan range of this instrument is 240-850 nm. The cell holder holds a cell filled with sample.

The emission monochromator selectively receives fluorescence emitted from the sample and the photomultiplier tube (PMT) measures the intensity of the fluorescence. The monochromator has a diffraction grating whose size is the same as that of the excitation monochromator to collect the greatest possible amount of light.

The detector in this system consists of photomultiplier tube for both photometry and monitor sides. Generally, the Xenon lamps used on spectrofluorimeter are characterized by very high emission intensity and an uninterrupted radiation spectrum. However, their tendency to unstable light emission will result in greater signal noise if no counter measure is incorporated. In addition, the non-uniformity in the radiation spectrum of the Xenon lamp and in the spectral

sensitivity characteristics of the photomultiplier tube (these criteria are generally called instrument functions) causes distortion in the spectrum. To overcome these factors, the photomultiplier tube monitors a portion of excitation light and feeds the resultant signal back to the photomultiplier tube for fluorescence scanning. This scheme is called the light-source compensation system. The slits widths are adjustable from the computer in units of bandpass or millimeters. This preserves maximum resolution and instant reproducibility. The steady-state fluorescence anisotropy measurements were performed with the same steady-state spectrofluorimeter fitted with a polarizer attachment (105UV polarizers), manufactured by POLACOAT Co., USA. The measurement was obtained by placing one polarizer on each of excitation and emission sides. The sample was taken in a Quartz cuvette (Hellma, 1 cm light path, capacity 3.5 ml, Model: 101-QS) with four walls transparent to measure the excitation and emission spectra.

2.3.3 Computational study

The Density Functional Theory (DFT) calculations were performed using the Gaussian 09 program suite [8]. Beckes three-parameter hybrid exchange functional with the Lee‑Yang‑Parr gradient-corrected correlation (B3LYP functional)[9] and the basis set 6-31G(+) level [10] were used in both the DFT and TD-DFT methods. All calculations were performed in methanol (e = 32.7) using the Integral Equation Formalism-Polarizable Continuum Model (IEF-PCM) for the solvent.

2.3.4 Other instruments

Cyclic voltammetry (CV) measurements were recorded on a Potentiostat/Galvanostate Model 263 A. The platinum, glassy carbon and Ag/AgCl electrodes were used as counter, working and reference electrodes, respectively and the scan rate was maintained to 50 mVs^{-1}.

The complexes were dissolved in acetonitrile (10 mL) and 0.1 M lithium perchlorate ($LiClO_4$) (100 Mg) was added to the solution (used as the supporting electrolyte). The whole experiment was conducted under inert atmosphere.

The dynamic light scattering (DLS) measurements of the aggregates of complexes were carried out in Zeta Sizer, model Nano ZS (ZEN 3600, Malvern Instruments, UK). Samples were filtered prior to the measurements with 0.22-μM filter (Durapore, PVDF). The wavelength of

the laser light was 6328 Å, and the scattering angle was 173°. At least five set of measurements were carried out for each sample at ambient conditions. The scattering intensity signal of the sample is passed to a digital signal processing board called a correlator, which compares the scattering intensity at successive time intervals to derive the rate at which the intensity is varying. This correlator information is then passed to a computer and the data was analyzed with the Zetasizer software to derive size information.

The size and shape of the nanoparticles were measured by scanning electron microscopy (SEM) using a JEOL JSM-6700F FESEM instrument at MNIT jaipur.

TEM images were obtained using a JEOL-2100F TEM at MNIT Jaipur. Samples were prepared by placing 3-4 drops of the appropriate nanoparticle solution on a 300-mesh, carbon coated Cu grid (EM sciences) and allowing the liquid to evaporate in air. The particle size distribution was based on 50 randomly selected particles. EDS analysis was carried out with the same instrument for TEM and a selected area was used for analysis.

The FT-IR spectra were recorded in ABB Boman MB 3000 instrument, FTIR Simadzu (IR prestige-21) and Perkin Elmer Spectrum 100. The complexes were mixed with dry potassium bromide (KBr) powder and pellets were prepared. The pellets have been used to record FT-IR.

^{1}H NMR, ^{13}C NMR and ^{31}P NMR spectra were recorded in a 400 MHz Brucker spectrometer using $CDCl_3$ as solvent and tetramethylsilane (TMS, δ = 0 ppm for ^{1}H and ^{13}C NMR), and phosphoric acid (H_3PO_4, δ = 0 ppm for ^{31}P NMR) as internal standard with a 400 MHz Brucker spectrometer instrument at IISER Mohali and BITS Pilani, Pilani campus.

High-resolution MS (HRMS) were carried out with a (TOF MS ES^+ 1.38 eV) VG Analytical (70-S) spectrometer and Q-Tof micro mass spectrometer instrument at IISER Mohali and BITS Pilani, Pilani campus.

Time correlated single photon counting (TCSPC) spectra of the iridium complex in THF was obtained through exciting the sample with a picosecond diode laser (IBH Nanoled) using a Horiba Jobin Yvon IBH Fluorocube apparatus (IACS, Kolkata) and Spectrofluorometer FLS920s Edinburgh (AIRF, JNU, New Delhi).

The solid state quantum yield of the thin film sample was measured using a calibrated integrating sphere in a Gemini Spectrophotometer (model Gemini 180) at IIT Kanpur and PTI QuantaMaster ^{TM} 400 in IACS Kolkata.

Luminescence images of HeLa cells and photo stability of the platinum(II) complex in water performed by drop casting the sample solution on a glass slide and images were captured using an Olympus IX 81 microscope provided with a digital camera.

Microwave reactions were carried out in a CEM Discover (mode l908010). All the reactions were performed under nitrogen atmosphere and the progress of the reaction was monitored using thin-layer chromatography (TLC) plates (pre-coated with 0.20 mm silica gel).

X-ray Single Crystal structure analysis: Single crystal X-ray diffraction data for the compounds were recorded on Bruker AXS KAPPA APEX-II CCD and Rigaku Mercury375/M CD (XtaLAB mini) diffractometer respectively by using graphite Monochromated Mo – K radiation at 100.0(1) K by using Oxford cryosystem. The data sets collected Bruker AXS KAPPA APEX-II [11] Kappa were collected using Bruker APEX-II suit, data reduction and integration were performed by SAINT V7.685A12 (Bruker AXS, 2009) and absorption corrections and scaling was done using SADABS V2008/112 (Bruker AXS). The data sets, which were collected on XtaLAB mini diffractometer, were processed with Rigaku Crystal Clear suite 2.0. The crystal structures were solved by using SHELXS2013 [12] and were refined using SHELXL2013 available within Olex2. All the hydrogen atoms have been geometrically fixed and refined using the riding model except the hydride anion, co-ordinating with Ir, which has been located from the difference Fourier map and were refined isotropically. All the diagrams have been generated using Mercury 3.1.1. Geometric calculations have been done using PARSTR and PLATONR. Powder X-ray diffraction (PXRD) was measured by using Rigaku miniflex II desktop X-ray diffractometer. Prof. Nigam's instrument model etc.,

2.3.5 Cell culture

For BMPP-Pt complex Human hepatocellular carcinoma cell line, Huh7 (kind gift from Dr Soma Banerjee) were cultured at 37°C, 5% CO_2, in Dulbecco's modified eagle medium (DMEM; Invitrogen) supplemented with 10% fetal bovine serum (FBS; Invitrogen), 100UmL^{-1} penicillin, 100μgmL^{-1} streptomycin (Invitrogen) was added to the culture medium. Cells were

typically grown to 60–70% confluency, rinsed in phosphate-buffered saline (PBS; Invitrogen) and placed into fresh medium prior to treatments. This work done by the help of Dr. Rajdeep Chaudhury [1] and his group.

For cell imaging studies of the complex [Pt(ppy)(en)]Cl three cancer cells, namely, HeLa (human cervical cancer cell), U87MG (human glioblastoma cell) and Nuro2a (mouse neuroblastoma cell) and normal cells namely 3T3-L1 (mouse fibroblast cell) were used. All the cells were purchased from National Center for Cell Science, Pune (India). Cells were cultured in Dulbecco's modified eagle medium (DMEM) supplemented with 10% fetal bovine serum (FBS) and 1% penicillin/streptomycin at 37ºC and 5% CO_2. Next, cells were seeded into 24-well tissue culture plate in presence of 500 µL DMEM medium and grown overnight. Next, aqueous solution of platinum(II) complex was added at a final of concentration of 170 µM to each well and incubated for different times. Next, cells were washed with PBS buffer solution, supplanted with 500 µL DMEM medium and used for imaging study. This work done by the help of Prof. N. R. Jana [13] and his group.

2.3.6 *In vitro* cytotoxicity assay

In-vitro cytotoxicity was performed as described previously by Chowdhury *et al*. [8]. Briefly, cells were cultured in 96 well plates. After 24h, cells were treated with different treatments for specific period of time. Thereafter, MTT (3-(4, 5-Dimethylthiazol-2-yl)-2, 5-Diphenyltetrazolium Bromide) (SRL) was added to each treated and control well and incubated for 4h. Formazan crystals were solubilized in DMSO (dimethyl sulfoxide) and readings were obtained at 570nm with a differential filter of 630nm using Multiscan Microplate Spectrophotometer (Thermo Scientific). Percentage of viable cells was calculated using the following formula: Viability (%) = (mean absorbance value of drug-treated cells) / (mean absorbance value of control) ×100. A concentration of 0.2% DMSO was found to be non-toxic and was used for dissolving BMPP-Pt, and used as control in cytotoxicity experiments.

2.3.7 Microscopic imaging and internalization

For microscopic imaging, cells were cultured overnight on coverslips in 6cm culture dishes, and were treated for 24h. Coverslip cultured cells were washed with 0.1 M PBS and fixed

in methanol at -20°C for 10min. The coverslips were mounted with antifade mountant containing DAPI (4'-6-diamidino-2-phenylindole) (Thermoscientific) on glass slide, which were visualized by confocal fluorescence microscope using FITC ($\lambda_{ex/em}$ 490/520) and DAPI ($\lambda_{ex/em}$ 372/456) filters. Cellular uptake was further confirmed by flow cytometer, in brief, the Huh7 cells after MSNPs exposure, cells were trypsinized, centrifuged and resuspended in PBS. The light side scatter intensity and shift in green fluorescent peak intensity was measured using flow cytometry (CytoFLEX, Beckman Coulter). Analysis of acquired data was performed using CytExpert software.

2.3.8 Co-localization Study

For nucleus co-localization studies HeLa cells were seeded into a 4-well chamber slide in 500 μL supplemented DMEM medium and allowed to adhere for overnight. Then cells were incubated with an aqueous solution of the complex 2 (final concentration, 170 μM) for 4 hrs. Next, cells were washed with PBS buffer solution and fixed with 4% paraformaldehyde for 20 min. Then cells were permeabilized by adding 500 μL 0.3% Triton X-100 in PBS solution for 20 min. Then, cell nucleus was stained with aqueous solution of propidium iodide. Next, fixed cells were mounted with 50% glycerol and imaged under fluorescence microscope.

2.3.9 Statistical analysis

The obtained data were analyzed using the Prism® software (Version 5.01; GraphPad Software Inc., USA). The effect of various treatments was statistically analyzed using one-way ANOVA test and the level of $p < 0.05$ was considered as statistically significant. All data points represent the mean of independent measurements. Uncertainties were represented as standard deviations in the form of bars.

2.4. References

[1] R. Choudhury, Assistant Professor, Department of Biology, BITS Pilani, Pilani campus, Pilani, India.

[2] C. Xu, Z. -Q. Wang, X.-M. Dong, X.-Q. Hao, X.-M. Zhao, B.-M. Ji, M.-P. Song, *Inorg. Chim. Acta*, 2011, **373**, 306.

[3] A.F. Rausch, M.E. Thompson, H. Yersin, *Inorg. Chem*., 2009, **48**, 1928.

[4] G.G. Guilbault, Practical fluorescence, Marcel Dekker Inc., New York, 1973.

[5] M.-H. Yang, P. Thirupathi, K. -H. Lee, *Org. Lett*., 2011, **13**, 5028.

[6] L.N. Neupane, J.M. Kim, C.R. Lohani, K.-H. Lee, *J. Mater. Chem*., 2012, **22**, 4003.

[7] S. Kaur, V. Bhalla, V. Vij, M. Kumar, *J. Mater. Chem. C*, 2014, **2**, 3936.

[8] M. J. Frisch, G. W. Trucks, H. B. Schlegel, G. E. Scuseria, M. A. Robb, G. Cheeseman, V. Barone, B. Mennucci and G. A. Petersson, et al., Gaussian 09, 2010, Revision C. 01,

Gaussian, Inc., Wallingford, CT, 2010.

[9] A. D. Becke, *J. Chem. Phys*., 1993, **98**, 5648.

[10] S. Markovicı and J. Tosovic, *J. Phys. Chem. A*, 2015, **119**, 9352.

[11] APEX2, SADABS and SAINT; Bruker AXS Inc. Madison, Wisconsin, USA, 2008

[12] M. Nardelli. J. Appl. *Crystallogr*. **28**, 1995, 569.

[13] N. R. Jana, Professor, Centre for Advanced Materials, Indian Association for the Cultivation of Science, Jadavpur, Kolkata 32, India.

.

.

Chapter III

PART-A

Water Soluble Luminescent Cyclometalated Platinum(II) Complex - A Suitable Probe for Bio-imaging Applications

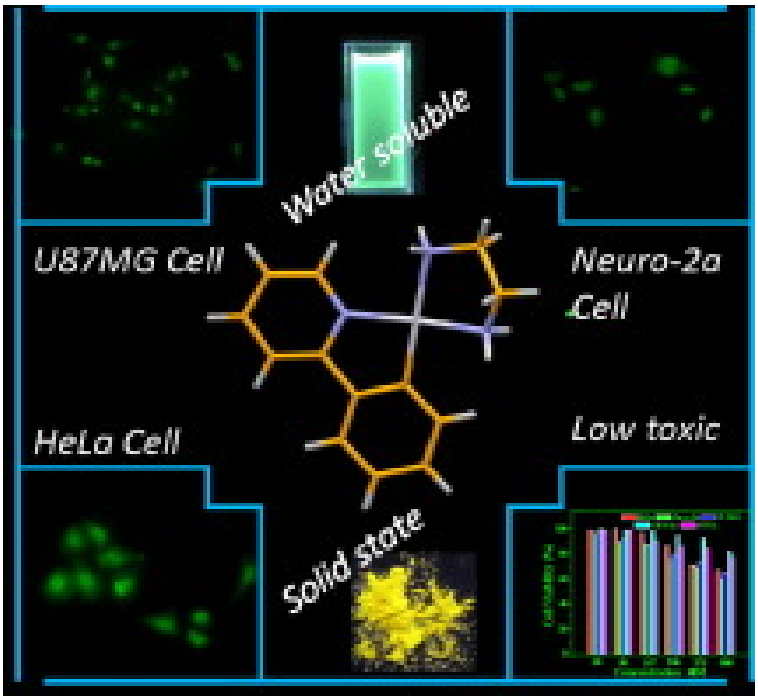

3A.1. Introduction

Bio-imaging is used to label the cells and cell organelles to understand the mechanistic pathways of biochemical reactions[1-3].The most desirable criteria for bio-imaging probes are a good thermal stability [4], water solubility [5-7], low cyto-toxicity [8-9], high cellular uptake [8-11] and selectivity for specific organelles [8-11]. Till date many types of bio-imaging luminescent probes like organic luminogens [4], quantum dots [9-13] and heavy metal based cyclometalated complexes [14-21] etc have been reported. Among these luminophores, heavy metal [Ir(III), Pt(II), Os(IV), Re(I) and Rh(III)] based complexes have received a special attention. These probes are superior in terms of phosphorescent emission at room temperature [22], higher stability [22], larger quantum yield [23-24], lower photo bleaching effect [23-24] and greater Stokes's shift [25] in comparison with other bio-imaging probes.

Platinum(II) is a d^8 system, preferably a 4-coordinated square planar geometry. In contrast, the d^6 metal ion complexes show distorted octahedral geometry. The aggregation property plays a significant role in self-assembling of non-biological entities into living systems[26]. The square planar geometry could be helpful in the formation of self-assembly or stacking[27-33]. The stacking of Pt(II) complex may result in higher emission quantum yields, longer excited state lifetimes and reduced reactivity as compared to the single component motifs[26]. One of the prime challenges in utilizing such complexes as probe molecule and in bio-imaging is water solubility. Very few water soluble platinum(II) complexes have been reported as bio-imaging probes. M. H. W. Law *et al.* have reported an amphiphilic and water-soluble platinum(II) complex $[Pt(C\hat{}N\hat{}N–C_{18})(P\{C_6H_4–SO_3\}_3)]^{2–}$, **I** as a biological probe [34].This complex was successfully localized in the plasma membrane of HeLa cell. L. Mishra *et al.* have also reported [35] $[\{Pt(en)L\}_2]PF_6$, **II** where LH_2 is N,N-bis(salicylidene)-p-phenylenediamine and en is 1,2-diamino ethane for nucleus staining. However, this complex is highly toxic (IC_{50} = 11.5 μM).

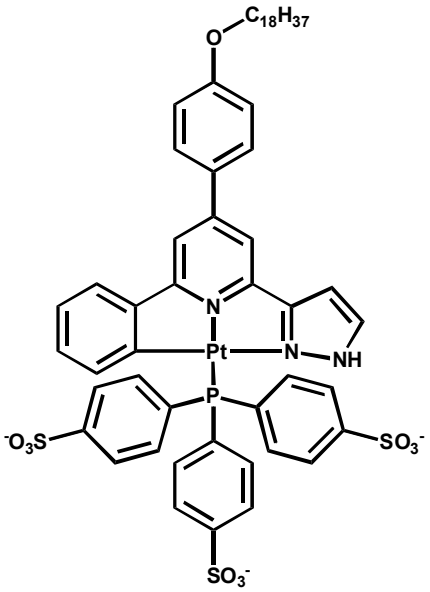

I

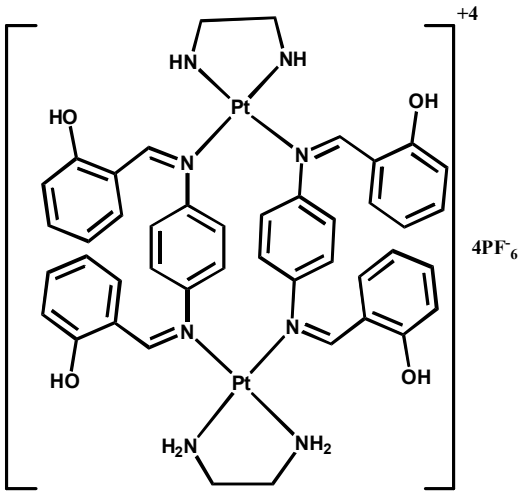

II

M. Selke *et al.* have reported [36] a platinum(II) complex $[Pt(Thpy)(HThpy)py]ClO_4$, **III** which was applied for nucleus staining and labelling of mitochondria with an IC_{50} of 3.29μM for this complex.

Che and co-workers have described [37] Pt(II)-allenylidene complex **IV** as nucleus staining, but it is also toxic (IC_{50} = 19 mM).

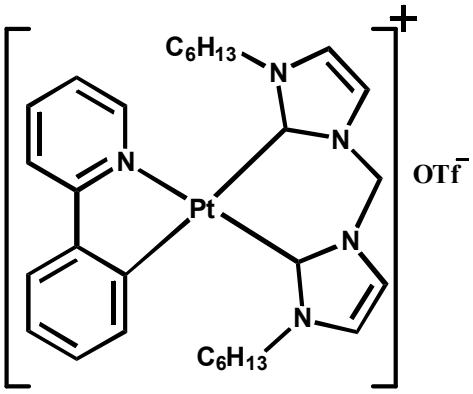

III

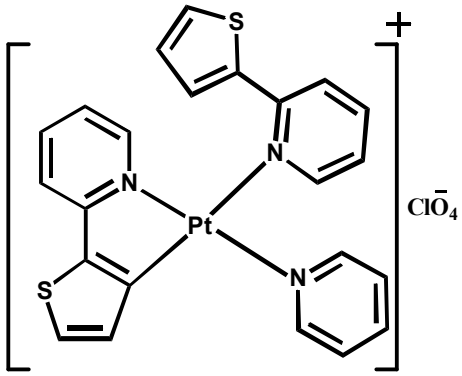

IV

Herein, we report a water soluble, strongly luminescent and less toxic [Pt(ppy)(en)]Cl complex as an efficient nuclear bio imaging probe.

3A.2 Results & Discussion

3A.2.1 Syntheses and Characterizations

The syntheses of complexes **1** and**2**are presented in scheme 1. The green synthetic approach has been applied for the syntheses of these complexes. Complex **1** has been synthesized by using K_2PtCl_4 as the platinum(II) precursor along with four equivalents of 2-phenyl pyridine. The reaction was completed using water as the solvent in presence of microwave (MW) in 10 minutes. The greenish yellow product was isolated from water as a solid mass and characterized by ^1H and ^{13}C NMR. The synthesized pendent complex **1** is one of the important precursors for synthesis of many luminescent Pt(II) complexes [37] .

The complex **2** was synthesized in two steps. It was resulted through chelation of ethylenediamine to platinum(II) by replacing two ligands (Cl^- and N-bonded phenylpyridine) from the metal. The structure of the complex **2** was determined by NMR spectroscopy and X-ray single crystal structure analysis (Figure. 1 & Table 2). ^1H NMR spectra of complex **2** showed aromatic proton signals in the range, δ = 7.1-8.7 ppm. The four protons of (CH_2-CH_2) of ethylenediamine ligand were observed as multiplets at δ = 2.67 ppm and the four N-H protons of ethylenediamine appear in the range, δ = 5.38–6.12 ppm. ^{13}C NMR spectra of complex **2** showed aromatic carbons signals in the range δ= 119-168 ppm. The two carbons of (CH_2-CH_2) of the ethylenediamine ligand were observed at δ = 48.3 and 44.0 ppm.

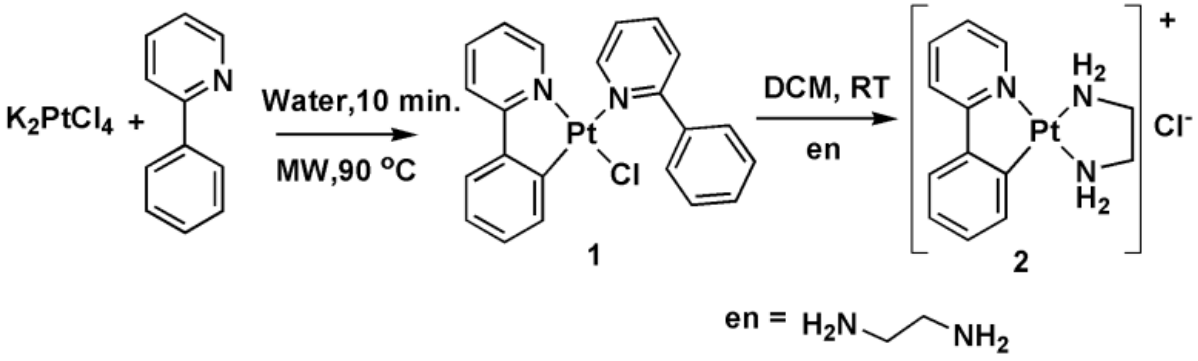

Scheme 1. Synthetic route of complexes **1** and **2**.

3A.2.2 Photo physical property

3A.2.2.1 Solution and solid state absorbance and emission behavior

Complex **2** exhibits a green emission in the solution which is changed into a bright yellow emission in the solid state (Figure 2). The packing diagram of the complex (Figure 1) clearly indicates the presence of π-π stacking which is being interplayed in between the phenyl rings of consecutive molecules. It shows a green emission in water with λ_{max} of 510 nm under excitation at 375 nm (Figure 3) and a yellow emission in the solid state with λ_{max} of 553 nm with exciting at 400 nm (Figure 4). This observation suggests that a new excited state *i.e.*, ^{3}MLLCT is formed from the existing ^{3}MLCT state (*vide supra*, molecular modeling) when the molecules gets assembled in solid state. Hence the energy of the MLLCT state of the complex gets lowered [green (solution) → yellow (solid)].

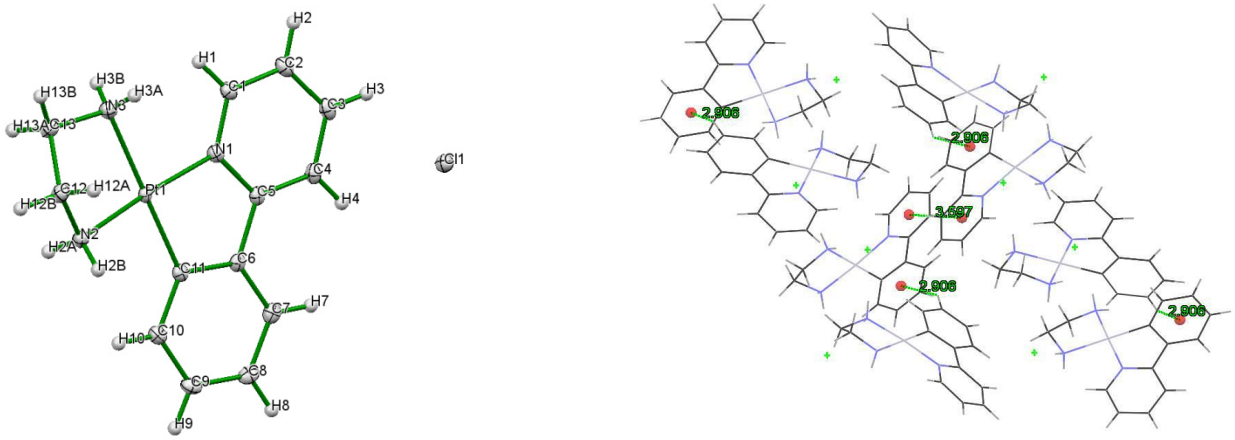

a **b**

Figure. 1 a) ORTEP diagram of complex **2** with 50% probability of ellipsoids; b) Crystal packing diagram of complex **2** showing a π···π type stacking interactions between pyridyl rings (3.597Å) and between C-H π (phenyl) to centroid of adjacent phenyl ring (2.906 Å).

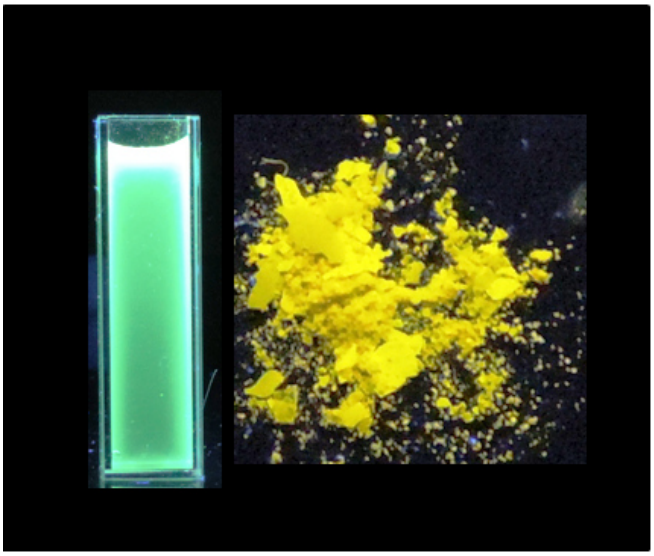

Figure. 2 Luminescent images of complex **2** under excitation of long wavelength of UV ray [λ_{ex}, 365 nm; solution (water, left); solid (right)].

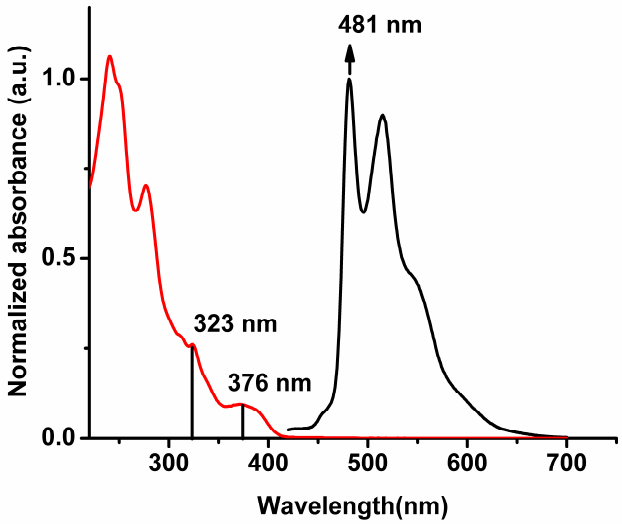

Figure. 3 UV-Vis absorption (left) and photoluminescence spectra (right) of $1x10^{-5}$ M complex **2** in MeOH.

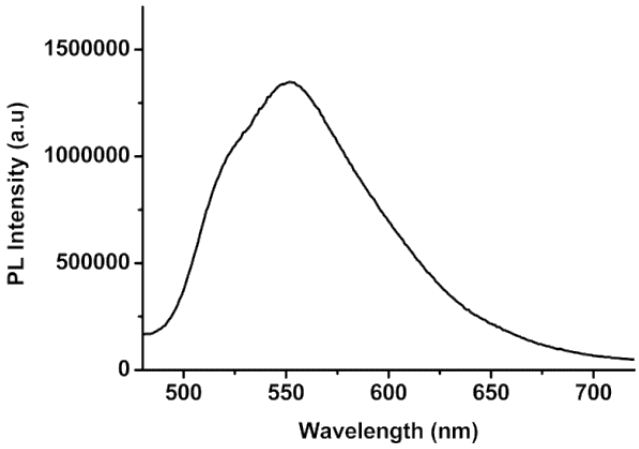

Figure. 4 Solid state photoluminescence spectra of complex **2**.

3A.2.2.2 DFT and TD-DFT Study

Single electron excitation with TD-DFT has produced ten different excitations from S_0-S_1 state to S_0-S_{10} states. First three excitations are reported (Table 1). The first and third excitation (S_0-S_1, S_0-S_3) wavelengths (371 nm and 306 nm, respectively) obtained from TD-DFT calculations matched well with the experimental absorption wavelengths in UV-Vis range (376 nm and 323 nm, respectively) (Figure 3). The oscillator strengths for these two transitions are higher as compared to S_0-S_2 (Table1) which indicates that these two transitions are more probable than the other. S_0-S_1 transition mainly involves HOMO and LUMO orbitals (Table 1). HOMO has a significant contribution from the platinum(II) ion and the pheyl part of the 2-phenylpyridine (Figure. 5); whereas, LUMO purely lies on the fused ring, co-ordinated to platinum(II). Thus, S_0-S_1 transition has a significant metal to ligand charge transfer (MLCT) character (Table 1). Ground state singlet to excited state triplet transition (S_0-T_1) has a calculated wavelength of 483 nm. Although, this transition is spin-forbidden, it is observed as a consequence of inter-system crossing. The S_0-T_1 transition wavelength obtained from TD-DFT calculation which is in agreement with the experimental maximum emission wavelength of 481 nm. This transition also involves the HOMO and LUMO orbitals, however to the lesser extent as compared to S_0-S_1 transition. That reflects the MLCT character observed in S_0-T_1 transition (Table 1).

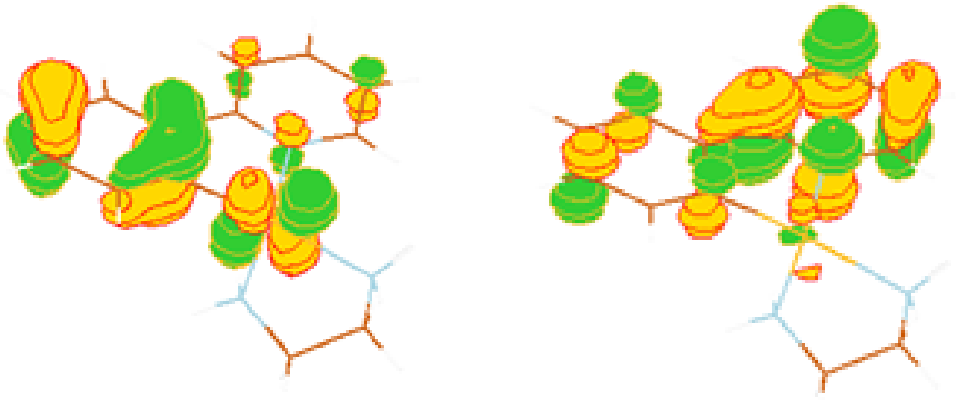

HOMO **LUMO**

Figure. 5 Frontier Molecular Orbitals for complex **2**. (Calculations are performed by GAMESS US software; for visualization of the molecular orbital, MOLDEN software was used).

Table 1:Excitedstateelectronicproperties of complex **2**inmethanol solvent.

Transition from S_0 to	λ_{cal}(nm)	E(eV)	F (Oscillator strength)	Assignments and Contribution of transitions	MLCT character(%)
S_1	371.70	3.34	0.035	HOMO→LUMO, 96.04%	31.69
S_2	346.08	3.58	0.010	HOMO-1→LUMO, 98.01%	84.97
S_3	306.70	4.04	0.092	HOMO-2→LUMO, 76.09%	10.34
T_1	483.24	2.57	0.0	HOMO→LUMO, 67.86%	22.39
T_2	412.51	3.01	0.0	HOMO-1→LUMO, 34.30% HOMO-2→LUMO, 33.39% HOMO→LUMO, 8.47%	29.74 4.54 2.79

3A.2.3 Application of 2 as bio-imaging probe

The highly luminescent water soluble platinum(II) complex, **2** has been used as a bioimaging probe. The cellular uptake study shows that **2** enter into both cancer and normal cells. However, the uptake is high in cancer cells as compared to normal cells (Figure. 6 and 7). Time dependence study shows that uptake of complex **2** increases with incubation time and

gradually localizes into cell nucleus (Figure 8 and 9). The fluorescence imaging study at different incubation time ranging from 15 min to 24 hrs shows that the complex **2** is localized in cytoplasm in the first one hour and then slowly localizes into the cell nucleus within 2 hrs (Figure 8 and 9). The co-localization study shows that the complex **2** predominantly co-localizes with nucleus staining dye with longer time of incubation (Figure 10). Luminescence intensity profile of the complex **2** and propidium iodide labeled HeLa cells further indicates the staining of the cell nucleus by the complex **2** (Figure 11). The complex **2** binds to nucleic acids of the nucleus possibly due to the intercalation with the nucleic acids stabilized by the π-π stacking interactions between the nucleic acid bases and aromatic ligand of complex [39].

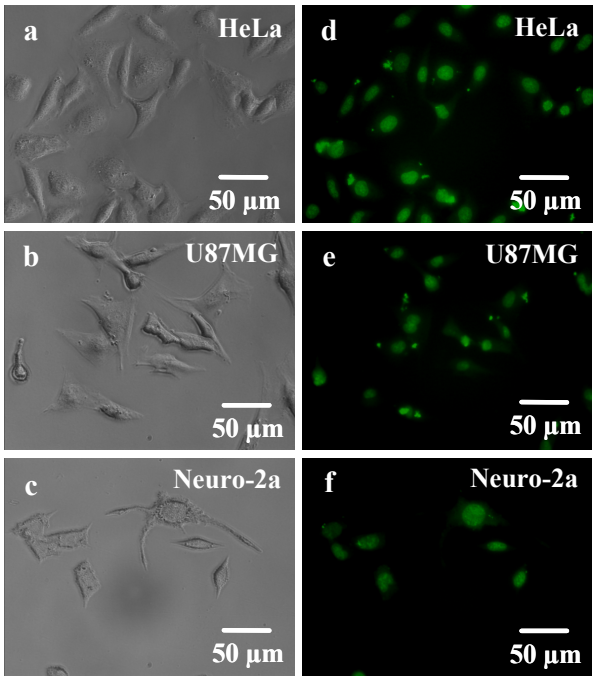

Figure. 6 Differential interference contrast images (a-c) and luminescence images (d-f) of complex **2** labeled HeLa, U87MG and Neuro-2a cells. Cells are incubated with complex **2** (final concentration of 170 µM) for 4 h and then washed cells are imaged under UV excitation.

The cellular toxicity of complex **2** towards the cancer cells (HeLa, U87MG and Nuro2a) and normal cells (CHO-K1 and 3T3-L1) has been determined by MTT assay. Figure 12 shows that cell viabilities were > 80% in presence of the tested concentration of complex **2** (in the range of 20-170 µM). The result indicates that complex **2** has low cytotoxicity in the labeling concentration range.

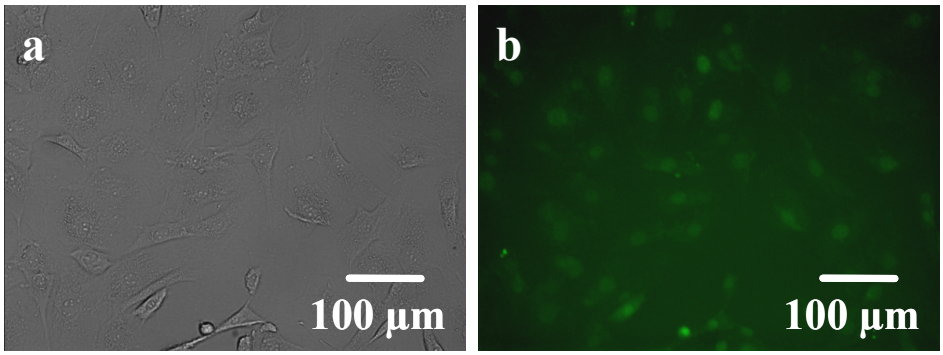

Figure. 7 Differential interference contrast (a) and luminescence image (b) of complex **2** labeled 3T3-L1 cells. Cells are incubated with it for 4 h (final concentration of 170 µM) and imaged under UV light.

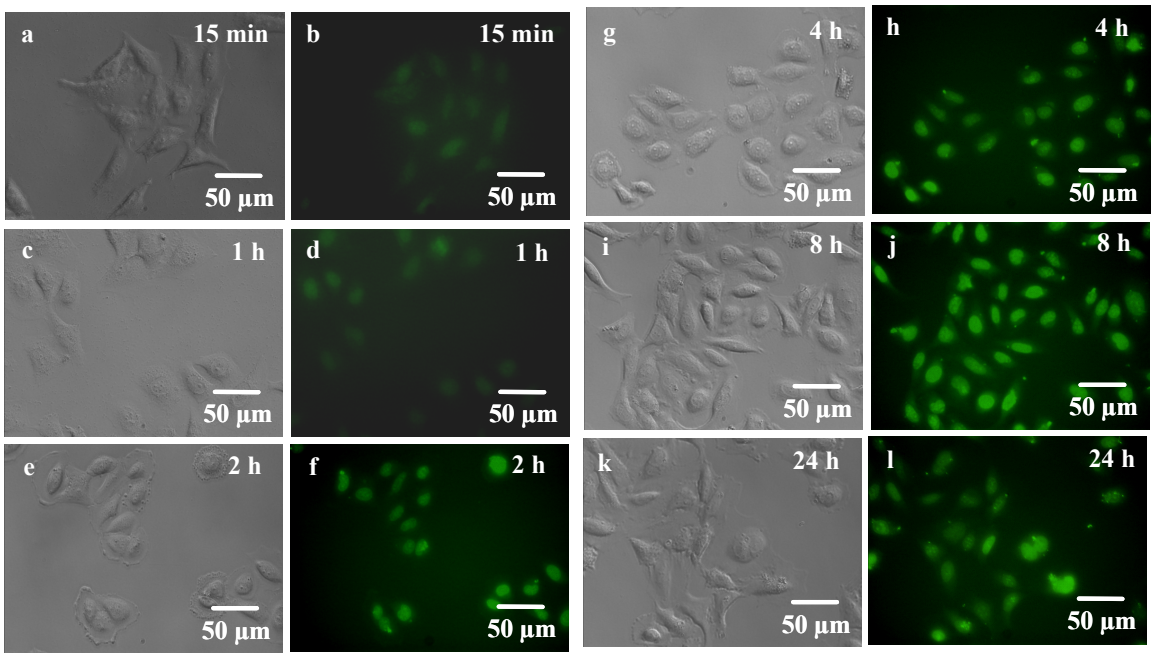

Figure. 8 Differential interference contrast image (a, c, e, g, i, k) and luminescence images (b, d, f, h, j, l) of live HeLa cells after different length of time in incubation (15 min to 24 h) with complex **2** at final concentration of 170 µM. The luminescence images are captured under UV excitation.

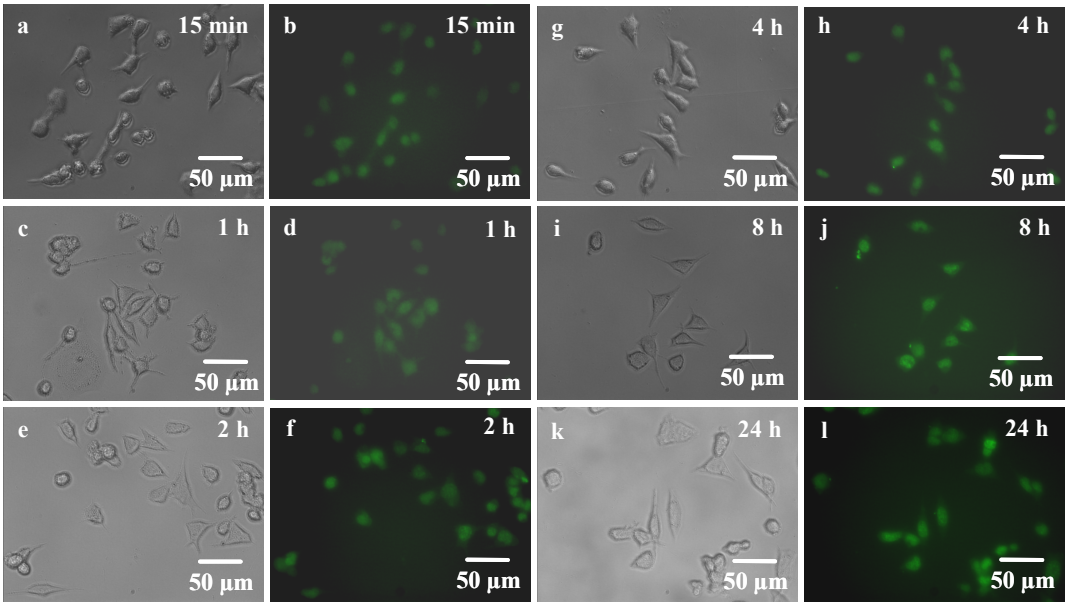

Figure. 9 Differential interference contrast image (a, c, e, g, i, k) and luminescence images (b, d, f, h, j, l) of live Neuro-2a cells after different length of time in incubation (15 min to 24 hrs) with complex **2** at final concentration of 170 µM. The luminescence images are captured under UV excitation.

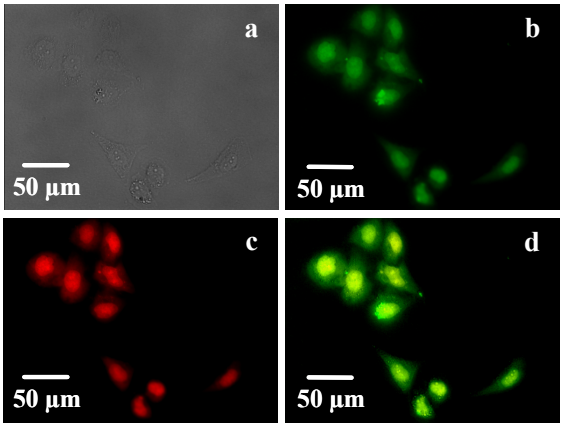

Figure. 10 Co-localization study of complex **2** and propidium iodide labeled HeLa cells. Fixed HeLa cells are imaged under differential interference contrast mode (a), UV excitation for imaging of complex **2** (b), green excitation for imaging of propidium iodide that label cell nucleus (c). Merged image of b and c shows significant co-localization of complex **2** and propidium iodide (d).

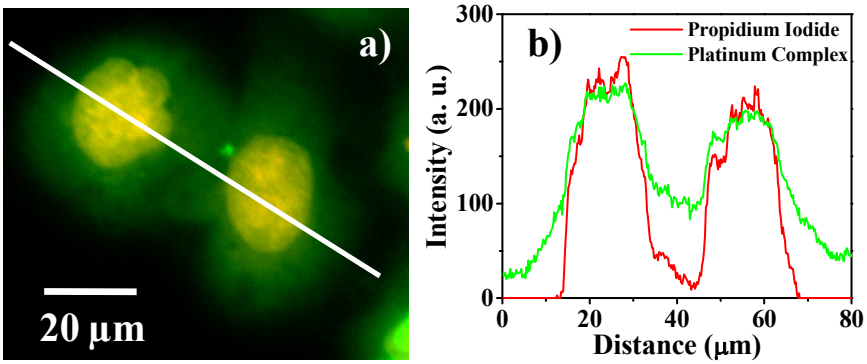

Figure. 11 a) High magnification luminescence merged image of complex **2** and propidium iodide labeled HeLa cells and b) luminescence intensity profile across the line shown in image a. Green and red line corresponding to complex **2** and propidium iodide, respectively.

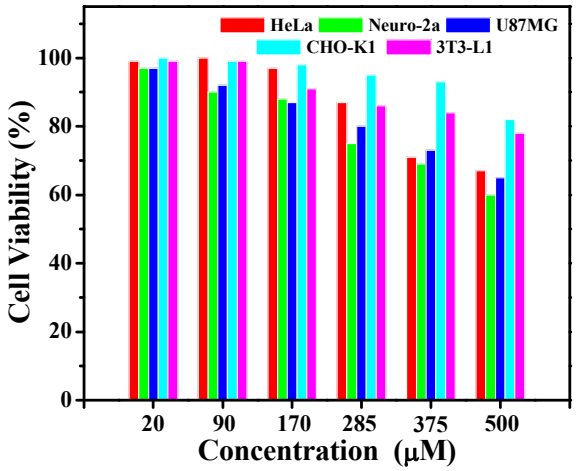

Figure. 12 Viability of different cells in presence of complex **2** of different concentrations. Cells are incubated with complex **2** of different concentrations for 24 hrs and then cell viability is determined assuming 100 % viability for control sample having no complex **2**.

We have measured the stability of complex **2** in pure fetal bovine serum (FBS) similar to plasma up to one week. The digital images and photoluminescence spectra of complex **2** shows the complex has high colloidal stability (Figure 13). We have studied the Z-stacking fluorescence imaging of complex **2** labeled HeLa cells to confirm the nucleus accumulation of complex. The Z-stacking images show that the most of the complex **2** is localized in cell nucleus (Figure 14).

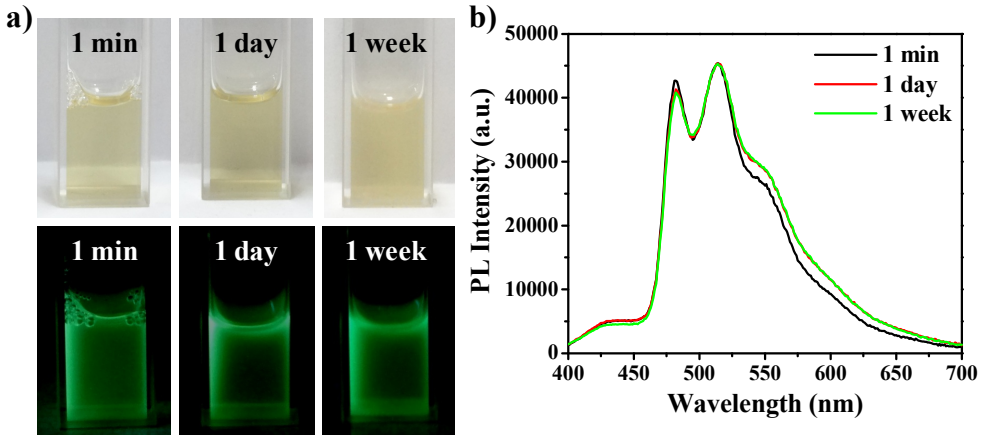

Figure. 13 The stability of complex **2** in pure fetal bovine serum (FBS). (a) Digital images of complex **2** in pure FBS after different times. Top and bottom row shows the images of solution under ordinary light and UV light. (b) The photoluminescence spectra of corresponding solution of complex **2** in pure FBS under 375 nm excitation. The result of the study shows that complex **2** has high colloidal stable in FBS and also intact its photoluminescence property.

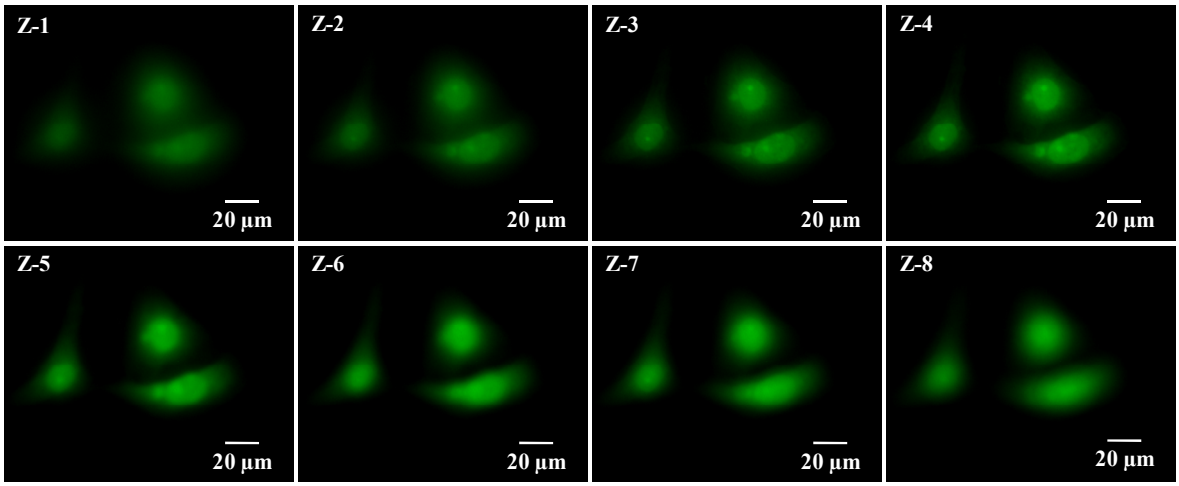

Figure. 14 A series of luminescence images of complex **2** labeled HeLa cells using at different Z planes from bottom to top with successive Z-axis slices of 6 µm each, demonstrating that the complex **2** is located in nucleus of cell as well as cell cytoplasm.

3A.3. Conclusion

A water soluble platinum(II) based complex was synthesized by a simple methodology. The solid state emission of the complex is different from its solution state which arises due to the formation of a new electronic state, ^{3}MLLCT. This complex spontaneously enters into cell cytoplasm and then localize preferably into cell nucleus. The cellular uptake of **2** by cancerous cells was observed higher as compared to the normal cells. Low cyto-toxicity of this complex facilitates for the possible application as bio-imaging probe

3A.4. Experimental Section

General synthesis of [C^NPtNCl] complex (Scheme 1**)**

K_2PtCl_4 (0.30 g, 7.2 mmol) and 2-phenyl pyridine (0.280 g, 18.1 mmol) were dissolved in 4 mL of water and kept in a microwave vial for 10 min under microwave condition at 100^0C. After 10 min green color precipitate was obtained and it was separated from water, dried under vacuum oven for 15 min. The crude product was recrystallized by ethanol giving green color solid product, Yield, (0.360 g, 92%).

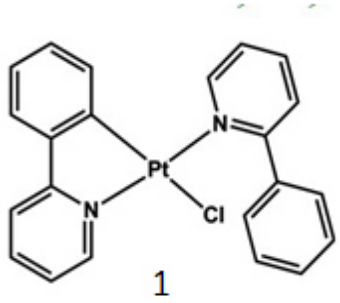

1

^{1}H NMR spectra of **1** , [^{1}H NMR (400 MHz, Chloroform-d) a = δ 9.63 (d, J = 6.0 Hz, 1H), b = δ 9.26 (d, J = 5.7 Hz, 1H), c = δ 8.10 (d, J = 5.2 Hz, 2H), d = δ 7.96 (t, J = 7.8 Hz, 1H), e = δ 7.74 (t, J = 7.6 Hz, 1H), f = δ 7.64 (s, 1H), g = δ 7.52 (d, J = 7.8 Hz, 2H), h = δ 7.36 (dt, J = 20.8, 6.9 Hz, 4H), i = δ 7.08 (t, J = 6.7 Hz, 1H), 7.03 – 6.97 (m, 1H), j = δ 6.89 (t, J = 7.4 Hz, 1H), k =6.22 (t, 1H), l = δ 6.20 (d, 1H)](Figure. 15). ^{13}C NMR spectra of **1**, [^{13}C NMR (101 MHz, $CDCl_3$) a = δ 167.16, b = δ 162.31, c = δ 154.35, d = δ 151.21, e = δ 144.20, f = δ 141.03, g = δ 139.80, 138.39, 137.67, h = δ 130.81, 129.75, 129.56, 129.27, 128.98, 127.83, 127.32, 127.21, i = δ 123.83, 123.17, 123.05, 121.69, j = δ 118.03](Figure. 16).

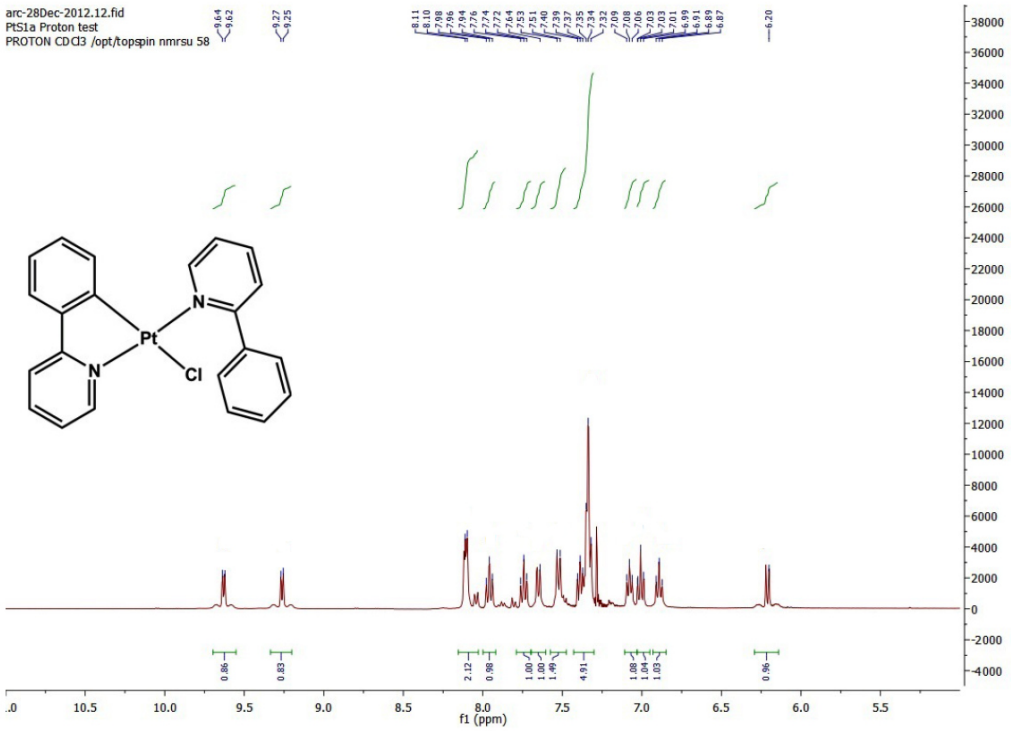

Figure. 15 ^{1}H-NMR spectum of complex **1**

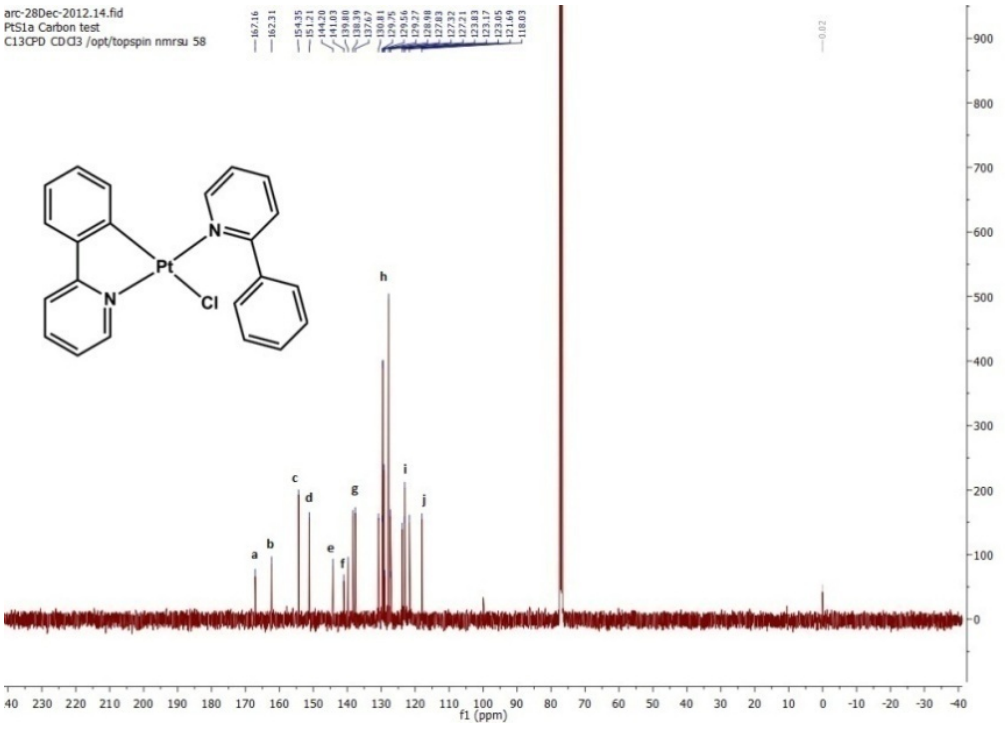

Figure. 16 ^{13}C NMR spectum of complex **1**

General synthesis of [Pt(ppy)(en)]Cl, 2 (Scheme 1)

It was synthesized by modifying the methodology as reported earlier [38]. Ethylenediamine (5.5 mmol) was added at room temperature to a stirred solution of complex **1** (1.85 mmol) in DCM (10 ml). After 5 minutes of stirring, the solvent was evaporated under reduced pressure and the crude product was purified by column chromatography (60-120 mess of silica gel) resulting a yellow solid powder (yield 72-82%).

Table 2. Crystal data and structure refinement for **2 (**CCDC No. 1404472) **.**

Empirical formula	C_{13} H_{16} N_3 Pt Cl
Temperature	100 K
Crystal system	Orthorhombic
Space group	P b c a (61)
Unit cell dimensions	a = 15.9527(10) Å α = 90°
	b = 8.5509(5) Å β = 90°
	c = 18.8487(13) γ = 90°
Volume	2571.15 Å
Z	8

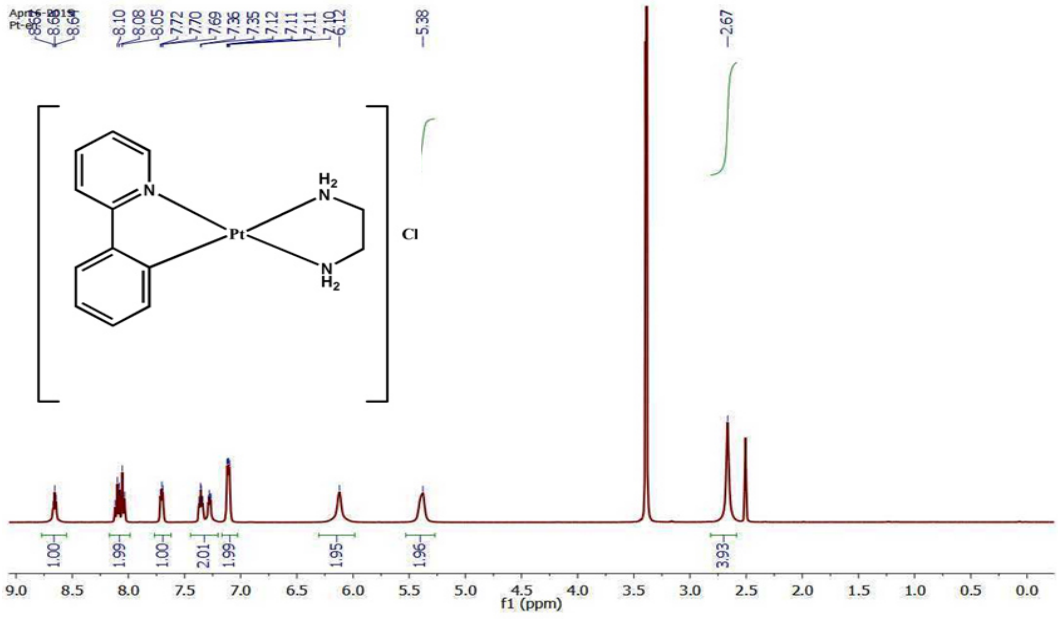

Figure. 17 ^{1}H-NMR spectum of complex **2**

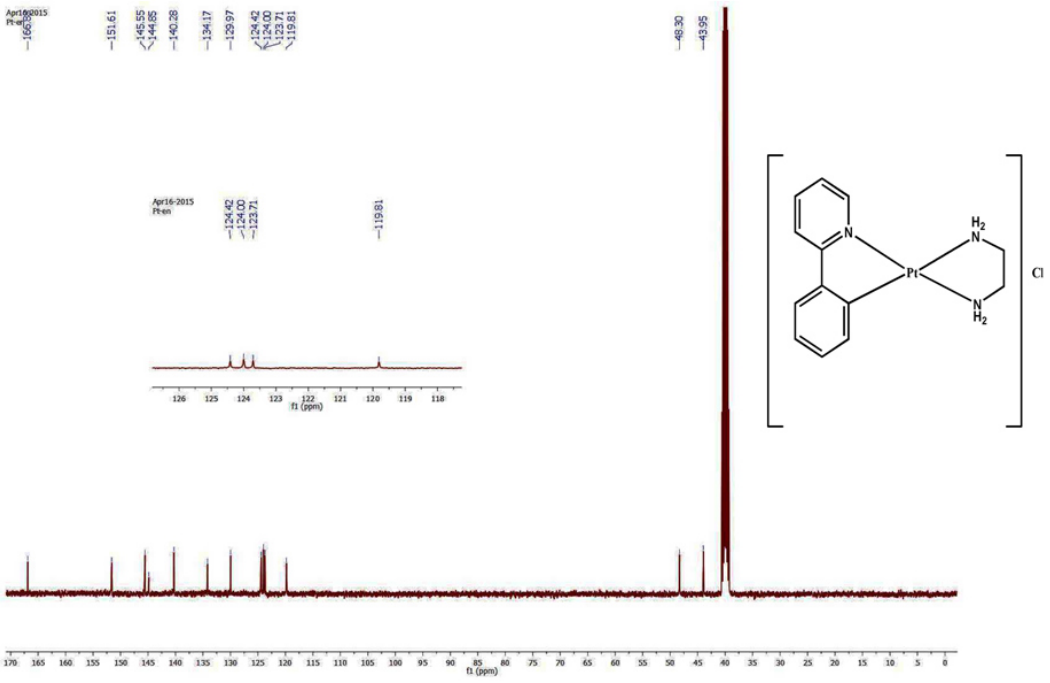

Figure. 18[13]C-NMR spectumof complex **2**

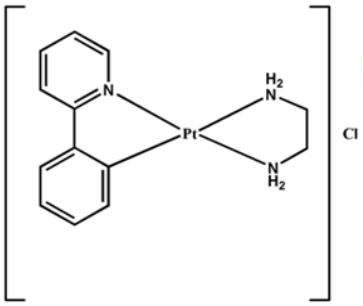

2

[1]H NMR spectra of **2**, [[1]H NMR (400 MHz, DMSO-d^6) 8.57 – 8.55 (m, 1H), 8.03 (dd, J = 11.1, 4.5 Hz, 2H), 8.03 (dd, J = 11.1, 4.5 Hz, 2H), 7.66 – 7.58 (m, 2H), 7.26 (dd, J = 7.4, 5.9 Hz,4H), 7.17 – 7.08 (m, 3H), 2.86 (s, 3H)(Figure. 17); **[13]C NMR**: (101 MHz, DMSO-d[6]) δ 150.35, 145.02, 142.78, 139.31, 132.63,

129.58, 123.61, 123.45, 122.70, 118.85, 43.64(Figure. 18).

3A. 5 References

[1] J. Yin, Y. Hu and J. Yoon, *Chem. Soc. Rev.,* 2015, **44**, 4619.

[2] Z. Guo, S. Park, J. Yoon, I. Shin, *Chem. Soc. Rev.,* 2014, **43**, 16.

[3] Q. Zhao, C. Huang and Fuyou L, *Chem. Soc. Rev*., 2011, **40**, 2508.

[4] J. R. Lacowicz, Springer, Principle of Fluorescence Spectroscopy, New York, 2006.

[5] Y. Xia, L. Dong, Y. Jin, S. Wang, L. Yan, S. Yin, S. Zhou and B. Song, *J. Mater Chem. B,* 2015*,* **3**, 491.

[6] S. Sahu, B. Behera, T. K. Maiti and S. Mohapatra, *Chem. Commun*., 2012, **48**, 8835.

[7] V. F. Moreira, Flora L. T. Greenwood and M. P. Coogan, *Chem. Commun*., 2010, **46**, 186.

[8] A. J. Amoroso and S. J. A. Pope, *Chem Soc. Rev*., 2015, DOI 10.1039/C4CS00293H.

[9] A. Chakraborty and N. R. Jana, *J. Phys Chem C*, 2015, **119**, 2888.

[10] X. Sun, X. Huang, J. Guo, W. Zhu, Y. Ding, G. Niu, A. Wang, G. O. Kiesewetter, Z. L. Wang, S. Sun, X. Chen, *J. Am. Chem. Soc*., 2014, **136**, 1706 .

[11] H. Kobayashi, M. Ogawa, R. Alford, P. L. Choyke and Y. Urano, *Chem. Rev*., 2010, **110**, 2620.

[12] X. Michalet, F. F. Pinaud, L. A. Bentolila, J. M. Tsay, S. Doose, J. J. Li, G. Sundaresan, A. M. Wu, S. S. Gambhir and S. Weiss, *Science*, 2005, **307**, 538.

[13] J. Zheng, P. R. Nicovich and R. M. Dickson, Annu. *Rev. Phys.Chem*. 2007, **58**, 409.

[14] J. F. Zhang, C. S. Lima, B. R. Choa and J. S. Kim, *Talanta*, 2010, **83**, 658.

[15] S. Wu, C. Zhu, C. Zhang, Z. Yu, W. He, Y. He, Y. Li, J. Wang and Z. Guo, *Inorg. Chem*., 2011, **50**, 11847.

[16] R. R. de Haas, R. P. M. van Gijswijk, E. B. van der Tol, H. J. M. A. A. Zijlmans, T. B.Schut, J. Bonnet, N. P. Verwoerd and H. J. Tanke, *J. Histochem. Cytochem*., 1997, **45**, 1279.

[17] R. R. de Haas, R. P. M. van Gijlswijk, E. B. van der Tol, J. Veuskens, H. E. van Gijssel, R. B. Tijdens, J. Bonnet, N. P. Verwoerd and H. J. Tanke, *J. Histochem. Cytochem*., 1999, **47**, 183

[18] R. Kumar, T. Y. Ohulchansky, I. Roy, S. K. Gupta, C. Borek, M. E. Thompson and P. N. Prasad, *ACS Appl. Mater. Interfaces*, 2009, **1**, 1474

[19] C. Y.-S. Chung, S. P.-Y. Li, M.-W. Louie, K. K.-W. Lob and V. W.-W. Yam, *Chem. Sci*., 2013, **4**, 2453

[19] D. Maggioni, F. Fenili, L. D'Alfonso, D. Donghi, M. Panigati, I. Zanoni, R. Marzi, A. Manfredi, P. Ferruti, G. D'Alfonso and E. Ranucci, *Inorg. Chem*., 2012, **51**, 12776

[20] R. W.-Y. Sun, A. L.-F. Chow, X.-H. Li, J. J. Yan, S. S.-Y. Chui and C.-M. Che, *Chem. Sci*., 2011, **2**, 728

[22] S. S. Pasha, P. Alam, S. Dash, G. Kaur, D. Banerjee, R. Chowdhury, N. Rath, A. RChoudhury and I. R. Laskar, *RSC Adv*., 2014, **4**, 50549.

[23] P. Alam, M. Karanam, A. R. Choudhury and I. R. Laskar, *Dalton Trans*., 2012, **41**, 9276

[24]P. Alam, P. Das, C. Climentc, M. Karanam, D. Casanova, A. R. Choudhury, P. Alemany, N. R. Jana and I. R. Laskar, *J. Mater. Chem. C*, 2014, **2**, 5618.

[25] T. D. wang and G. Triadafilopoulos, *Gastrointestinal Endoscopy*. 2005, **61**, 686.

[26] M. Mauro,A. Aliprandi, D. Septiadi, N. S. Kehr and L. D. Cola, *Chem. Soc. Rev*., 2014, **43**, 4144.

[27] V. H. Houlding and V. M. Miskowski, Coord. *Chem. Rev*., 1991, **111**, 145.

[28] V. M. Miskowski and V. H. Houlding,*Inorg. Chem*., 1991, 30, 4446.

[29] C. A. Strassert, M. Mauro and L. De Cola, Adv.*Inorg. Chem*., 2011, **63**, 48.

[30] I. M. Sluch, A. J. Miranda, O. Elbjeirami, M. A. Omary and L. M. Slaughter, *Inorg. Chem*., 2012, **51**, 10728.

[31] B. Ma, J. Li, P. I. Djurovich, M. Yousufuddin, R. Bau and M. E. Thompson, *J. Am. Chem. Soc*., 2005, **127**, 28.

[32] D. Kim and J. L. Bredas, *J. Am. Chem. Soc*., 2009, **131**, 11371.

[33] M. Kato, C. Kosuge, K. Morii, J. S. Ahn, H. Kitagawa, T. Mitani, M. Matsushita, T. Kato, S. Yano and M. Kimura, *Inorg. Chem*.,1999, **38**, 1638.

[34] C. K. Koo, K. L. Wong, C. W. Y. Man, H. L. Tam, S. W. Tsao, K. W. Cheah and M. H. W. Lam, *Inorg. Chem*., 2009, **48**, 7501.

[35] N. Kumari, B. K. Maurya, R. K. Koiri, S. K. Trigun, S. Saripella, M. P. Coogan and L. Mishra, *Med.Chem.Comm*., 2011, **2**, 1208.

[36] S. W. Lai, Y. Liu, D. Zhang, B. Wang, C. N. Lok, C. M. Che and M. Selke, *Photochem.Photobiol*. 2010, **86**, 1414.

[37] X. S. Xiao, W. L. Kwong, X. Guan, C. Yang, W. Lu and C. M. Che, *Chem. Eur. J*., 2013, **19**, 9457.

[38] Nardelli, *Appl. Crystallogr*., 1995, **28**, 569.

[39] R. Sangeetha Gowda, R. Blessy Baby Mathew, C. N. Sudhamani, H. S. Bhojya Naik, *Biomedicine and Biotechnology*. 2014, **2**, 1.

Chapter III

PART-B

Syntheses of 'Aggregation Induced Emission (AIE)'Active Cyclometalated Platinum(II) Complexes And Their Biological Activities

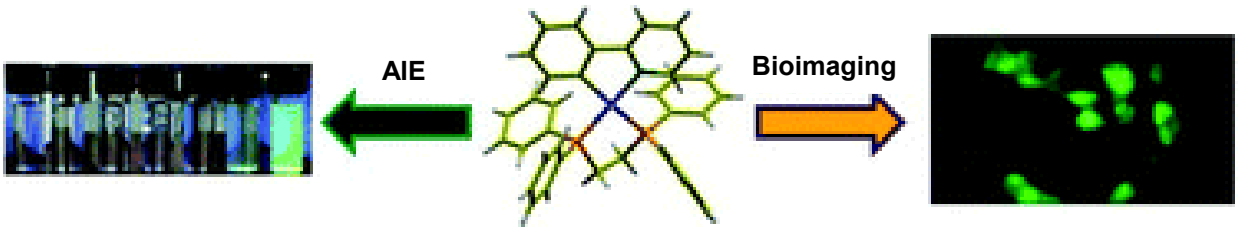

3B.1.Introduction

Phosphorescent heavy metal complexes like platinum(II) and iridium(III) are becoming increasingly important to scientists with respect to their applications in different fields such as, bioimaging[1], sensing[2] and organic light emitting devices (OLEDs)[3] due to their high luminescence quantum yields, color tunability, fair stability, excellent emission properties and straightforward synthetic routes[4]. In these cases, 100% internal quantum efficiency can be achieved due to strong spin orbit coupling[5].The strong emission of the luminophores (organic as well as organometallic complexes) often quenched in their aggregated form called 'Aggregation Caused Quenching (ACQ)' effect[6]. This is one of the major challenges to apply these materials in practical applications. In 2001, Tang and co-workers[7] achieved tremendous success in developing the anti–ACQ fluorophores called 'Aggregation Induced Emission (AIE)' compounds. This emission phenomenon is manifested by compounds exhibiting significant enhancement of their light-emission in solid state whereas weak emission in solution. To date, many AIE fluorophores have been reported[8]but the development of heavy metal-based complexes with AIE properties is still limited[9]. The reports of Pt(II) complex with this unusual property is rare[10]. Yam and Che reported[11] AIE active Pt(II) complexes. The proposed mechanism of AIE in case of Pt(II) is restricted intramolecular rotation (RIR)[12], hydrogen bonding[11] which can lead to suppression in molecular motion. Apart from these, significant contribution of MMLCT excited state to the lowest excited states lead to strong emission in solid state[12].

The normal luminophores suffer from basic problems like interference from background and scattered light[13-14]. The development of AIE active Pt(II) complexes is effective solution to overcome these problems. The AIE active Pt(II) compounds with such properties such as low photo-bleaching, low light scattering and rich Photophysical and strong emission in the solid state make these complexes as promising candidates for bioimaging[11].

In chapter 3A, we reported a water soluble and emissive platinum(II) complex in bioimaging. Although, this compound has low cytotoxity and has the ability to penetrate the cell membrane, but the emission intensity remains weak in the solid state. Recently there has a tremendous thrust to synthesis 'Aggregation Induced Emission (AIE)'active molecules for

bio imaging. On this aspect, in the following chapter, the syntheses of three AIE active cyclometalated complexes [Pt(C^N)(CH^N)Cl] (**1**), Pt(C^N)P^P]Cl where [C^N = 2-phenylpyridine; P^P = Bis(diphenylephasphino) ethane (**2**) and *cis*- 1,2-Bis (diphenylephasphino) ethene (**3**)], studied their Photophysical properties have been reported. The computational studies of one of the complexes**2**was performed and correlated with its spectroscopic observations. Complex **2** is used for cytotoxicity study against non-resistant and *cis*-platin- resistant cell line showing very good results[14]. Utilizing its AIE and rich Photophysical properties, we have used complex **2** in bio-imaging applications.

3B.2. Results & Discussion

3B.2.1. Syntheses and Characterization

The syntheses of all three complexes **1**, **2** and **3** are presented in Scheme 1. The green synthetic approach has been applied for the syntheses of these complexes. The synthetic methodology of **1**has already been discussed in chapter 3A. The synthesized pendent complex **1** is one of the important precursors for synthesis of many luminescent Pt(II) complexes[15].

Scheme 1 Synthetic route and chemical structures of complexes **1**, **2** and **3**

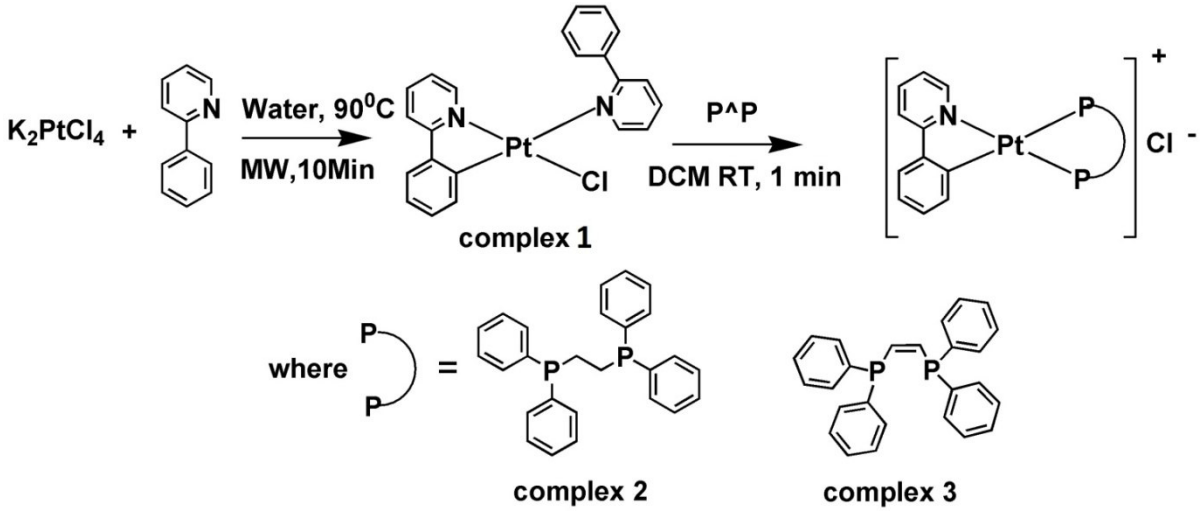

M. G. Haghighi *et al.* has reported the synthesis of **2** in two steps by using the following platinum(II) precursors, (i) [PtMe(κ^1C-ppy)(dppe)] (ii) [Pt(ppy)(CF_3CO_2)(SMe_2)]

[16]. Herein, the syntheses of bis-chelate phosphine complexes **2** and **3** were carried out by using complex **1** in a facile and in very short reaction time. Reaction between **1** and bis(diphenylphosphine)ethene (dppe) / bis (diphenylphosphine)ethylen (dppen) in (1:1) ratio resulted complexes **2** and **3** after stirring the reaction mixture for one minute at RT. in DCM. The complexes **2** and **3** were characterized by ^{1}H, ^{13}C and ^{31}P NMR.

^{1}H NMR spectra of complex **2** shows aromatic proton signals in the range δ = 6.8 - 8.3 ppm, the four protons of (CH_2-CH_2) of the dppe ligand were observed as multiplets at δ = 2.63 ppm. The ^{13}C NMR spectra of the complexes **2** and **3** correspond to their structure. The ^{31}P NMR of this complex shows two distinct singlets at δ = 41.39, for the P *trans* to N with $^{1}J_{(PtP)}$ = 3772 Hz, and δ = 51.16, for the P *trans* to C with a much lower value of $^{1}J_{(PtP)}$ = 1877 Hz due to the *trans* influence of C being much greater than that of N. The range of $^{1}J_{(PtP)}$ between 1877-3762 Hz indicates *cis* coordination of the phosphine ligand[17]. The ethylene (CH=CH) proton signal for the dppen ligand appears at δ = 7.2 ppm as a multiplate [18]. The ^{31}P spectrum of complex **3** shows two doublet of doublets, one at δ = 43.8 ppm with $^{3}J_{(PP)}$ = 17 Hz and $^{1}J_{(PtP}$ = 3782 Hz for P *trans* to N, and δ = 59.0 ppm with $^{3}J_{(PPa)}$ = 17 Hz and $^{1}J_{(PtPb)}$ = 1839 Hz for P *trans* to C, the lower value of $^{1}J_{(PtP)}$ suggests *trans* effect of carbon with respect to nitrogen.

3B.2.2. Aggregation Induced Emission(AIE) activity of 2 and 3

The complexes **2** and **3** are soluble in solvents such as, dichloromethane (DCM), dimethyl formamide (DMF), 1,4-dioxane, methanol, acetonitrile etc, but are insoluble in water as well as in hexane. These complexes show very week emission in all these solvents but they are intensely emissive in the solid state. These observations hint that all three complexes are expected to show AIE behaviour. In order to investigate this AIE property, DCM and hexane solvents were used for complexes **2** and **3**.For complexes **2** and **3**, different amounts of hexane fraction (f_h = 0-90 %) (Figure1 and 2) were added to their solutions in DCM, (keeping the concentration of each solution remains same to5 x 10^{-5}M).

Maximum emission intensity was observed at f_h = 90 %, for both the complexes. The emission intensity was increased by19 times for **2** and 20 times for **3** as compared with their original respective solution (f_h = 0%) intensities.

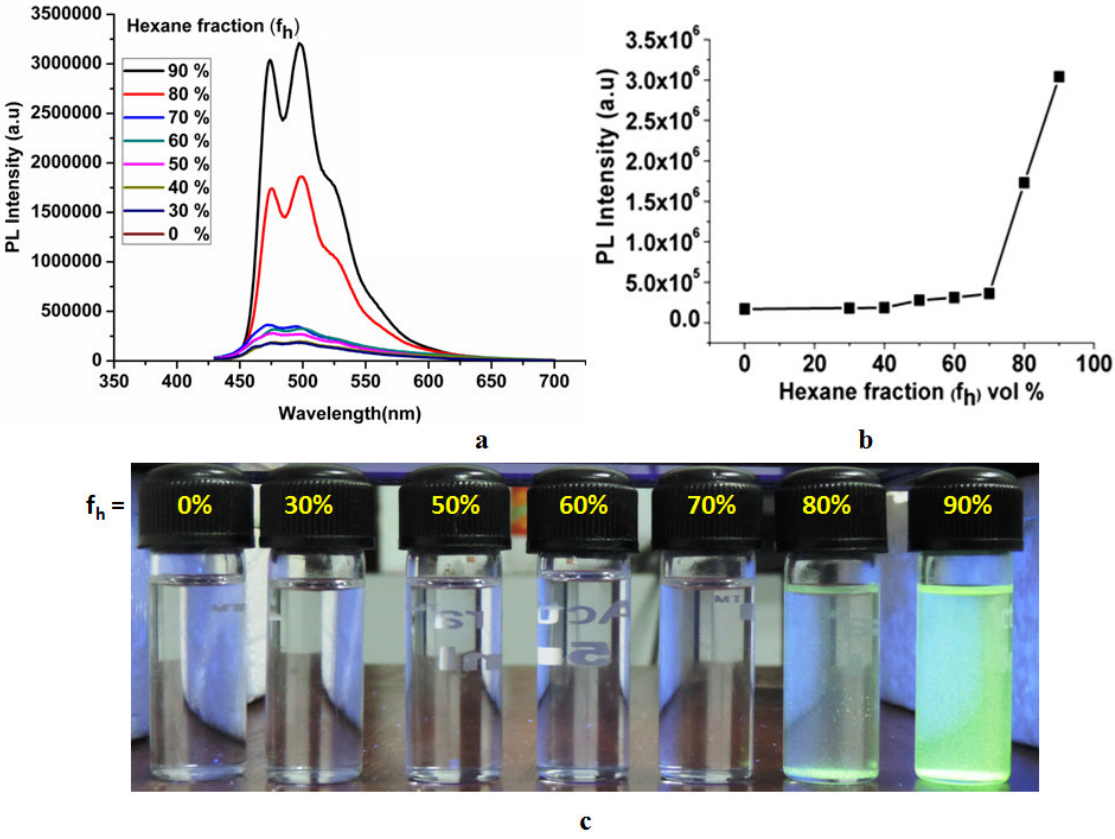

Figure.1(a) PL spectra of **2** in DCM/hexane mixed solvents with different fraction of hexane (f_h) with excitation at 385 nm; (b)The changes of PL peak intensity with different f_h (at 512 nm); (c)Luminescent images of **2** (radiated with an ultraviolet light at 365 nm) in DCM−hexane mixed solvents with the concentration kept at 2×10^{-5} M.

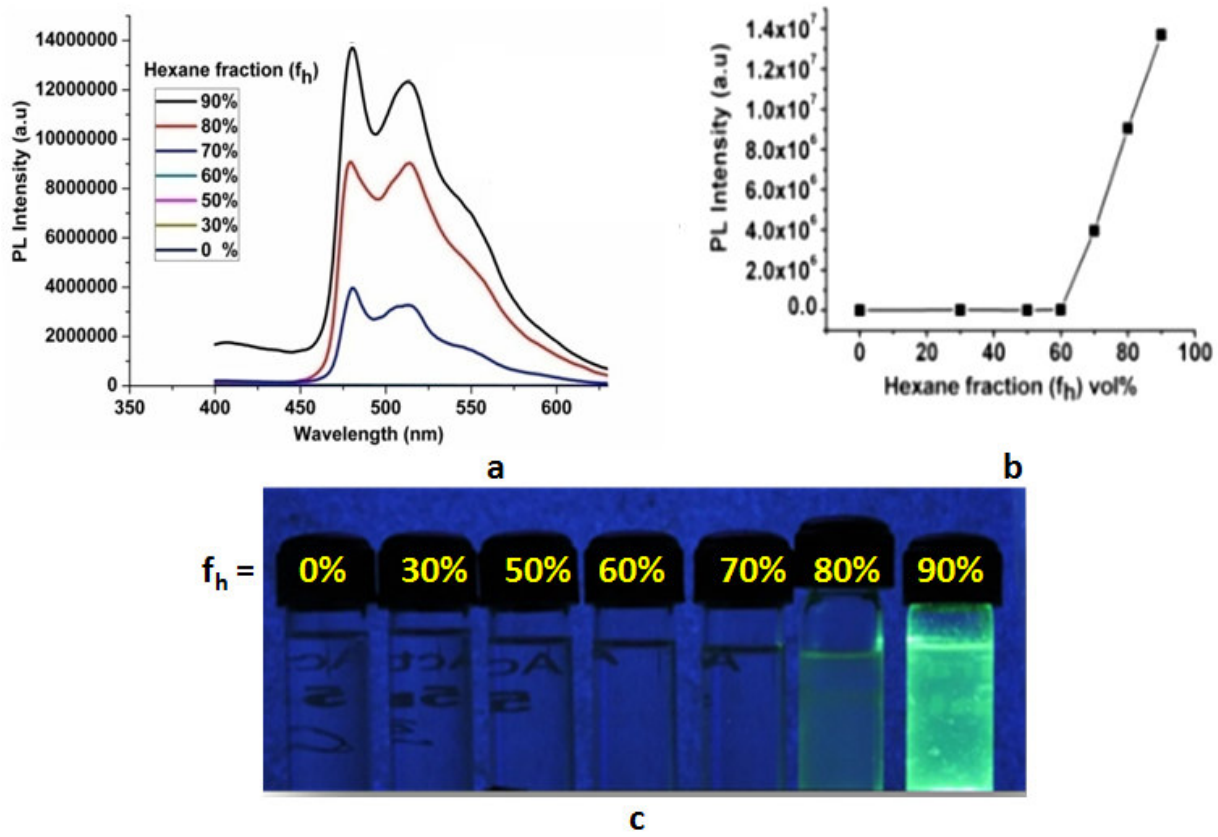

Figure. 2 (a) PL spectra of **3** in DCM/hexane mixed solvents with different f_h with excitation at 385 nm; (b) The changes of PL peak intensity with different f_h (at 517 nm); (c) Luminescent images of **3** (radiated with an ultraviolet light at 365 nm) in DCM−hexane mixed solvents with the concentration kept at 2×10^{-5} M.

To understand the origin of the AIE property, the crystal-packing of **2** was examined (Figure.3, 4 and Table 1). The crystal structure of **2** exhibits many C-H....π interactions in the range of 2.81-2.99 Å (Figure3). These interactions may be responsible for restricted rotation of the phenyl rotors present in these molecules in their solid states and hence the complexes exhibit AIE activity.

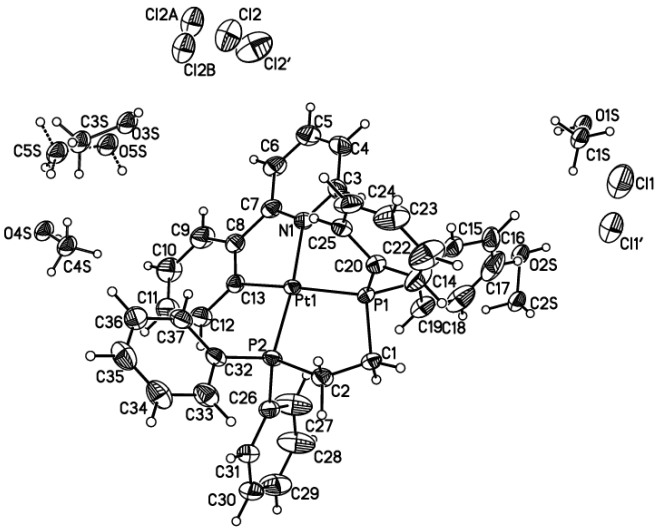

Figure. 3 ORTEP diagram for **2** showing the square planer geometry at the Pt(II) site (The crystal containing solvents, a 7 half occupancy MeOH and 2 half occupancy water (total 3.5MeOH and 1.0 water per Pt)

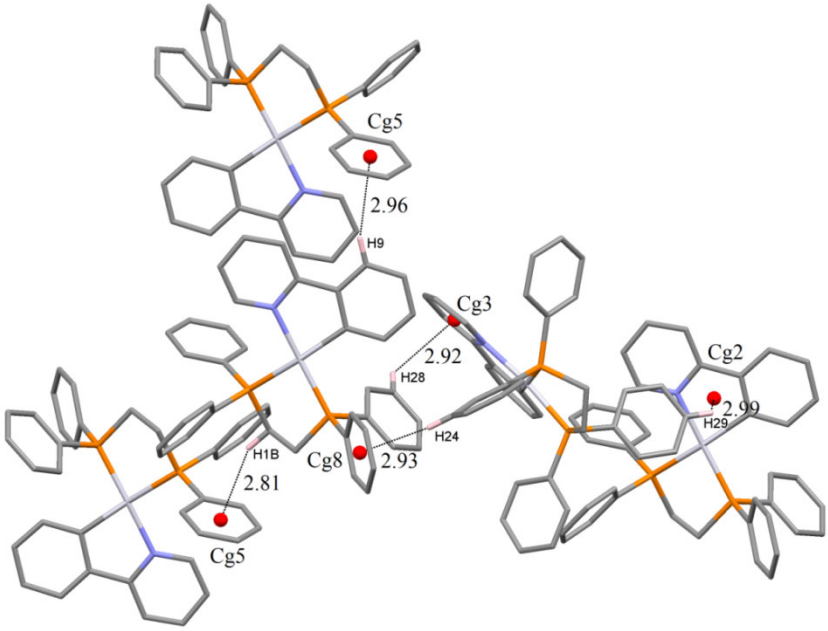

Figure. 4 Crystal packing diagram of complex **2** short contacts H1B—Cg5 = 2.81Å, H24—Cg8 = 2.93 H28—Cg3 = 2.92, H29—Cg2 = 2.99 and H9—Cg5 = 2.96Å (the counter ion is omitted for clarity).

Table 1. Crystal data and structure refinement for **2 (** CCDC No. 1007679)**.**

Empirical formula	$C_{38}H_{36}ClP_2Pt$	
Formula weight	815.16	
Temperature	100(2) K	
Wavelength	0.71073 Å	
Crystal system	Monoclinic	
Space group	C 2/c	
Unit cell dimensions	a = 18.0210(14) Å	α= 90°
	b = 23.0522(17) Å	β= 92.576(3)°
	c = 16.6920(13) Å	γ= 90°
Volume	6927.2(9) $Å^3$	
Z	8	
Density (calculated)	1.563 Mg/m^3	
Absorption coefficient	4.251 mm^{-1}	
F(000)	3232	
Crystal size	0.378 x 0.211 x 0.108 mm^3	
Theta range for data collection	2.443 to 27.610°.	
Index ranges	-14≤h≤23, -29≤k≤30, -21≤l≤21	
Reflections collected	40670	
Independent reflections	8011 [R(int) = 0.0308]	
Completeness to theta = 25.242°	99.6 %	
Absorption correction	Semi-empirical from equivalents	
Max. and min. transmission	0.7457 and 0.6632	
Refinement method	Full-matrix least-squares on F^2	
Data / restraints / parameters	8011 / 99 / 441	
Goodness-of-fit on F^2	1.056	
Final R indices [I>2sigma(I)]	R1 = 0.0271, wR2 = 0.0720	
R indices (all data)	R1 = 0.0361, wR2 = 0.0767	
Extinction coefficient	n/a	
Largest diff. peak and hole	1.099 and -0.565 $e.Å^{-3}$	

The solid state emission of complexes **2** and **3** were found to be 23.3 and 34.5 times higher than that of their respective solution state (f_h = 0 %) emission (Figure.5 and 6). The solid state quantum efficiency (QE) for the complexes **2** and **3** were measured and found to 0.253 and 0.247, respectively. The solution quantum efficiency was found to be 0.0010 and 0.0009, respectively. So, the solid state QE for the complexes **2** and **3** goes to $\phi_{solid}/\ \phi_{solution}>$ 250 (*i.e.*, **2** and **3** show 253 and 274 times higher QE than their respective solutions states). Hence, a significant rise of QE is observed.

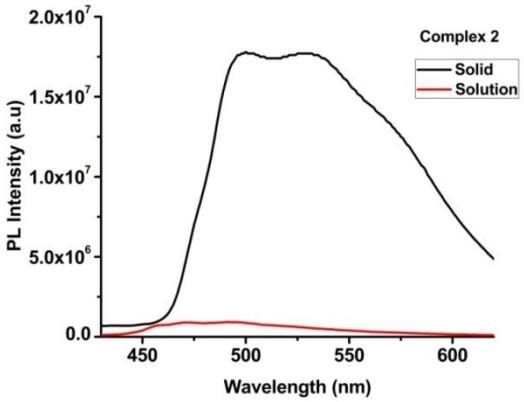

Figure. 5 PL spectra of complex **2** in DCM (10^{-5}M) and solid state.

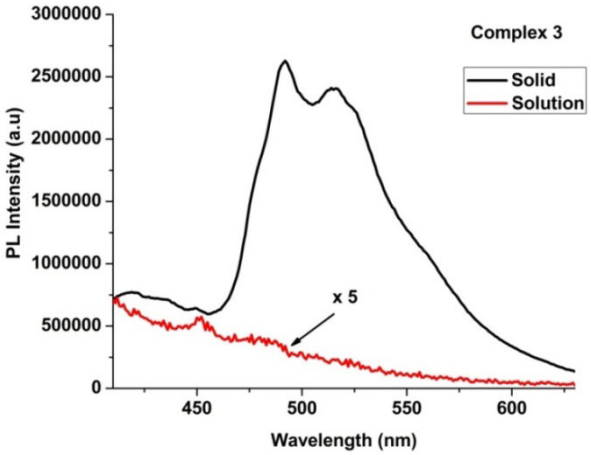

Figure. 6 PL spectra of**3** in DCM (λ_{max}, 480 nm and 510 nm) and solid state (λ_{max}, 490 nm and 517 nm)

Table.2 Photophysical property of **2** and **3**

Complex	UV-Vis absorption[a] nm, ($\varepsilon x10^4$, $M^{-1}cm^{-1}$)	PL solution (λ_{max}) (nm)[b]	PL solid state (λ_{max}) (nm)	Φ [c] (solution)	Φ [d] (solid)
2	269 (9.2), 327 (2.05), 360 (0.77)	470, 492	500, 530	0.0010	0.096
3	267 (8.40), 330 (1.60), 371 (0.44)	480, 510	490, 517	0.0009	0.106

[a] Spectra were recorded in degassed DCM at rt with 10^{-5}[M], [b] Recorded in DCM; [c] Solution quantum efficiency (QE) (ϕ_{sol}) has been measured with respect to quinine sulphate (in 0.1M H_2SO_4, QE=0.55, excitation, 480nm); Solid state absolute luminescence QE (ϕ_{solid}) has been recorded using integrating sphere.

3B.2.3 DFT and TD-DFT Study of 2

The computed energy gap of complex 2in between the ground singlet state and first excited singlet state is 362.6 nm (Figure7). This is in agreement with experimental absorption wavelength from spectroscopic study (Figure 8). The oscillator strength is high as compared to previously reported[19] iridium(III) complexes indicating a stronger S_0 to S_1 absorption. The energy gap between ground singlet state to first excited triplet state (491.1 nm) (Figure.7, Table 3) is in accordance with emission wavelength obtained from spectroscopy. Although emission is an excited state property, results based on ground state optimization qualitatively describes the process. Assignments of transitions (Table 3) show the relative involvement of different frontier orbitals in absorption and emission spectra.

DFT results revealed that chlorine atom makes major contribution towards HOMO, along with platinum(II). However, LUMO is exclusively distributed over the fused ring attached to platinum(II) (Figure. 7).This data along with the assignments, indicate the strong possibility of metal-ligand charge transfer transition (MLCT) in this complex (Table 3).

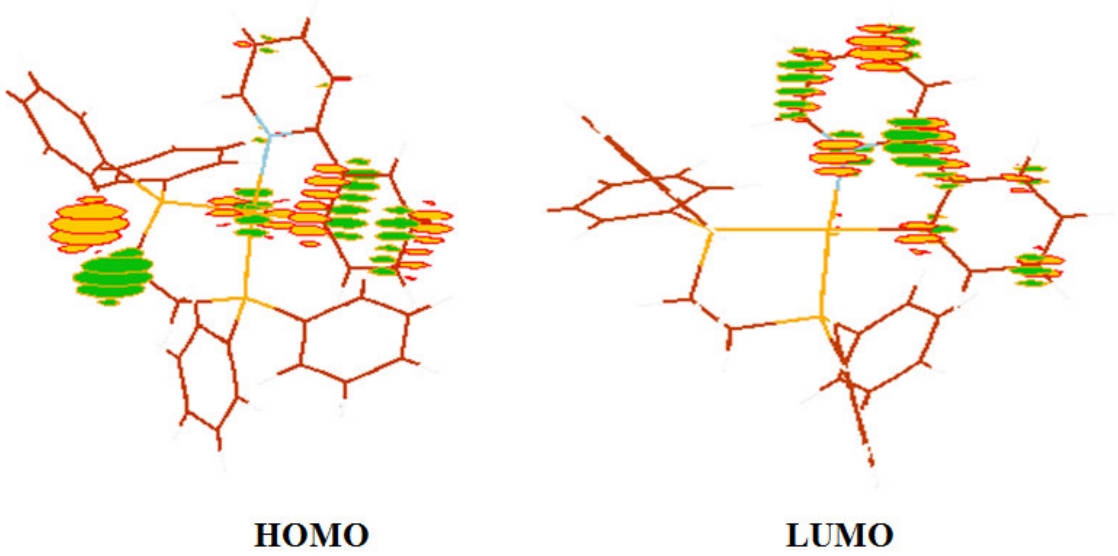

Figure.7 Frontier molecular orbitals for platinum(II) complex **2**. Major contribution of HOMO comes from the counter ion, chlorine and Pt(II) atom. LUMO is distributed over the fused ring. These orbitals are obtained from DFT calculations of the platinum complex after ground state optimization. Calculations are performed by GAMESS US software. Visualization of the molecular orbital is through MOLDEN software

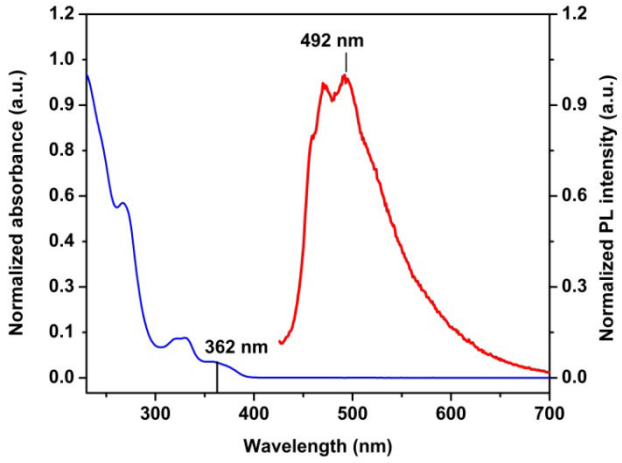

Figure. 8 UV–Vis absorption (blue) and photoluminescence (red) spectra of complex **2** in CH_2Cl_2 of 10^{-5} M solution in DCM.

Table 3: Calculated excitation wavelength (λ_{cal}), oscillator strength (f) and transition energies (E) (TDDFT/B3LYP calculation in DCM solvent) for lowest energy transitions of **2**. All the excitations reported here initiate from singlet ground-state.

Transition from S_0 state to lowest excited states	**λ_{cal} (nm)**	**E (eV)**	**f (Oscillator strength)**	**Assignments and orbital contributions**
S_1	362.6	3.42	0.047	HOMO-1 to LUMO 38.8% HOMO to LUMO 56.2%
T_1	491.1	2.52	0.0	HOMO-1 to LUMO 26.3% HOMO to LUMO 33.64%

3B.2.4 Cellular imaging of 2

Human hepatocellular carcinoma cells, Hep3B were treated with increasing doses of platinum(II)complex, **2** for varied time points and the cell viability was determined through several assays. As shown in Figure 9a, the platinum(II) complex **2** showed increased cytotoxicity in Hep3B cells in a dose-dependent manner as determined by MTT assay. The IC_{50} of the complex was found to be around 5μM at 24h. Similar comparable results were obtained with WST-1 and Trypan Blue assay. Time kinetic study was also performed by incubating the cells with increasing doses of platinum(II) compound for 24, 48 and 72h. With increase in time of treatment with platinum(II) compound, the cell viability was found to be significantly decreased (Figure9b).

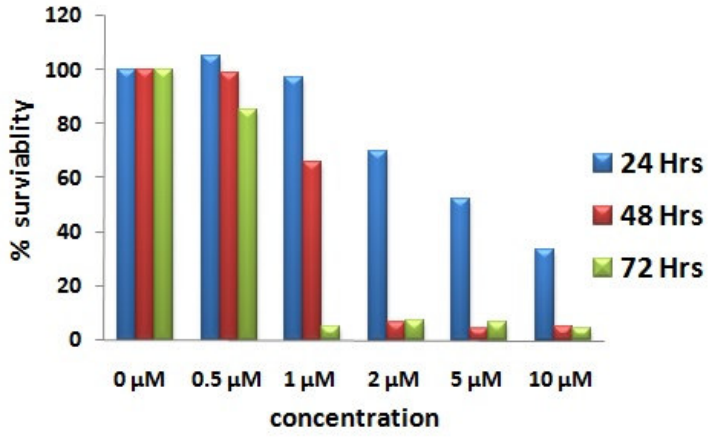

a

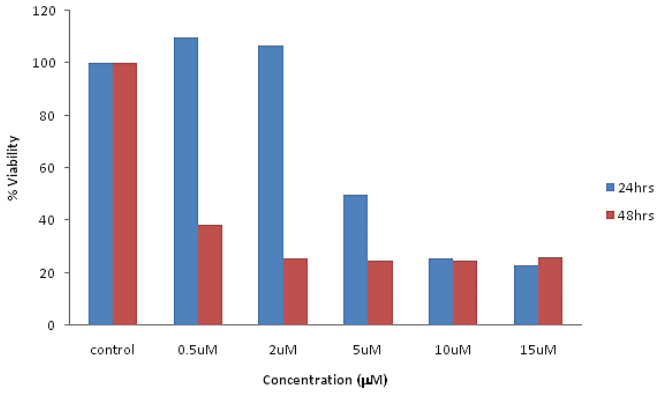

b

Figure. 9 The kinetic cytotoxic study of **2** a) MTT assay b) WST assay**.**

Further, this complex **2** was successfully checked for cellular internalization potential through fluorescence imaging of live Hep3B cells (Figure10). An exclusive staining of the nucleus of live cells was observed. The platinum(II) compounds are well known for their ability to form DNA-adducts. We speculate that the cytotoxicity that we observed in Hep3B cells can be attributed to the increased internalization potential of the drug and also to its property of binding to cellular DNA. Hence, the use of this compound provides one with dual option, not only for its use as an anti-cancer drug, but also as a cell-visualization or bio-imaging agent because of its fluorescence upon aggregation property and good cell membrane permeability.

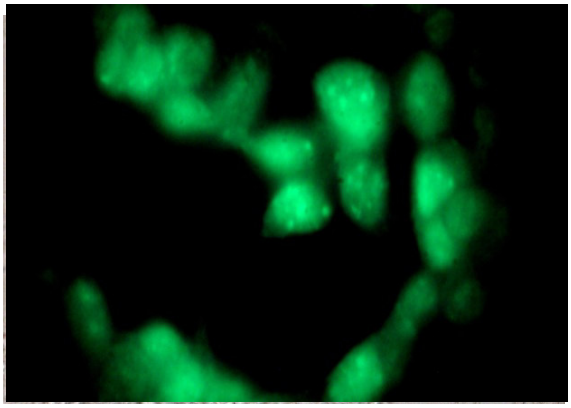

Figure. 10 Fluorescence image of Hep3B cells with complex **2** showing internalization and staining nucleus

3B. 3 Conclusion

A facile and short time synthetic methodology has been developed for Pt(II) cyclometalated complexes. The synthesized complexes are showing 'aggregation induced emission (AIE)' behavior. The IC_{50} of platinum(II) compound found to be around 5μM for **2**. The complex **2** penetrate the cell membrane and stains live cancer cells, as observed from in vitro studies on Hep3B cells.

3B. 4 Experimental Sections

General synthesis of [C^NPtNCl], 1

The synthetic methodology was discussed in chapter 3A.

General syntheses for complexes 2 and 3; To a stirred solution of complex **1** (1 equivalent) in DCM (6 mL), chelate phosphine ligands for complex **1**, 1,2-bis(diphenylphosphino)ethane and for complex **2**, cis-1,2-Bis(diphenylphosphino)ethylene (1 equivalent) was added and the reaction mixture was stirred for 1 minute, the crude product was purified by column chromatography using 60-120 silica mesh giving pure products. Complex **2**, green solid, 94 % yield; complex **3** green solid, 85% yield.

^{1}H NMR spectra of 2, [^{1}H NMR (400 MHz, Chloroform-d) a = δ 8.22 (t, J = 4.9 Hz, 1H), b = δ 8.09 – 7.91 (m, 6H), c = δ 7.85 (ddt, J = 11.7, 6.6, 1.6 Hz, 4H), d = δ 7.75 (dt, J = 7.9, 1.7 Hz, 1H), e = δ 7.68 – 7.48 (m, 12H), f = δ 7.15 (t, J = 7.6 Hz, 1H), g = δ 7.08 – 7.00 (m, 1H), h = δ

6.94 (ddt, J = 7.3, 5.8, 1.3 Hz, 1H), i = δ 6.84 (tt, J = 7.5, 1.5 Hz, 1H), j = δ 2.75 – 2.44 (m, 4H)](Figure. 11). ^{13}C NMR of complex **2**, [^{13}C NMR (101 MHz, $CDCl_3$) a = δ 152.48, b = δ 147.34, c = δ 141.47, d = δ 134.25, 134.14, e = δ 133.94, 133.82, 132.75, 132.73, f= δ 130.12, 130.02, 129.61, 129.49, g = δ 127.02, 126.56, 126.33, 125.74, 125.13, h = δ 120.45](Figure. 12).

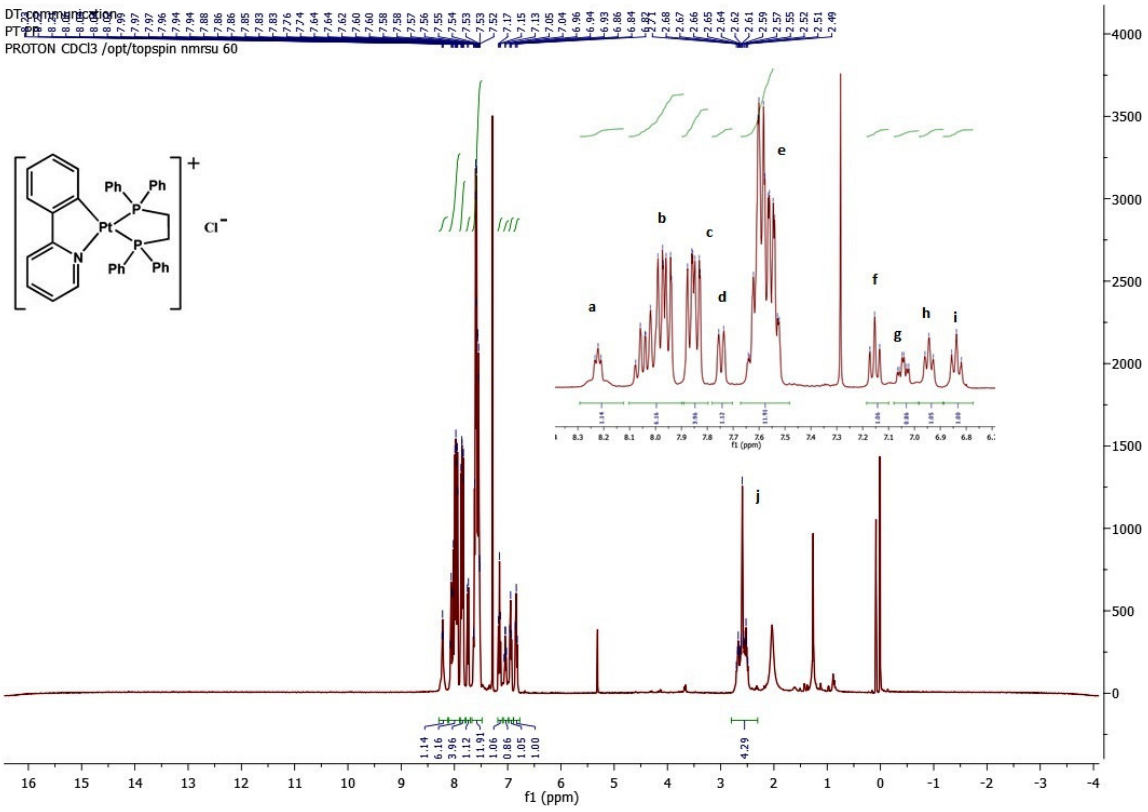

Figure. 11 ^{1}HNMR spectrum of complex **2**

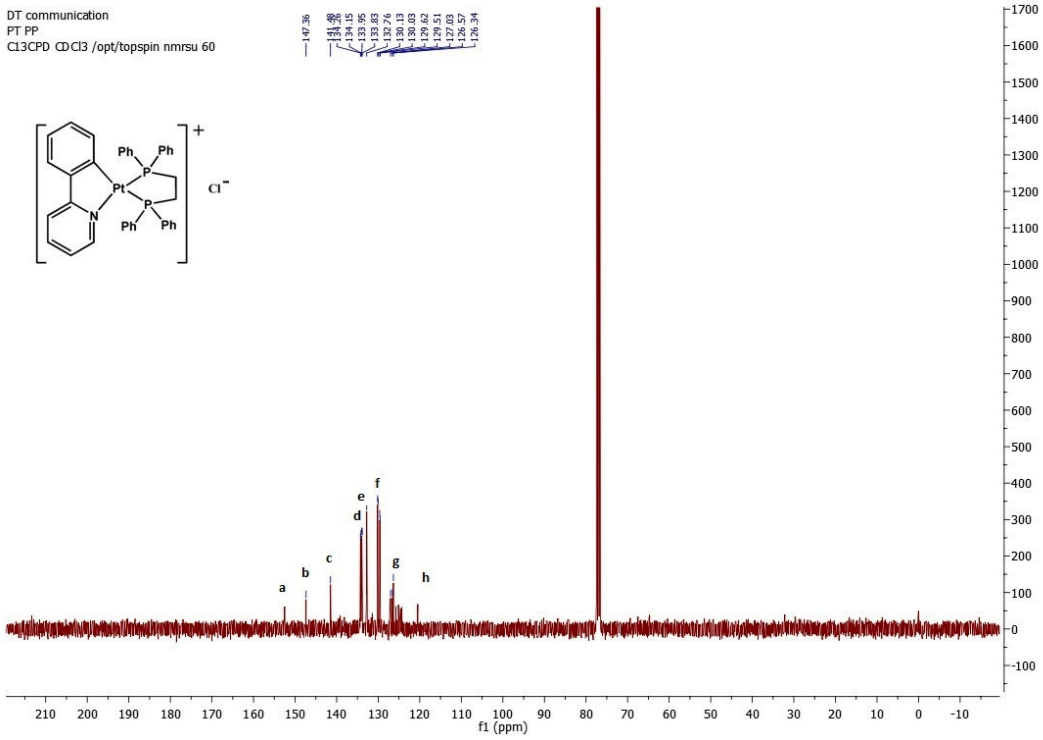

Figure. 12 ^{13}CNMR spectrum of complex **2**

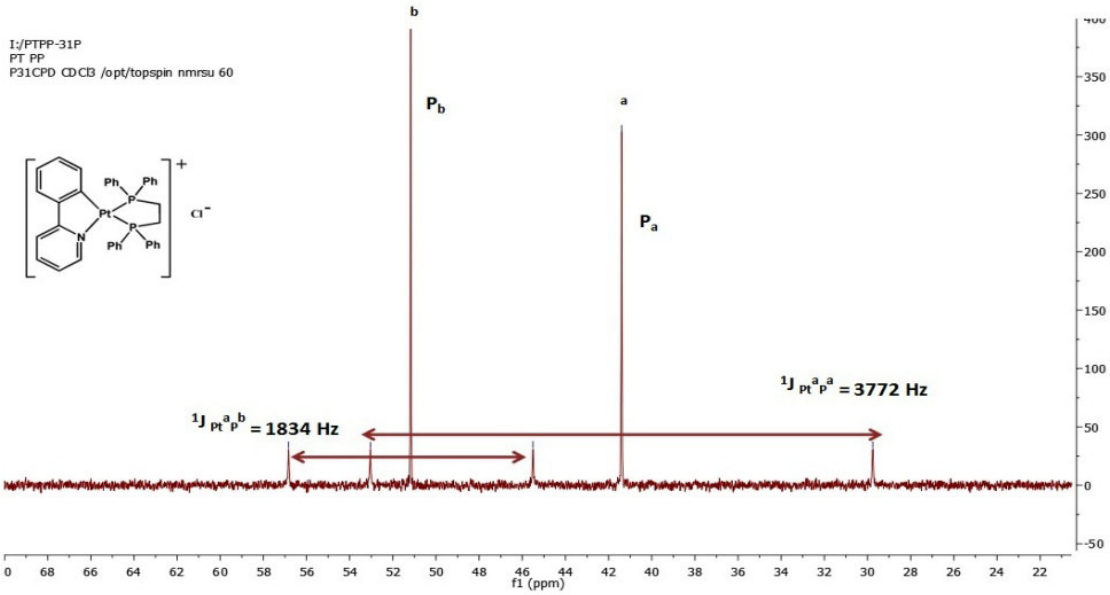

Figure. 13 ^{31}P NMR spectrum of complex **2**

^{1}H NMR spectra of **3** [^{1}H NMR (400 MHz, Chloroform-*d*) a = δ 8.50 (t, *J* = 4.8 Hz, 1H), b = 8.22 – 8.05 (m, 1H), c = 8.01 (d, *J* = 7.2 Hz, 1H), d = 7.89 (dd, *J* = 12.7, 7.4 Hz, 4H), e = 7.77 (dt, *J* = 16.1, 7.9 Hz, 6H), f=7.56 (ddt, *J* = 17.5, 9.7, 7.1 Hz, 13H), g = 7.32 (td, *J* = 7.2, 3.0 Hz, 1H), h = 7.15 (dt, *J* = 24.1, 7.0 Hz, 2H), i = 6.92 (t, *J* = 7.3 Hz, 1H)] (Figure. 14). ^{13}C NMR spectra of **3** [^{13}C NMR (101 MHz, $CDCl_3$) a = δ 152.76, b = δ 147.30, c = δ 141.97, d = δ 134.15, 134.03, e = δ 133.73, 133.61, 132.79, f= δ 130.29, 130.19, 129.76, 129.64, g = δ 126.94, 126.64, 126.45, h= δ124.89, i = δ 120.73] (Figure. 15). ^{31}P NMR (101 MHz, $CDCl_3$, δ 44 (1P), δ 59.

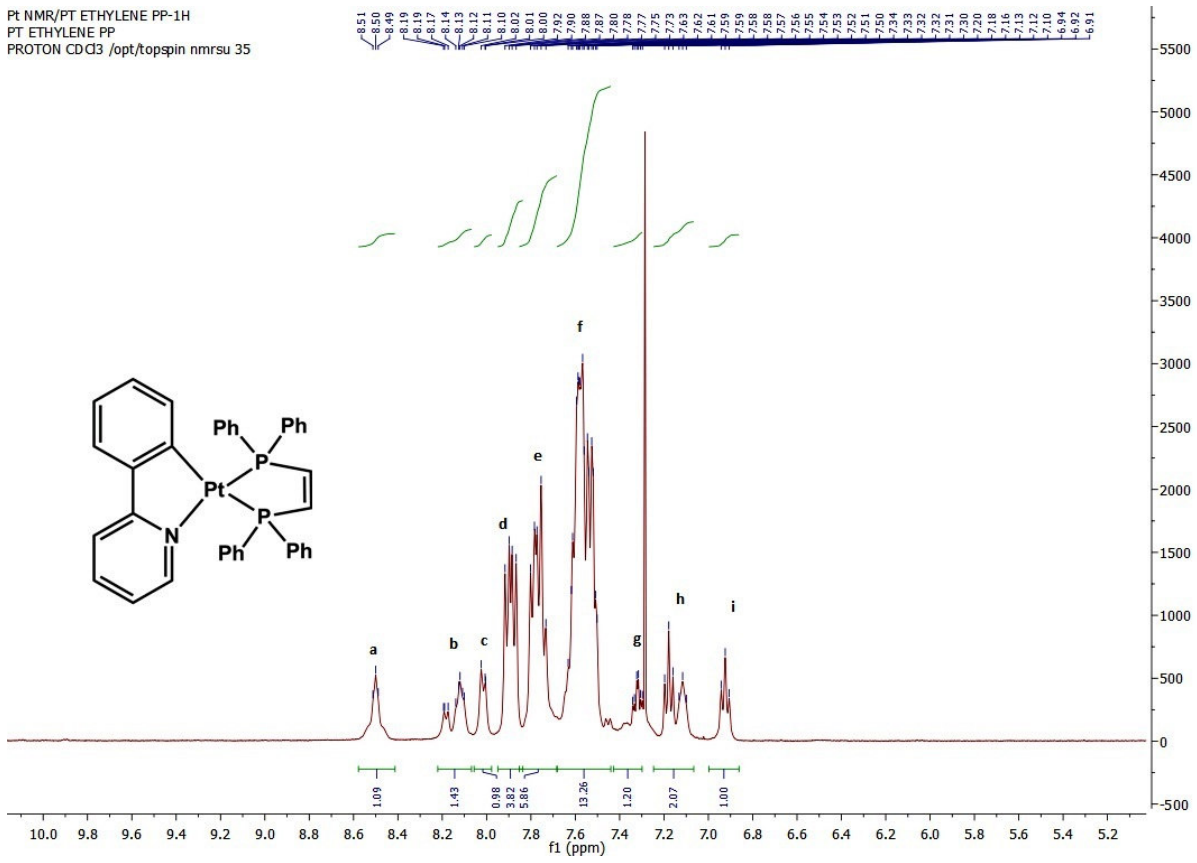

Figure. 14 ^{1}HNMR spectrum of complex **3**

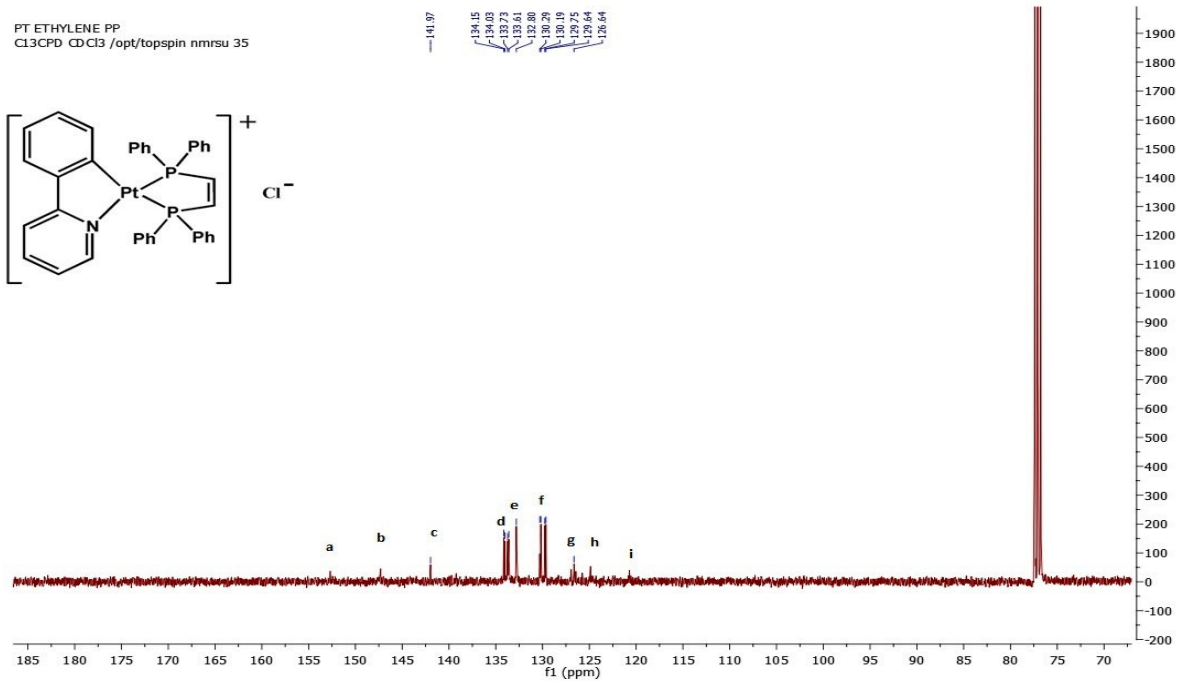

Figure. 15 ^{13}C NMR spectrum of complex **3**

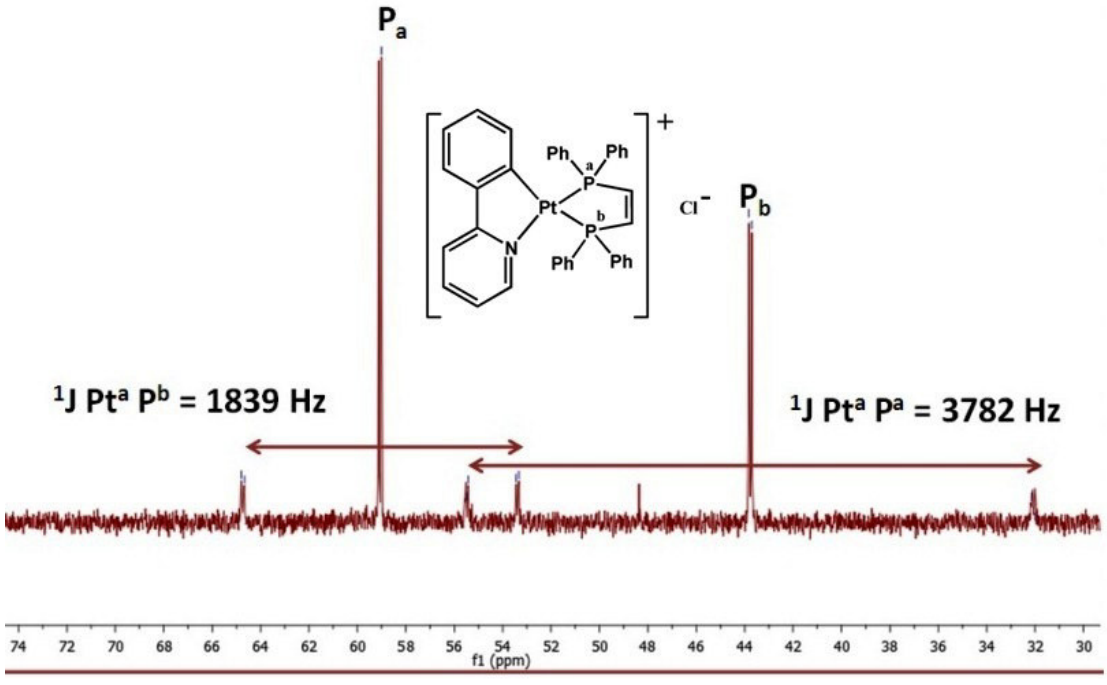

Figure. 16 ^{31}P NMR spectrum of [Pt(Pppy)(dppen)]Cl (**3**)

3B. 5. References

[1] (a) Q. Zhao, T. Y. Cao, F. Y. Li, X. H. Li, H. Jing, T. Yi and C. H. Huang, *Organometallics*, 2007, **26**, 2077; (b) Q. Zhao, F. Y. Li and C. H. Huang, *Chem. Soc. Rev*., 2010, **39**, 3007; (c) X. Mou, Y. Q. Wu, S. J. Liu, M. Shi, X. M. Liu, C. M. Wang, S. Sun, Q. Zhao, X. H. Zhou and W. Huang, *J. Mater.Chem*., 2011, **21**, 13951.

[2](a) Q. Zhao, F. Li and C.Huang, *Chem. Soc. Rev*., 2010, **39**, 3007; (b) M. L. Ho, Y. M. Cheng, L. C. Wu, P. T. Chou, G. H. Lee, F. C. Hsu and Y. Chi, *Polyhedron*, 2007, **26**, 4886; (c) Q. Zhao, S. J. Liu, F. Y. Li, T. Yi and C. H. Huang, *Dalton Trans*., 2008, 3836;(d) G. G. Shan, H. B. Li, H. Z. Sun, D. X. Zhu,H. T. Cao and Z. M. Su, *J. Mater. Chem. C*, 2013, **1**, 1440

[3](a) J. D. Slinker, A. A. Gorodetsky, M. S. Lowry, J. Wang, S. Parker, R. Rohl, S. Bernhard and G. G. Malliaras, *J. Am. Chem. Soc*., 2004, **126**, 2763; (b) P. T. Chou and Y. Chi, *Chem.–Eur. J*., 2007, **13**, 380, (c) B. Ma, P. I. Djurovich and M. E. Thompson, *Coord. Chem. Rev*., 2005, **249**, 1501; (d) S. R. Forrest and M. E. Thompson, *Chem. Rev*., 2007, **107**, 923.

[4] W.-Y. Wong , C.-L. Ho; *Coord. Chem. Rev*., 2009, **253**, 1709.

[5](a) B. Tong, Q. Mei, S. Wang, Y. Fang, Y. Menga and Biao Wang, *J. Mater. Chem*., 2008, **18**, 1636; (b) M. A. Baldo, D. F. O'Brien, Y. You, A. Shoustikov, S. Sibley, M. E. Thompson and S. R. Forrest, *Nature*, 1998, **395**, 151; (c) M. A. Baldo, S. Lamansky, P. E. Burrows, M. E. Thompson and S. R. Forrest, *Appl. Phys. Lett.*, 1999, **75**, 4; (d) E. Turner, N. Bakken, and J.Li, *Inorg. Chem*., 2013, **52**, 7344.

[6] C. H. Huang, F. Y. Li and W. Huang, *Introduction to OrganicLight-Emitting Materials and Devices*, Press of Fudan University, Shanghai, 2005.

[7] Y. Hong, J. W. Y. Lam and B. Z. Tang, *Chem. Soc. Rev*., 2011, **40**, 5361.

[8] (a) T. Han, X. Feng, B. Tong, J. Shi, L. Chen, J. Zhi and Y. Dong, *Chem. Commun*., 2012, **48**, 416; (b) X. T. Chen, Y. Xiang, N. Li, P. S. Song and A. j. Tong, *Analyst,* 2010, **135**, 1098;

[9](a) Q. Zhao, L. Li, F. Y. Li, M. X. Yu, Z. P. Liu, T. Yi and C. H. Huang, *Chem. Commun*., 2008, 685; (b) P. Alam, M. Karanam, A. Roy Choudhury and I.R. Laskar,*Dalton Trans*., 2012, **41**, 9276 ; (c) K. W. Huang, H. Z. Wu, M. Shi, F. Y. Li, T. Yi and C. H. Huang, *Chem.Commun*., 2009, 1243; (d) C. H. Shin, J. O. Huh, M. H. Lee and Y. Do, *Dalton Trans*., 2009, 6476.

[10](a) S.Liu, H. Sun, Y. Ma, S.Ye, X.Liu, X. Zhou, X. Mou, L. Wang, Q. Zhao and W.Huang, *J. Mater. Chem*., 2012, **22**, 22167; (b) H. Honda, Y. Ogawa, J. Kuwabara, and T. Kanbara, *Eur. J. Inorg. Chem*. 2014, 1865.

[11] V. W.-W. Yam, K. M.-C. Wong, and N. Zhu, *J. Am. Chem. Soc*. 2002, 1**24**, 6506.

[12] C. A. Strassert, C. H. Chien, M. D. G. Lopez, D. Kourkoulos,D. Hertel, K. Meerholz and L. De Cola, *Angew. Chem., Int. Ed*., 2011, **50,** 946.

[13] (a) H. Yoshika and K. Nakatsu, *Chem. Phys. Lett*., 1971, **11**, 255.(b) B. K. An, D. S. Lee, J. S. Lee, Y. S. Park, H. S. Song and S. Y. Park, *J.Am. Chem. Soc*., 2004, **126**, 10232.

[14] (a) T. Okada, I. M. El-Mehasseb, M. Kodaka, T.Tomohiro, K.-i.Okamoto, and H. Okuno, *J. Med. Chem*. 2001, **44**, 4661; (b) I. M. El-Mehasseb, M Kodaka, T.Okada, T.Tomohiro, K.-i. Okamoto, H. Okuno, *J. Inorg. Biochem*. 2001, **84**, 157.

[15](a) M. M. Mdleleni, J. S. Bridgewater, R. J. Watts, and P. C. Ford, *Inorg. Chem*., 1995, **34**, 2334 (b) J.-Y. Cho, K, Y. Suponitsky, J. Li, T. V. Timofeeva .S. Barlow , S. R. Marder, *J. Organomet. Chem*., 2005, **690**, 4090; (c) D. M. Jenkins and S.Bernhard, *Inorg. Chem*. 2010, **49**, 11297. (d) N. Godbert, T. Pugliese, I. Aiello, A.Bellusci, A. Crispini, and M. Ghedini, *Eur. J. Inorg. Chem*., 2007, 5105.

[16] M. G. Haghighi,. S. M. Nabavizadeh, M. Rashidi, and M. Kubicki, *Dalton Trans*., 2013, **42**, 13369.

[17] (a) F. Raoof, A. R. Esmaeilbeig, S. M. Nabavizadeh, F. N. Hosseini, and M. Kubicki, *Organometallics* 2013, **32**, 3850; (b) S. M. Nabavizadeh, H.R. Shahsavari, M. Namdar, M. Rashidi, *J. Organ. Chem*., 2011, **696** 3564; (c) M. G. Haghighi, M.Rashidi, S. M. Nabavizadeh, S Jamali and R. J. Puddephatt, *Dalton Trans*., 2010, **39**, 11396.

[18] R. H. Vaz, R. M. Silva, J. H. Reibenspies and O. A. Serra, J. Braz. *Chem. Soc*., 2002 , **13**, 82.

[19] P. Alam, I. R. Laskar, C. Climent, D. Casanova, P. Alemany, M. Karanam, A. R. Choudhury, J. R. Butcherd, *Polyhedron*, 2013, **53**, 286.

Chapter III

PART-C

Evaluation of a Novel Platinum(II) Based AIE Compound-Encapsulated Mesoporous Silica Nanoparticles for Cancer Theranostic Application

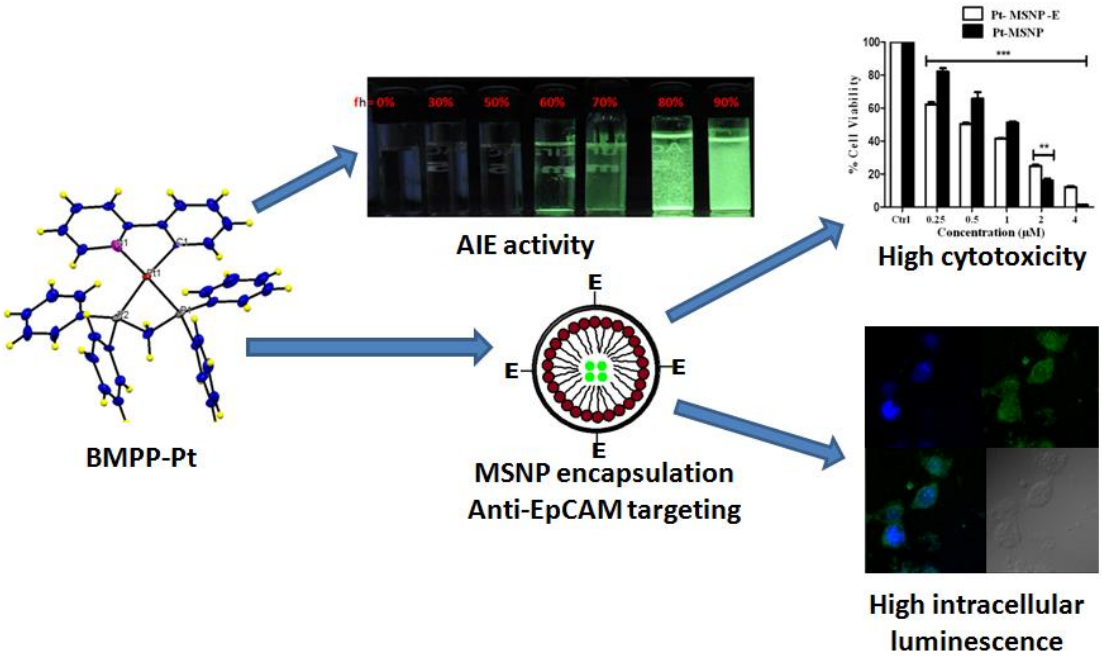

3C.1.Introduction

Due to the advancement in many key technologies and development of novel treatment modalities, diagnosis and treatment of cancer has improved significantly over the past few decades. Nevertheless, it is still a formidable task to follow tumor growth and treatment responsiveness in real time for an improved understanding of the disease and to take a better clinical decision for the choice of therapy. The idea of cancer theranostics is a relatively recent development and was introduced around 2010, [1] mainly to address the requirement for personalized medicine. Personalized on co-treatment depends heavily on real time monitoring of the treatment response, so that treatment modulation can be performed at the appropriate time. The integration of therapeutic and diagnostic agents to develop a theranostic technology provides a powerful means for simultaneous and real time monitoring of therapeutic responses. In the current clinical scenario, the imaging part of any theranostic approach is restricted to MRI, PET and CT technologies. Although these have widespread applications, it is sometimes difficult to distinguish between normal and malignant tissue using these techniques[2]. There are several classes of luminescent materials that have been tested for diagnostic purposes, especially, organic dyes and fluorescent proteins. However, organic dyes suffer from poor water solubility which restricts their use in bio-imaging applications. Also, organic fluorophores suffer from photo bleaching, low fluorescence intensities and intrinsically small Stokes shifts which produce scattered light interference[3]. Quantum dots (QDs) have also been widely used in bio-imaging due to their high photo stability owing to their inorganic nature, high quantum yields and broad absorption bands[3-5]. Nonetheless, QDs suffer from a few disadvantages surface defects can affect their combination of holes and electrons and create temporary traps, which results in blinking, undesired for bio-imaging applications [6]. QDs also suffer from a high amount of nonspecific adsorption *via* electrostatic interactions, a feature that was even found to be true for PEG (polyethylene glycol)-containing nano particles, making them undesirable for selective targeting[6-7]. Also, most luminescent materials exhibit strong luminescence in their diluted solutions, but this tends to be weakened or quenched at higher concentrations, a phenomenon known as ‘Aggregation-Caused Quenching (ACQ)’[8]. This quenching effect limits their application in targeted imaging, because with better targeting, their concentration in the targeted tissue will increase which will reduce their luminescence, and hampering the purpose of diagnosis. In 2001, Tang and coworkers [9] discovered an exactly opposite behavior to ACQ

which was observed in hexaphenylsilole and they named this new phenomenon 'Aggregation Induced Emission' (AIE). The formation of aggregates increased their fluorescence quantum yields by more than 300 fold, transforming them into strong emitters in the solid state. Often, the mechanism behind the AIE phenomenon is explained using the 'Restriction of Intramolecular Rotation' (RIR) concept[9-10]. An excited AIE molecule in dilute solution may undergo non-radiative decay competing with emission. In contrast, in the solid state, the intramolecular rotations associated with the non-radiative pathway in solution are restricted, causing the molecules to decay preferentially *via* radiative channels and thus showing a strong luminescence upon excitation. Since 2001, AIE-based materials have been widely investigated for various biological applications including biological probes, immunoassay markers, PAGE visualization agents, in bio-imaging and so on. As AIE complexes exhibit strongly enhanced fluorescence emission as their concentration increases, it can be a perfect choice for tissue targeted imaging.

Nanoparticles delivery systems have demonstrable advantages, including extension of circulating half-life, passive accumulation at tumor sites due to the enhanced permeability and retention (EPR) effect, active targeting of cancer cells, reduced toxicity, and integration of multiple functionalities in a unified entity[1, 11-13]. Among various nano-delivery systems used, mesoporous silica nanoparticles (MSNPs) have several advantages over others including a good dispersity and tailorable size and structure, which ensure controllable in vivo pharmacokinetics and a predictable outcome[13-16]. MSNPs are more flexible, versatile, and robust than conventional nano delivery systems such as polymer nanoparticles, liposomes etc. The manufacturing process of MSNPs is also relatively simple and economic, which is important to fulfill the future clinical demand and the commercialization. Although nanoparticles have been extensively explored for targeted delivery of many different drugs and other bioactive substances, to date very few reports have been published on AIE encapsulated nanoparticles for bio-applications.

Herein, we report the design and synthesis of a platinum(II) based AIE active molecule [bis(diphenylphosphino)methanephenylpyridineplatinum(II)]chloride, referred henceforth as BMPP-Pt. In the initial experiments, it has been proved that this molecule exhibits a strong fluorescence intensity as well as potent cytotoxic activity. To improve its cellular delivery, we encapsulated this compound into MSNPs (named Pt-MSNPs) and modified the surface of the

MSNPs with an aptamer against an Epithelial Cellular Adhesion Molecule (EpCAM) for cancer cell targeting (named Pt-MSNP-E). We evaluated its cytotoxic potency, mode of action, cellular bio-imaging, and potential for application as a single compound based theranostic modality.

3C.2. Results and discussion

3C.2.1. Synthesis and characterization

We prepared a Pt(II) based AIE molecule in a two step reaction. Firstly, ppyCl-Pt(**1**) (Scheme 1) was prepared. In the second step, **1**was reacted with chelate phosphine [bis(diphenylphosphino)methane](Scheme 1) to obtain BMPP-Pt(**2**). Purification of **2** was performed using column chromatography with 60–120 silica meshes. The final product was characterized by NMR spectroscopy(Experimental section) and single crystal XRD.

Scheme. 1 Synthetic route of BMPP-Pt, **2**.

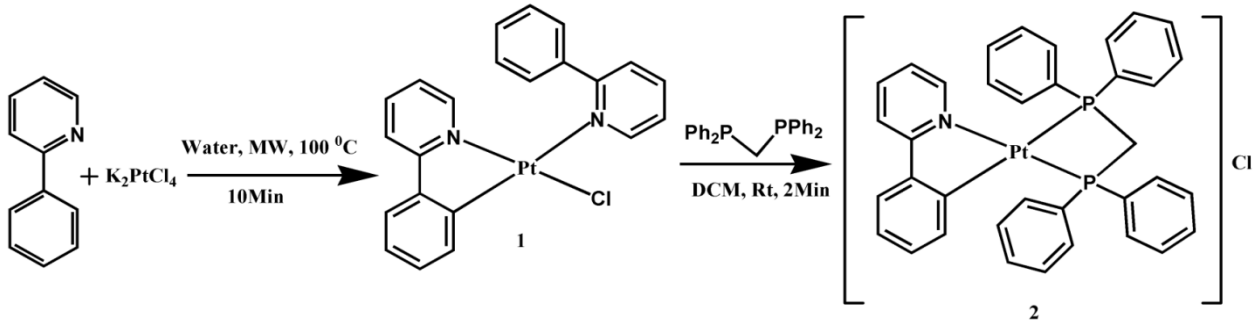

In the final compound**2**, all the aromatic proton signals are observed at δ =6.8–8.5 ppm and two protons of the P–CH_2–P fragment appeared at δ = 4.8 ppm. All the aromatic carbon signals are observed at δ = 124–169 ppm and one carbon of P–CH_2–P appeared at δ = 120.49 ppm for **2**. The two phosphorus signals are observed at −25.6 and −25.9 ppm. From HRMS data, the major fragmented peak appeared as [M − Cl]+ at m/z 733.1502. Suitable single crystals of **2** were grown from the slow evaporation of methanolic solution. Electronic structure calculations of the **2** complex were performed to gain some insight into the differences between the complex in dilute solution and in the solid state, as well as to characterize the nature of the fluorescent emissive state. There are important differences between the geometry of the optimized ground state of the **2** complex and its monomer in the crystal structure. In the optimized ground state, the two phosphorus atoms lie on the same plane as the phenylpyridine ligand (ppy), thus, the

(P)2–Pt–ppy fragment of the complex lies on one plane. In the molecular crystal, this planarity is partially lost (Figure 1) with a P1–Pt–N1–C1 dihedral angle close to 160°.

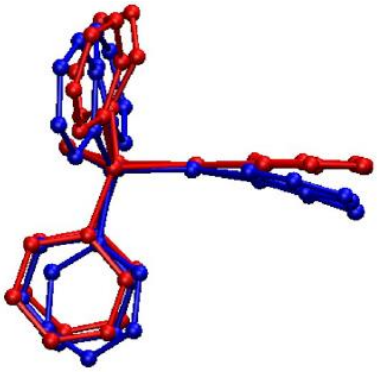

Figure. **1** Optimized BMPP-Pt ground state structure (in red) overlapped with the crystal's monomer structure (blue) showing the loss of planarity in the latter between the phenyl pyridine ligand and the Pt(P) 2 fragment. Hydrogen atoms are omitted for the sake of clarity.

We attribute this difference to the presence of neighboring complexes in the crystal structure. In particular, the BMPP-Pt complexes form dimers in the molecular crystal, interacting *via* the ppy ligands which partially overlap (Figure. 2). The shortest distance between the atoms of ppy ligands of the neighboring complexes is d(C∧N) = 3.381 Å. This separation between the ppy ligands is short enough, indicating the presence of interactions between both ligands in the ground state and possibly in the excited state.

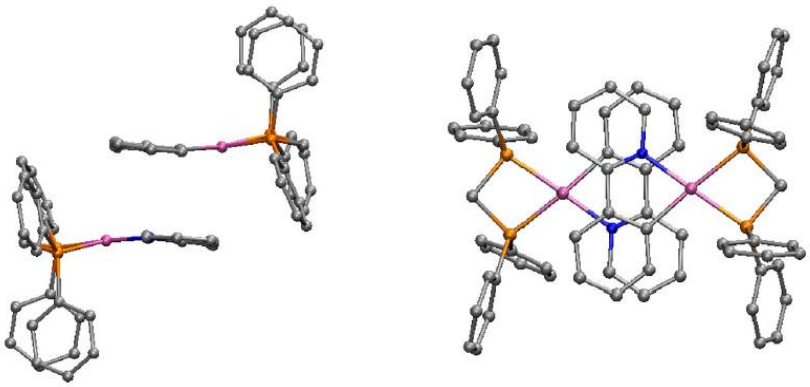

Figure. **2** Dimers of the BMPP-Pt complex present in the crystal structure (Side view on the left and top view on the right). Hydrogen atoms are omitted for the sake of clarity.

Comparisons of relevant geometrical parameters for both structures are given in Table 1. The calculated vertical excitation energy to the lowest absorbing singlet state (S_1) is 3.38 eV and

mainly corresponds to an HOMO-to-LUMO transition. These molecular orbitals are shown in Figure. 3. The HOMO mainly corresponds to a π-type orbital of the ppy ligand with some admixture of a d-type orbital of the platinum(II), while the LUMO is a π*-type orbital of the ppy ligand. The S_1 state is therefore a ligand centered(LC) π-π* state on the ppy ligand with a certain degree of metal-to-ligand charge transfer (MLCT) character. We also computed the S_1 state of the crystal's dimer since, as a first approximation, it may be representative of the kind of aggregate that the BMPP-Pt complex may form.

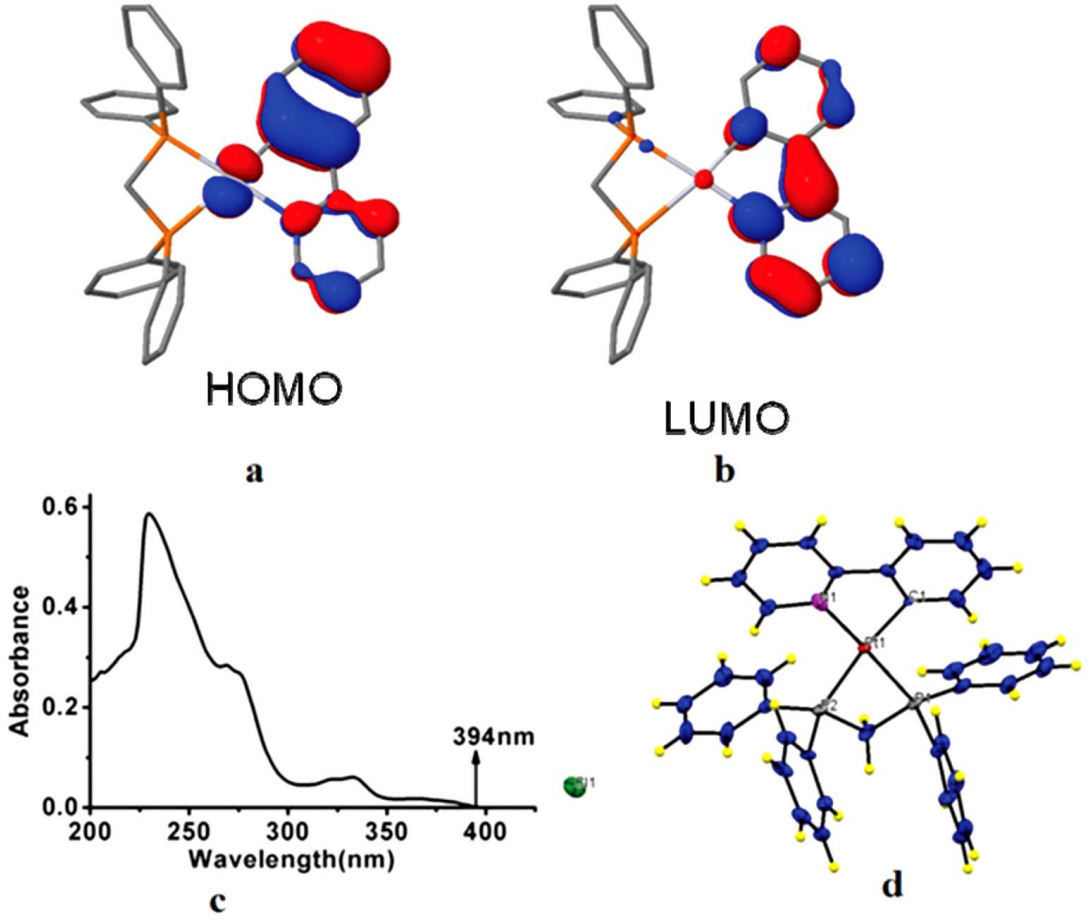

Figure. **3** Top view of the (a) HOMO and (b) LUMO of the BMPP-Pt ground state (hydrogen atoms omitted for the sake of clarity); (c) absorption spectrum of BMPP-Pt at 0.69×10^{-5} M dichloromethane and (d) ORTEP diagram of BMPP-Pt.

Table. 1 Relevant bond lengths and dihedral angles of the BMPP-Pt complex in the crystal's monomer geometry and the optimized ground state structure.

Geometry	Pt-P (Å)	Pt-P (Å)	Pt-N (Å)	Pt-C (Å)	P-Pt-N-C (°)	P-Pt-C-C (°)
Crystal monomer	2.272	2.301	2.041	2.026	161	167
Optimized S_0	2.451	2.312	2.113	2.039	178	179

The S_1 state of the dimer is also a HOMO-to-LUMO transition with an excitation energy of 3.24 eV, that is 0.05 eV lower than the crystal's monomer (3.29 eV). This is already indicative that there is a certain interaction between the two complexes of the dimer in the S_1 state. The molecular orbitals corresponding to this excited state are shown in Figure. 4. The HOMO can be described as an anti-bonding combination of the HOMOs on each monomer, while the LUMO is a bonding combination of the LUMOs of each monomer. Certainly, the S_1 state in the dimer is delocalized, involving both complexes.

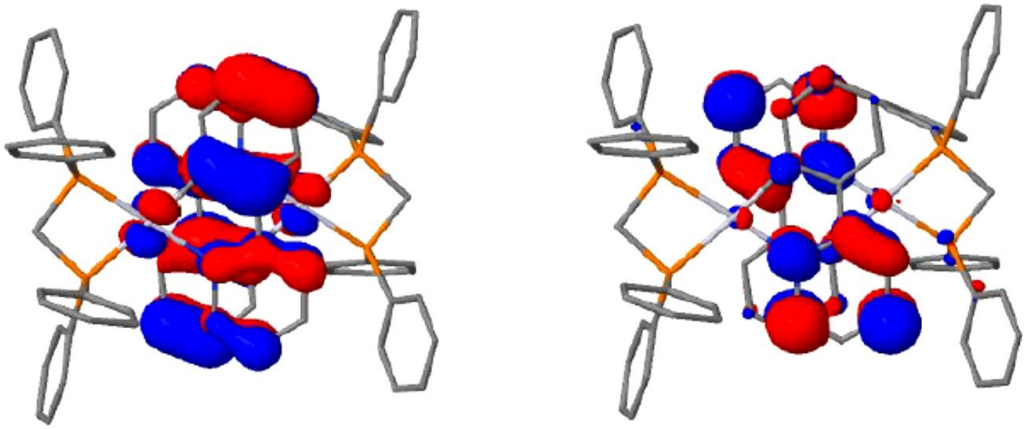

Figure. **4** Top view of the HOMO (left) and LUMO (right) of the BMPP-Pt dimers present in the crystal structure. Hydrogen atoms are omitted for the sake of clarity.

3C.2.2 Aggregation Induced Emission

BMPP-Pt was found to be well soluble in dichloromethane(DCM) and insoluble in hexane, and thus these solvents were chosen to investigate the AIE behavior of BMPP-Pt. Photoluminescence (PL) spectra of a series of solutions(0–90%) in DCM/hexane were recorded

and a gradual enhancement of the emission intensity with increasing concentration of DCM was observed (Figure. 5).

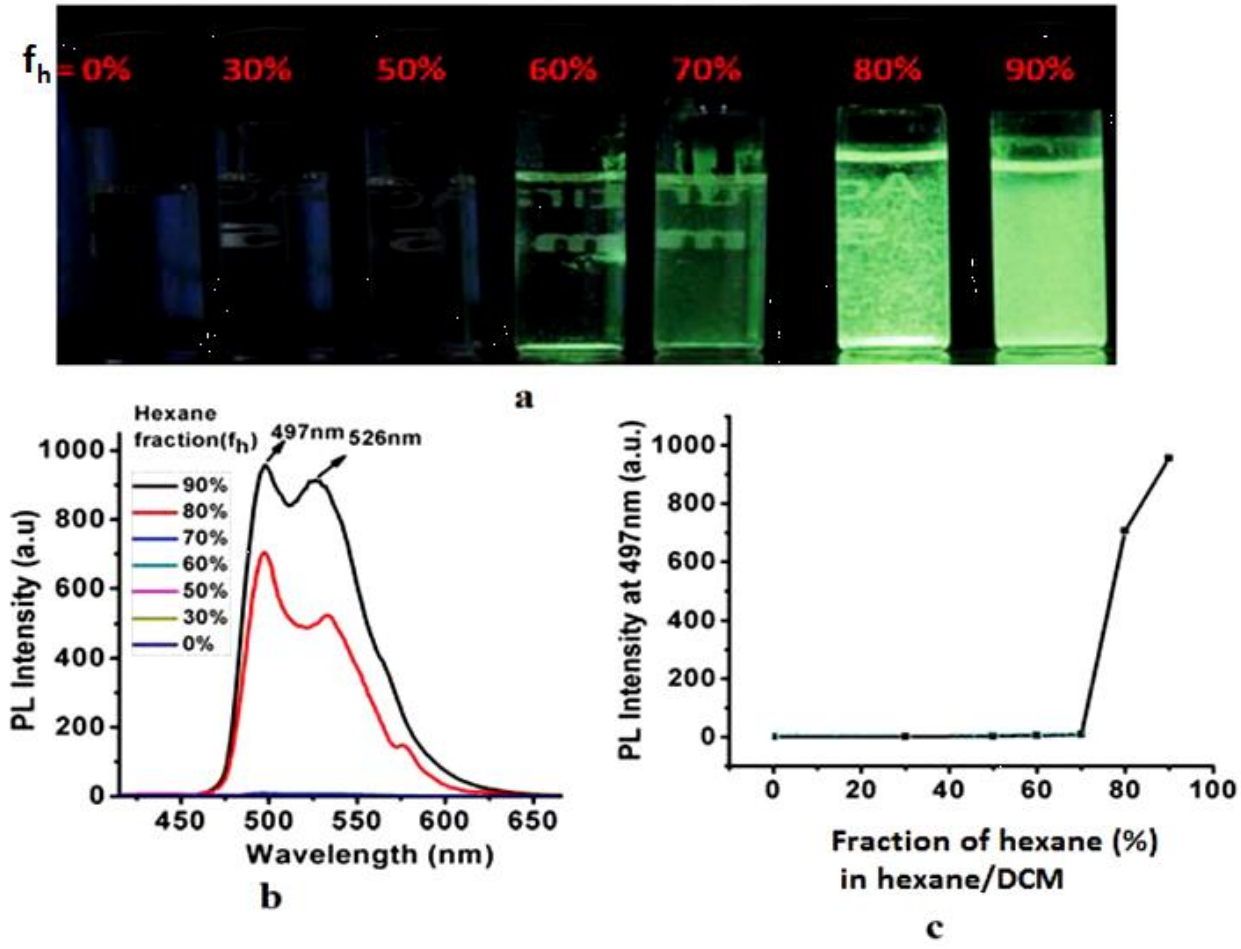

Figure. 5 (a) Luminescent images of BMPP-Pt (λ_{ex} = 365nm) in different fractions of dichloromethane (DCM) in hexane with keeping the concentration of BMPP-Pt as 2×10^{-5} M; (b) The corresponding photoluminescence spectra of BMPP-Pt in DCM-hexane mixed solvents (λ_{ex} = 365nm); (c) The plot of changing PL intensity with varying concentration of DCM into hexane (λ_{max} = 498 nm).

In the range of 0% to 70%, no detectable emission intensity change was found presumably because of low aggregate formation, whereas from 70% to 90%the emission intensity is very high because of the greater extent of aggregate formation. As this compound is highly emissive in the solid state and has an amphiphilic nature, it can be considered for applications in bio-imaging.

3C.2.3 Encapsulation and functionalization of 2 into mesoporous silica

Scheme 2 Preparation of BMPP-Pt loaded MSNPs (3), modification of the MSNPs with GOPS (4) and conjugation of an anti-EpCAM aptamer with the GOPS modified MSNPs (5)

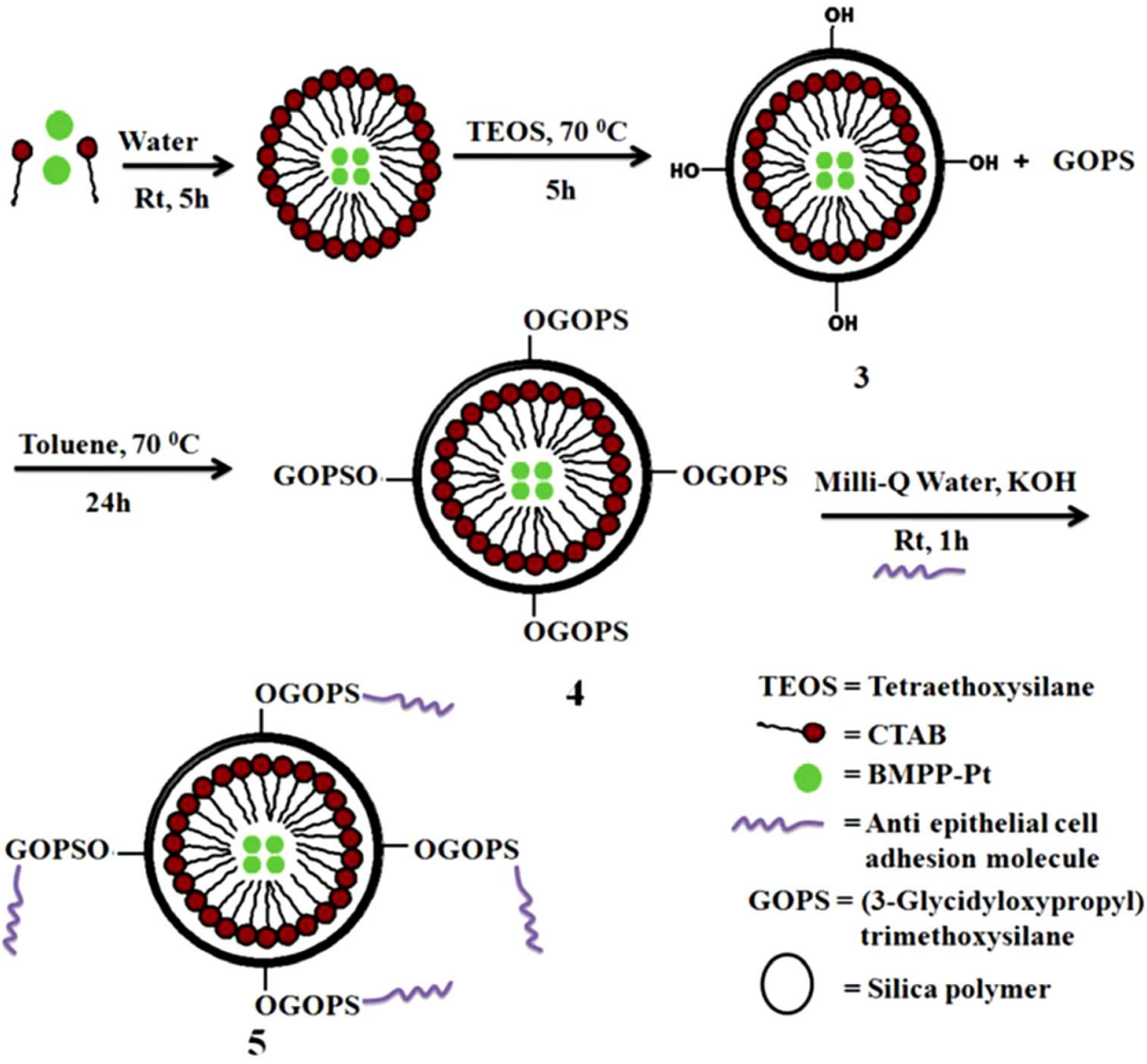

As the water solubility of BMPP-Pt was very poor, it was challenging to develop a delivery system for this compound. We have prepared BMPP-Pt encapsulated mesoporous silica nanoparticles (Pt-MSNPs) to circumvent the solubility problems well as to make a tumour-targeted delivery system for BMPP-Pt. Different nano-formulations have been developed to

provide increased safety and efficacy for cancer therapy. Among them, mesoporous silica nanoparticles (MSNPs) have attracted substantial attention due to their advantageous structural properties, which have made them applicable for diverse biomedical applications including bio-imaging for diagnostics, biosensing, biocatalysis, scaffold engineering, drug delivery etc. In addition, these can be used for easy functionalization with a targeting ligand[14-15].For encapsulation of BMPP-Pt in MSNPs, first a micellar solution of BMPP-Pt was prepared using CTAB as the surfactant (Scheme 2). Into the micellar solution of CTAB–BMPP-Pt, tetraethoxysilane (TEOS) was then introduced topolymerize into mesoporous silica. The solid crude product was filtered, washed with water and methanol several times and vacuum dried to yield Pt-MSNPs (Scheme 2). These BMPP-Pt encapsulated MSNPs were further modified by conjugating them with an anti-EpCAM aptamer to the surface.

To conjugate with the aptamer, initially the surface of Pt-MSNPs was modified with glycidoxypropyltrimethoxysilane (GOPS)that resulted in Pt-MSNP-GOPS and then the anti-EpCAM aptamer was added to the aqueous solution of Pt-MSNP-GOPS, incubated for one hour and washed with phosphate buffer to produce the anti-EpCAM aptamer conjugated BMPP-Pt loaded MSNPs (named Pt-MSNP-E; Scheme 2). After the synthesis of Pt-MSNPs, Pt-MSNP-GOPS and Pt-MSNP-E, these have been characterized by FTIR, DLS, zeta potential and TEM techniques.

The FTIR spectra of Pt-MSNPs and Pt-MSNP-GOPS, as shown in Figure6 show common peaks, which are characteristic to mesoporous silica at 1032 cm^{-1} (Si–O–Si stretching) and aliphatic C–H stretching peaks at 2925 cm^{-1} and 2856 cm^{-1} due to CTAB. The peak observed at 721 cm^{-1} is due to the epoxy group present in Pt-MSNP-GOPS.

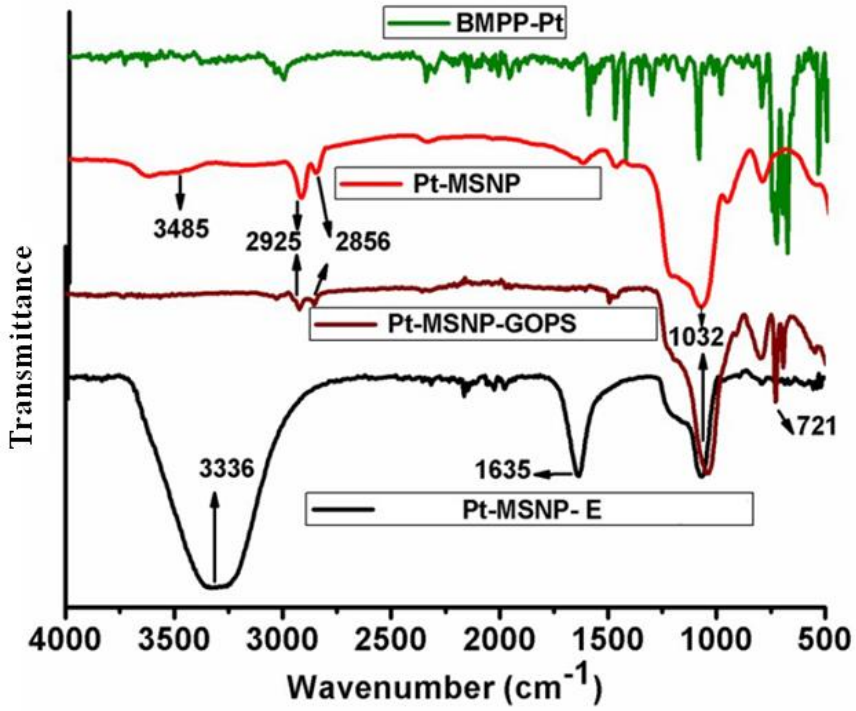

Figure. **6** FTIR spectra of free BMPP-Pt, Pt-MSNPs, Pt-MSNP-GOPS and Pt-MSNP-E

Furthermore, the absence of the broad absorption peak due to the –OH (3485 cm^{-1}) group in Pt-MSNP-GOPS when compared with Pt-MSNPs confirms the successful modification of the surface with GOPS. The IR spectrum of Pt-MSNP-E shows two peaks at 3336 cm^{-1} and 1635 cm^{-1} which are attributed to the –OH and C=N stretching frequencies, respectively. These two new peaks and the disappearance of the epoxy peak at 721 cm^{-1} strongly support the conjugation of the anti-EpCAM aptamer on the surface of mesoporous silica. We further studied the size and shape of the different MSNPs by transmission electron microscopy (TEM). All the particles exhibited a perfect spherical shape. Both blank MSNPs and BMPP-Pt loaded MSNPs have a diameter in the range of ~100 nm while after anti-EpCAM aptamer conjugation, the diameter of the particles increased to ~200 nm (Figure. 7). This increase in size supports the occurrence of sequential addition of GOPS and aptamer on Pt-MSNPs. The EDX results show that the total nitrogen content in Pt-MSNP-GOPS and Pt-MSNP-E is 0.84 and 2.04 (in wt%), respectively. The increased nitrogen concentration further supported the successful attachment of the anti-EpCAM aptamer on the surface of Pt-MSNP-GOPS (Figure. 8, Figure. 9, Tables 2 and 3).

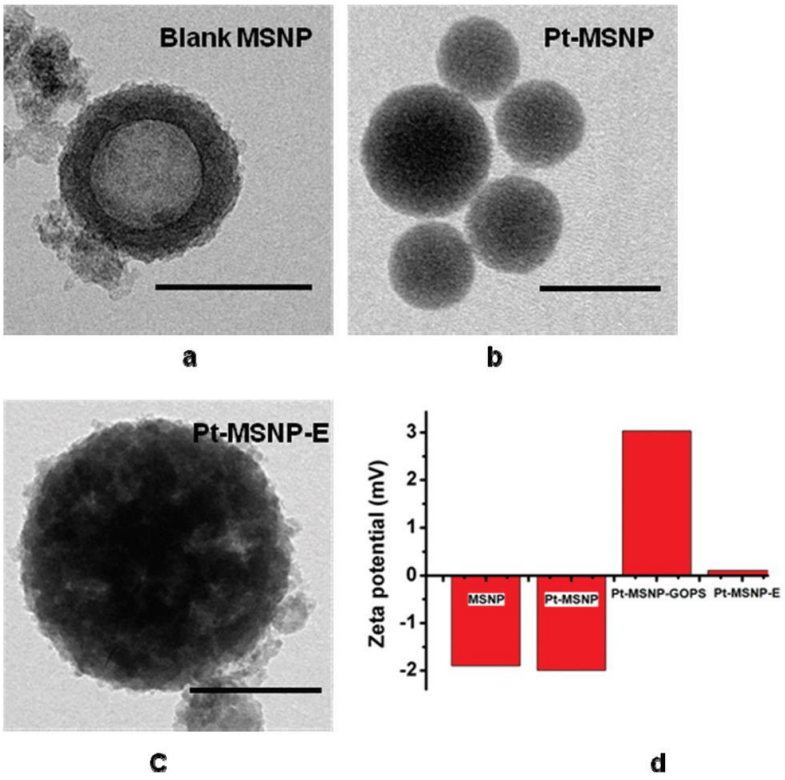

Figure. **7** Transmission Electron Microscopy images of (a) blank MSNPs; (b) Pt-MSNPs; (c)Pt-MSNP-E; and (d) zeta potential of blank MSNPs, Pt-MSNPs, Pt-MSNP-GOPS and Pt-MSNP-E.

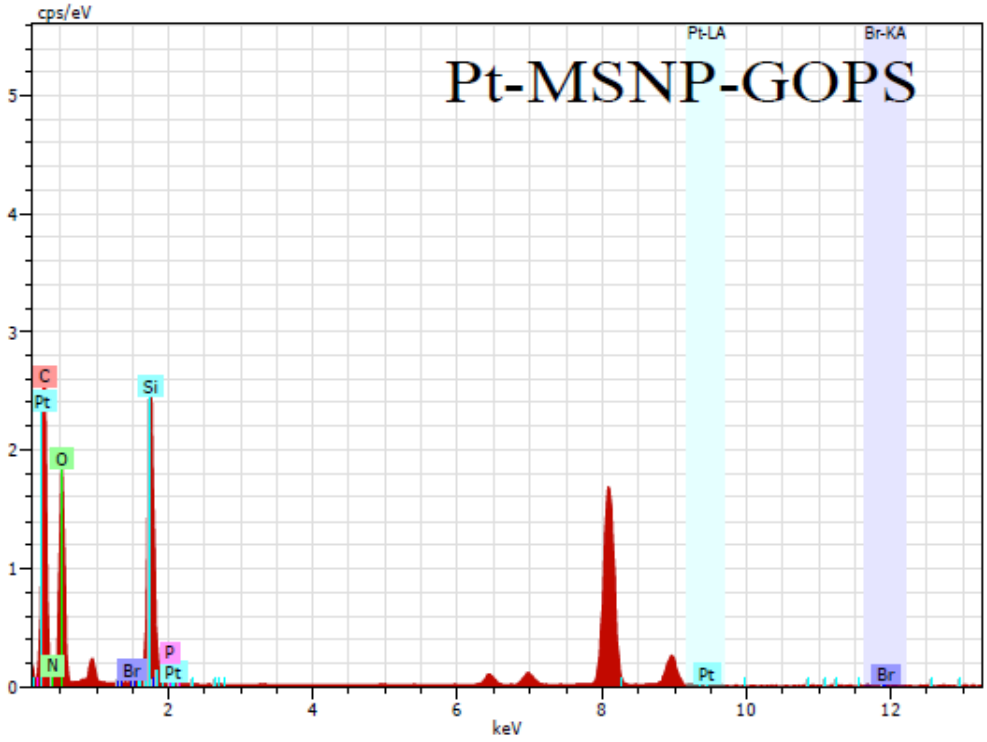

Figure. **8** EDX spectrum of Pt-MSNP-GOPS

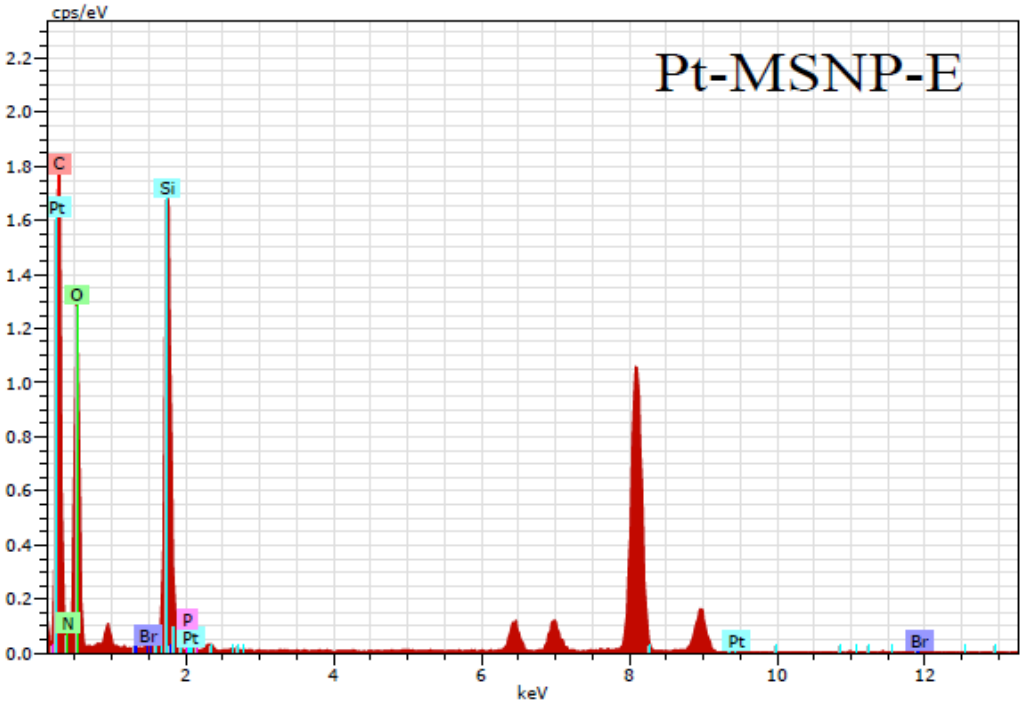

Figure. **9** EDX spectrum of Pt-MSNP-E

Table. **2** Concentration of elements present in Pt-MSNP-GOPS from EDX analysis

El	AN	Series	unn. C[wt.%]	norm. C[wt.%]	Atom. C[at.%]	Error (1 Sigma)[wt.%]
C	6	K-series	81.36	81.36	88.04	2.50
Si	8	K-series	8.79	8.79	7.14	0.29
O	14	K-series	8.52	8.52	3.94	0.06
N	7	K-series	**0.90**	**0.90**	**0.84**	**0.06**
Pt	78	L-series	0.39	0.39	0.03	0.07
P	15	K-series	0.02	0.02	0.01	0.03
Total			100.00	100.00	100.00	

Table. **3**Concentration of elements present in Pt-MSNP-E

El	AN	Series	unn. C[wt.%]	norm. C[wt.%]	Atom. C[at.%]	Error (1 Sigma)[wt.%]
C	6	K-series	81.36	81.36	88.04	2.50
Si	8	K-series	8.86	8.86	7.17	0.29
O	14	K-series	7.08	7.08	4.73	0.10
N	7	K-series	**2.13**	**2.13**	**2.04**	**0.08**
Pt	78	L-series	0.37	0.37	0.02	0.08
P	15	K-series	0.01	0.01	0.00	0.03
Total			100.00	100.00	100.00	

Also, in the TEM image, the core of the blank MSNPs appeared to be less dense than that of Pt-MSNPs or Pt-MSNP-E. This may be due to the fact that the core of the blank MSNPs was made up of the empty micelle, whereas the core of the BMPP-Pt loaded MSNPs had a significant quantity of the Pt compound. We also quantified the surface charge of different MSNPs by measuring the zeta potential of the particles. The results obtained from zeta potential measurements show that the surface charge on MSNPs, MSNPs-Pt, Pt-MSNP-GOPS and Pt-MSNP-E are −1.90, −1.99, +3.03 and +0.105, respectively (Figure. 7). This observation is in good support that the surface groups present in blank MSNPs, MSNPs-Pt, Pt-MSNP-GOPS and Pt-MSNP-E are hydroxyl, hydroxyl, epoxy and then aptamer, respectively.

Pt-MSNPs, Pt-MSNP-GOPS and Pt-MSNP-E were found to show green emission in water with emission maxima at 479, 478 and 479 nm, respectively (Figure. 10). After the synthesis of Pt-MSNPs, we investigated the total loading of BMPP-Pt into MSNPs with a UV-VIS spectroscopic study. To estimate the total amount of BMPP-Pt that has been incorporated into the mesopores of mesoporous silica, the absorbance of a set of known concentration solutions of BMPP-Pt (in the range of5 μg mL^{-1} to 25 μg mL^{-1}) has been recorded and then the absorbance value (at λ_{max} =

233 nm) was plotted vs. the concentration. Thereafter, 1 mg of Pt-MSNPs and 10 µl of HCl were added into 2 ml of DCM in a round-bottom flask, stirred overnight and then the absorbance spectra were recorded.

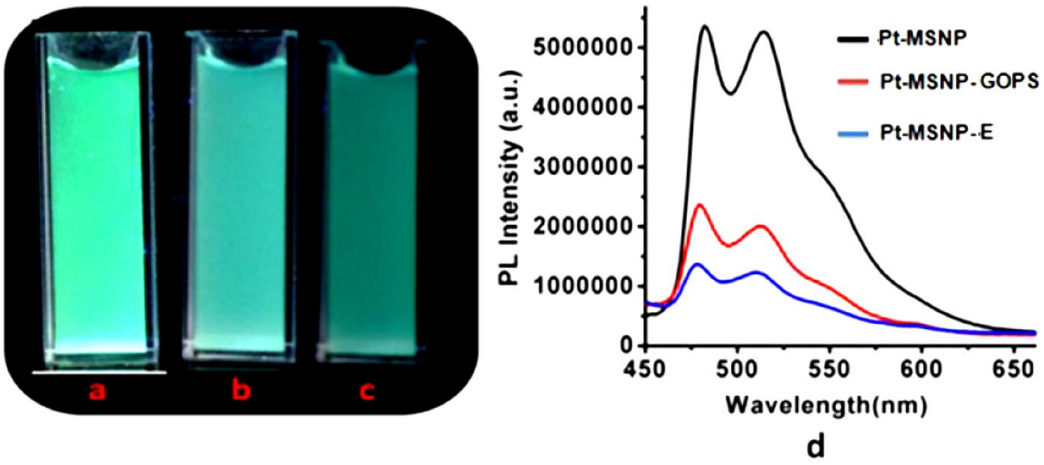

Figure. **10.** Luminescent images(left) of (a) Pt-MSNPs (b)Pt-MSNP-GOPS (c) Pt-MSNP-E (d) and their PL spectra (right) λ_{ex} = 365nm in water (c = 2mg/ml).

All the incorporated Pt(II) compounds were expected to be expelled out from the mesopores into the solution. The concentration of this unknown solution has been determined through extrapolation into the calibration curve as stated earlier, and the amount is determined to be 28 µg of BMPP-Pt per mg Pt-MSNP (Figure. 11 and Table 4).

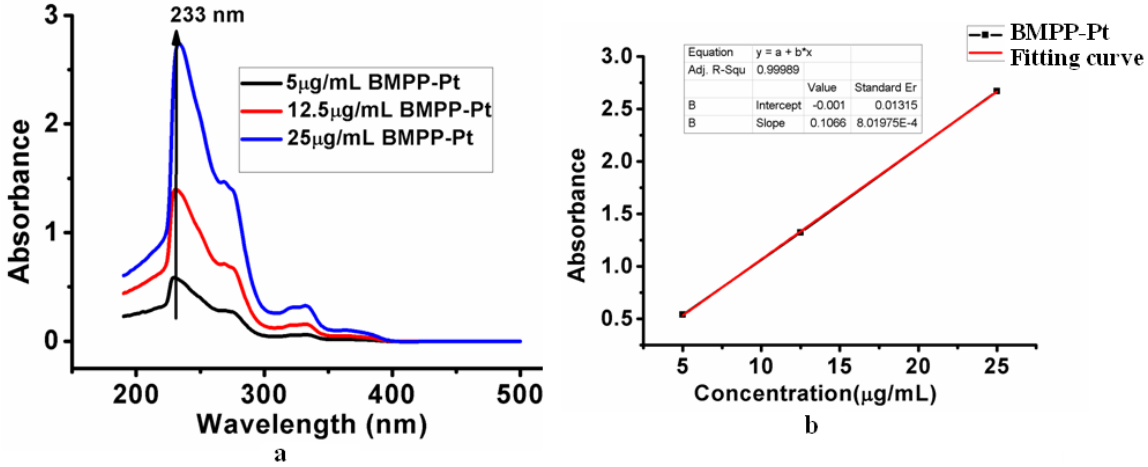

Figure. **11**(a) Absorption spectra of BMPP-Pt at different concentrations; (b) shows linear fitting of absorbance vs. concentration.

Table. **4** Releasing study of BMPP-Pt from **3** (at λ_{max}, 233nm)

Time (in h)	Absorbance (a.u.)
0	0.0163
6	0.0121
48	0.0178
72	0.0135
96	0.0132
120	0.0139
144	0.0142
168	0.0131
192	0.0134
216	0.0132

3C.2.4 Analysis of cellular uptake of Pt-MSNPs

Over the last few years, cancer research has focused on the optimization of clinical methodologies to better target tumours through development of new therapeutic strategies. In this context, MSNPs have shown considerable promise as potential versatile drug delivery vehicles[17-18].However, to date, the major hindrance with MSNP-based therapy has been identifying and tagging of fluorescent molecules that can track NPs, as well as ones that can regulate their target-specific entry. In this study, we have encapsulated the BMPP-Pt complex in MSNPs. BMPP-Pt is an 'aggregation induced emission' compound and hence it is a promising candidate as fluorescent tracker that can be loaded in MSNPs and monitored or used for cancer diagnosis. In our study, to confirm the internalization of the AIE active BMPP-Pt complex, we exposed Huh7 liver cancer cells to free BMPP-Pt for 24 h. Confocal microscopy analysis revealed that these compounds are internalized, though the fluorescence signal was weak (Figure. 12). Thereafter, to evaluate whether encapsulation of BMPP-Pt into MSNPs can

enhance their cellular internalization properties, Huh7 liver cancer cells were treated with BMPP-Pt and Pt-MSNPs and were monitored for their relative fluorescence in comparison with free BMPP-Pt compounds.

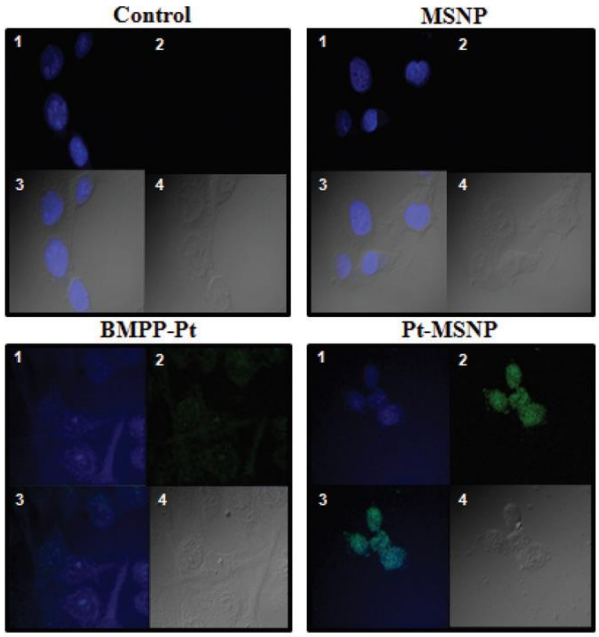

Figure. 12 Internalization studies of MSNPs, BMP-Pt and Pt-MSNPs by confocal microscopy. Huh7 cells were seeded on cover slips and treated for 24 h with either MSNPs, BMP-Pt or Pt-MSNPs and were counter stained with DAPI. Fluorescence was observed under a confocal microscope and represented. For each panel, 1: DAPI (nuclear stain); 2: green fluorescence from BMPP-Pt; 3: overlay of both 1 and 2; 4: phase contrast image for cellular morphology [18b].

Interestingly, confocal microscopic analysis detection of intra-cellular green fluorescence showed an increased fluorescence signal in Pt-MSNPs as compared to free BMPP-Pt or untreated control in Huh7 cells after exposure of 24 h (Figure. 12). Cells treated with free BMPP-Pt exhibited only a weak emission, whereas BMPP-Pt encapsulated MSNPs showed a strong intracellular green emission, signifying a better internalization efficiency of the Pt-MSNP compound compared to free BMPP-Pt (Figure. 12). It has been observed in many studies that MSNP encapsulation enhances cellular uptake of different active compounds[19-23].The increased internalization efficiency and their diagnostic potential further prompted us to investigate and compare the cytotoxic properties of Pt-MSNPs with BMPP-Pt.

3C.2.5.Pt-MSNPs induce cytotoxicity in Huh7 cancer cells

The cytotoxic potential of the BMPP-Pt compound was evaluated in the Huh7 cells through MTT assays (Figure. 13). The compound was found to be highly cytotoxic, apart from its intracellular AIE property that was evident from the previously discussed results. This allowed us to consider the BMPP-Pt compound as a potential theranostic agent which could be utilized for both the detection and treatment of cancer cells. As the previous data showed that encapsulation of BMPP-Pt into MSNPs enhanced their cellular uptake, we compared the cytotoxic potential of free BMPP-Pt to that of MSNP encapsulated BMPP-Pt. Both free BMPP-Pt and Pt-MSNPs showed a considerable cytotoxic effect on Huh7 cells (Figure. 13a and b) with the IC_{50}values from both treatments at around 1 μM. Blank MSNPs show only a very low level of cell death, even at a very high concentration(Figure. 14).

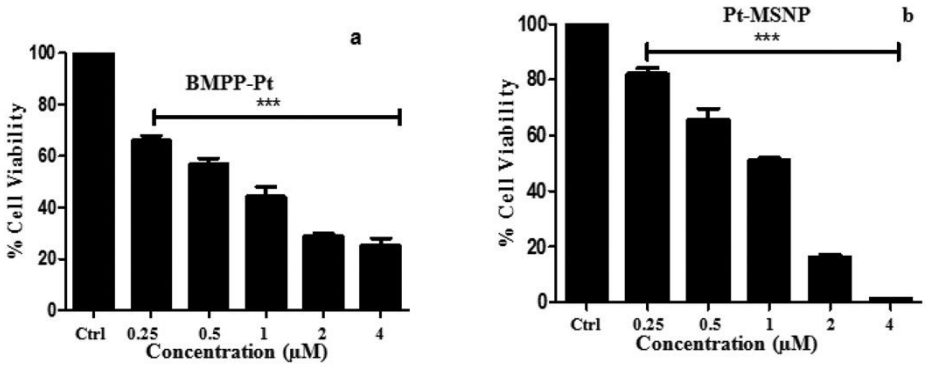

Figure. 13 Effects of BMP-Pt and Pt-MSNPs treatment on cytotoxicity of Huh7 cells. (a & b) Cells were treated with different concentrations of BMP-Pt and Pt-MSNPs, respectively, for 24 h and cell viability was analyzed through a MTT assay and is represented as a bar diagram. The symbol (*) represents a significant difference ($p < 0.05$) as compared to un-treated control cells [18b].

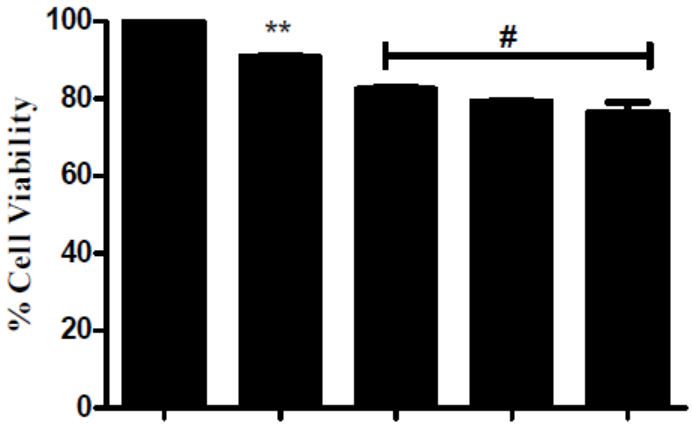

Figure. **14** Effect of blank MSNP on viability of Huh7 cells, analyzed by MTT assay after 24 h treatment of each. [Symbol (**) represents significant the difference($p<0.05$) as compared to untreated cells; Symbol (#) represents no significant difference].

3C.2.6 Anti-EpCAM aptamer functionalized Pt-MSNPs show increased internalization and cytotoxicity

The silica nanoparticles, especially those with mesopores, have attracted the interest of the scientific community due to their potential to be applied in the nanomedicine field [24]. When compared to organic nanocarriers, MSNPs are more resistant to pH, temperature variations and also to mechanical stress, which render them an improved capacity to protect the drug cargo when in contact with body fluids [17-18]. Here, we observed that the MSNPs can be loaded with the BMPP-Pt complex which can have both cytotoxic as well as diagnostic properties. Because of its well acclaimed properties in the nanomedicine field, and supported by our results discussed above, we were interested in functional modification of the Pt-MSNP complex with cancer cell specific targeting molecules. The objective was to develop a single compound based theranostic agent that can be targeted specifically to cancer cells. An epithelial cell adhesion molecule (EpCAM) is known to be highly expressed in most of the solid tumours, including the liver[25-27].It has been reported as a putative cancer stem cell marker, and it is regarded as a target antigen for cancer therapies using antibodies and aptamers[28-31]. Also, an aptamer based tumour targeting can overcome the inherent issues associated with antibodies, such as larger size and immunogenicity. The aptamer against EpCAM was procured and used as a surface functionalization agent on the Pt-MSNP complex.

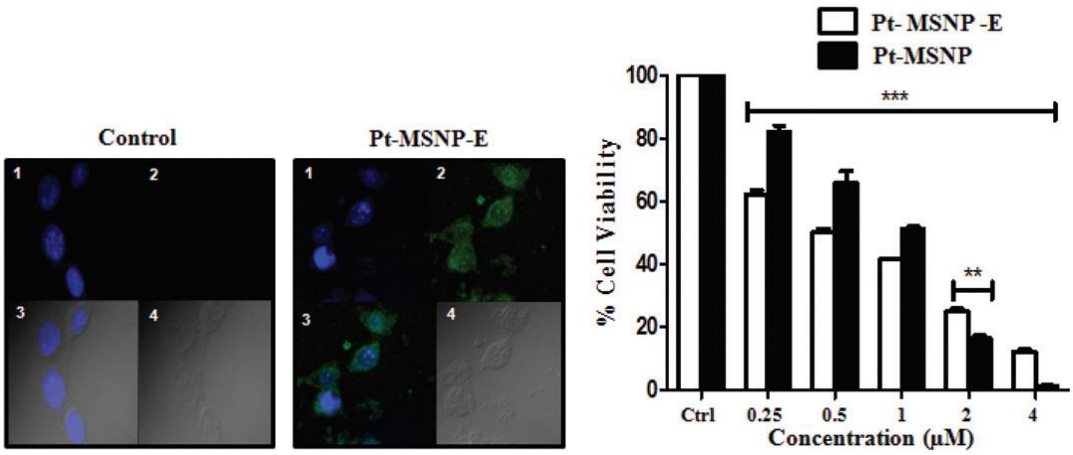

a **b**

Figure. 15 Internalization and cytotoxic effect of Pt-MSNP-E treatment on Huh7 cells. (a) Confocal images of the internalized Pt-MSNP-E in Huh7 cells after 24 h of treatment (left: untreated cells; right: Pt-MSNP-E treated cells). For each panel, 1: DAPI (nuclear stain); 2: green fluorescence from BMPP-Pt; 3: overlay of both 1 and 2; 4: phase contrast image for cellular morphology. (b) Representation of cell viability of Huh7 cells after treatment of Pt-MSNPs and Pt-MSNP-E post 24 h exposure analyzed through a MTT assay. The symbol (*) represents a significant difference ($p < 0.05$) as compared to the control cells.

The cellular uptake study of the anti-EpCAM aptamer functionalized Pt-MSNP complex was performed through confocal microscopic images which confirmed the internalization of the same in Huh7 cells (Figure. 15a). Furthermore, the Pt-MSNP-E appeared to impart cytotoxicity in Huh7 cells, as analyzed through the MTT assay (Figure. 15b). Interestingly, in addition to its effective internalization when compared to the Pt-MSNP complex, the Pt-MSNP-E compound showed significantly better cytotoxicity in Huh7 cells in the concentration range of 0–1 μM, when exposed for 24 h. However, it showed partly lower cytotoxicity beyond the concentration range of 1 μM, which is rationalized as follows: nanoparticles which are attached with the anti-EpCAM aptamer (Pt-MSNP-E) would probably be internalized in the tumour cells through receptor mediated endocytosis whereas nanoparticles without the aptamer (Pt-MSNPs) could be internalized through other different pathways like, pinocytosis. As receptor mediated endocytosis is dependent on the number of that specific receptor on the surface of the cell, it may get saturated at high ligand concentrations [31] whereas the non-aptamer tagged nanoparticles do not

face such hindrance as their entry is independent of receptor saturation. Probably due to this reason, Pt-MSNP-E exhibited better cellular internalization and higher cytotoxicity at low concentrations compared to Pt-MSNPs; whereas at high concentrations, Pt-MSNPs exhibited better cytotoxicity.

3C.3.Conclusion

A new Pt(II) based AIE active complex was synthesized. Platinum(II) based compounds like, *cis*-platin are extensively utilized even today for cancer therapy. This compound was then successfully incorporated into the mesopores of silica. Strategies were thereafter developed to conjugate functional entities like, EPCAM on the surface of MSNPs to improve their selectivity towards the cancerous cell. Cellular internalization of the free and MSNP encapsulated AIE compounds was compared and studied in cancer cells. Also the EPCAM conjugated MSNP-Pt complex were investigated for their cellular internalization potential and cytotoxic property. In summary, we for the first time report the use of novel Pt-based AIE molecules incorporated in EPCAM functionalized MSNPs as future theranostic regimen for cancer cells. Our study can revolutionize both early detection and therapy of cancer cells and also monitors their treatment *in situ*.

3C.4. Experimental section

Synthesis of [Pt(ppy)(ppyH)(Cl)] (ppyCl-Pt) (ppy = 2-phenylpyridine):

We have discussed in chapter 3A and 3B.

Synthesis of BMPP-Pt: It was prepared by following the similar technique as reported by our group earlier[32].To a stirred solution of ppyClPt (1 equivalent) in DCM (6 mL), chelate phosphine [bis(diphenylphosphino)methane] (1 equivalent) was added and the reaction mixture was stirred for 2 minutes to complete the reaction. The crude product was purified by column chromatography using 60-120 silica mesh. ^{1}H NMR (400 MHz, Chloroform-d)(Figure.16) δ 8.36 (s, 1H), 8.15 (td, J = 8.1, 1.4 Hz, 1H), 8.01 (d, J = 8.1 Hz, 1H), 7.98 – 7.87 (m, 4H), 7.84 – 7.65 (m, 6H), 7.60 – 7.40 (m, 13H), 7.28 – 7.22 (t, 1H), 7.19 (t, J = 7.8 Hz, 1H), 7.06 – 6.99 (m, 1H), 6.95 (t, J = 7.2 Hz, 1H), 4.92 (t, J = 10.5 Hz, 2H).^{13}C NMR (101 MHz, Chloroform-d) δ 167.02, 152.29, 147.53, 141.73, 138.37, 133.88, 133.76, 133.45, 133.31, 132.80, 132.53, 131.34, 129.99,

129.88, 129.62, 129.49, 126.59, 125.00, 124.57, 120.49; ^{31}P NMR (101 MHz, Chloroform-d) (Figure 17) green solid, 95 % yield.HRMS: $[M\text{-}Cl]^+$ at m/z 733.1502 (Figure 18).

Table 5. Crystal data and structure refinement for **2**.

Empirical formula	C_{36} H_{32} Cl N O P_2 Pt	Z	2
Formula weight	787.10	Density (calculated)	1.706 Mg/m^3
Temperature	100(2) K	Absorption coefficient	4.801 mm^{-1}
Wavelength	0.71073 Å	F(000)	776
Crystal system	Triclinic	Crystal size	0.426 x 0.349 x 0.185 mm^3
Space group	P^{-1}	Theta range for data collection	1.928 to 36.404°.
Unit cell dimensions	a = 11.9184(9) Å α = 68.702(3)° b = 12.1854(9) Å β = 64.622(3)° c = 13.4699(10) Å γ = 62.360(3)°	Index ranges	-19≤h≤19, -20≤k≤20, -22≤l≤22
Volume	1532.4(2) $Å^3$	Reflections collected	52264

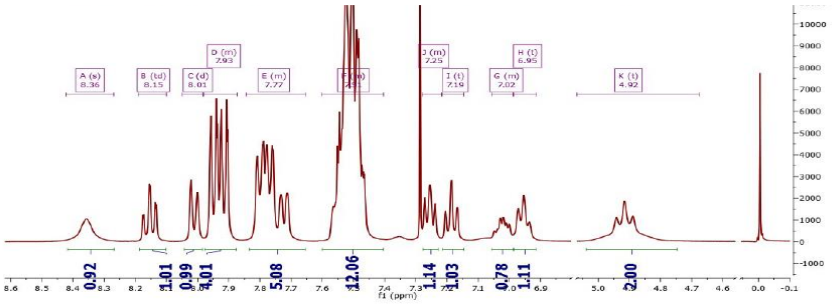

Figure. 16 ^{1}H NMR spectrum of BMPP-Pt

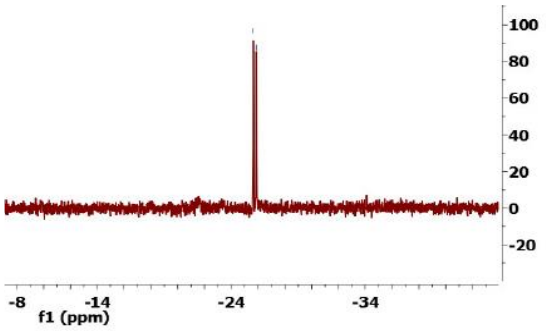

Figure. 17 ^{31}P NMR spectrum of BMPP-Pt

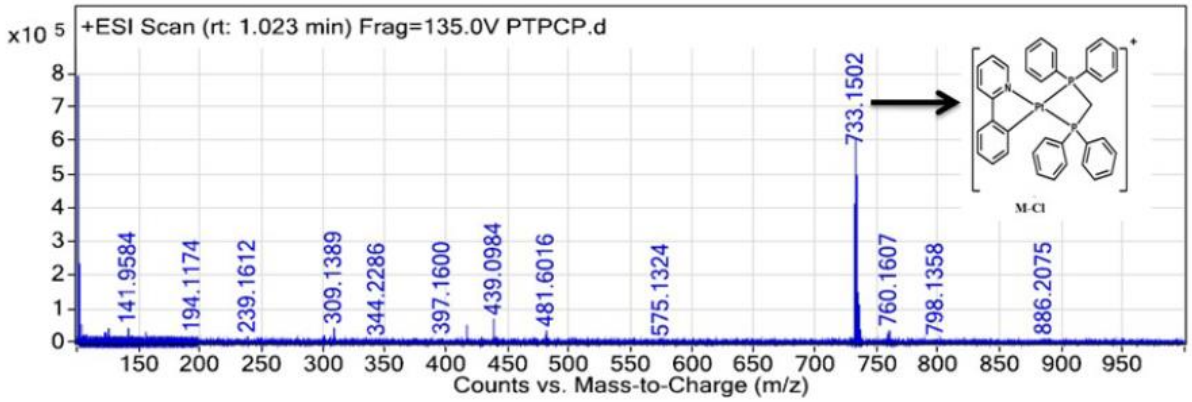

Figure. 18 Mass spectrum of BMPP-Pt

Synthesis of BMPP-Pt-MSNPs(Scheme 2): 0.150 g (0.00027mM) of CTAB was dissolved in 75ml of milli Q water. Then, sodium hydroxide (2M in milli Q water, 0.5 ml) and BMPP-Pt in THF (0.030 g, 0.000039mM) was introduced to the CTAB solution drop wise sequentially. The mixture was stirred at room temperature for five hours and then the temperature of it was adjusted to 80°C. Tetraethoxysilane (TEOS, 1 mL) was added drop wise to the reaction mixture containing surfactant with vigorous stirring. The mixture was allowed to react for 12h which produced a white precipitate. This solid crude product was filtered off, washed with de-ionised water and UV grade methanol for several times and dried it in vacuum drying oven at 35°C for 2h and obtained a pure product, BMPP-Pt-MSNPs.

Synthesis of BMPP-Pt-MSNP-GOPS(Scheme 2): A suspension of 0.3g of BMPP-Pt-MSNPs (mesoporous silica nanoparticles) in toluene (25 ml) was mixed with 0.4 ml of 3-glycidoxypropyltrimethoxysilane (GOPS) and the mixture was refluxed at 70°C for 24h, washed it with toluene and methanol for several times followed by drying at 60°C.

Synthesis of BMPP-Pt-MSNP-GOPS-EpCAM (Scheme 2): The mixture of 1.5mg of BMPP-Pt-MSNP-GOPS, 20µl of EPCAM aptamer (1M) and 250µl of KOH (1M) was dissolved in 1ml of milliQ water was incubated for 1h. Then, the reaction mixture was washed with phosphate buffer resulting BMPP-Pt-MSNP-GOPS-EpCAM.

Preparation of solutions of BMPP-Pt to prove AIE activity: 10^{-5}M stock solution of BMPP-Pt was prepared in DCM. Four 5 ml glass tubes were taken and labelled them as 0%, 30%, 50%,

60%, 70%, 80% and 90%. 0.5 ml stock solution was added to each of the labelled tubes. Then, the hexane with the following amounts, 0ml, 1.5ml, 2.5ml, 3.0ml, 3.5ml, 4ml and 4.5ml were added to 0%, 30%, 50%, 60%, 70%, 80% and 90%, labelled tubes, respectively so that the total volume of each glass tube turned into the same total volume (5 ml).

3C.5.References

[1] T. H. Kim, S. Lee and X. Chen, *Expert review of molecular diagnostics*, 2013, **13**, 257.

[2] L. K. Griffeth, *Proc (Bayl Univ Med Cent)*, 2005, **18**, 321.

[3] U. Resch-Genger, M. Grabolle, S. Cavaliere-Jaricot, R. Nitschke and T. Nann, *Nature methods*, 2008, **5**, 763.

[4] P. Zrazhevskiy, M. Sena and X. Gao, *Chemical Society Reviews*, 2010, **39**, 4326.

[5] J. Li and J.-J. Zhu, *Analyst*, 2013, **138**, 2506.

[6] L. O. Cinteza, *Journal of Nanophotonics*, 2010, **4**, 042503-042536.

[7] J. V. Jokerst, T. Lobovkina, R. N. Zare and S. S. Gambhir, *Nanomedicine*, 2011, **6**, 715.

[8] W. Z. Yuan, P. Lu, S. Chen, J. W. Lam, Z. Wang, Y. Liu, H. S. Kwok, Y. Ma and B. Z. Tang, *Adv Mater*, 2010, **22**, 2159.

[9] J. Luo, Z. Xie, J. W. Lam, L. Cheng, H. Chen, C. Qiu, H. S. Kwok, X. Zhan, Y. Liu and D. Zhu, *Chemical communications*, 2001, 1740.

[10] Y. Hong, J. W. Lam and B. Z. Tang, *Chemical communications*, 2009, 4332.

[11] A. Babu, N. Amreddy and R. Ramesh, *Ther Deliv*, 2015, **6**, 115.

[12]S. P. Egusquiaguirre, M. Igartua, R. M. Hernández and J. L. Pedraz, *Clinical and Translational Oncology*, 2012, **14**, 83.

[13] C. Argyo, V. Weiss, C. Bräuchle and T. Bein, *Chemistry of materials*, 2013, **26**, 435.

[14] R. Chowdhury, S. Chowdhury, P. Roychoudhury, C. Mandal and K. Chaudhuri, *Apoptosis*, 2009, **14**, 108.

[15] W. Zhang, W. Liu, P. Li, F. Huang, H. Wang and B. Tang, *Analytical chemistry*, 2015, **87**, 9825.

[16] Y. Yuan, S. Xu, X. Cheng, X. Cai and B. Liu, *Angewandte Chemie International Edition*, 2016, **55**, 6457.

[17] F. Tang, L. Li and D. Chen, *Adv. Mater.*, 2012, **24**, 1504.

[18] (a) R. Sun, W. Wang, Y. Wen and X. Zhang, *Nanomaterials*, 2015, **5**, 2019-2053; (b) Dr. Rajdeep choudhury, Assistant professor, Department of biology, BITS Pilani, Pilani campus, India.

[19] M. Fisichella, H. Dabboue, S. Bhattacharyya, G. Lelong, M. L. Saboungi, F. Warmont, P. Midoux, C. Pichon, M. Guerin, T. Hevor and J. P. Salvetat, *J Nanosci Nanotechnol*, 2010, **10**, 2314.

[20] J. Wang, Z. Teng, Y. Tian, T. Fang, J. Ma, J. Sun, F. Zhu, J. Wu, X. Wang, N. Yang, X. Zhou, S. Yun and G. Lu, *J Biomed Nanotechnol*, 2013, **9**, 1882.

[21]Slowing, II, J. L. Vivero-Escoto, C. W. Wu and V. S. Lin, *Adv Drug Deliv Rev*, 2008, **60**, 1278.

[22] F.-Y. Liu, Y.-H. Wu, S.-J. Zhou, Y.-L. Deng, Z. Y. Zhang, E.-L. Zhang and Z.-Y. Huang, *Oncology reports*, 2014, **32**, 835.

[23] L. Kelland, *Nature reviews. Cancer*, 2007, **7**, 573.

[24] J. M. Wagner and L. M. Karnitz, *Molecular pharmacology*, 2009, **76**, 208.

[25] A. F. Moreira, D. R. Dias and I. J. Correia, *Microporous and Mesoporous Materials*, 2016, **236**, 141.

[26] B. Terris, C. Cavard and C. Perret, *Journal of hepatology*, 2010, **52**, 280.

[27] O. Kimura, Y. Kondo, T. Kogure, E. Kakazu, M. Ninomiya, T. Iwata, T. Morosawa and T. Shimosegawa, *BioMed research international*, 2014, **2014**.

[28] Y. Li, R. W. Farmer, Y. Yang and R. C. Martin, *BMC cancer*, 2016, **16**, 228.

[29] M. Das, W. Duan and S. K. Sahoo, *Nanomedicine: Nanotechnology, Biology and Medicine*, 2015, **11**, 379

[30] X. Xie, F. Li, H. Zhang, Y. Lu, S. Lian, H. Lin, Y. Gao and L. Jia, *European Journal of Pharmaceutical Sciences*, 2016, **83**, 28

[31] E. DR, A. Poloukhtine, V. Popik, A. Tsourkas, *Nanomedicine*, 2013, **9**, 194

[32] S. S. Pasha, P. Alam, S. Dash, G. Kaur, D. Banerjee, R. Chowdhury, N. Rath, A. Roy Choudhury and I. R. Laskar, *RSC Adv.*, 2014, **4**, 50549.

Chapter IV

Synthesis of New 'Aggregation Induced Emission' Active Platinum(II) Complexes and Dry Approach to Encapsulate these into Mesoporous Silica

1. Introduction

In the past few decades, there has been an enormous interest on platinum(II) based phosphorescent complexes due to their rich spectroscopic and luminescence properties such as high luminescence quantum yields, long emission lifetimes, large Stoke shifts, excellent emission properties, easy colour tunability and high photo-stability as compared to the traditional fluorescent dyes[1-4].These intriguing properties made the platinum(II) complexes extensively useful to explore for many real life applications such as chemo-sensors, non-linear optical (NLO) materials, photo catalysts, optical power limiting materials (OPL) and organic light emitting devices (OLEDs) etc [5-9]. However, the square planar structure of cyclometalated Pt(II) complexes often form excimer (or exciplex) because of Pt─Pt or π–π interactions upon excitation [10-14].These interactions would generate a new metal–metal-to-ligand charge transfer (MMLCT) excited state which results the broad and red shifted emission in comparison to monomeric emission[15]. The Pt─Pt and π–π interactions are found to very sensitive to external stimuli and hence drew attention in promising applications *e.g.*, optical recording, memory sensing and display devices[16-21].

In the last several years, it is observed that the development of AIE luminophores which are mainly limited with organic luminophores, but the AIE active metal complexes, specially with Pt(II) complexes have not been explored adequately [22-26]. The luminescent Pt(II) complexes has an astounding records in the field of bio-imaging. Unfortunately, the background fluorescence scattered light and water solubility of such complexes posed a great obstacle into these applications. The development of biocompatible mesoporous silica encapsulated AIE material could be a better alternative to tackle such problems [27]. Impregnation of luminescent materials into the mesoporous silica has received an immense interest to the scientists because these result a high thermal and photo stabilities, bio-compatibility, large accessible pore sizes and periodic nano-scale pore spacing. In general, the methodologies adopted to incorporate the luminescent materials into the silica pores were mainly of wet based techniques [28-31]. The design, syntheses and investigation of mechanistic pathways of AIE Pt(II) complexes are an immense and exigent task for organometallic-chemists[24-26].

In this current chapter, we have synthesized the ligands (L2-L5) by linking a bulky rotating unit into one of the coordinating sites of 2-aminopyridine, ethane-1,2-diamine, 1,3-propane diamine and 1,6-hexane diamine (Scheme 1). Then we have synthesized four AIE active monocyclometalated Pt(II) complexes (**2-5**) by reacting of the intermediate complex, **1** (synthetic procedure is discussed in chapter 3) with L2-L5 (Scheme 1.The complexes, **3-5** have been successfully incorporated into the pores of mesoporous silica in a simple dry technique with a concomitant sharp change of emission color. Additionally, the investigation of mechanoluminescence properties of **3-5** has been carried out.

2. Results and discussion

2. 1 Syntheses and characterization

Scheme1. Synthetic routes of compounds, L2- L5 and 1-5.

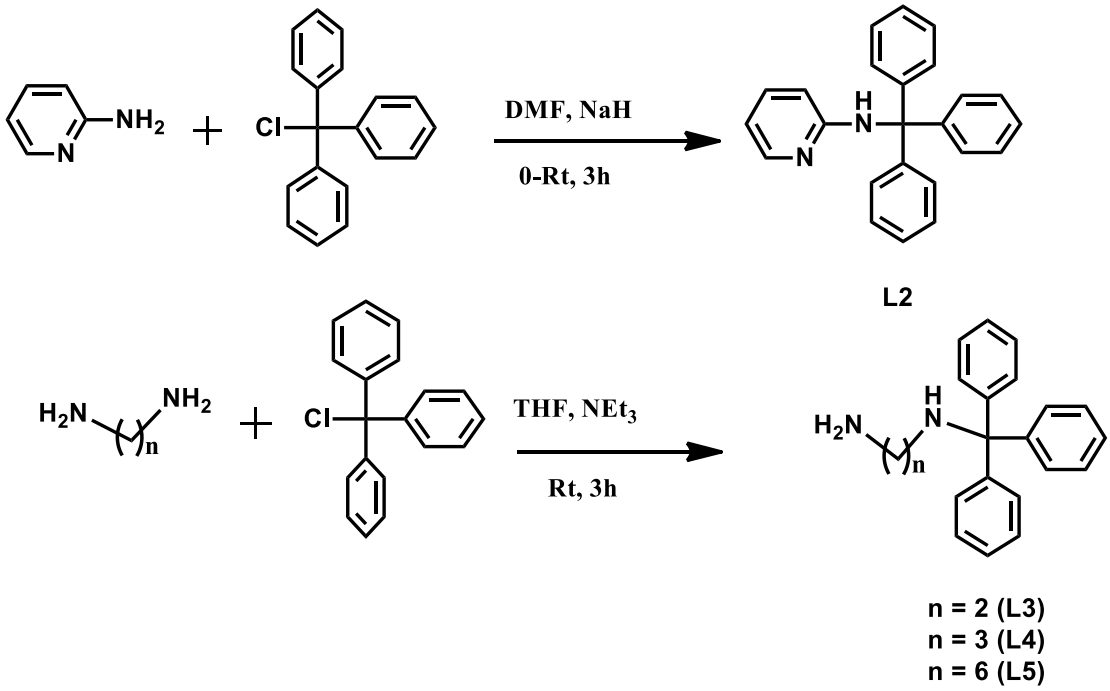

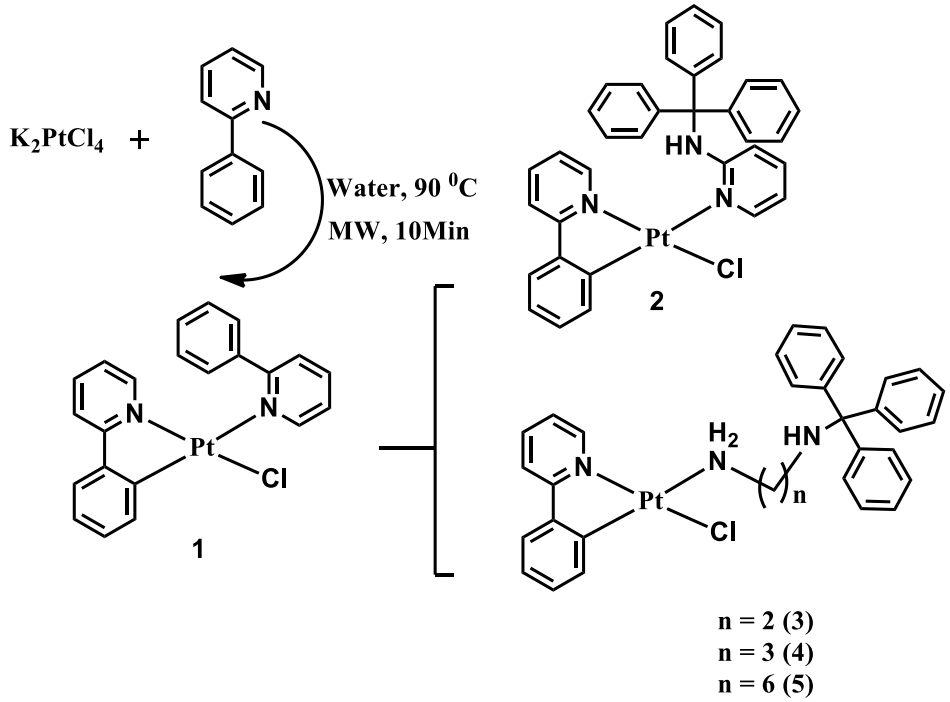

Complexes **2-5** were synthesized in a one-pot reaction by the reaction of**1**with**L2**, **L3**,**L4** and **L5**, respectively (**Scheme 1**). All the ligands(**L2-L5**) and complexes (**1-5**) were fully characterized by ^{1}H,^{13}C NMR and some of the compounds are also characterized by HRMS. The ^{1}H NMR spectrum of **L2** showed all the aromatic proton signals at δ = 7.08-8.78 ppm. The ^{13}C NMR spectrum of **L2** displayed one up field resonance signal at 70.48ppm which was assigned for sp^3 carbon of trityl group; rest of all the aromatic carbon peaks of **L2** appeared in between δ110-159ppm.The ^{1}H NMR spectrum of **L3** showed the two triplets in between 1.63-2.84ppm which were assigned two aliphatic $–CH_2$ protons and all the aromatic protons were appeared in the range of 7.19-7.53ppm. Similarly, **L4** and **L5** exhibited all the aromatic peaks in the range of 7.19-7.51ppm and 7.18-7.51ppm, respectively and all the aliphatic proton peaks in the range of 1.61- 2.82ppm and1.23-2.72ppm,respectively. The ^{13}C NMR spectrum of **L3, L4** and **L5** displayed trityl aliphatic carbon peak at 70.95, 70.92 and 70.85ppm, respectively.

The structure characterization of **1** was discussed in chapter **3B**. The ^{1}H NMR spectrum of **2** showed all the aromatic protons in the range of 5.5-9.8ppm. The ^{13}C NMR spectrum of **2** showed all the aromatic carbons in the range of 111.65-167.21ppm and trityl aliphatic carbon peak at 71.26ppm. The ^{1}H NMR spectrum of **3** showed two aliphatic ^{1}H signals at δ = 4.51 ppm (as triplet) and δ = 3.16 ppm (as broad singlet). The ^{13}C NMR spectrum of **3** displayed three up

field resonance signals at 70.98, 48.68 and 44.47 ppm which were assigned for sp^3 carbon of trityl group and two for ethylenediamine carbons, respectively. From HRMS data, the major fragmented peak appeared as $[M-Cl]^+$ at m/z 651.2009 and 2[M+H] at m/z 1376.3616 attributed to the dimeric species. Similarly, the ^1H NMR spectrum of **4** and **5** shows all the aromatic proton signals in the range of 6.99-9.51ppm and aliphatic protons in the range of 1.91-3.36ppm.

2. 2 Photo physical properties of complexes 1-5

The absorption spectrum of **2** was recorded in dichloromethane which shows three distinct absorption bands *i.e.*, 249-310nm, 312-357nm and broad peak from 358-412nm. Based on the nature of the spectrum and their similarity to the earlier reports, [10-15] the spectral bands were tentatively assigned to $^1\pi$-π^*, ^{1}MLCT and ^{3}MLCT transitions, respectively (Figure 1). After optimizing ground state, it is observed that HOMO of **2** is mainly located on Pt(II) metal ion and phenyl ring of phenyl pyridine and LUMO majorly located on pyridyl ring of phenyl pyridine(Figure 1). The experimentally obtained band gap(3 eV) of **2** is well matched with the theoretical one (3.4 eV).

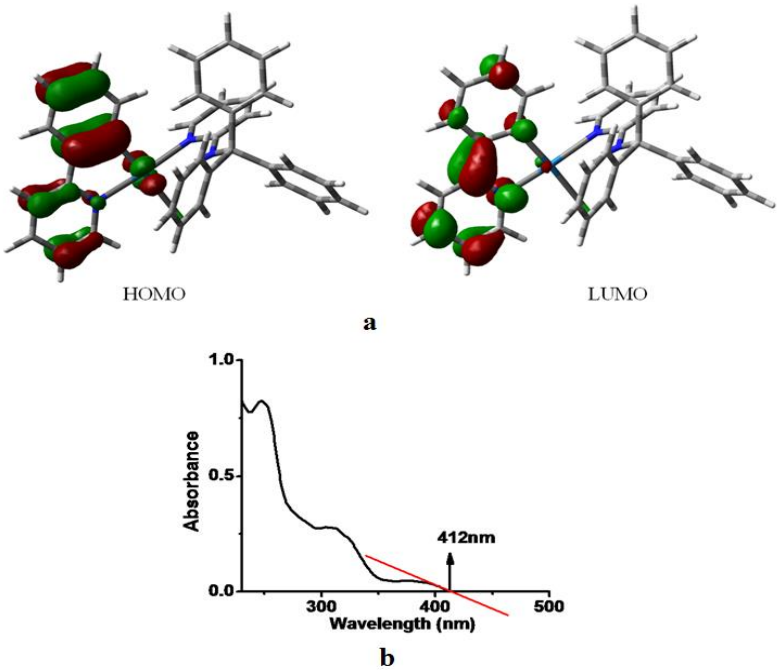

Figure.1 a) DFT based ground state optimized HOMO and LUMO orbitals of **2**; b) Absorption spectrum of **2** in DCM solution (c. $1x10^{-5}$ M)

The UV-Vis electronic absorption spectrum of **3** was recorded in dichloromethane which exhibited three distinct absorption bands *i.e.*, 300-350nm, 352-420nm and 425-465nm. Based on the nature of the spectrum and their similarity to the earlier reports [10-15], the spectral bands were tentatively assigned to $^{1}\pi$-π^*, ^{1}MLCT and ^{3}MLCT transitions, respectively(Figure 2a).

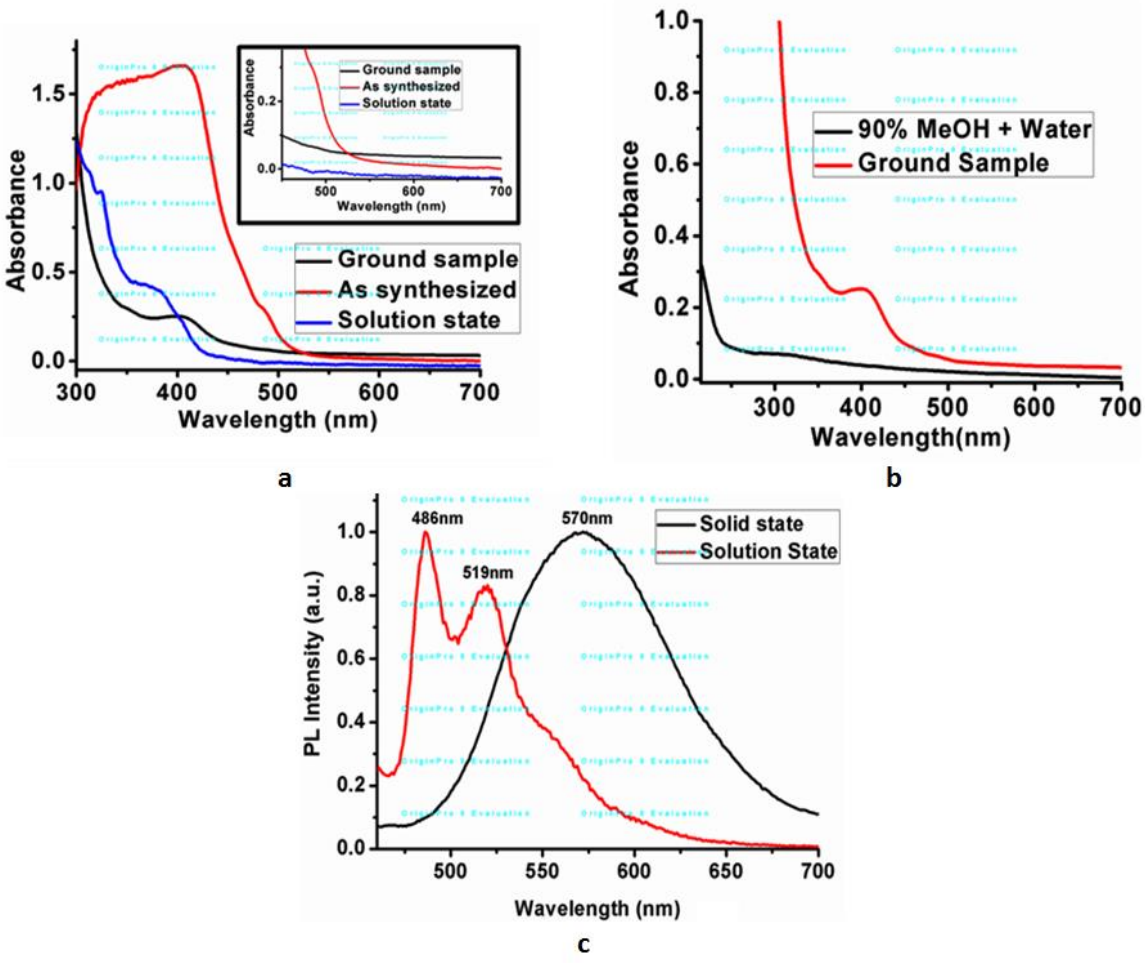

Figure. 2(a) Absorption spectrums of **3** in various states; (b) Emission spectrums of **3** in various states(for solution state absorption and emission 10^{-5} M DCM solution was used).

These transitions were, further supported by time-dependent density functional theory (TD-DFT) where the transition energy to the low-lying singlet states (S_0-S_1 and S_0-S_2) were calculated to 384 nm (oscillator strength, f = 0.0150) and 353 nm (f = 0.0056), respectively and the lowest triplet states at 462 (S_0-T_1) and 390 nm (S_0-T_2), respectively (Table 1). These two transitions, S_0-S_1 and S_0-S_2 were mainly comprised of HOMO → LUMO (94.0%) and (HOMO

– 2) → LUMO (97.0%) transitions, respectively (Table 1). The electron distribution in S_0-S_1 and S_0-S_2 transitions, which is shown in Figure3C, imply that there are significant MLCT character [for LUMO, there is almost nil electron density found on Pt(II) for isovalue plot of 0.03 electrons/Bohr^3 in comparison to the corresponding HOMO and HOMO – 2] (Table 1). The calculated %MLCT was found to be ~56, ~74 and ~32 for S_0-S_1 and S_0-S_2 and S_0-T_1 transitions, respectively. But the vibronic features observed at the experimentally obtained solution emission spectrum of **3** clearly indicating the presence of π- π* character into the low-lying excited state (Figure. 3b). Hence, the low-lying excited state should be a mixed character of π-π* with MLCT.

Table 1:Vertical excitation energies calculated for the lowest lying singlet and triplet states for **3**.

State	ΔE	Oscillator strength (f)	Assignments
T_1	2.69 eV (462 nm)	0	HOMO-3→LUMO (7%) HOMO-3→LUMO+1 (3%) HOMO-1→LUMO(6%) HOMO→LUMO (74%)
T_2	3.18 eV (390 nm)	0	HOMO-3→LUMO+1(5%) HOMO-1→LUMO(71%) HOMO→LUMO(14%)
S_1	3.23 eV (384 nm)	0.0150	HOMO-1→LUMO(2%) HOMO→LUMO(94%)
S_2	3.51 eV (353 nm)	0.0056	HOMO-2→LUMO(97%)

Table 2: Major contribution of metal and ligand atomic orbitals (AO)into FMO and their corresponding energy values for **3**.

State	FMOs	Major Orbital Contribution	Energy (eV)
Ground state	HOMO	36% d(Pt), 41% p (phenyl pyridine)	−5.82
	HOMO-1	53% d(Pt), 26% p (phenyl pyridine)	−6.15
	HOMO-2	75% d(Pt), 19% s (Pt)	−6.20
	LUMO	54% p (phenyl pyridine)	−1.80
	LUMO+1	57% p (phenyl pyridine)	−1.15

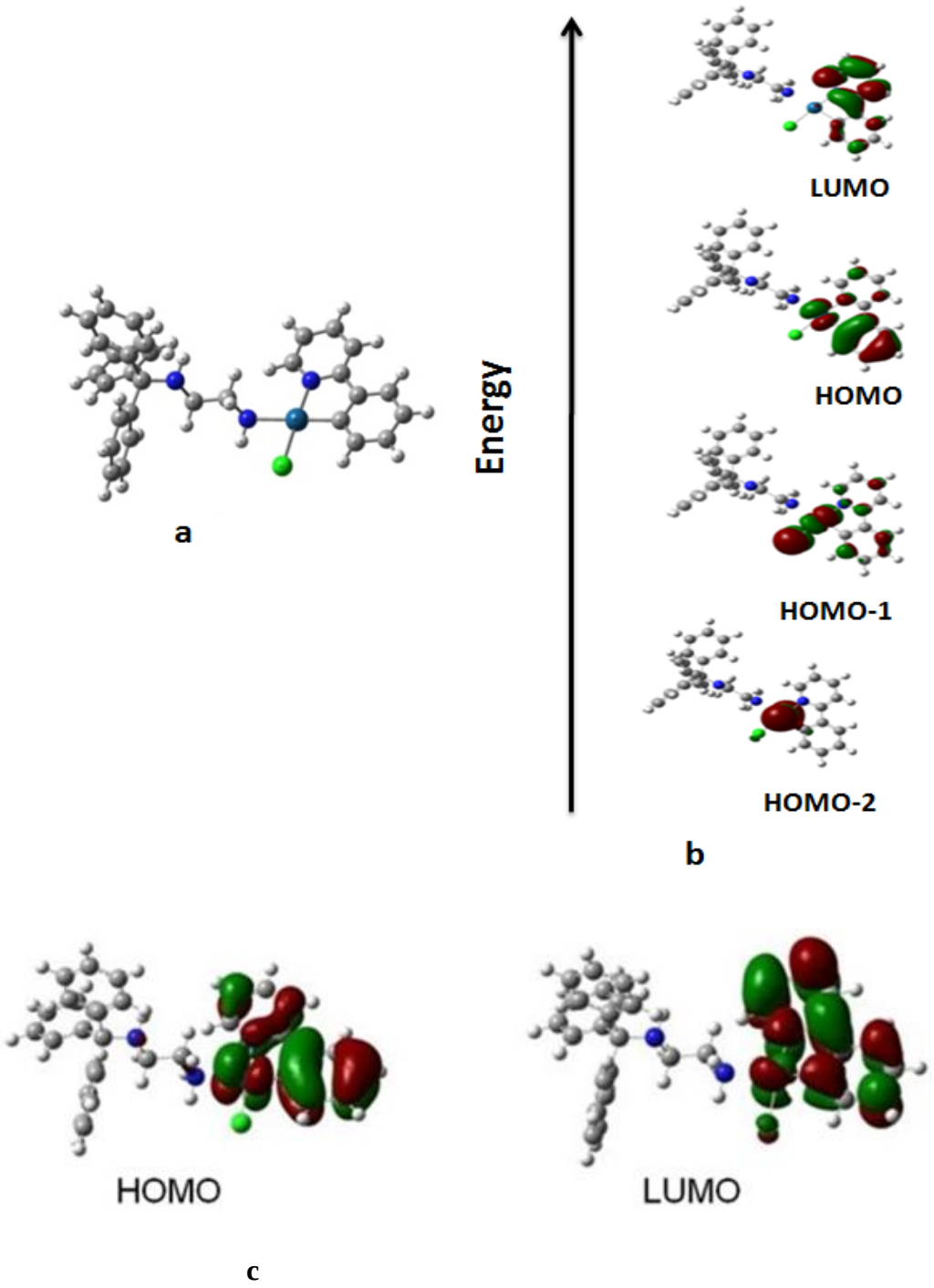

Figure. 3(a) Optimized structure of the complex at B3LYP/6-31G(d, p)Ú LanL2DZ level; (b) TD-DFT based transition energy calculations and the electron distribution in the following

orbitals (HOMO, LUMO, HOMO –1 and HOMO – 2); (c) DFT based ground state optimized HOMO and LUMO orbitals of **3**.

The solid state UV-Vis absorption spectrum of crystalline sample **3** displayed a long range relatively broader and stronger absorption band ranging, 300-450nm as compared to the solution phase absorption band. With following this stronger band, a low energy band, 470-510nm was again followed by a long tail which was extended up to 600nm (Figure2a). The low energy band at λ_{max} = 487nm was observed in solid state only and, predictably not found in solution absorbance spectrum, the nature of this band would be assigned to metal-metal-to-ligand charge transfer (^{3}MMLCT) transitions (Figure2a). Basically, the ^{3}MMLCT state was generated from Pt(II) eximer [10-15]. In the study of emission spectrum, the low energy vibronic structure (1313 cm^{-1}) with λ_{max} at 486 and 519 nm (in DCM) and a broad relatively low energy emission spectrum with λ_{max} at 570 nm (in solid state) may be assigned to $^3\pi$-π^* transitions mixed with ^{3}MLCT and ^{3}MMLCT transitions, respectively (Figure 2c). The time resolved photoluminescence measurements (Figure4a-e) was carried out of complex **3**, the life time was found to decrease linearly with increasing concentration (at c=$1x10^{-4}$– $5x10^{-4}$ M, λ_{em} = 570nm;t = 116ns → 94ns) which was indicative of the presence of Pt(II)–Pt(II) interactions. The FMO analysis of **3** exhibited dπ-pπ type of mixing in the lowest lying HOMO which was mainly confined on the Pt(II) and phenyl part of phenylpyridine (Figure 3b & Table 2).However, the LUMO was mainly consisted of the π* orbital of the ligand phenylpyridine. Here, it is worth mentioning that the triphenyl ligand and the spacer part (ethylene diamine) do not provide any contribution to the HOMO-LUMO orbital.

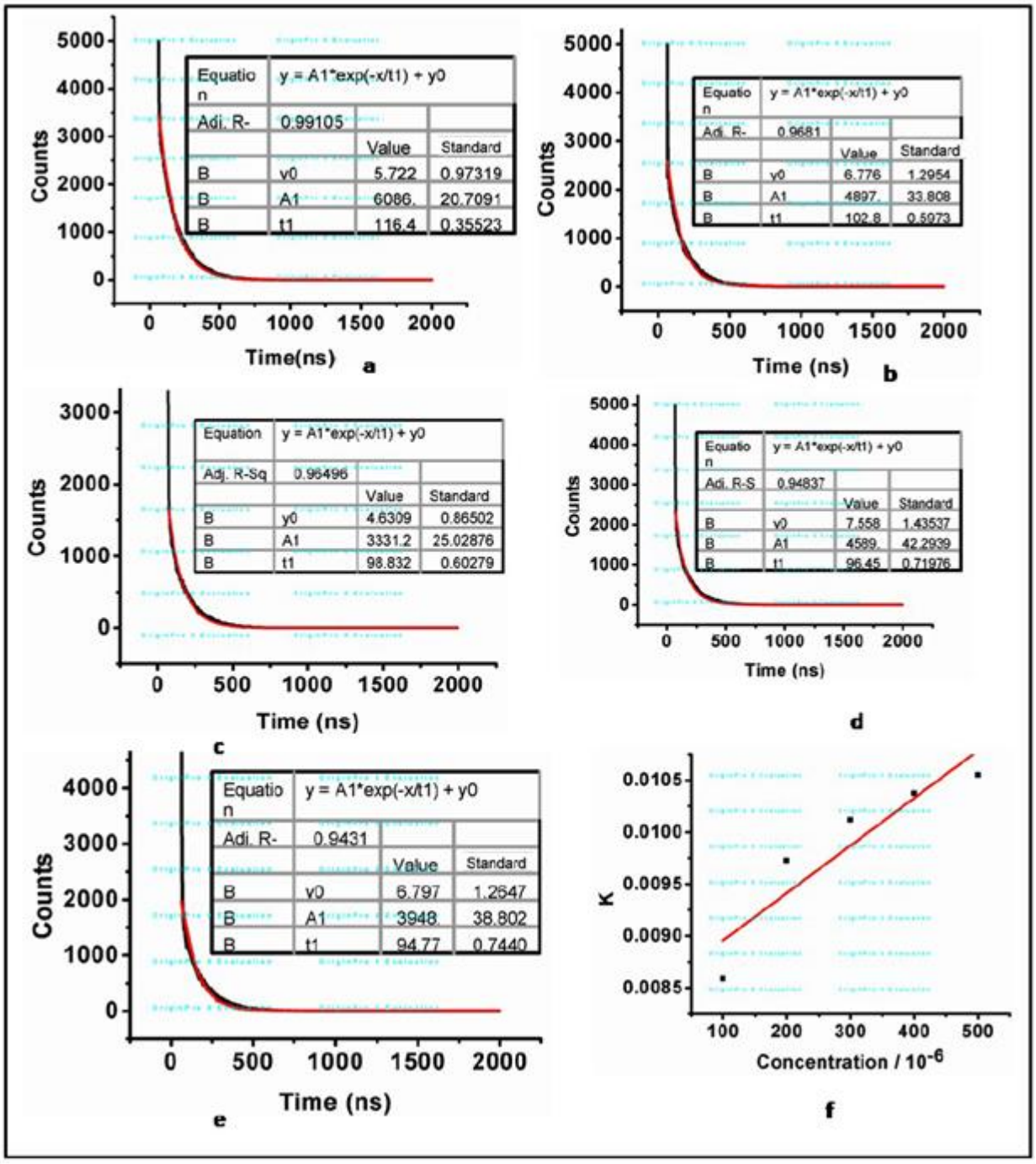

Figure. 4 (a), (b), (c),(d) & (e)show lifetime decay curve of **3** in the range of concentration, $1x10^{-4} - 5x10^{-4}$M [Life time, for a = 116.6ns (c, 1 x 10^{-4}M); for b = 102.8ns (c, 2 x 10^{-4}M);for c = 98.8ns (c, 3 x 10^{-4}M); for d = 96.4ns (c, 4 x 10^{-4}M); for e = 94.7ns (c, 5 x 10^{-4}M)]. (f) It shows plot of the measured luminescence decay constants (K), (Y-axis) versus concentration (X-axis) of **3**.

The pictorial representation of FMO for **4** and **5** are given in Figure 5. HOMO is mainly located in both complexes on phenyl ring, platinum(II) and chloride ion, LUMO is mainly located on pyridine ring.

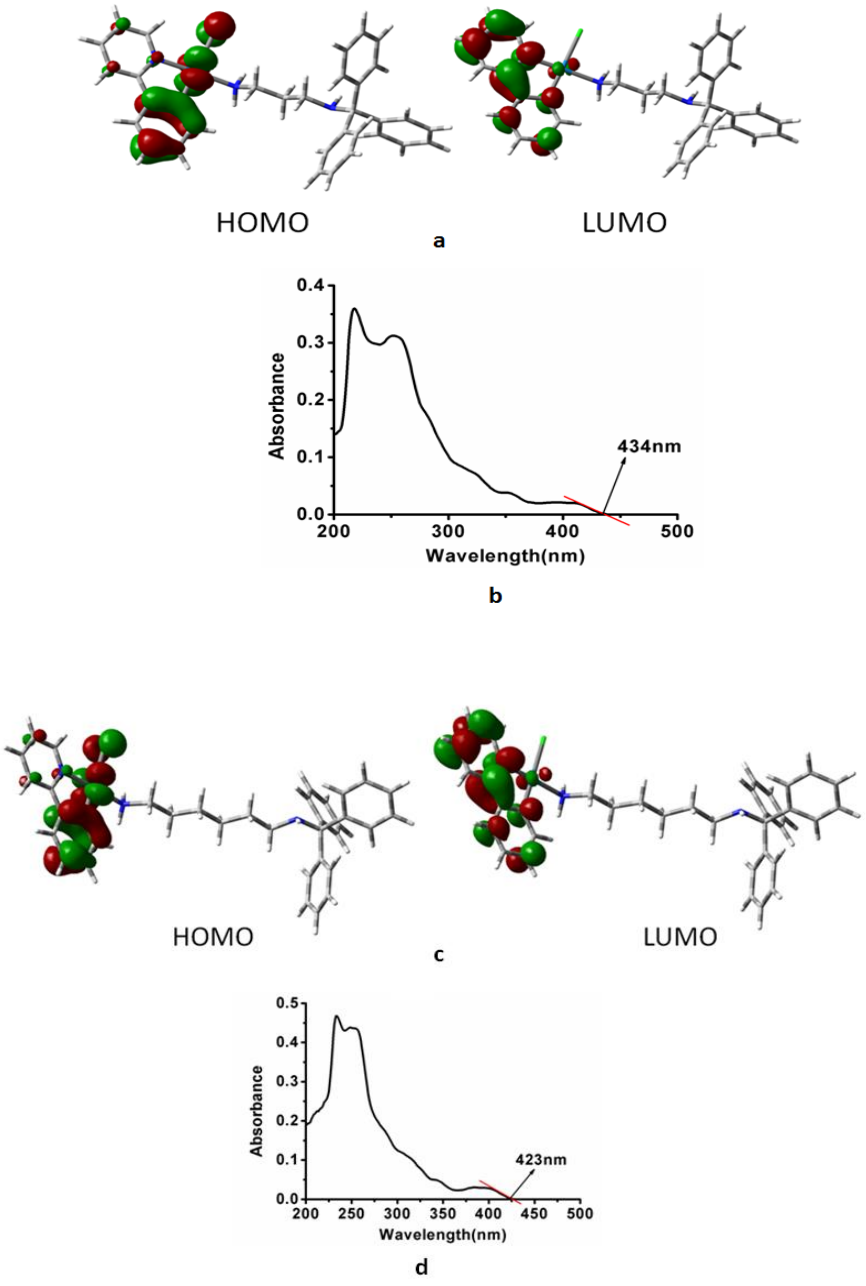

Figure. 5 (a) DFT based ground state optimized HOMO and LUMO orbitals of **4**; (b) Absorption spectrum of **4** in DCM solution (c. $1x10^{-5}$ M)(c) DFT based ground state optimized HOMO and LUMO orbitals of **5**; (d) Absorption spectrum of **5** in DCM solution (c. $1x10^{-5}$ M).

2. 3 Aggregation Induced Emission(AIE)

The complexes **1**-**5** are soluble in common organic solvents such as, dichloromethane (DCM), tetrahydrofuran (THF), dimethyl formamide (DMF), 1,4 dioxane, methanol, acetonitrile etc, but are insoluble in water as well as in hexanes. These complexes show very weak emission in all these solvents but they are intensely emissive in the solid state. These observations hint that all five complexes are expected to show AIE behavior. In order to investigate this AIE property, water was used as poor solvent for complex **1**, acetonitrile for **2** and methanol for complexes **3**, **4** and **5**.

For the case of **1**,different amounts of water fractions (f_w = 0-90%) were added to the pure THF solution of **1** with keeping the same concentration of each solution to 1x 10^{-5} M. The emission intensity increased gradually with increasing f_w resulting in a cloudy solution indicating the formation of aggregates. The maximum emission intensity was observed with f_w= 90% which was 12.5 times higher than the intensity of its solution in pure THF (Figure 6).

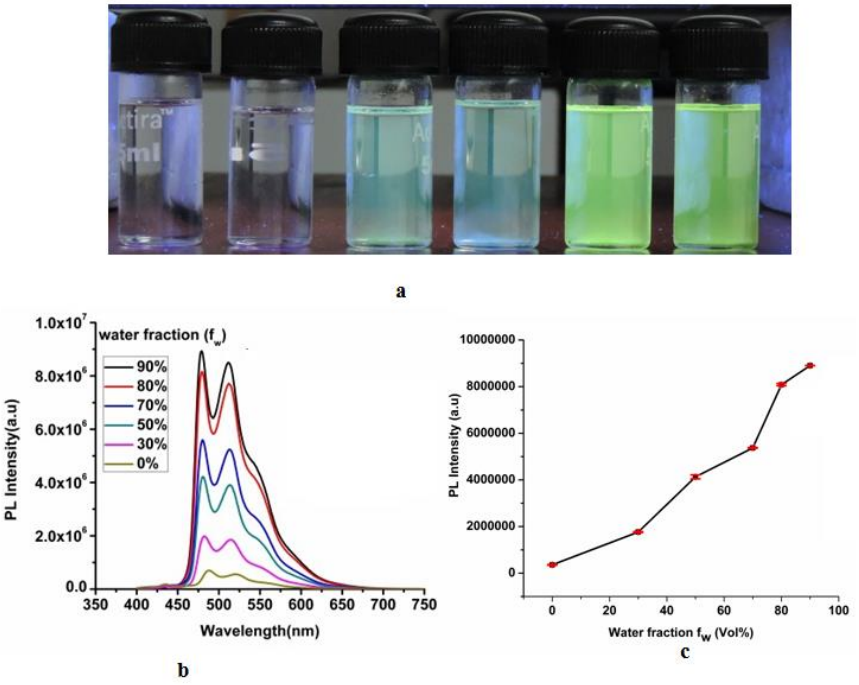

Figure.6 (a) Luminescent images of **1** (λ_{ex}, 365 nm) in water−THF mixed solvents (c, 2 × 10^{-5} M);(b) PL spectra of **1**in THF/water mixed solvents with different f_w (λ_{ex}, 385 nm); (c) the variation of PL peak intensity with f_w (λ_{max} = 487 nm).

To understand the origin of the AIE property, the crystal-packing of **1** was examined (Figure 7). The crystal data of **1** was reported by P. C. Ford *et. al* [31]. The crystal structure of complex **1** shows short contacts, which are mainly C-H.....π type of interactions and falls in the range of 2.64- 2.85 Å (Figure 7). This length is shorter than the summation of the vander Waals radius of C and H. These interactions may be responsible to restrict the rotation of the phenyl rings present in these molecules in their solid states and hence the complex exhibits AIE activity.

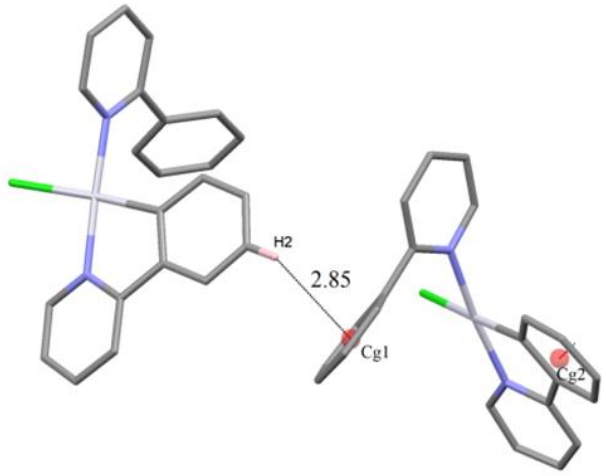

Figure. 7 Crystal packing diagram of complex **1** showing C-H....π type short contacts, H2-Cg1 = 2.85 Å and H8-Cg2 2.64 Å.

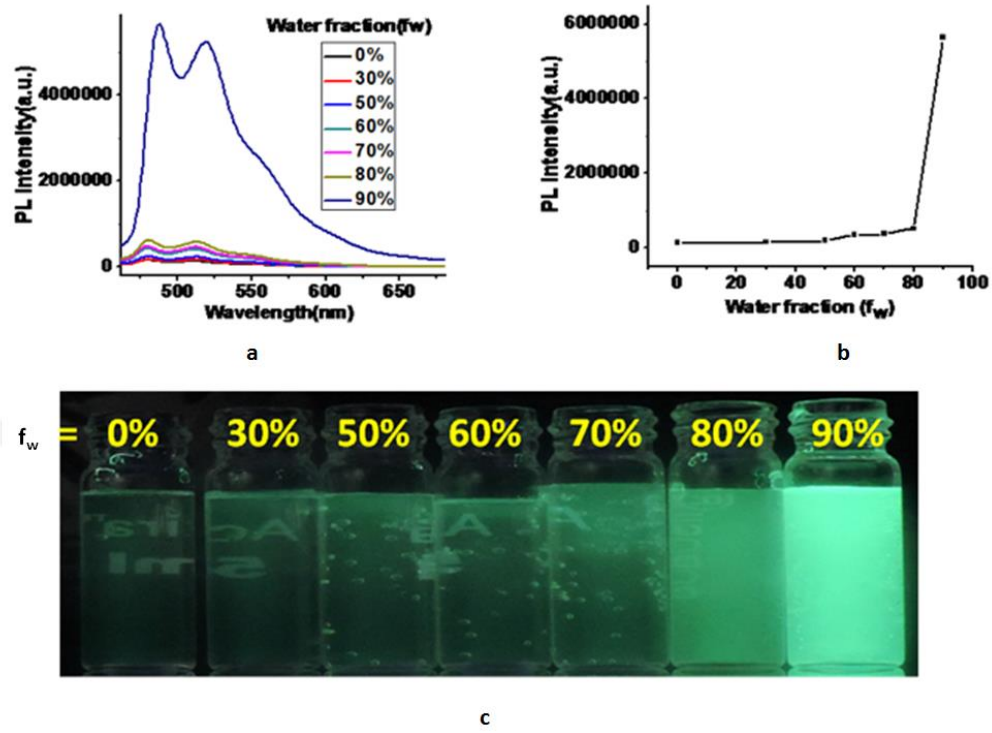

Figure. **8** (a) PL spectra of **2** in ACN/water mixed solvents with different f_w with excitation at 385 nm; (b) the variation of PL peak intensity with f_w; (c) luminescent images of **2** (λ_{ex}, 385 nm) in ACN/Water mixed solvents (c, 2×10^{-5} M).

For the case of complex **2**, different amounts of water fractions (f_w = 0-90%) were added to the pure ACN solution of **2** with keeping the same concentration of each solution to $1x\ 10^{-5}$ M. The emission intensity increased gradually with increasing f_w resulting in a cloudy solution indicating the formation of aggregates(Figure 8).

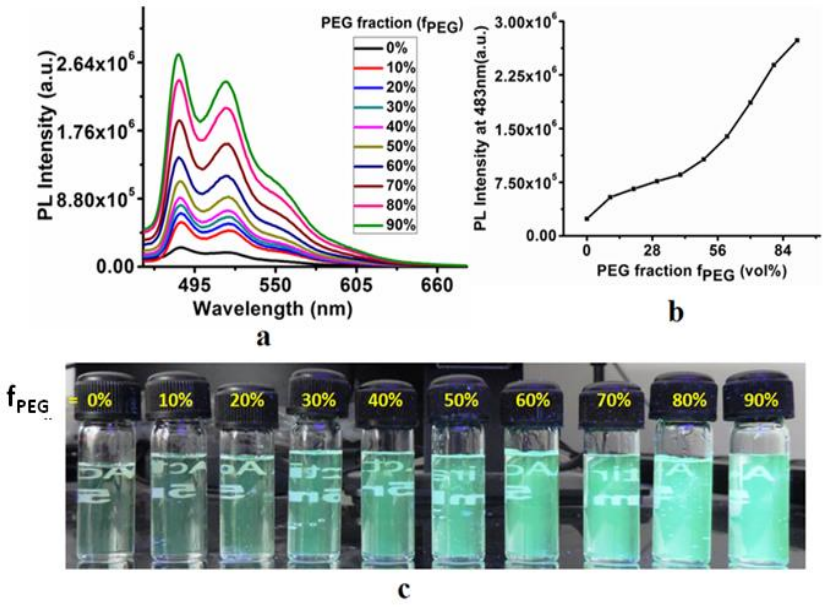

Figure. **9**(a) PL spectra of **2** in PEG/ACN mixed solvents with different f_{PEG} with excitation at 385 nm; (b) the changes of PL peak intensity with different f_{PEG}; (c) luminescent images of **2** (λ_{ex}, 385 nm) in PEG/ACN mixed solvents with the concentration kept at 2×10^{-5} M respectively.

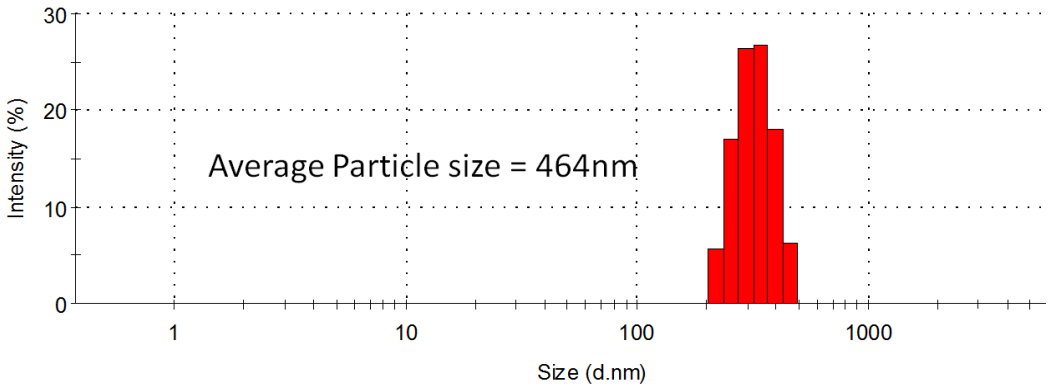

Figure.10 Average particle size distribution of complex **2**

A set of solutions of complex **2** of different solvent mixture of ACN and polyethylene glycol (PEG, viscous solvent) is prepared in the range of 0-90%. The enhancement of emission intensity was observed with gradual increasing concentration of PEG(Figure 9). This experiment hints that the mechanism of AIE activity of **2** is probably operated through restricted intra

molecular rotation (RIR). However, the obtained average particle sizes from DLS confirmed the formation of aggregates at f_w= 90% (sizes ~464 nm) (Figure 10).

To investigate the AIE property, the emission spectrum of**3** was recorded in different MeOH-H_2O fractions (0-90%). The emission spectrum of **3** in MeOH exhibited a green emission with λ_{max} at 485 and 518 nm which was not showing any appealing enhancement in photo luminescent (PL) intensity while gradually increasing with addition of water fractions (f_w) up to the range of 10-60%. A sudden 39.4 times enhancement of PL intensity was observed at f_w=70% with red shifted emission (λ_{max} = 600nm). The maximum PL intensity was achieved at f_w= 90% which was observed 62.1 times higher than its methanolic solution (Figure 11). However, the sizes obtained from FESEM confirmed the formation of aggregates at f_w= 70% and f_w= 90% with the size range of 114-150 nm and 85-104 nm, respectively (Figure 12). The suspended particles from f_w= 90% was centrifuged, filtered and dried.

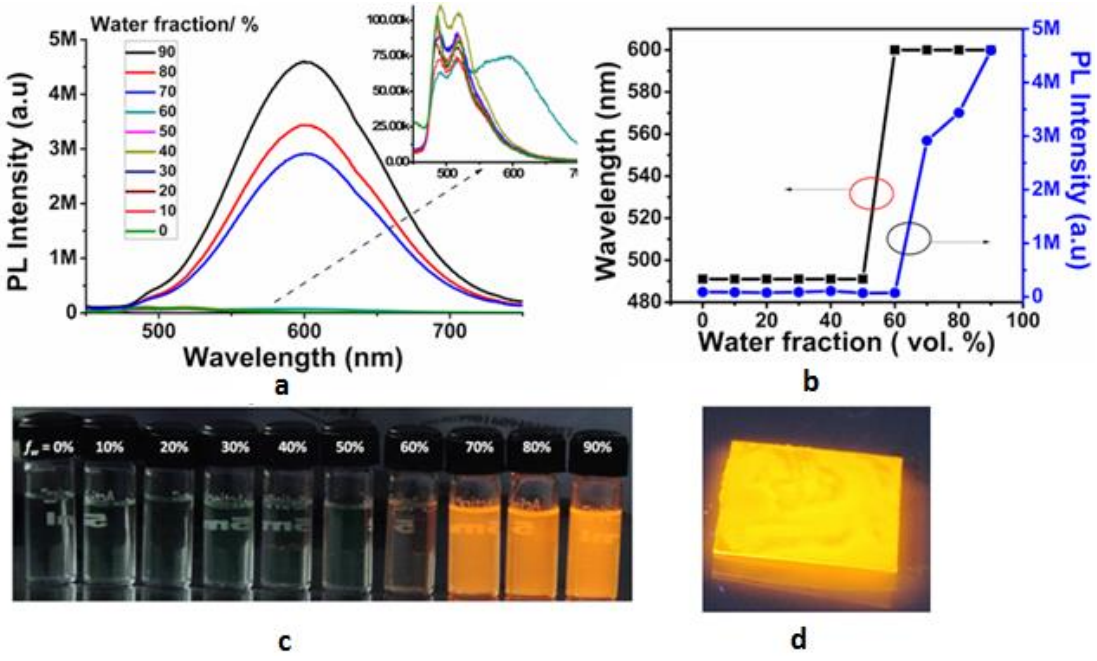

Figure. 11 (a) Emission spectra of **3** in a MeOH / water mixture (0-90%); (b) Plot of maximum emission intensity (I) and wavelength of **3** versus water fraction; (c of **3** $1x10^{-5}$ M); (c) Photographs of **3** in MeOH/water mixtures taken under UV illumination; (d) Image of solid thin film of **3** under UV light at λ_{ex} 365 nm.

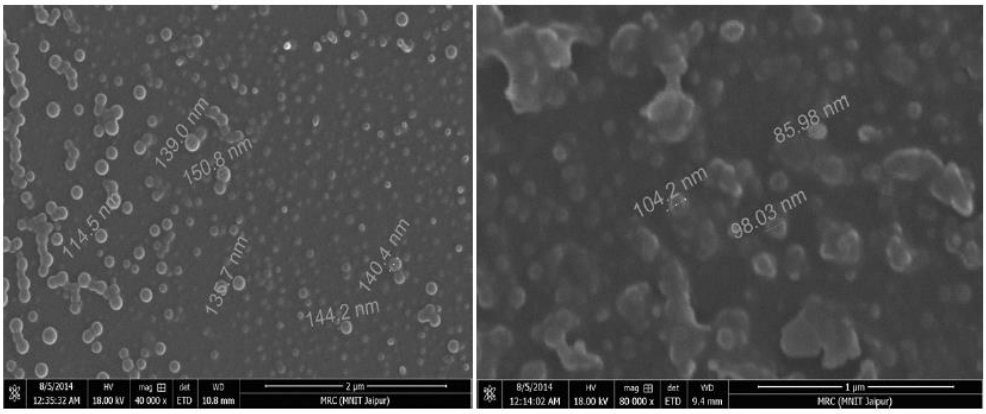

a b

Figure. 12 FESEM images of (a)70% water in MeOH/water and (b) 90% water in MeOH/water mixtures of **3**.

The PL spectra of **3** were found to be non emissive in common organic solvents because of active rotation of propeller-shaped trityl group in the solution state. The PL spectrum of **3** was recorded in different polyethylene glycol (PEG)-MeOH mixtures (Figure. 13). The PL intensity was found to increase with increasing PEG fraction (f_{PEG}). A maximum PL intensity was achieved at f_{PEG} = 90% which was 12 times higher than its pure methanolic solution. The PL enhancement with increasing concentration of PEG revealed that the RIR which may block the nonradiative channels and opened up the radiative channels. The absolute quantum yield of the solution of**3**in DCM was measured to 12.35% and 0.4% in solid and solution states, respectively which supported the strong emissive property in the solid state.

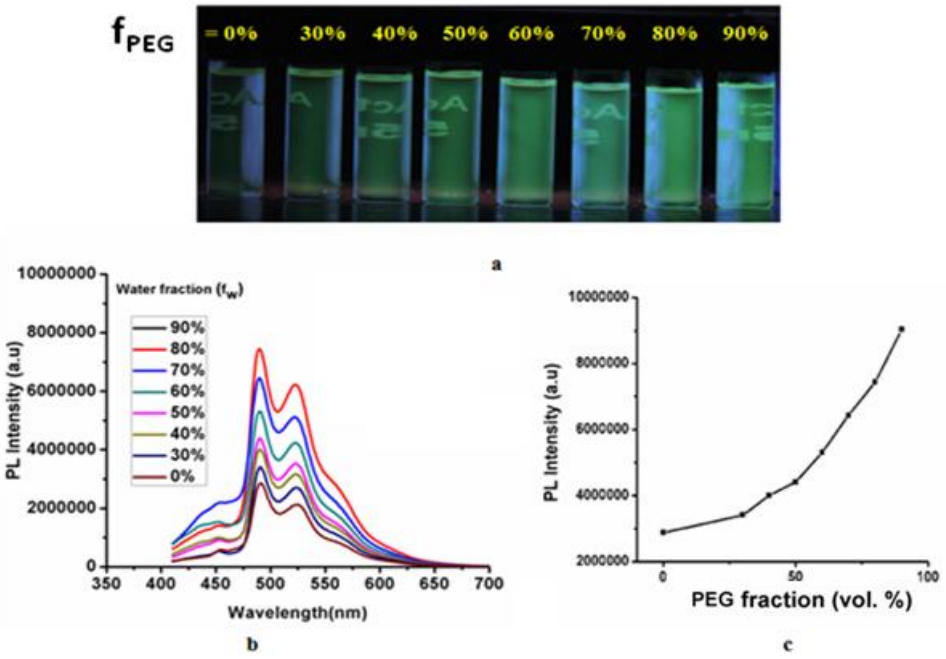

Figure. 13(a) Luminescent images of **3**(irradiated with an ultraviolet light at 365 nm) in PEG−Methanol mixed solvents with the concentration kept at 1×10^{-5} M; (b) PL spectra of **3** in methanol/Poly(ethylene glycol) (PEG) mixed solvents with different fraction of water (f_{PEG}) with excitation at 365 nm; (c) the changes of PL peak intensity (λ_{max}= 486nm) with different f_{PEG}.

Similarly to investigate the AIE property, the emission spectra of **4** and **5** were recorded in different MeOH-H_2O fractions (0-90%). The emission spectra of **4** and **5** in MeOH exhibited a green emission with λ_{max} at 485 and 518 nm, respectively which were not showing any appealing enhancement in photo luminescent (PL) intensity while gradually increasing addition of water fractions (f_w), up to the range of 0-80%. A sudden enhancement of PL intensity was observed at f_w = 90% with red shifted emission (λ_{max} = 600nm). The maximum PL intensity was achieved at f_w = 90% in both the cases(Figure 14 and 15).

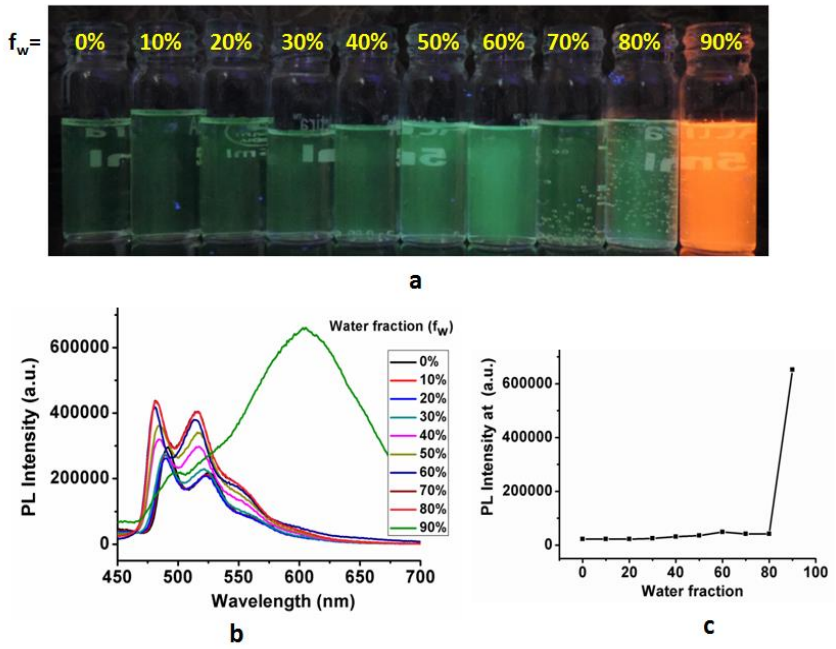

Figure. **14** (a) Photographs of **4** in MeOH/water mixtures taken under UV illumination; (b) Emission spectra of **4** in a MeOH / water mixture (0-90%); (c) Plot of maximum emission intensity (I) versus water fraction (c, $1x10^{-5}$ M).

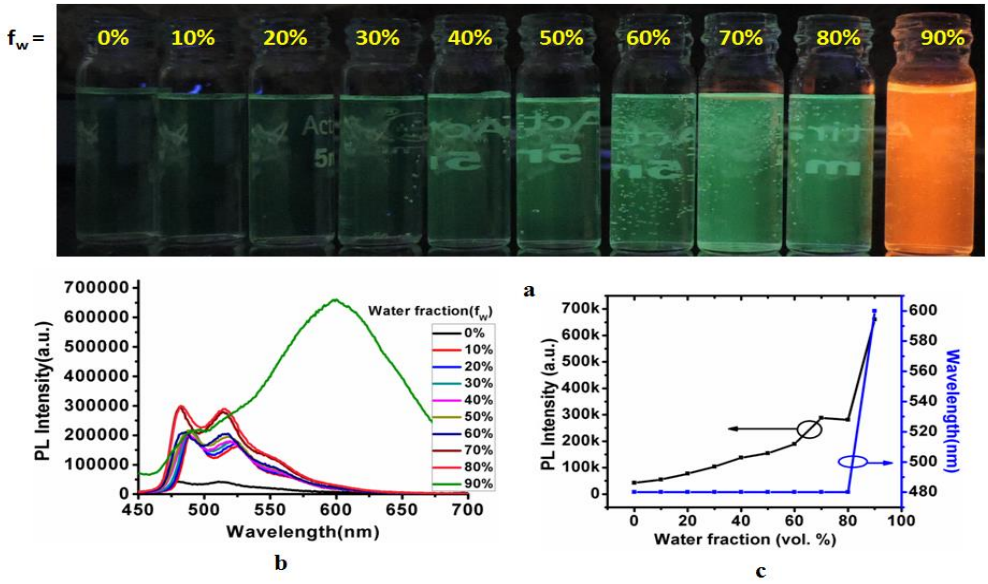

Figure. **15** (a) Photographs of **5** in MeOH/water mixtures taken under UV illumination; (b) Emission spectra of **5** in a MeOH/water mixture (0-90%) with gradually increasing concentration of methanol in the mixture; (c) Plot of maximum emission intensity (I) and wavelength (λ_{max}) of **5** versus water fraction (c, $1x10^{-5}$ M).

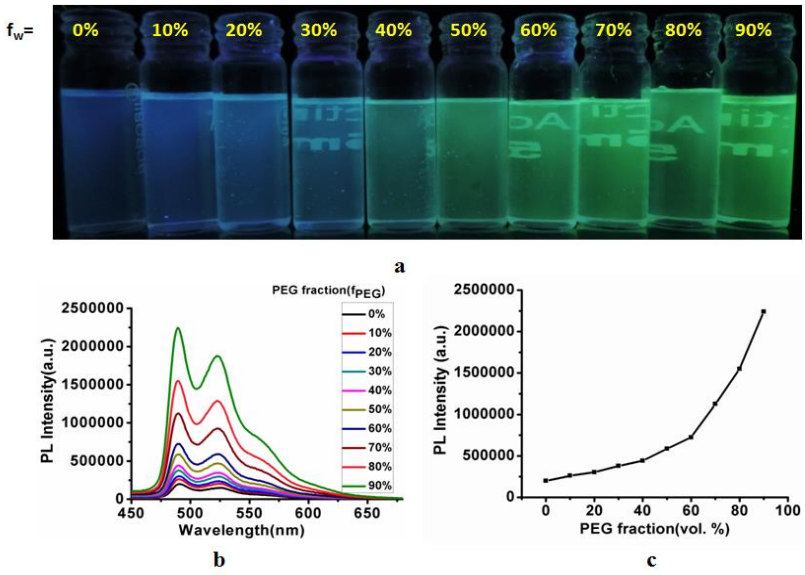

Figure.16 (a) Luminescent images of **4** (λ_{ex}, 365 nm) with increasing concentration of PEG in PEG–Methanol mixed solvents (c, 1×10^{-5} M); (b) PL spectra of **4** in methanol/Poly(ethylene glycol) (PEG) mixed solvents with different fraction of water (f_{PEG}) with excitation at 365 nm; (c) the changes of PL peak intensity with different f_{PEG}.

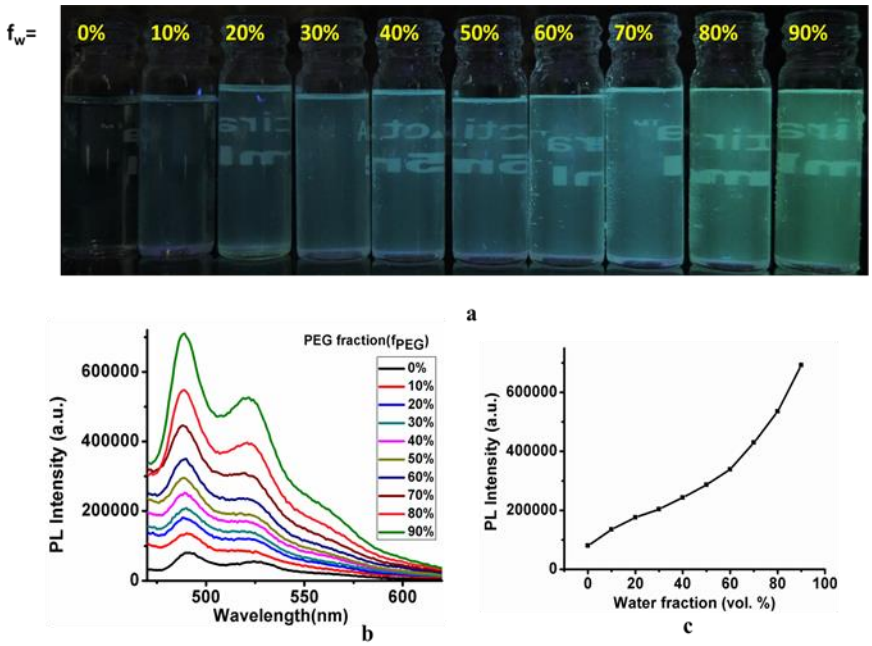

Figure.17 (a) Luminescent images of **5** (λ_{ex}, 365 nm) in PEG–Methanol mixed solvents (c, 1×10^{-5} M); (b) PL spectra of **5** in methanol/Poly(ethylene glycol) (PEG) mixed solvents with different fraction of PEG (f_{PEG}) with excitation at 365 nm; (c) the changes of PL peak intensity with different f_{PEG} (λ_{max} = 486nm).

To prove the mechanism of AIE of **4** and **5**, we have prepared a set of solutions of PEG and methanol combinations (0-90%). By increasing the percentage of viscous solvent PEG, the emission intensity of **4** and **5**is gradually increased. The increment of PL intensity is probably occurring due to the RIR effect (Figure 16 and 17). It is to be noted that the emission coloris drastically changed for the cases of**3**, **4** and **5** from green to orange, while it remains intact for**1** and **2** with increasing concentration of water (f_w ~90%).Based on these observations and the time-resolved photoluminescence study (*vide infra*), it is proposed that the complexes, **3-5** exist in excimeric forms, while **1-2** remain in monomeric entity in the solid state. The relatively larger distance of the bulky substituents from the metal centre and flexibility of the ligands, L3-L5 able them to allow another Pt(II) complex molecule to approach the former one to form, Pt(II)-Pt(II) excimeric complexes. The bulky substituents present in the complexes,**1-2** are lying very closely to the Pt(II) centre and hence another Pt(II) molecule couldn't come closer to the other one, avoiding the formation of excimer.

2. 4.Mechanoluminescence property

A noticeable change in the emission behavior was observed when the complexes **3, 4** and **5**were ground in a mortar-pestle. In these cases, the yellow emissive complexes, **3, 4** and **5**

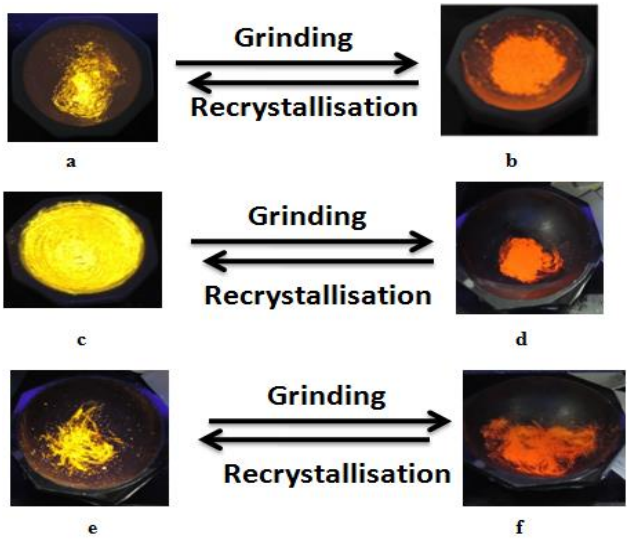

Figure.18 (a, c and e) Luminescent images of pristine complexes, **3, 4** and **5** respectively**;** (b, d and f) after grinding the complexes, **3, 4** and **5** respectively(photograph taken under 365 nm UV excitation).

(Emission maxima, λ_{max} = 570 nm) were turned into orange emissive complexes **3a, 4a** and **5a** (λ_{max} = 600 nm, 598 nm and 601nm respectively). These were reverted into the original complexes, **3, 4** and **5** after recrystallizing the ground compounds from DCM (Figure 18 and 19). The change of such emission behavior was attributed to mechanoluminescence (ML).

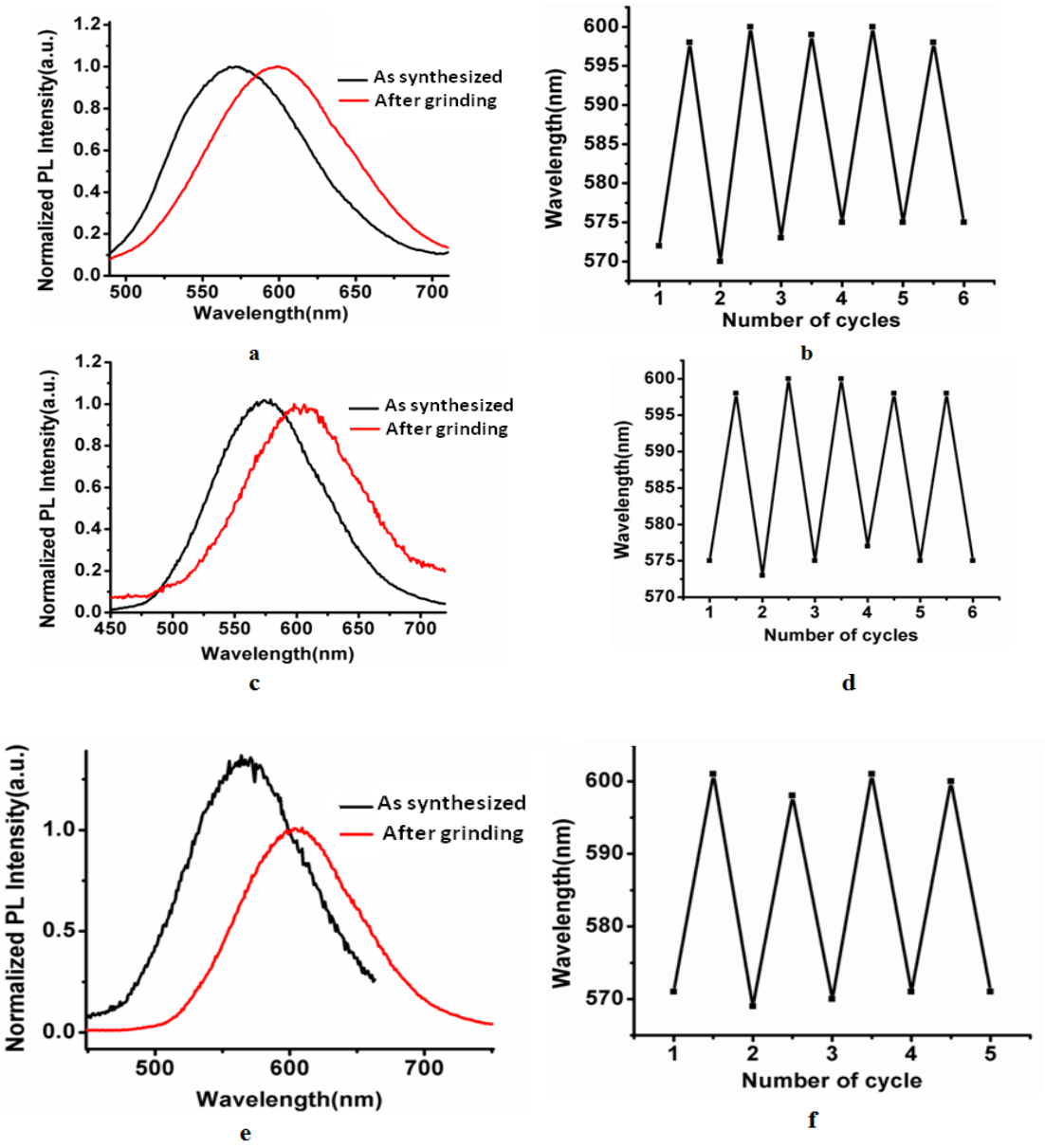

Figure. 19 (a, c and e)Emission spectra of as-synthesized and ground complexes, **3, 4** and **5** respectively**;** (b, d and f) Maximum emission wavelength change upon repeated grinding–recrystallisation cycles of as-synthesized and ground complexes **3, 4** and **5** respectively.

The mechanism of ML behavior of **3** was attempted to explore with the help of powder X-ray diffraction (PXRD) and differential scanning calorimetric (DSC) experiments (Figure 20 and 21).

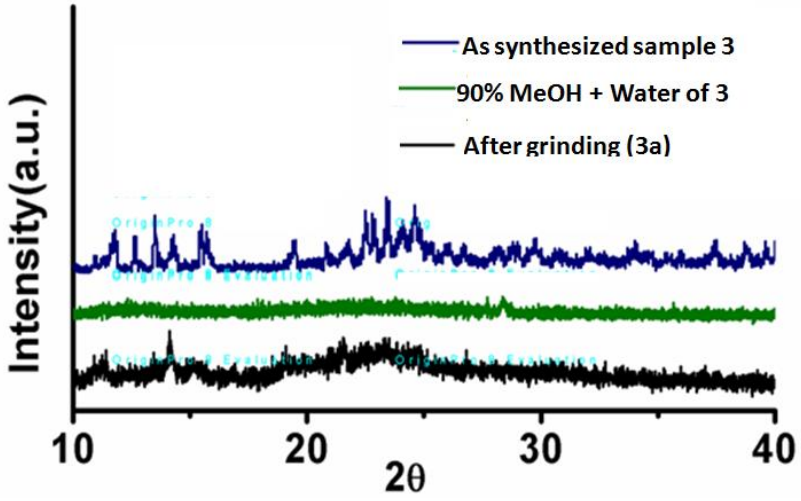

Figure. 20 Powder XRD of **3**in various states.

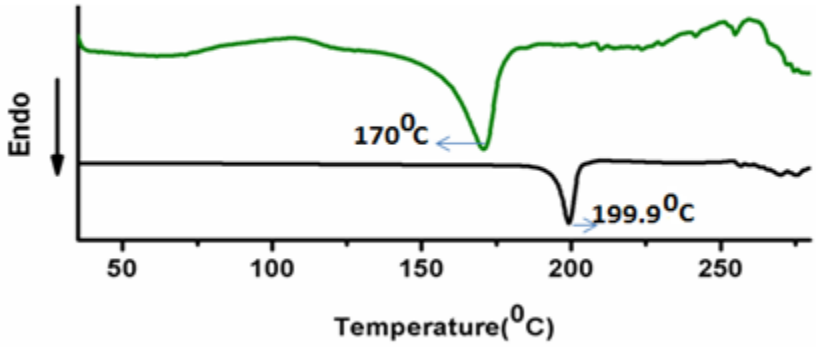

Figure. 21 DSC curve of **3** before grinding (black) and after grinding (green)

The recorded powder XRD curves showed sharp and intense peaks in case of **3** which revealed the crystalline packing mode of the complex. However, the powder XRD curves of the ground sample exhibited low-intensity peaks which were appeared as broad, indicating the amorphous nature. The powder XRD data revealed that the change in the emission property was truly attributed to the change from crystalline to amorphous phase transition (Figure 20). This

fact was further supported by DSC experiment which showed a clear endothermic melting peak in both cases (199.9 and 170.0°C) while a glass transition peak (t = 61°C) followed by a broad exothermic re-crystallization peak at *ca.* 100°C was observed in the case of ground sample (Figure 21). To understand the cause of ML in regard to molecular level, it is further looked into the differences of absorbance. A sharp difference in absorbance spectrum of orange-emitting complex, **3a** with the original yellow complex, **3** was observed (Figure 2). The complex, **3a** resulting a prominent absorbance peak at ~410nm, along with a lowering absorbance was observed as compared to the corresponding peak of **3** in solid phase absorbance (Abs. ~1.70 *vs* ~0.25). With the following prominent absorbance peak in **3a,** a level off tail was extended beyond 650nm, but the absorbance of **3** was drastically reduced at longer wavelength [425 (abs: 1.5) - 525 nm (abs: 0.1)] and then the absorbance value tends to nearly zero (Figure 2). Although, in contrast to **3,** there was no strong absorbance peak observed in the range of 470-510nm, a long and more red-shifted tail was observed and it was extended beyond 650nm. The observation of red-shifted absorbance and emission of **3a** (in comparison to **3**) would suggest ML behavior was resulted in a stronger Pt-Pt stacking interaction [13]. Hence, it would be speculated that the two Pt(II) in **3** were moved in on grinding. The complex, **3** was regenerated after recrystallisation of **3a** from DCM. The same difference in absorbance spectra have been observed for the cases of **4** and **5** with their corresponding ground states (**4a** and **5a**). The fact led us to conclude that the similar mechanism have been played behind the ML properties of **4** and **5**. Being the complexes **1** and **2** in monomeric forms, no change of emission color was observed upon grinding as per our expectation.

2. 5 Encapsulation into mesoporous silica pores

Interestingly, the yellow light emissive complexes **3, 4** and **5** were transformed into green emitting complexes after a mild crushing these with meso-structured silica (MS silica) (Figure 22).Several experiments were carried out to investigate the reason behind such unusual property.

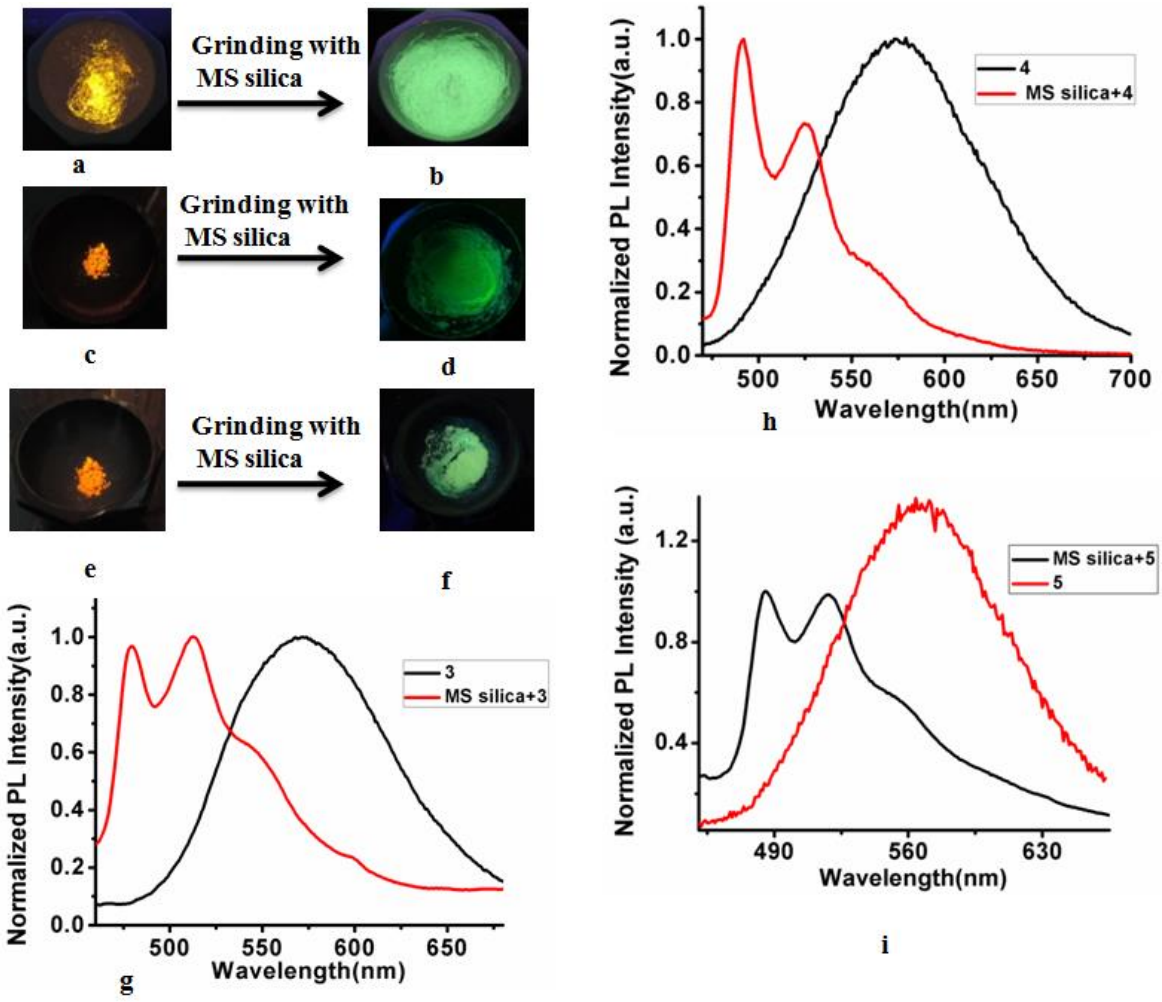

Figure. 22 (a, c and e) Luminescent images of pristine complexes, **3, 4** and **5** respectively**;** (b, d and f) after grinding the complexes (**3**, **4** and **5**respectively) with MS silica(photograph taken under 365 nm UV); (g, h and i) Emission spectra of **3, 4** and **5** as synthesized and after grinding with MS silica respectively**.**

Initially, the PL spectrum of **3**at a fixed concentration (10^{-4} M in DCM) was recorded in presence of sequentially added different amounts of MS silica (0, 20, 40, 60, 80, 100 and 120

mg). In this case, the PL intensity was gradually decreased with increasing amount of MS silica (Figure 23). This experiment was indicative of encapsulation of **3** into the MS silica pores.

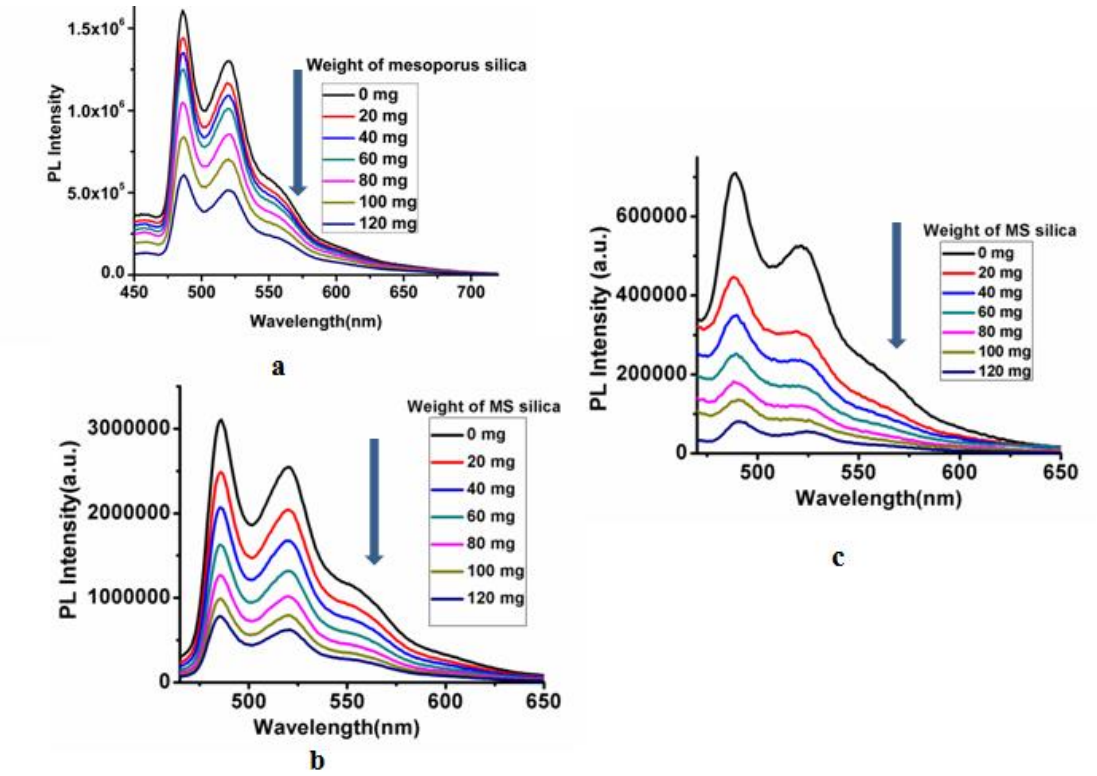

Figure. 23 a, b and c are PL spectra of **3, 4** and **5,** respectively with different amounts of MS silica in DCM (0 to 120mg) (λ_{ex} = 365 nm).

The green emitting MS silica (**3b** or **4b** or **5b**) were washed in a Soxhlet extraction apparatus for 48h which guaranteed the removal of any adherents present on the surface of MS silica. The washed MS silica displayed a bright green emission and the fact supporting the impregnation of **3** or **4** or **5** into the void pores of MS silica. There was not observed of any difference in powder XRD patterns (Figure 24) of the bare MS silica with the **3b** or **4b** or **5b,** which further supporting the encapsulation of the platinum(II) complexes **3**, **4** and **5** into the pores of MS silica.

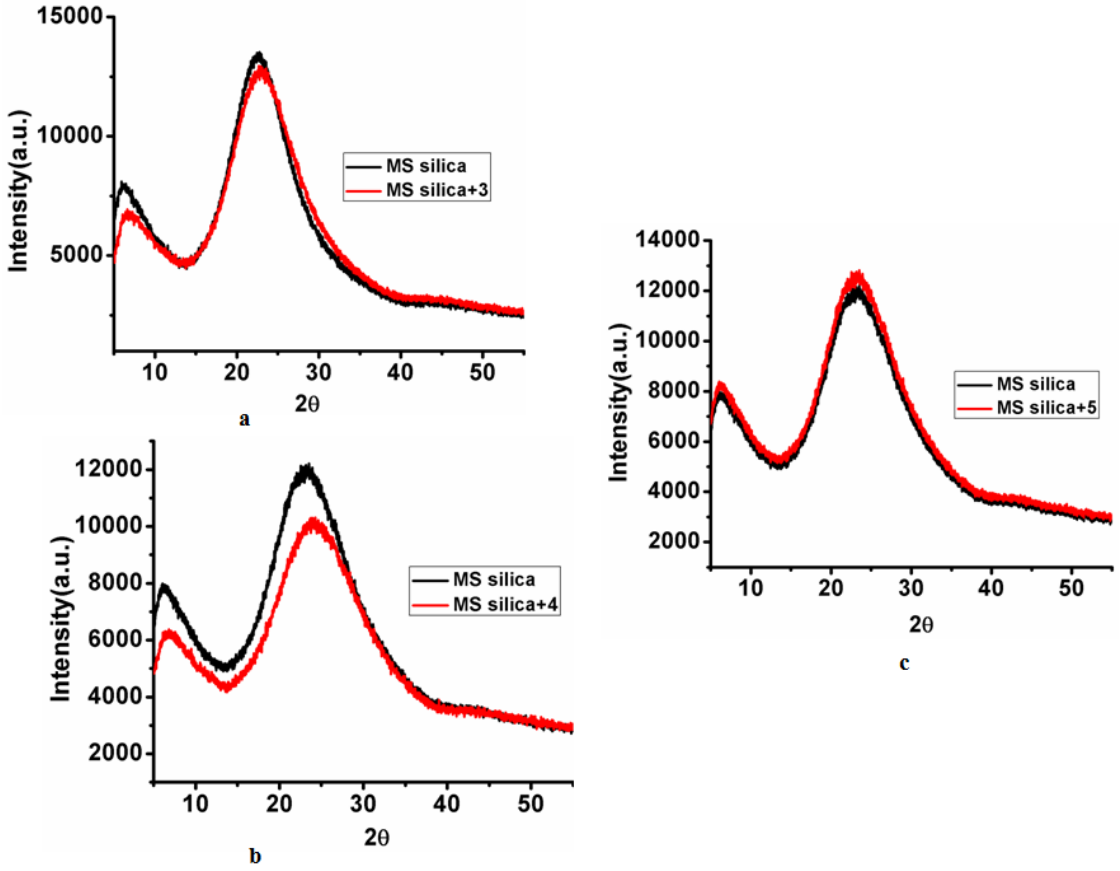

Figure. 24 a, b and c are powder XRD of bare MS silica (black) and **3b**, **4b**, **5b** (red) respectively.

The surface area of the encapsulated MS silica was measured by BET experiment and the comparative surface areas of bare MS silica, encapsulated **3, 4** and **5** were found to 750 and 387, 375 and 392m^2/g, respectively (Table. 3) which obviously proving the occupation of Pt(II) complexes **3**, **4** and **5** into the pores of MS silica.

Table 3: Textural data (measured by N_2 adsorption-desorption isotherms) of the porous materials estimated by BET experiment

	Surface Area (m^2/g)
Mesostructured silica	750
Complex **3** encapsulated mesostructured silica	387
Complex **4** encapsulated mesostructured silica	375
Complex **5** encapsulated mesostructured silica	392

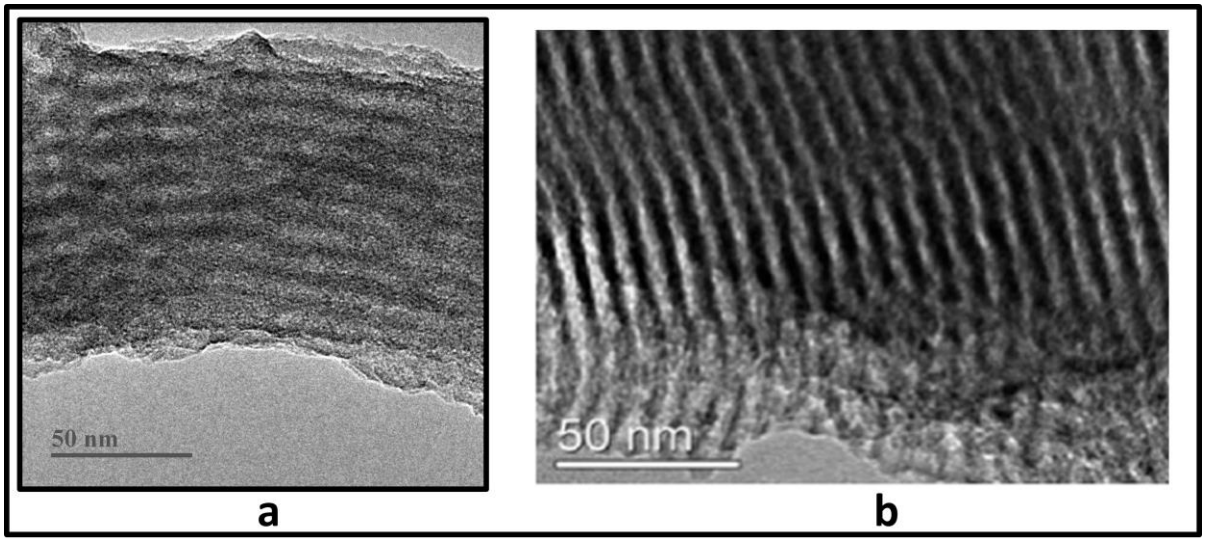

Figure. **25** HRTEM images of (a) **3** encapsulated MS silica (b) bare MS silica

HRTEM image was recorded in case of **3b**. The recorded HRTEM image of **3b** showed the faded lattice fringes in comparison to the bare MS silica (Figure 25) which was further indicative of filling up of void pores. **3b** emitted green light which was similar to the green emissive **3** in DCM. Such observation supports that the framework of the MS silica remain unchanged under crushed condition. Thus, the similar emissive nature of **3b** with the emission profile in solution phase of **3**, led us to conclude that the eximeric Pt(II) complexes (**3**, **4** and **5**) were dissociated into the monomeric units under crushed condition and thereby facilitating these smaller sized monomeric units to occupy the empty pores of MS silica. On performing the

similar experiments with complexes, 1-2 to incorporate into the mesopores of silica couldn't succeed. The rigid sterically hindered bulky substituents might be the reason behind of such observation.

3. Conclusion

Strategically designed AIE active platinum(II) complexes **2-5** were synthesized by a simple route. ML behavior of **3, 4** and **5** were studied which demonstrated a transition from crystalline to amorphous state in aggregated form. In molecular state, a strong Pt-Pt interaction was observed after crushing. A simple and dry approach of impregnation of **3, 4** and **5** into the pores of the mesostructured silica with concomitant sharp change of emission color has been interestingly observed. Investigation showing the rationale behind of such color change was the dissociation of Pt(II)-excimer into monomeric units.

4. Experimental Section

We procured **L1** from Sigma Aldrich company.

General Synthesis of L2: 2-Aminipyridine (1eq) and sodium hydride(1eq) were dissolved in 4 ml of DMF and stirred at 0^0C for 30min. After that tritylchloride (eq) added then stirred for 2h.The crude product was purified by column chromatography using 60-120 silica mesh giving pure products. Yield(90%).**^{1}H NMR** (400 MHz, $CDCl_3$) δ 8.78 (s, 1H), 7.40 – 7.32 (m, 6H), 7.19 (m, *J* = 14.5, 8.3, 4.6 Hz, 12H). **^{13}C NMR** (101 MHz, DMSO) δ 158.22, 147.27, 145.97, 136.24, 129.23, 127.99, 126.72, 113.17, 110.86, 70.48.

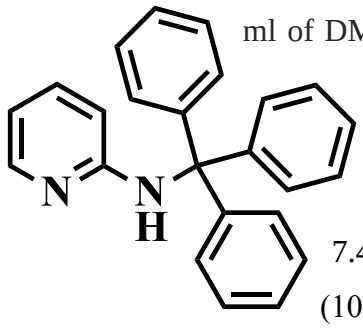

General Synthesis of L3(N^1-tritylethane-1,2-diamine): It was synthesized by following the method as described in the literature.**^{1}HNMR** (400 MHz, $CDCl_3$) δ 7.55−7.48 (m, 5H), 7.35−7.27 (m, 7H), 7.25−7.17 (m, 3H), 2.83 (t, J = 6.0 Hz, 2H), 2.23 (t, J = 6.0 Hz, 2H), 1.63 (s, 3H).

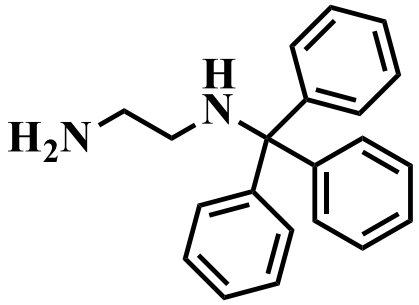

General Synthesis of L4(N^1-tritylpropane-1,3-diamine): **^{1}H NMR** (400 MHz, $CDCl_3$) δ 9.50 (dd, *J* = 5.9, 0.9 Hz, 1H), 7.79 (td, *J* = 8.0, 1.6 Hz, 1H), 7.61 – 7.53 (d, 1H), 7.52 – 7.40 (m, 7H), 7.34 – 7.29 (m, 4H), 7.28 (s, 2H), 7.24 – 7.16 (m, 3H), 7.15 – 7.04 (m, 3H), 7.00 (dt, *J* = 6.4, 2.9 Hz, 1H), 3.32 (dt, *J* = 13.4, 6.8 Hz, 2H), 2.35 (t, *J* = 6.5 Hz, 2H), 2.01 – 1.84 (m, 2H).

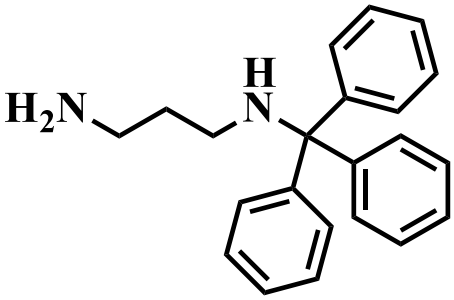

General Synthesis of L5(N^1-tritylhexane-1,6-diamine): **^{1}H NMR** (400 MHz, $CDCl_3$) δ 7.54 – 7.47 (m, 6H), 7.37 – 7.28 (m, 6H), 7.23 – 7.18 (m, 3H), 2.73 – 2.63 (m, 3H), 2.13 (t, *J* = 7.0 Hz, 2H), 1.38 – 1.23 (m, 7H). **^{13}C NMR** (101 MHz, $CDCl_3$) δ 146.34, 128.66, 127.72, 126.14, 70.85, 43.49, 42.20, 33.82, 30.87, 27.23, 26.88.

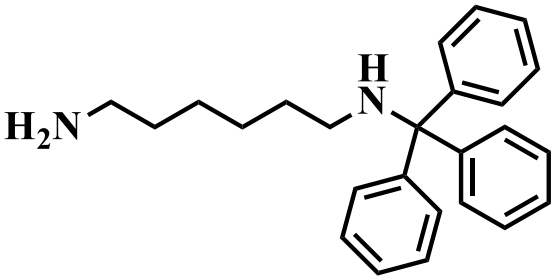

General Synthesis of 1: We have discussed in chapter **3A**

General synthesis of complex 2[4]: **1**(1eq) and **L2** (1eq) were dissolved in 4 ml of 2-ethoxyethanol and refluxed the mixture for 2h. After 2h,the greenish coloured solid product was formed. The crude product was recrystallized by ethanol producing a green colour solid product, yield(80%).**^{1}H NMR** (400 MHz, $CDCl_3$) δ 9.71 (dd, *J* = 5.8, 0.9 Hz, 1H), 8.80 (s, 1H), 8.45 (dd, *J* = 16.0, 8.0 Hz, 1H), 7.83 (td, *J* = 8.0, 1.5 Hz, 1H), 7.66 (d, *J* = 7.9 Hz, 1H), 7.47 (t, *J* = 9.9 Hz, 1H), 7.44 – 7.31 (m, 6H), 7.31 – 7.07 (m, 12H), 7.01 (td, *J* = 7.5, 1.2 Hz, 1H), 6.63 – 6.50 (td, 1H), 6.43 (d, *J* = 11.1 Hz, 1H), 6.13 (d, *J* = 8.8 Hz, 1H).**^{13}C NMR** (101MHz, $CDCl_3$) δ167.21, 156.50, 150.97, 150.72, 144.69, 143.88, 141.18, 138.78, 136.58, 131.88,130.09,128.81, 128.27, 123.70, 123.35, 121.91, 118.12, 113.92, 111.65,71.26.

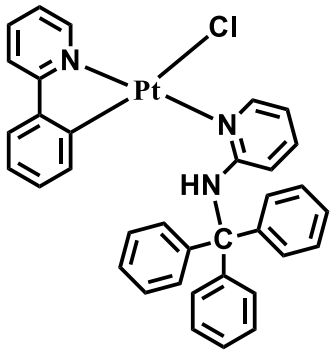

General Synthesis of 3: 0.00048 mmol of 1, 0.00072mmol of **L3** were mixed in 2-ethoxy ethanol and refluxed it overnight at 100^0C. Then, the solvent was evaporated under reduced pressure and the crude product was collected and product was purified by column chromatography (60-120 mess of silica gel). Yield, 69%.**^{1}H NMR** (400MHz, $CDCl_3$) δ 9.49 (dd, J = 5.9, 0.9 Hz, 1H), 7.77 (td, J = 8.0, 1.6 Hz, 1H), 7.52 (m, J = 7.4, 6.0 Hz, 7H), 7.40 (m, J = 5.9, 3.2 Hz, 1H), 7.36 – 7.19 (m, 10H), 7.14 – 7.00 (m, 3H), 4.66–4.30(t, 2H), ; **^{13}C NMR** (101 MHz, CDCl3) δ 166.53, 150.89, 145.41, 145.08, 139.98, 138.26, 129.98, 128.76, 128.58, 128.08, 126.64, 123.83, 123.43, 122.08, 118.20, 70.98, 48.64, 44.47 2.54 – 2.36 (t, 2H).**HRMS**: [M-Cl]+ at m/z 651.2009 and 2[M+H] at m/z 1376.3616

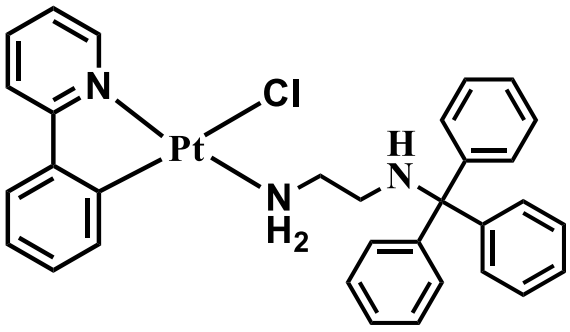

General Synthesis of complex 4: 0.00048 mmol of **1**, 0.00072mmol of **L4** were mixed in 2-ethoxy ethanol and refluxed it overnight at 100^0C. Then, the solvent was evaporated under reduced pressure and the crude product was collected and product was purified by column

chromatography (60-120 mess of silica gel). Yield, 58%.**^{1}H NMR** (400 MHz, $CDCl_3$) δ 9.50 (dd, *J* = 5.9, 0.9 Hz, 1H), 7.79 (td, *J* = 8.0, 1.6 Hz, 1H), 7.59 – 7.53 (m, 1H), 7.51 – 7.39 (m, 7H), 7.31 (dd, *J* = 7.1, 1.5 Hz, 4H), 7.28 (s, 2H), 7.24 – 7.17 (m, 3H), 7.14 – 7.05 (m, 3H), 7.00 (dt, *J* = 6.4, 2.9 Hz, 1H), 3.32 (dt, *J* = 13.4, 6.8 Hz, 2H), 2.35 (t, *J* = 6.5 Hz, 2H), 2.00 – 1.84 (m, 2H).**^{13}C NMR** (101 MHz, $CDCl_3$) δ 166.63, 151.03, 145.65, 145.11, 139.66, 138.40, 130.08, 128.92, 128.64, 127.91, 126.40, 123.84, 123.56, 122.08, 118.13, 71.18, 47.05, 41.72, 32.30.

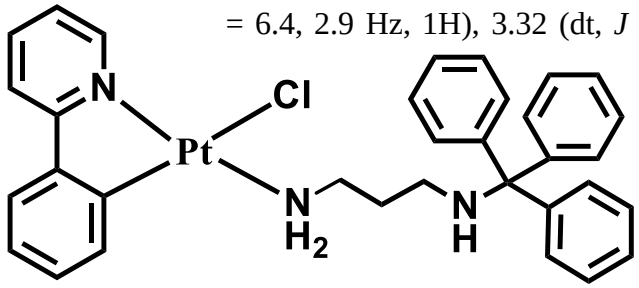

General synthesis of complex 5:0.00048 mmol of **1**, 0.00072mmol of **L5** were mixed in 2-ethoxy ethanol and refluxed it overnight at 100°C. Then, the solvent was evaporated under reduced pressure and the crude product was collected and product was purified by column chromatography (60-120 mess of silica gel). Yield, 71%.**^{1}H NMR** (400 MHz, $CDCl_3$) δ 9.48 (dd, *J* = 5.9, 0.9 Hz, 1H), 7.79 (td, *J* = 8.0, 1.6 Hz, 1H), 7.59 – 7.53 (m, 1H), 7.51 – 7.39 (m, 7H), 7.31 (dd, *J* = 7.1, 1.5 Hz, 4H), 7.28 (s, 2H), 7.24 – 7.17 (m, 3H), 7.14 – 7.05 (m, 3H), 7.00 (dt, *J* = 6.4, 2.9 Hz, 1H), 2.73 – 2.63 (m, 3H), 2.13 (t, *J* = 7.0 Hz, 2H), 1.38 – 1.23 (m, 7H). **^{13}C NMR** (101 MHz, $CDCl_3$) δ 166.63, 151.03, 145.65, 144.21, 139.76, 137.40, 131.07, 129.52, 128.64, 127.01, 126.70, 124.04, 123.76, 122.78, 119.16, 71.28, 46.05, 41.02, 31.20 29.05, 27.15, 25.07.

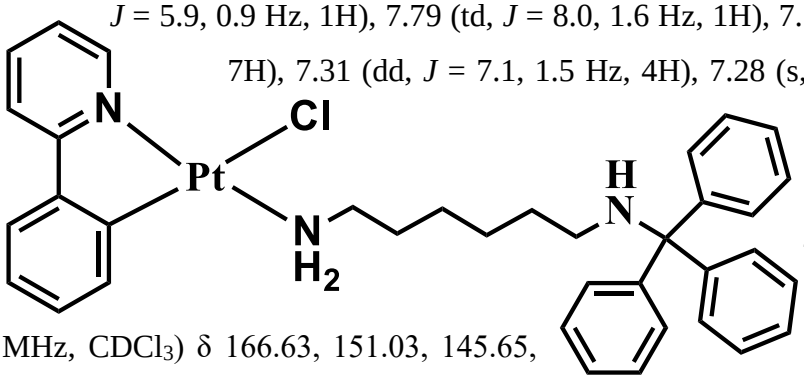

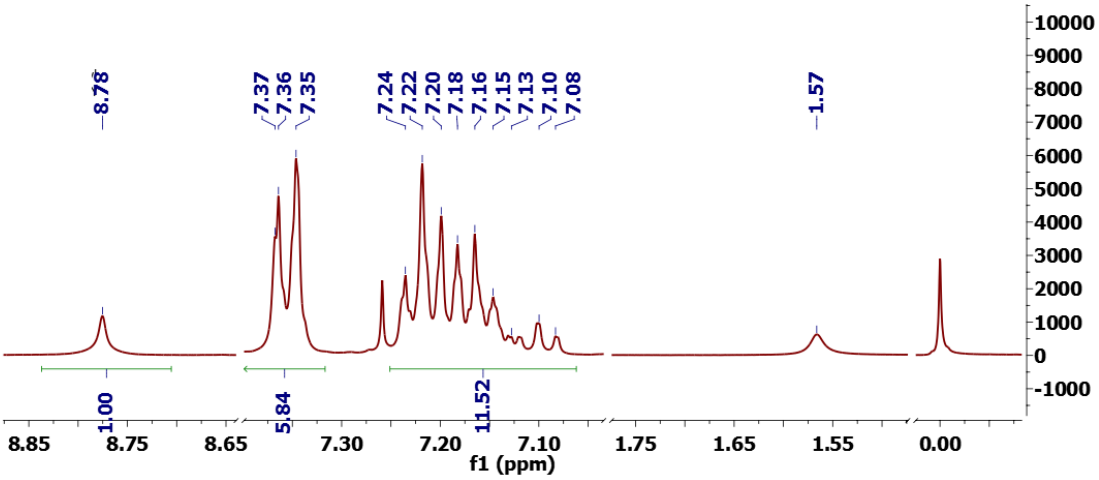

Figure. **26** ^{1}HNMR spectrum of **L2**

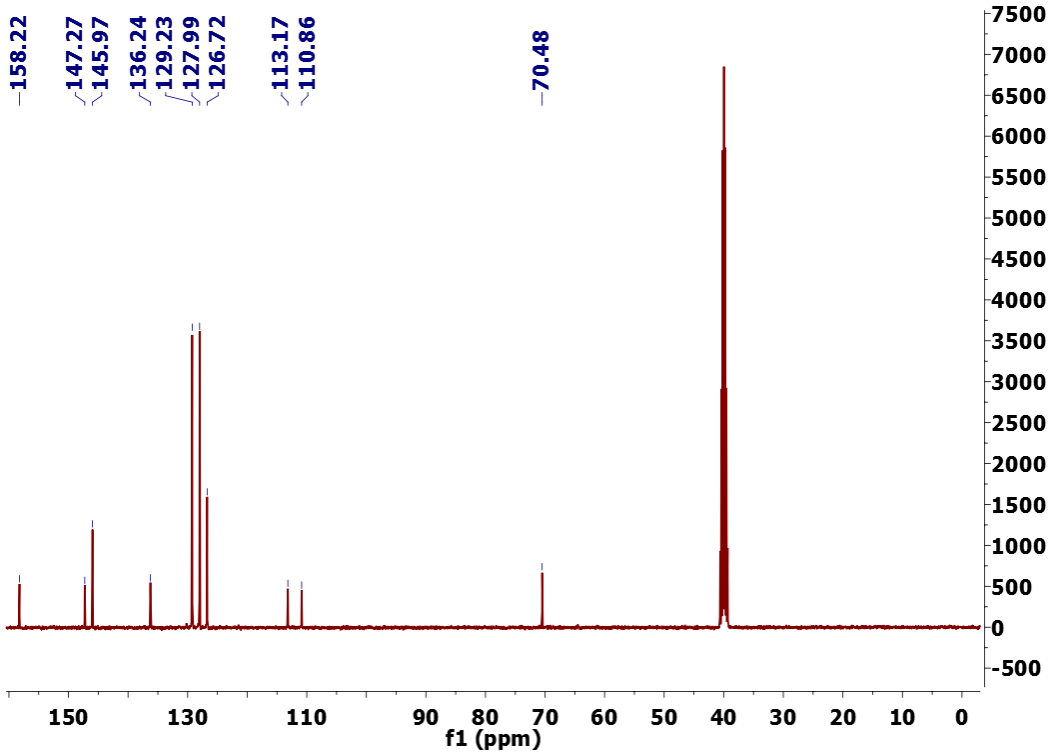

Figure. **27** ^{13}C NMR spectrum of **L2**

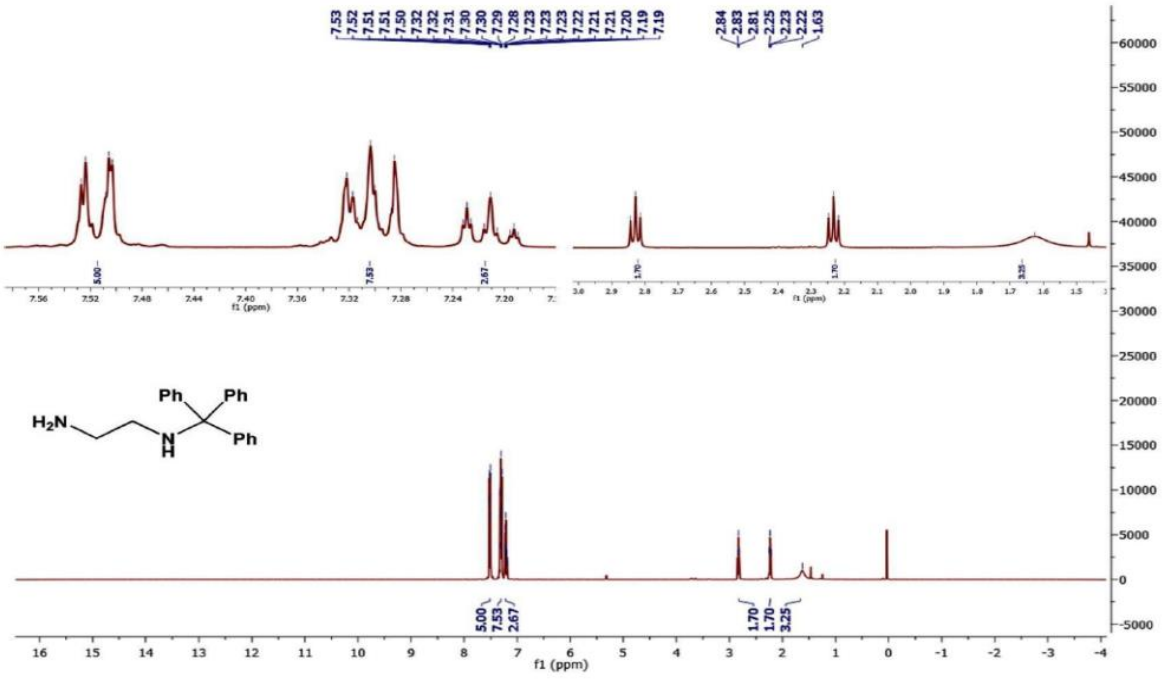

Figure. **28** [1]HNMR spectrum of **L3**

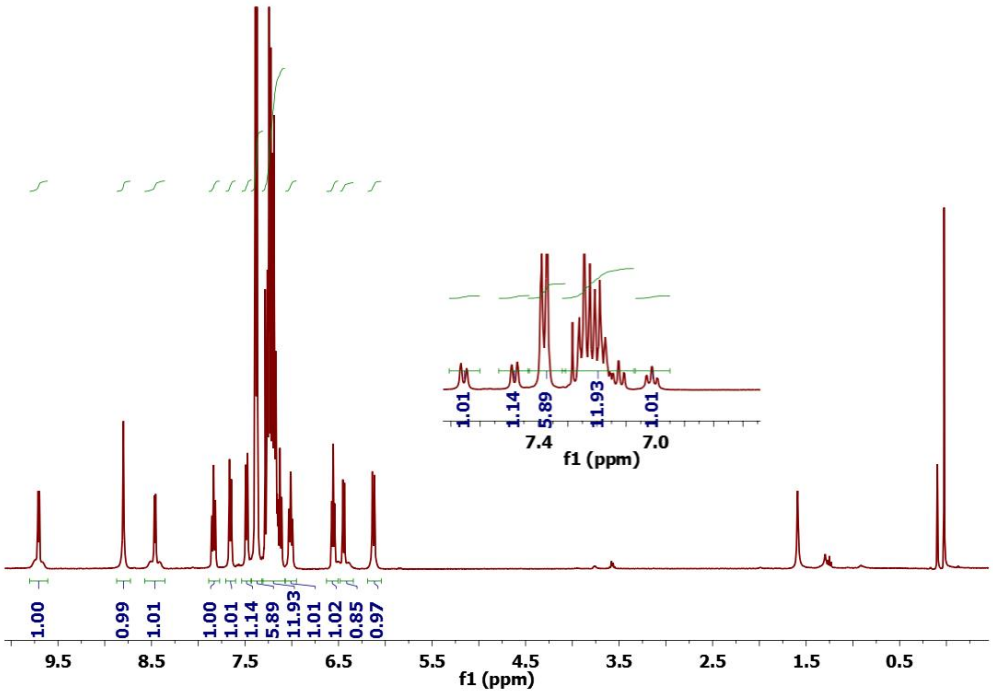

Figure. **29** [1]HNMR spectrum of **2**

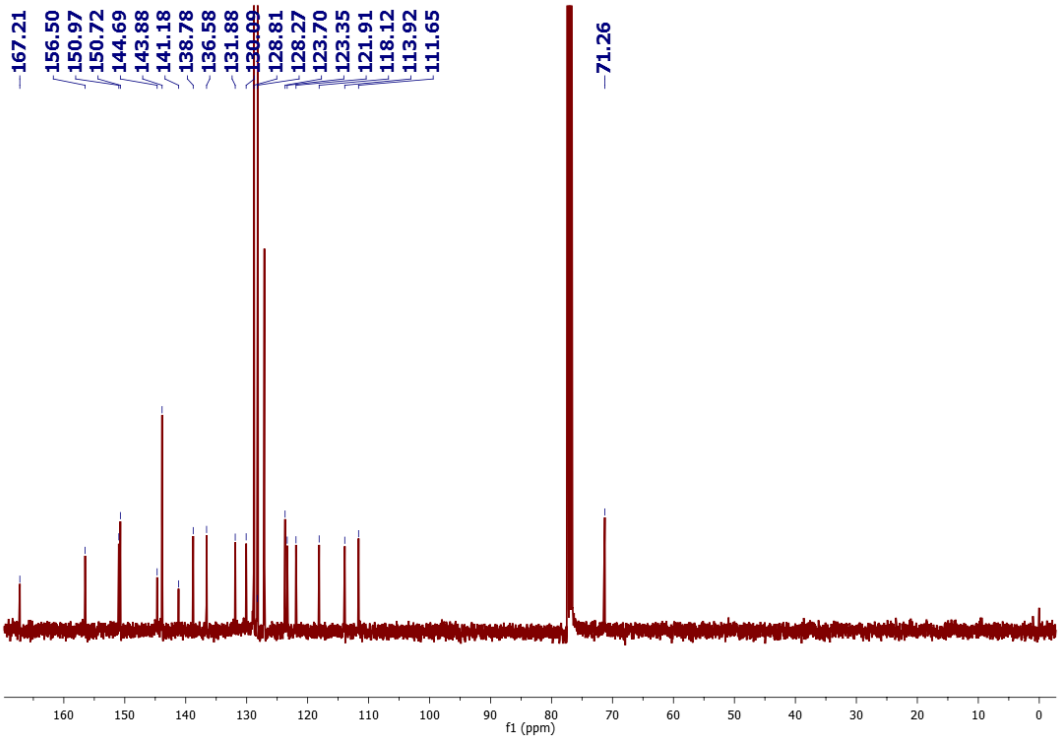

Figure. **30** ^{13}C NMR spectrum of **2**

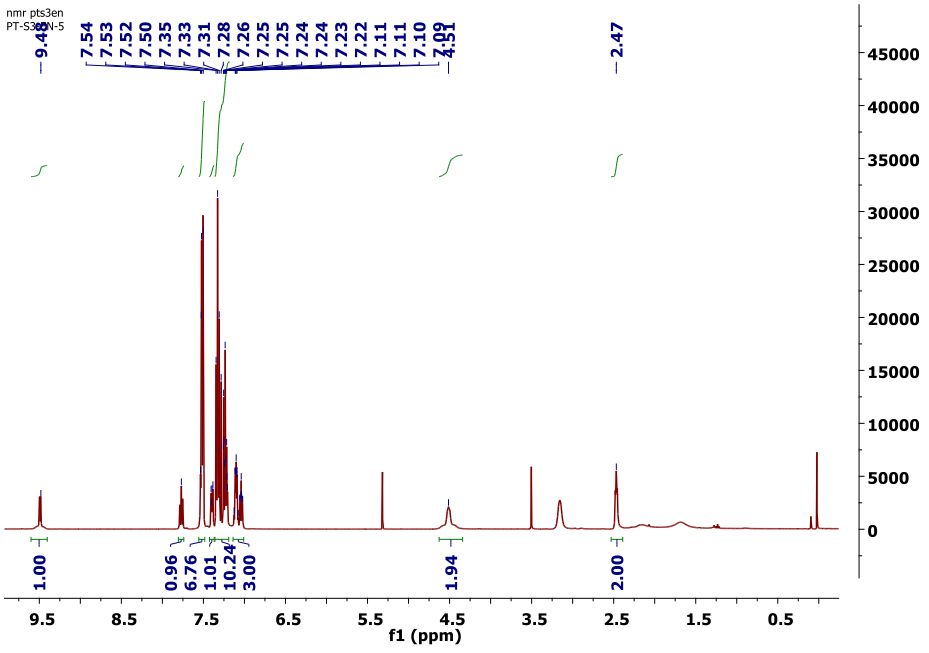

Figure. 31 ^{1}HNMR spectrum of **3**

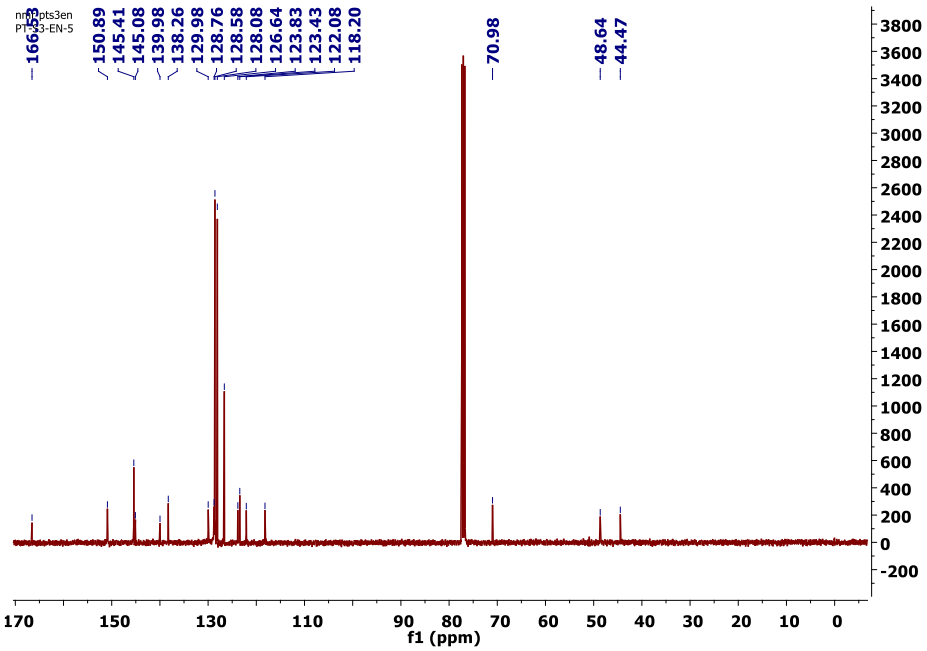

Figure. 32 ^{13}CNMR spectrum of **3**

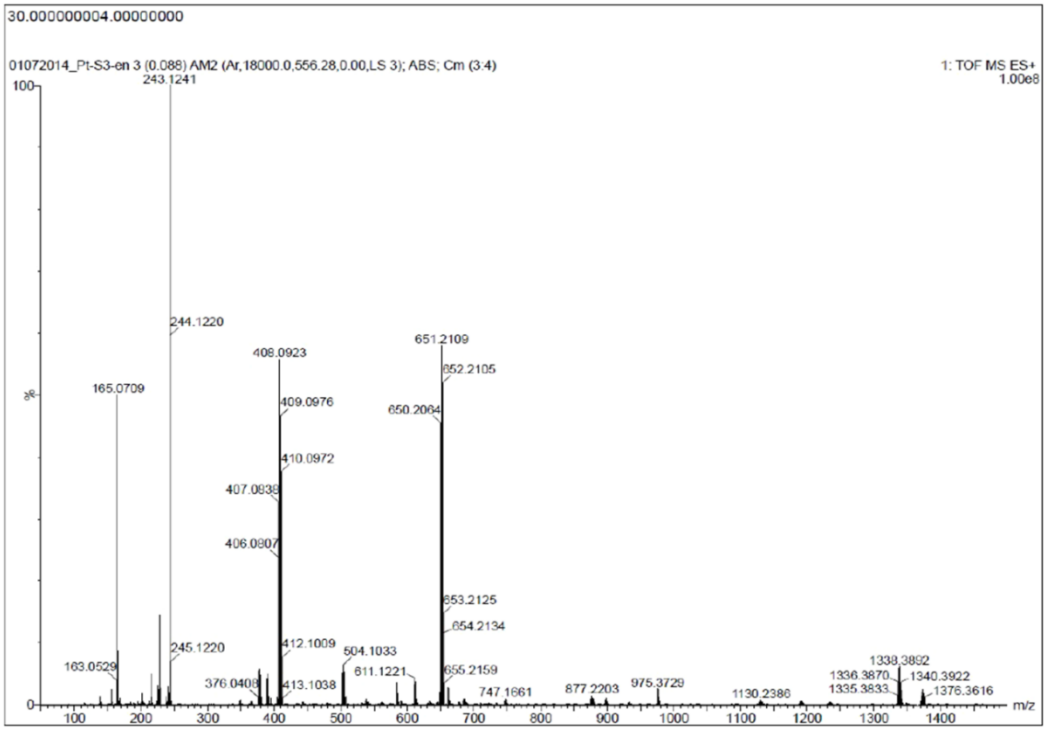

Figure. 33 Mass spectrum of **3**

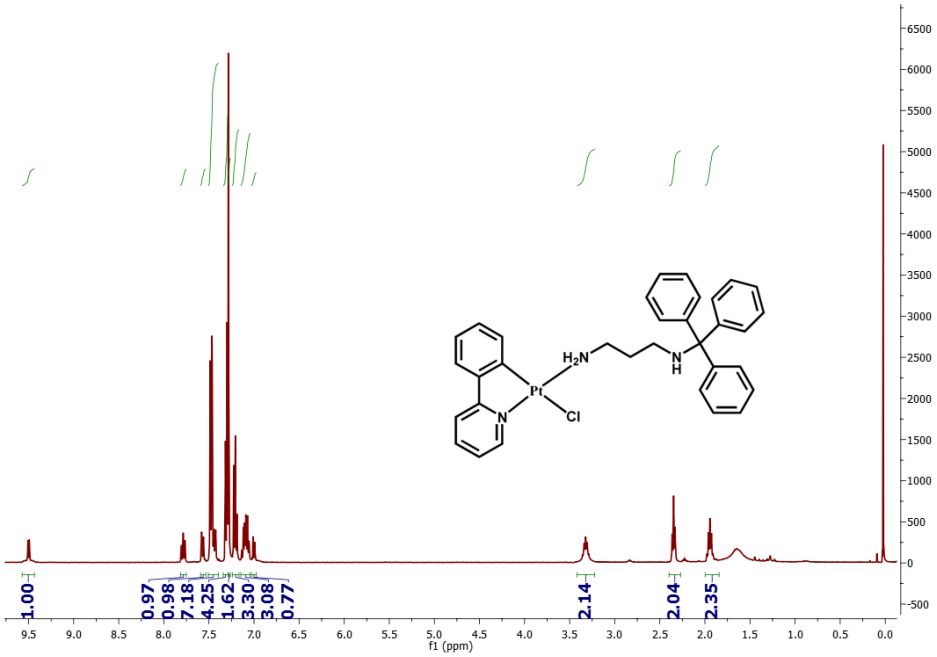

Figure. **34** ^{1}H NMR spectrum of **4**

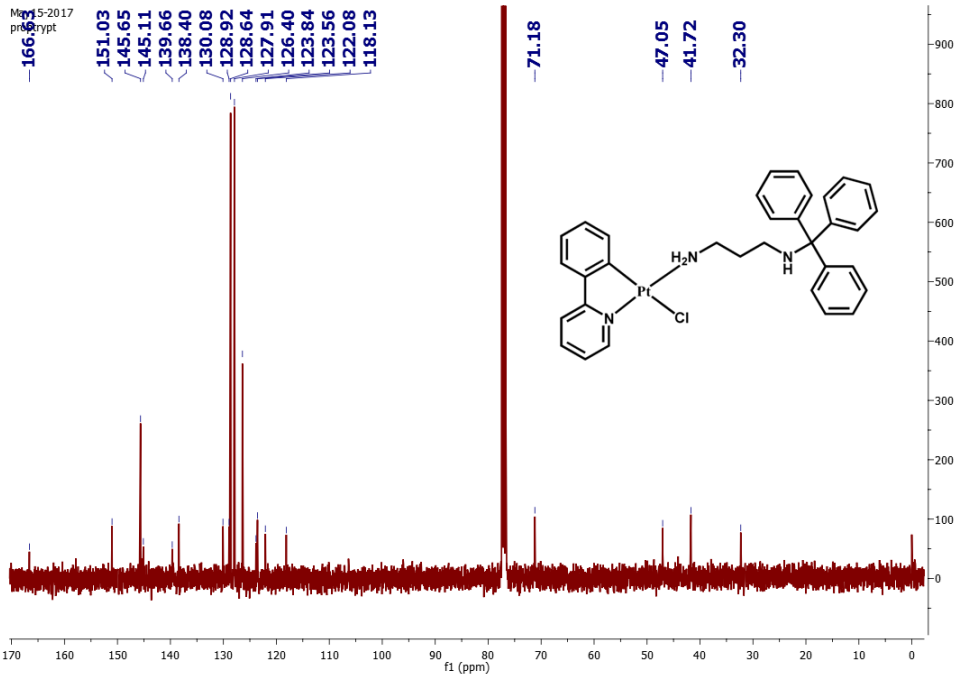

Figure. **35** ^{13}C NMR spectrum of **4**

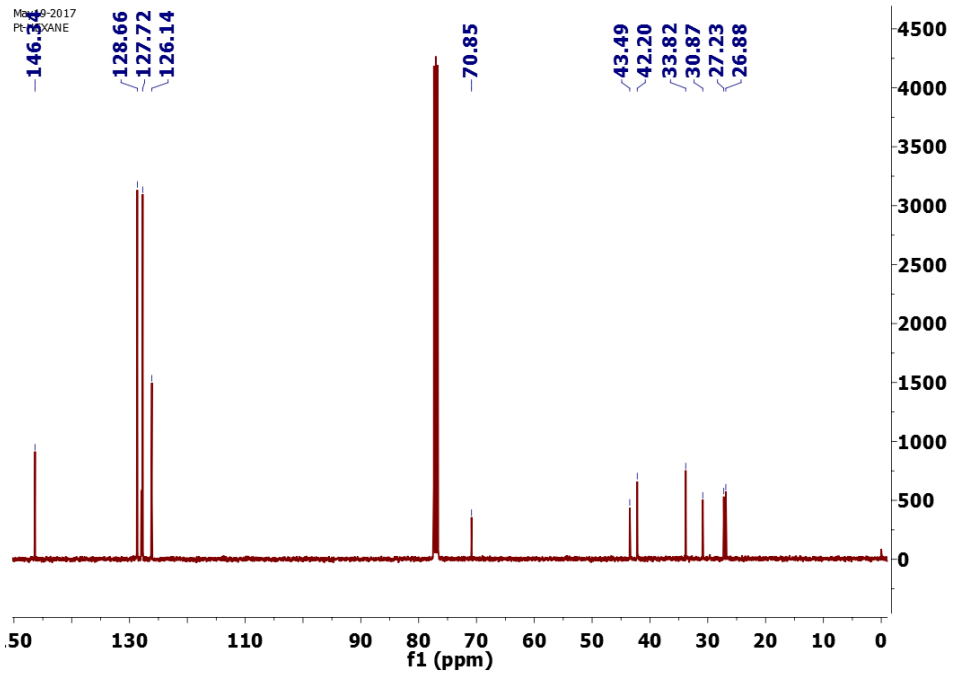

Figure. **36** ^{13}C NMR spectrum of **5**

5. References

[1]V. H. Houlding and V. M. Miskowski, *Coord. Chem. Rev.*, 1991, **111**, 145

[2] V. W.-W. Yam, K. M.-C.Wong, N. Zhu, *J. Am. Chem. Soc*., 2002, **124**, 6506

[3] W.-Y. Wong, G.-J. Zhou, X.-M. Yu, H.-S. Kwok, B.-Z. Tang, *Adv. Funct. Mater*., 2006, **16**, 838

[4] S. S. Pasha, P. Das, N. P. Rath, D. Bandyopadhyay, N. R. Jana, I. R. Laskar, *Inorg.Chem. Commun.*,2016, **67**, 107.

[5] W. -Y. Wong, C. -L. Ho, *Coord. Chem. Rev*. 2009, **253**, 1709

[6] C. K. M. Chan, C. -H .Tao, H. -L. Tam, N. Zhu, V. W. -W. Yam K. -W Cheah, *Inorg. Chem.*, 2009, **48**, 7;

[7] T. T. Feng, F. Q. Bai, L. M. Xie, Y. Tang, H. X. Zhang, *RSC Adv.*, 2016, **6**, 11648

[8] S. Seokhwan, L. Hwan Gyu, L. Nopl, R. Minwoo, K. Cheehun, L. Jihoon, A. Hogeun, C. Minchu, *J. Nano Sci. Nanotechno.*, 2016, **16**, 2028

[9] Y. Dai, H. Xiao, J. Liu, Q. Yuan, P. Ma, D. Yang, C. Li, Z. Cheng, Z. Hou, P. Yang, Jun Lin, *J. Am. Chem. Soc*., 2013, **135**, 18920.

[10] K. M. -C. Wong and V. W. -W. Yam, *Acc. Chem. Res*., 2011, **44,** 424

[11]P. Pinter, H. Mangold, I. Stengel, I. Munster T. Strassner, *Organomet.*, 2016, **35**, 673

[12] J. Zhanga, G. Daic, F. Wud, D. Lie, D. Gao, H. Jina, S. Chenf, X. Zhuf, C. Huanga, D. Han, *J. Photochem. Photobio. A: Chem.*, 2016, **316**, 12

[13]M. Bachmann, D. Suter, O. Blacque and K. Venkatesan, *Inorg. Chem*., 2016, **55**, 4733

[14] J. J. Stace, P. J. Ball, V. Shingade, S. Chatterjee, A. Shiveley, W. L. Fleeman, A. J. Staniszewski, J. A. Krause, W. B. Connick, *Inorg. Chim. Acta*, 2016, **447**, 98.

[15] K. H. -Y. Chan, H. S. Chow, K. M. -C. Wong, M. C. -L. Yeung, V. W. -W. Yam, *Chem. Sci*., 2010, **1**, 477.

[16] M. L. Muro, C. A. Daws, F. N. Castellano, *Chem. Commun*., 2008, 6134

[17]T. Abe, T. Itakura, N. Ikeda, K. Shinozaki, *Dalton Trans*., 2009, 711

[18] J. S. Field, C. D. Grimmer, O. Q. Munro, B. P. Waldron, *Dalton Trans*.,2010, **39**, 1558

[19] X. Zhang, J. Wang, J. Ni, L. Zhang, Z. Chen, *Inorg. Chem*., 2012, **51**, 5569

[20] J. R. Kumpfer, S. D. Taylor, W. B. Connick S. J. Rowan, *J. Mater. Chem*., 2012**, 22**, 14196

[21] M. Krikorian, S. Liu, T. M. Swager, *J. Am. Chem. Soc*., 2014, **136**, 2952.

[22] C. H. Huang, F. Y. Li, W. Huang, Introduction to Organic Light-Emitting Materials Devices, Press of Fudan University, Shanghai, 2005.

[23] Y. Hong, J. W. Y. Lam, B. Z. Tang, *Chem. Soc. Rev*., 2011,**40**, 5361.

[24] S. Liu, H. Sun, Y. Ma, S. Ye, X. Liu, X. Zhou, X. Mou, L. Wang, Q. Zhao, W. Huang, *J. Mater. Chem*., 2012, **22**, 22167

[25] H. Honda, Y. Ogawa, J. Kuwabara and T. Kanbara, *Eur. J. Inorg. Chem*., 2014, 1865

[26]S. S. Pasha, P. Alam, S. Dash, G. Kaur, D. Banerjee, R. Chowdhury, N. Rath, A. R. Choudhury, I. R. Laskar,*RSC Adv.*, 2014, **4**, 50549.

[27] Z. Li, J. C. Barnes, A. Bosoy, J. F. Stoddart, J.I. Zink, *Chem. Soc. Rev*., 2012, **41**, 2590.

[28] O.H. Park, S.Y. Seo, J. I. Jung, J. Y. Bae, and B. S. Bae, *J. Mater. Res*., 2003, **18**, 5

[29]Q.G. Meng, P. Boutinaud, A. C. Franville, H. J. Zhang , R. Mahiou, *Microp. Mesop. Mater.*, 2003, **65**, 127

[30] H. M. Yu, H. D. Liang, Z.-Z. Yan, *J. Coord. Chem.*, 2011,**64**, 440

[31] M. M. Mdleleni, J. S. Bridgewater, R. J. Watts and P. C. Ford, *Inorg. Chem.*, 1995, **34**, 2334.

Chapter V

PART-A

Synthesis of an 'Aggregation Induced Emission' Active Salicylaldehyde Based Schiff Base: Study of Mechanoluminescence and Sensitive Zn(II) Sensing

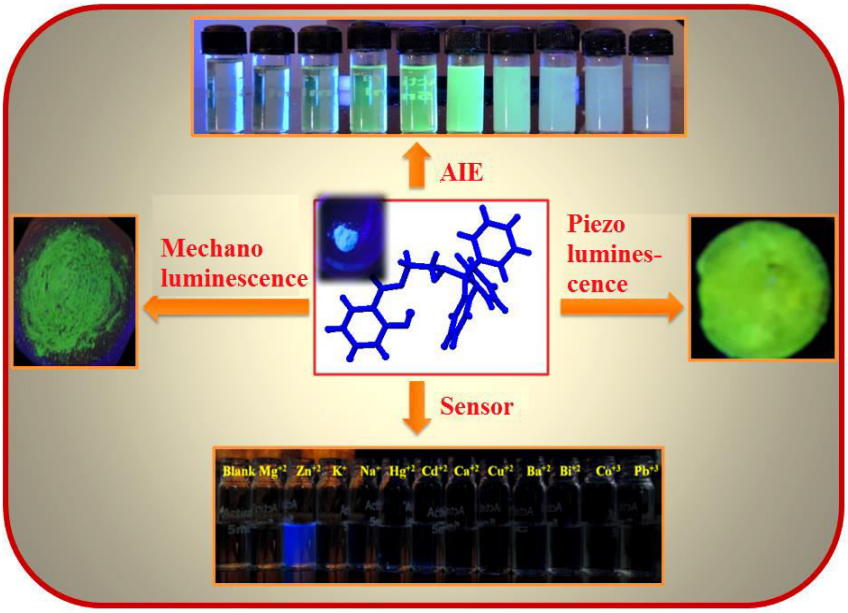

5A.1 Introduction

Luminescent materials have been getting a great deal of attention in research world since the last two decades, because of their utility in various fields, such as in organic light emitting diodes[1-3], bio-imaging[4-10], chemo sensors[11-15] etc. There has been a serious issue for the use of these materials successfully for solid state applications because of detrimental 'Aggregation Caused Quenching' (ACQ) effect[15-20]. To overcome this effect, 'Aggregation Induced Emission' (AIE)[15-20] was introduced. This phenomenon opened up a new avenue for applications of solid state luminescent materials. The study of the property of mechanoluminescence (ML) of luminescent materials results in a huge interest from the scientific communities because of their importance in applications such as pressure sensors, luminescent switches, memory devices, healthcare, security inks etc[21-23]. The ML property is resulted from the external stimuli such as applied pressure, grinding, stress, shearing, rubbing, milling and crushing of the solid state[21-33]. In 1993 Gawinecki *et al*. [34] reported low molecular weight mechano-responsive pyridinium perchlorate compound (**i**), which is the first report on ML.

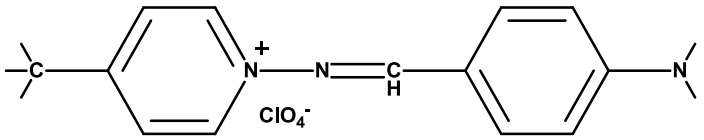

i

Mishra *et al*. [35] reported4-(1,3-Dioxo-2,3-dihydro-1H-phenalen-2-ylmethyl)-N-pyridin-3-yl-benzamide(**ii**) and 4-(1,3-Dioxo-2,3-dihydro-1H-phenalen-2-ylmethyl)-N-pyridin-4-yl-benzamide (**iii**) which are ML active with emission wavelength difference of 31nm and 45nm, respectively.

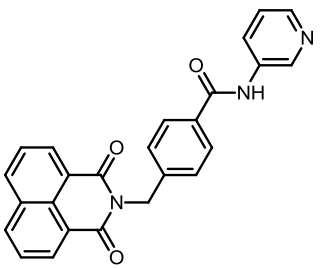

ii

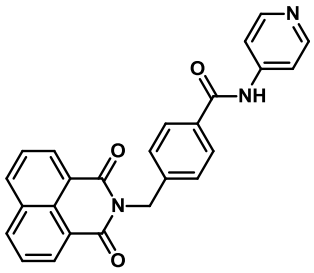

iii

Yang *et al*. [36] reportedML turn on of Zn(II) complex which was synthesized based on a new Salen-type tetradentate N_2O_2 bisoxime chelate ligand (H2L) derived from 1-phenyl-3-methyl-4-benzoyl-5-pyrazolone (PMBP) and 1,2-bis(aminooxy)ethane. Fujihara *et al*. also reported[37] [Pt(ppy)L] [ppy = 2-phenylpyridinato, L = Glycinato(**iv**), Alaninato (**v**), Leucinato (**vi**), Isoleucinato (**vii**), Phenylalaninato (**viii**) and Sarcosinato (**ix**)] which exhibited ML with a difference in wavelength 88nm, 68nm, 28nm, 20nm, 6nm and 45nm, respectively.

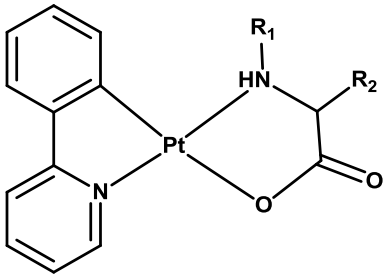

R_1 = H, R_2 = H: Glycinato (**iv**)
R_1 = H, R_2 =CH_3: Alaninato (**v**)
R_1 = H, R_2 = i_{Bu}: Leucinato (**vi**)
R_1 = H, R_2 = s_{Bu}: Isoleucinato (**vii**)
R_1 = H, R_2 =CH_2Ph: Phenylalaninato (**viii**)
R_1 = H, R_2 = H: Sarcosinato (**ix**)

Most of the reported ML active materials have been suffering from ACQ effect and showing a limited wavelength difference before and after grinding part[21-33],which restricting them for useful applications. The ML property if it is observed in AIE active materials can alleviate such problems. Additionally, the AIE active materials are more susceptible to exhibit ML property.

Tang *et al*. [38] reported a compound 2-amino-3-{E[4(dibutylamino)benzy-lidene] amino}maleonitrile (**x**) which was identified as AIE active and showing ML property.

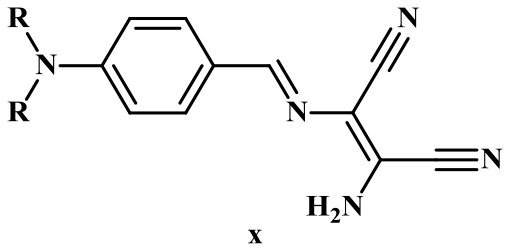

R= $(CH_2)_3CH_3$

x

Laskar et al. [16]has also reported Schiff-base based AIE active ML (E)-2-[(pyridin-2-ylimino)methyl]phenol (**xi**) with the observation of maximum emission wavelength difference by 23nm. In continuation of our earlier work, we have designed and synthesized of an 'aggregation induced emission' (AIE) active materials possessing ML property in a simplified approach.

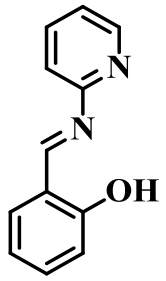

xi

Zn(II) ion is a biologically important metal, which is involved in many biological reactions. The deficiency of Zn(II) in children can cause growth retardation, delayed sexual maturation, infection susceptibility and diarrhea. Consumption of excess Zn(II) ion can cause ataxia and lethargy[39-43]. Thus, it is necessary to have a convenient process to detect Zn(II) in environment. Although many reports are there for luminescent based Zn(II) sensing[44-46], but sensing with AIE active compounds are rarely found[47].

Herein, we have reported an AIE active simple organic molecule **2** which has been synthesized by a simple technique. This compound exhibits reversible and irreversible ML property depending upon the shearing or axial stress acting upon the compound resulting a wide separation of emission wavelength. A thorough study of the mechanism of AIE and ML property of **2** has been carried out. Additionally, the selective sensing of Zn(II) with **2** has been elaborated.

5A.2Results and discussion

5A.2.1Synthesis and Characterization

Trityl chloride was reacted with ethylenediamine which produced trityl substituted ethylenediamine[48], **1**. The compound**1** was reacted with salicylaldehyde by using Schiff-base synthetic methodology and generated **2** (Scheme 1). ^{1}H NMR and the mass spectra of **1** support the formation of the compound, **1**. The solid product, **2** was purified by recrystallization and characterized by ^{1}H, ^{13}C NMR and single crystal XRD.

Scheme1. Synthetic route and chemical structures of **1** and **2**

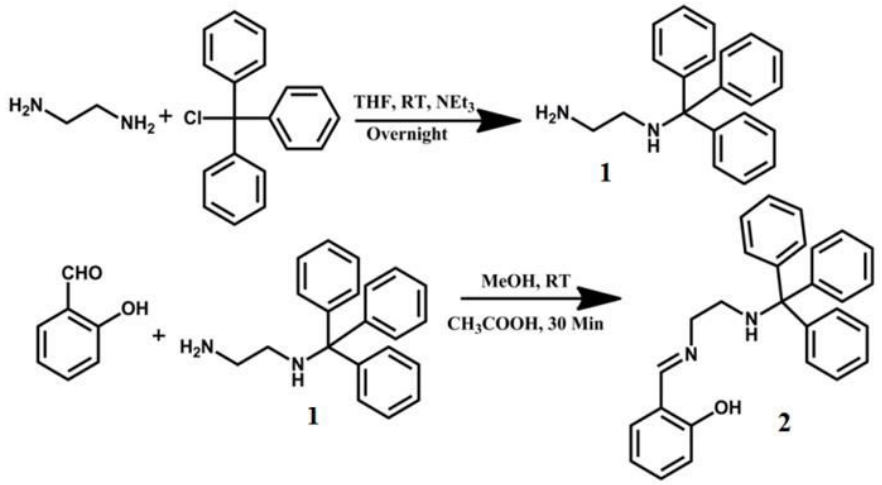

^{1}H NMR spectrum of **2** shows aromatic proton signals in the range δ = 7.21−7.51ppm, the four protons of (CH_2-CH_2) are observed as double triplets at δ = 2.51 and 3.74ppm, -OH and HC=N protons are observed as singlet at δ = 13.42 and 8.44ppm,respectively. The ^{13}C NMR spectra of **2** shows aromatic carbon signals in the range δ = 116.93−161.19ppm, the three aliphatic carbon signals at 44.18, 60.25, 70.69ppm and C=N carbon signal observed at δ 165.68ppm. The single crystal of **2** was obtained by slowly evaporating solvent at room temperature. The crystal structure of **2** is triclinic system with space group $P\bar{1}$. Each unit cell contains two molecules which are oriented in anti-parallel to each other. There is one intra-molecular hydrogen bonding (N1....H1-O1, 1.895Å) as shown in the packing diagram(Figure 1a).

5A.2.2 Photo physical property

2 shows low energy absorbance bands with λ_{max}, at 402nm and 411nm, respectively when it is recorded in polar methanol and DMSO. On recording emission spectra in the same solvents, **2** shows a broad emission band with λ_{max} 449nm and 451nm, respectively (Figure 1). In non-polar solvents (THF and DCM), it has not been observed any noticeable absorption in the range, 400nm-450nm and a structured blue-shifted emission is observed with λ_{max}, ~407nm (Figure 1b). These results imply that the nature of transition in **2** shows intramolecular charge transfer/twisted intramolecular charge transfer (ICT/TICT) transition[49-51]. To support the fact, the geometry of **2** was optimized by Gaussian 09[52]. The results exhibits that the HOMO states are mainly

localized in one of the appended phenyl rings of trityl group and LUMO states are mainly localized on salicylaldehyde phenyl ring (Figure 2).

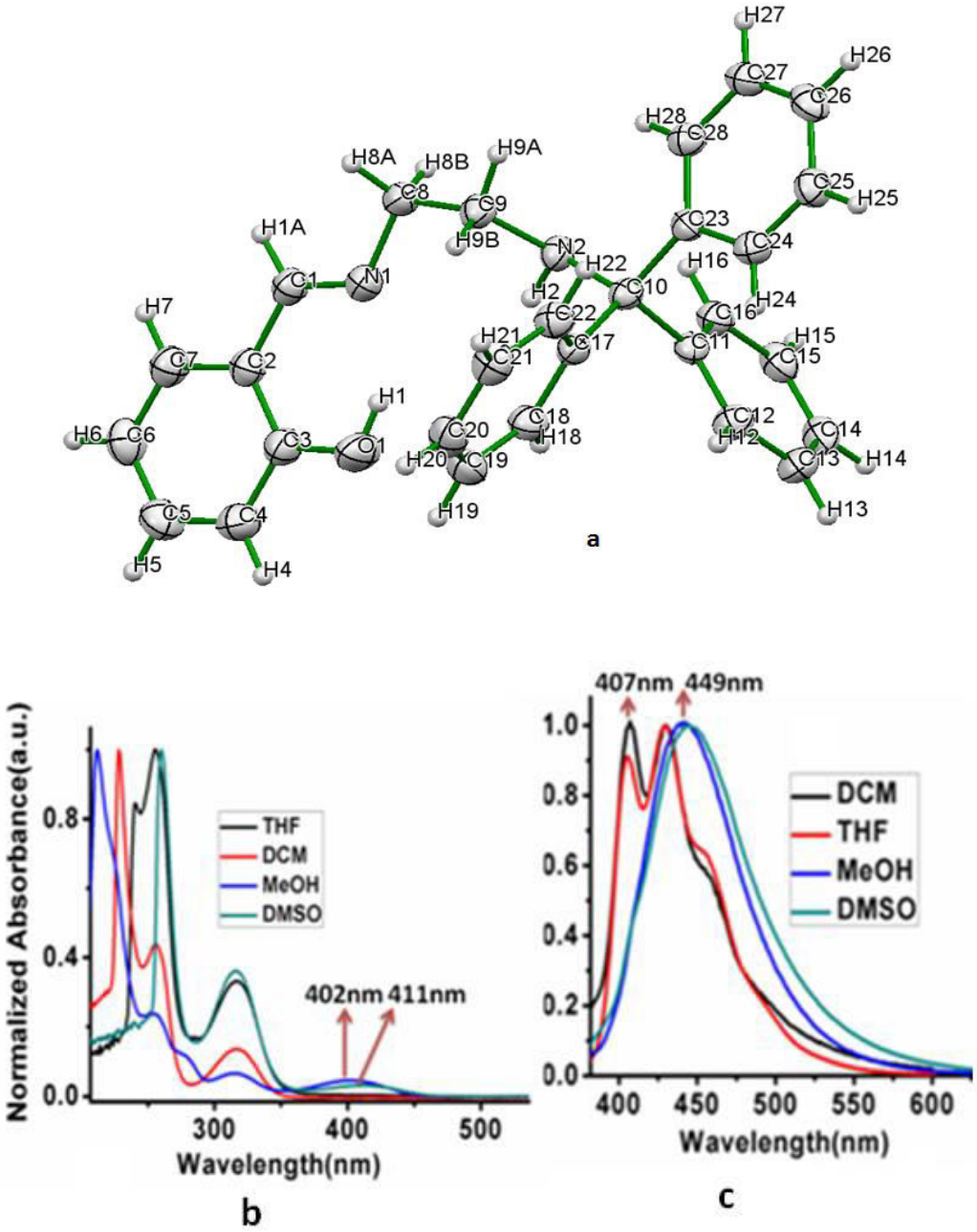

Figure. 1 a) ORTEP diagram of 2 with 50% probability of ellipsoids 2; b) absorption; c) photoluminescence spectra ($\lambda_{ex\ c}$= 365nm) of **2** in solvents with different polarity [tetrahydrofuran (THF); dichloromethane (DCM); methanol (MeOH); dimethylsulphoxide (DMSO)] at a concentration, $1x10^{-5}$M.

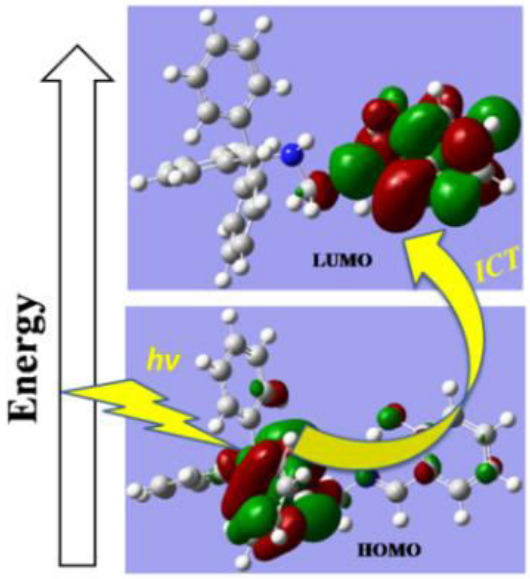

Figure. 2 DFT based ground state optimized HOMO and LUMO orbitals of **2**

Hence, the localization of HOMO on the donor part of the molecule (trityl) and localization of LUMO on the acceptor part of the molecule (salicyldehyde) ensuring the ICT/TICT transition. The calculated band gap is found to 3.2eV which corresponds to the experimentally obtained band gap (3.6eV). The TD-DFT calculation shows a good agreement with the experimentally obtained absorption band with λ_{max} at 315nm (ε =11157 $Lmol^{-1}cm^{-1}$) (λ_{calc} ~290nm, f = 0.5148), 255nm (ε = 36313.5 $Lmol^{-1}cm^{-1}$) (λ_{calc}~236 nm, f = 0.0224), 228nm (ε = 82137 $Lmol^{-1}cm^{-1}$) (λ_{calc} ~228 nm, f = 0.3064) in DCM (Figure 3 and Table 1)

Table 1: Vertical excitation energies and corresponding orbital contributions of **2**

Transition from S_0 state to lowest excited states	**Experimental Absorption peak maxima(nm)**	**λ_{cal}(nm)**	**E_{cal} (eV)**	**Oscillator strength(f)**	**Assignments (orbital contribution)**
S_1	315	290	4.27	0.5148	HOMO → LUMO (91.39%)
S_2	255	236	5.24	0.0224	HOMO-1 → LUMO (63.82%) HOMO → LUMO (2.54%)
S_3	228	228	5.43	0.3064	HOMO-6 → LUMO (56.84%)

The structured emission was observed by **2** in non-polar solvents with a distinct two peaks at λ_{max}, 407 and 432nm (Figure 1c). The separation of these peaks corresponds to ~1421cm^{-1} which is attributed to the vibrational progressions related to the stretching frequency of C–C double bonds at the aromatic ligands[53-55].

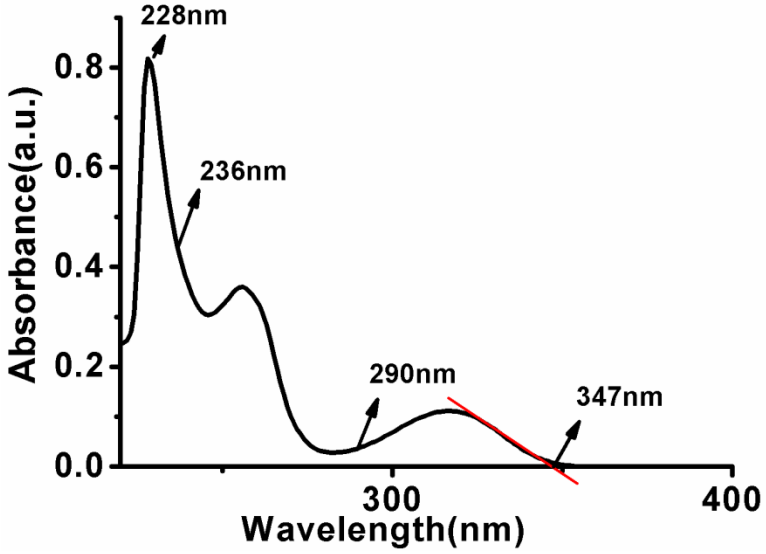

Figure. 3 Absorption spectrum of **2** in DCM at a concentration, 1x10^{-5}M.

In the crystal structure of **2**, the packing diagram shows head to tail arrangement of two molecules and that extends in one-dimension (Figure 4). The arrangement of molecules in one-dimensional packing with ladder type structure is substantiated the formation of J- aggregation (Figure 4) [56]. Furthermore, spectroscopic study shows red-shifted absorption (λ_{max} = 360nm) and emission (λ_{max} = 445nm) band supporting the formation of j-aggregation (Figure 5) [57].

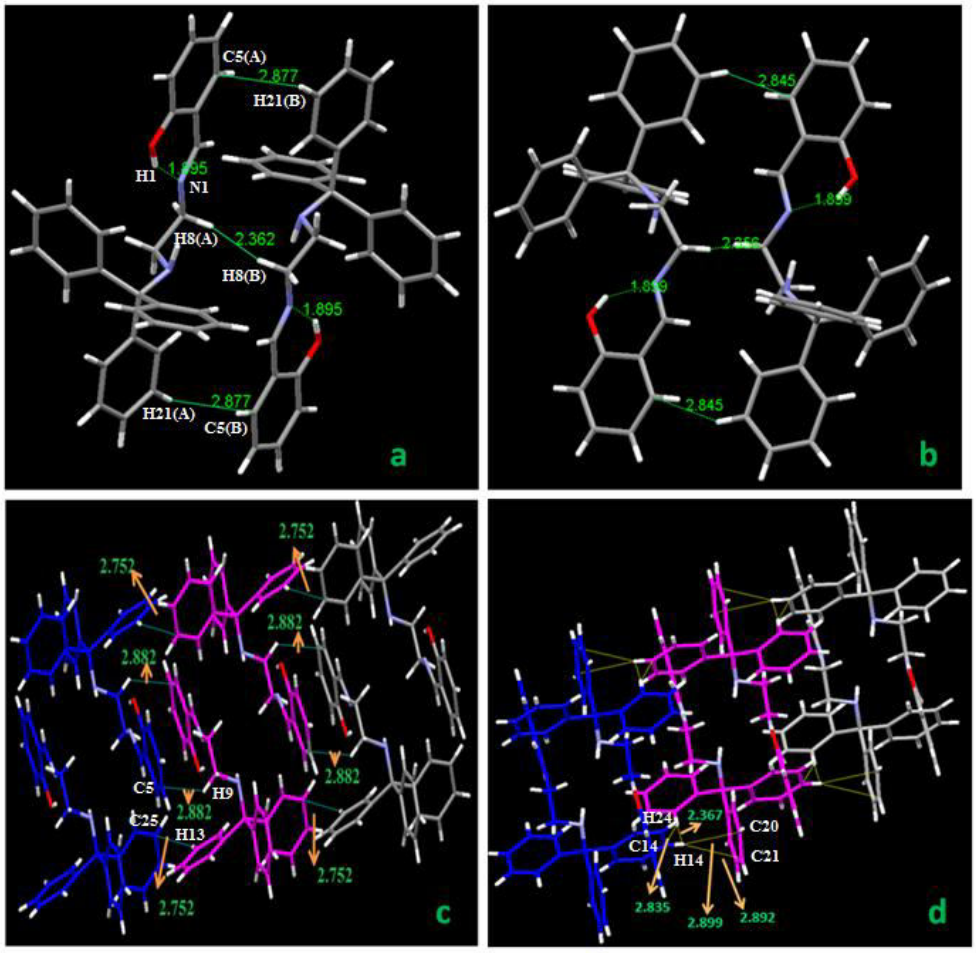

Figure 4 (a) and (c) show packing diagram of **2** at room temperature; (b) and (d) show packing diagrams of **2** at liq. N_2 temperature (short contacts are shown in Figure in Å unit)

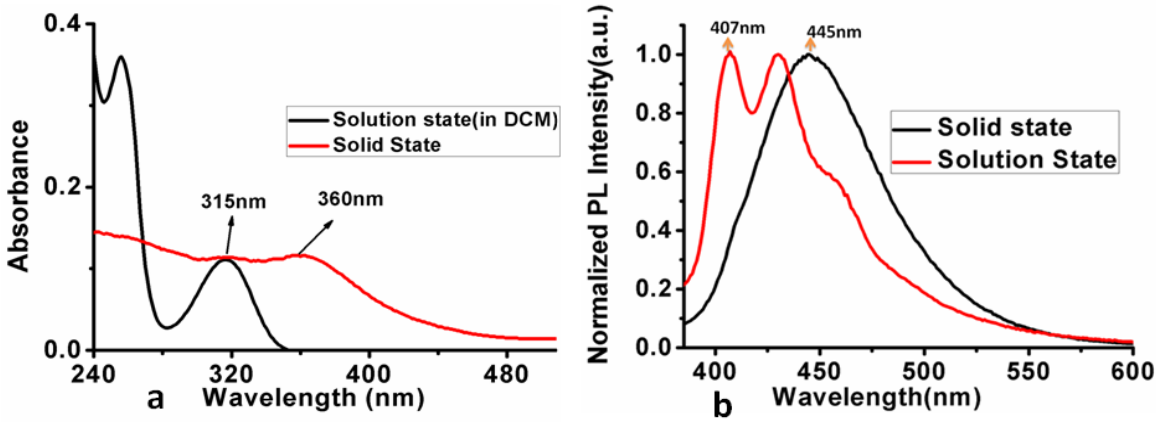

Figure.5 a) Shows absorption spectra of **2** in solution(in DCM; C =1×10^{-5}M) and solid state; b) Shows emission spectra of **2** in solution(in DCM; C = 1×10^{-5}M) state and solid state.

5A.2.3 Aggregation Induced Emission

Compound **2** is completely soluble in methanol, whereas it is insoluble in water. The combinations of these two solvents have been used to examine the AIE property similar as described earlier in chapter 4. After this experiment, three notable observations are shown: firstly, the emission intensity increases from 0% to 50% water concentration, secondly, PL intensity gradually decreases from 50% to 90% and thirdly, the emission wavelength shifts from 449nm to 497nm (from 0% to 50%) (Figure 6). It is performed of several experiments to investigate the causes of such variations of PL intensity.

A set of solutions have been prepared of **2** with different solvent mixture of methanol and polyethyleneglycol (PEG, viscous solvent) in the range of 0-90% (to a fixed amount of methanol, with gradually increasing order of PEG) which lead to the enhancement of emission intensity (Figure 7). This experiment shows that the mechanism of AIE activity of **2** is mainly operated through restricted intramolecular rotation (RIR). In the packing diagram (Figure 4a and 4c), it is observed that the rotating unit phenyl groups are involved in intermolecular short contacts and hence responsible for showing restricted intramolecular rotation that blocks the non-radiative channels and the observation of enhancement in emission intensity.

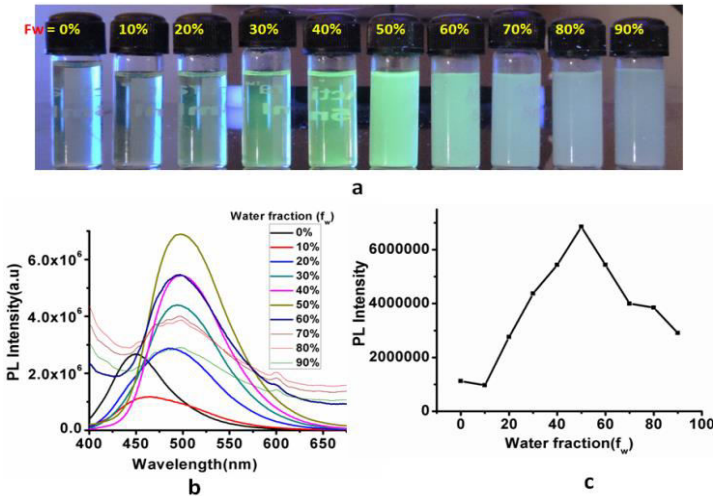

Figure. 6 (a) Luminescent images of **2** (λ_{exc} = 365nm) in water-MeOH mixed solvents with the concentration kept at 2×10^{-5} M; (b) PL spectra of **2** in MeOH/water mixed solvents with different f_w with excitation at 365nm; (c) The changes of PL peak intensity with different f_w (λ_{max} at 497 nm).

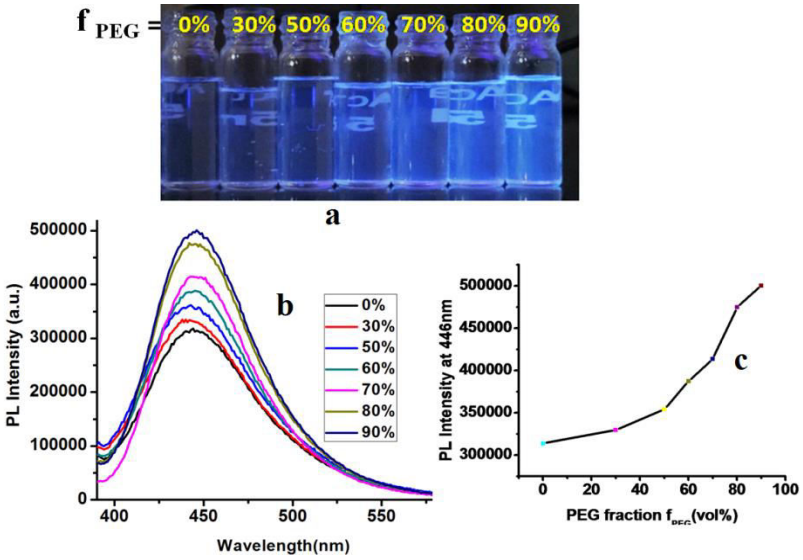

Figure. 7 a) Luminescent images of **2** (irradiated at 365nm by UV lamp); b) PL spectra of **2** in MeOH/PEG mixed solvents with different fraction of PEG (f_{PEG}) with exciting at 365nm; c) Plot of PL peak intensity change with different fraction of PEG in PEG-MeOH mixed solvents (f_{PEG}) (λ_{max} =449 nm) keeping the conc. at 2×10^{-5} M.

The 50% and 90% water fraction solutions were centrifuged, filtered and the residue at each fraction were collected. Then these were characterized by powder XRD. At 50% water fractions, the observed diffraction peaks are sharp and intense indicating the crystalline nature whereas at 90% fractions, broad peaks are observed indicating amorphous nature (Figure 8). Although RIR effect should increases the PL intensity with increasing concentration of water, but oppositely acting the transformation from crystalline to amorphous texture reduces the PL intensity. Hence at 50% water fraction the PL intensity become optimum and then it decreases further with increasing concentration of water till 90%.

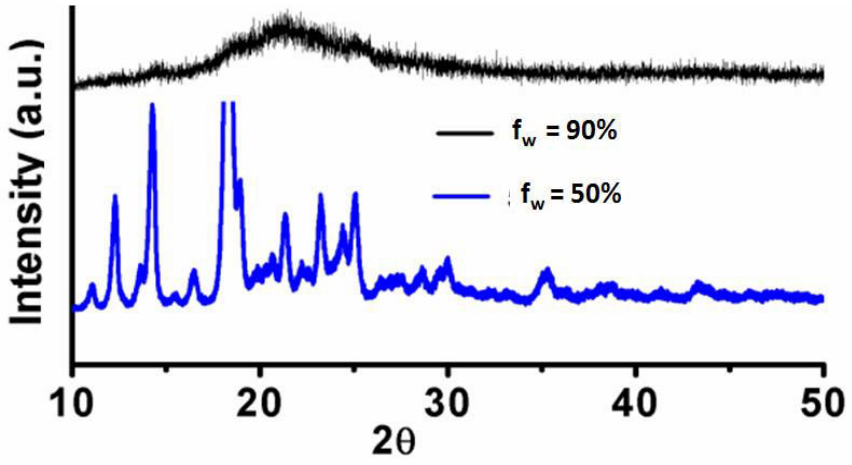

Figure. 8 Powder XRD of **2**.

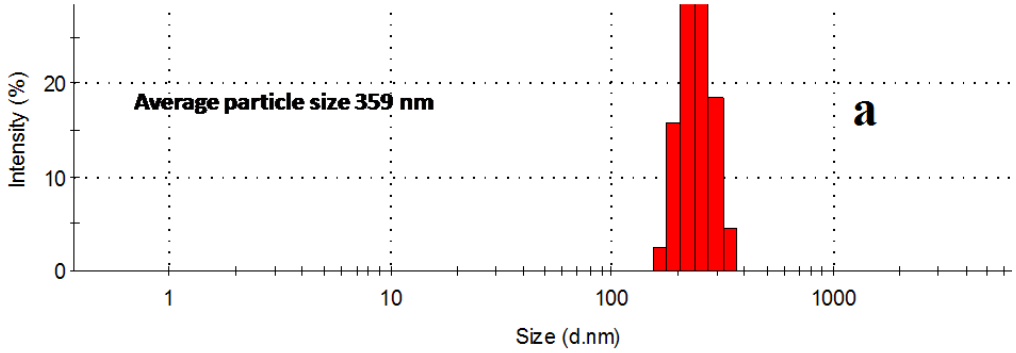

Figure. 9 Average particle size distribution of **2** at 50% methanol volume fractions in MeOH/Water mixture.

Because of increment in the polarity from 0% (only MeOH) to 50% (MeOH & water mixture is more polar than pure methanol) excited state of **2** interacts with dipoles of solvent molecules leading to a stabilization of ICT/TICT excited state with lowering energy resulting a red-shifted emission (Figure 7). The formation of aggregation was confirmed by DLS study and the average size of the aggregates is 359 nm at f_w = 50% (Figure 9).

5A.2.4 Mechanoluminescence (ML)

The blue emitting compound, **2** (λ_{max} = 445nm) in solid state is transformed into a green emitting form, **2a** (λ_{max} = 512nm) upon grinding (Figure 10) with a quite large shifting of emission wavelength (67nm).

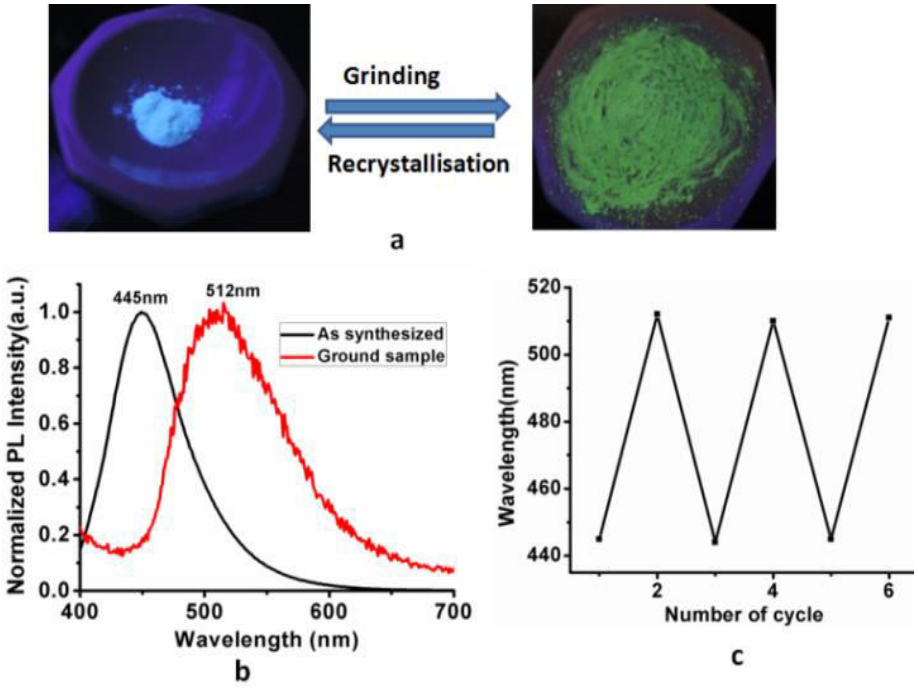

Figure. 10 (a) Shows luminescent images of as-synthesized, **2** and the sample after grinding of **2** (photograph taken under 365 nm UV illumination); (b) Emission spectra of as-synthesized solid and the sample after grinding of **2**; (c) Maximum emission wavelength change upon repeated grinding-recrystallization cycles of **2**.

Powder XRD pattern of **2** shows a sharp and intense peaks which indicates the crystalline nature, whereas the observation of relatively lower intense peaks of the ground sample, **2a**, pointing less / or semi crystalline nature (Figure 11). The peak position for the ground sample is changed from the original one.

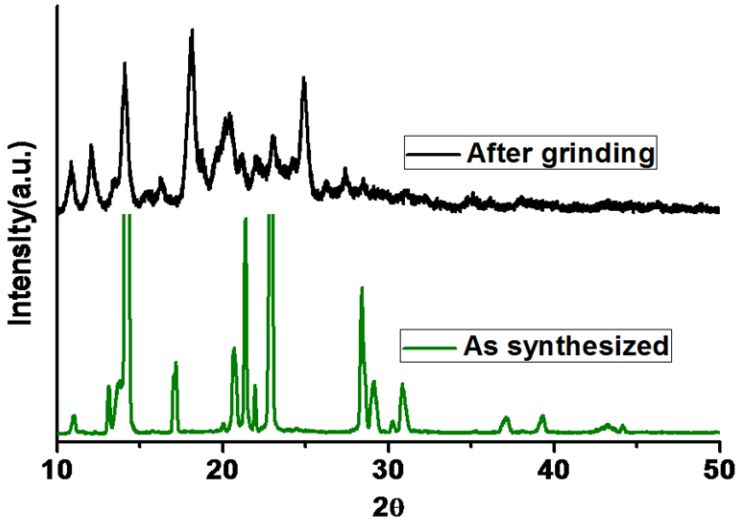

Figure. 11 Powder XRD of as-synthesized, **2** and after grinding of **2**

Additional support of such transition has been obtained from differential scanning calorimetry study. Both **2** and **2a** show the same melting point at ~104^{0}C, whereas only **2a** showing glass transition temperature at 49^{0}C (Figure 12). The ground compound, **2a** remains stable in solid phase for long days (checked up to 15 days). It is reverted into the original compound, **2** after dissolving it into dichloromethane followed by recrystallization.

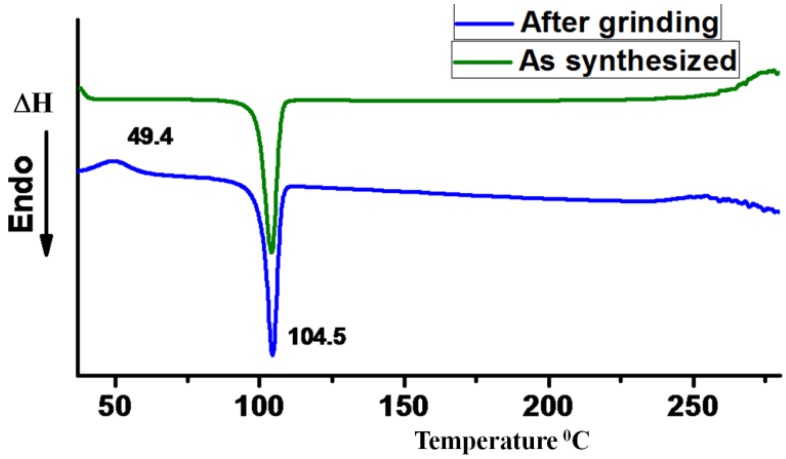

Figure. 12 DSC curve of **2** before grinding (green) and after grinding (blue) (glass transition temperature, 49.4 ºC; melting temperature, 104.5ºC)

On applying pressure with a hydraulic press (10ton pressure kept for 5min), **2** is transformed into a green emitting complex, **2b** (λ_{max} = 445nm→ 520nm). In the following case,

2b is slowly reverted into the pristine form, **2** (10h). On lowering the temperature of **2** to the temperature of liquid nitrogen (78K), the emission colour of **2** is changed into bluish-green (λ_{max} = 445nm → 490nm) (Figure 13) which is transformed reversibly into the original compound.

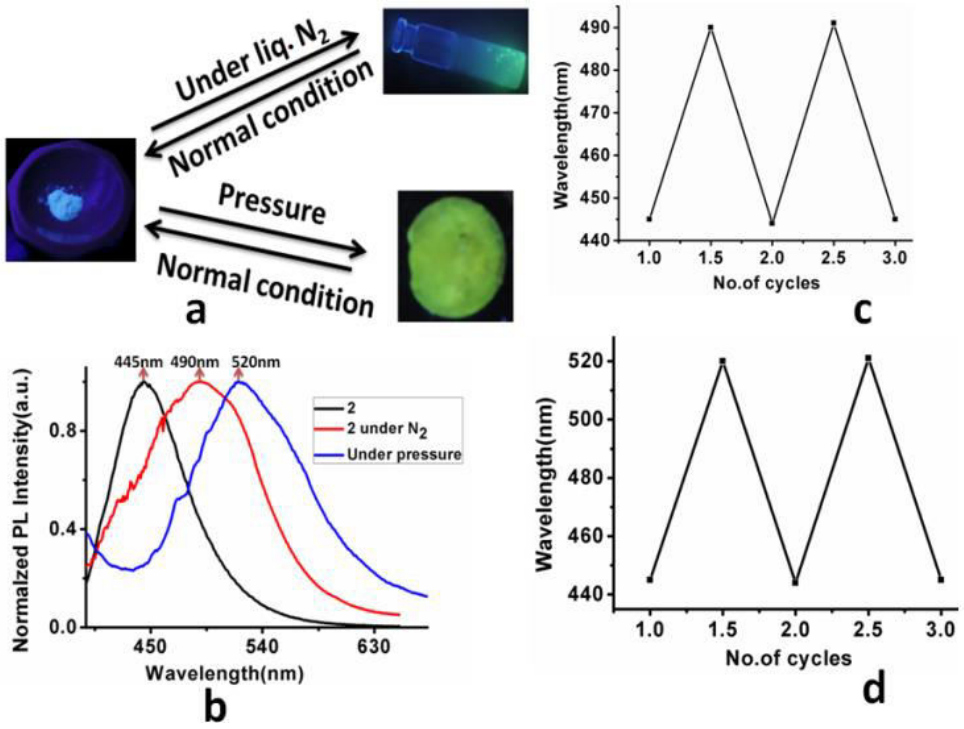

Figure. 13 (a) Shows luminescent images of **2** under various conditions (λ_{exc} = 365nm); (b) Emission spectra of as-synthesized solid, under liq.N_2 and under hydraulic pressure of **2**; after removal of triggers (hydraulic press / rising of temperature) the emission spectra (blue/red) is reverted to the original one (black); (c) Change of maximum emission wavelength upon changing condition of room temperature and liq.N_2 of **2** for several times (room temperature, λ_{max} = 445nm and liq N_2 temperature, λ_{max} = 490nm); (d) Maximum emission wavelength change upon repeated under pressure to normal condition cycles of **2.**

To investigate the mechanism behind different luminescence behavior with several external triggers [temperature, axial force (using hydraulic press) and shearing force], crystal structures have been obtained from the crystal data collecting at room temperature and low temperature (90K, Figure 4b, Figure 4d and Figure 14) of the same crystals of **2**. The packing diagram obtained from room temperature crystal data showing two molecules are placed in antiparallel orientation forming a molecular pair held by several interactions (two H-bonding and three short

contacts) (Table 2a). A long range one-dimensional chain type pattern is generated through interactions of each of these molecular pairs to the neighbouring pair which are held with a total of four interactions and repeating themselves in an one-dimension (Figure 4c &Table 2a). Each of these one dimensional chains is again involved in interacting sideways (through a total eight interactions) to another one which is sited parallel to it and the pattern extends in both sides forming a two-dimensional sheet (Figure14a).It is to be noted that the complex **2** exhibited ML property by reversible transformation under applying an axial force (by hydraulic) and the same is observed by lowering the temperature up to 90K. But it is transformed irreversibly under applying shearing force (grinding in a mortar pestle). From the crystal structure at the room temperature, it is observed that the presence of several short contacts bind the two molecules that lead to form a molecular pair positioned in a symmetric fashion. On comparison of this structure with the one recorded at low temperature (90K), there has no noticeable changes observed (including short-contacts) within the molecular pair. Hence there has no appreciable change observed on the structure of molecular pairs by lowering temperature. Furthermore, comparison to the next level of structure where the molecular pair unit itself involved to interact with the neighbouring molecular pair leading to one-dimensional molecular chain (two inequivalent short contacts are present, 2.882 and 2.752Å, between two molecular pairs (Figure 4c)).But on comparative study of it with the one whose X-ray structural data is recorded at liq. N_2 temperature, there has no significant structural changes observed (four new molecular interactions observed) (Figure 4d). This minor structural change on lowering temperature results a change in electron distribution and hence the emission colour. But the overall structures regain the original symmetry and hence the stable form with gradual rising of temperature. This phenomenon can be extended to the case which rationalizes the reversible transformation that occurs by applying normal stress (hydraulic press) and this fact can be related to the elastic mechano luminescent. From these studies, it is speculated that reason behind the irreversible transformation as observed under shearing stress (grinding) can be rationalized by the permanent deformation occurring into the molecular pairs from their regular arrangements. The crystal data for the compounds **2** (at 293K and 90K) and **2b** (at 293K) have been given in Table 3, 4 and 5, respectively.

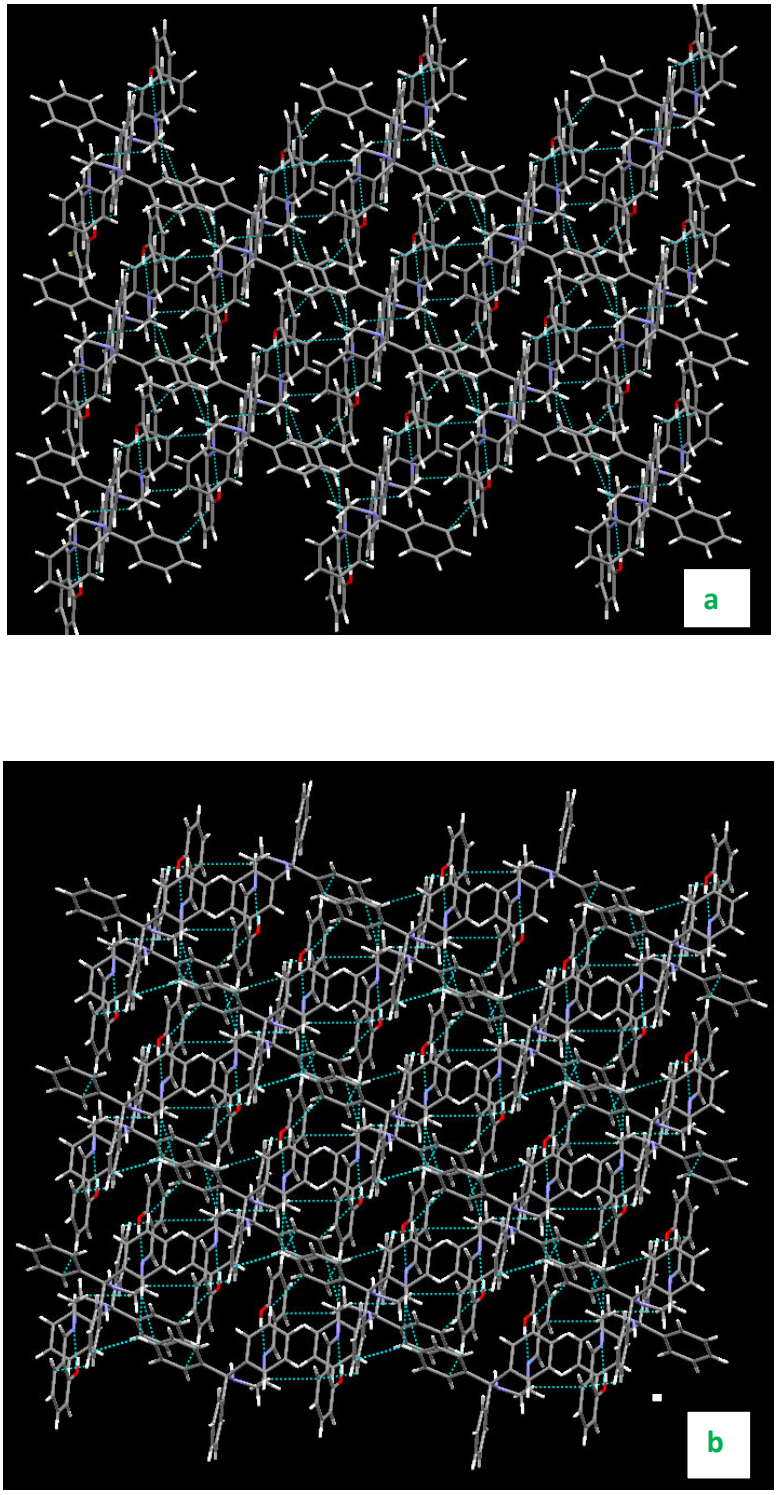

Figure. 14 a) Shows packing diagram of **2** at room temperature; b) Shows packing diagrams of **2** at liq. N_2 temperature (interaction shown in Figure in Å unit)

Table.2 H-bonding interactions and short-contacts (Å) present within a molecule, within a molecular pair and between molecular pairs (a, for the structure collected at room temperature; b, the structure collected at 90K)

a

S. No	Type of interactions	Within a molecule	Within molecular pair interactions	Molecular pair to molecular pair interactions
1	Hydrogen bond	N1...H1 = 1.895 Å	---	---
2	Inequivalent short contacts	---	C5...H21= 2.873 Å H8...H8 = 2.357 Å	C5...H9 = 2.882 Å C25...H13 = 2.752 Å

b

S. No	Type of interactions	Within a molecule	Within molecular pair interactions	Molecular pair to molecular pair interactions
1	Hydrogen bond	N1...H1 = 1.899 Å	---	---
2	Inequivalent short contacts	---	C5(A)...H21(B) = 2.845Å H8(A)...H8(B) = 2.356 Å	H14(A)...C20(B) = 2.899 Å H14(A)...C21(B) = 2.892 Å H24(B)...C14(A)= 2.835 Å H24(B)...H14(A) = 2.367 Å

5A.2.5 Sensory Application

AIE active **2** has a great potential to sense metal cation, because of the presence of O, N coordinating sites with appropriate ring-size ligands. The emission intensity of **2** in methanol was very weak (λ_{max} 449nm; λ_{exc} 365nm) because of *cis-trans* isomerisation of **2** with respect to C=N moiety and rotation of triphenyl group in solution state. The weakly emissive solution of **2** is transformed into a bright blue solution in presence of Zn(II) salts. We have studied the selectivity test and found that there has no change of emission colour in the presence of different metal ions such as Mg^{2+}, Zn^{+2}, K^{+}, Na^{+}, Hg^{+2}, Cd^{+2}, Ca^{+2}, Cu^{+2}, Ba^{+2}, Bi^{+3}, Co^{+2} and Pb^{+2} (Figure 15a & Figure 15b). At room temperature reaction, none of the congeners of Zn(II) [Mg(II), Cd(II) and

Hg(II)] results any emission after addition of **2** into their respective salts [$Mg(NO_3)_2$, $Cd(NO3)_2$ and $HgCl_2$] in methanol.

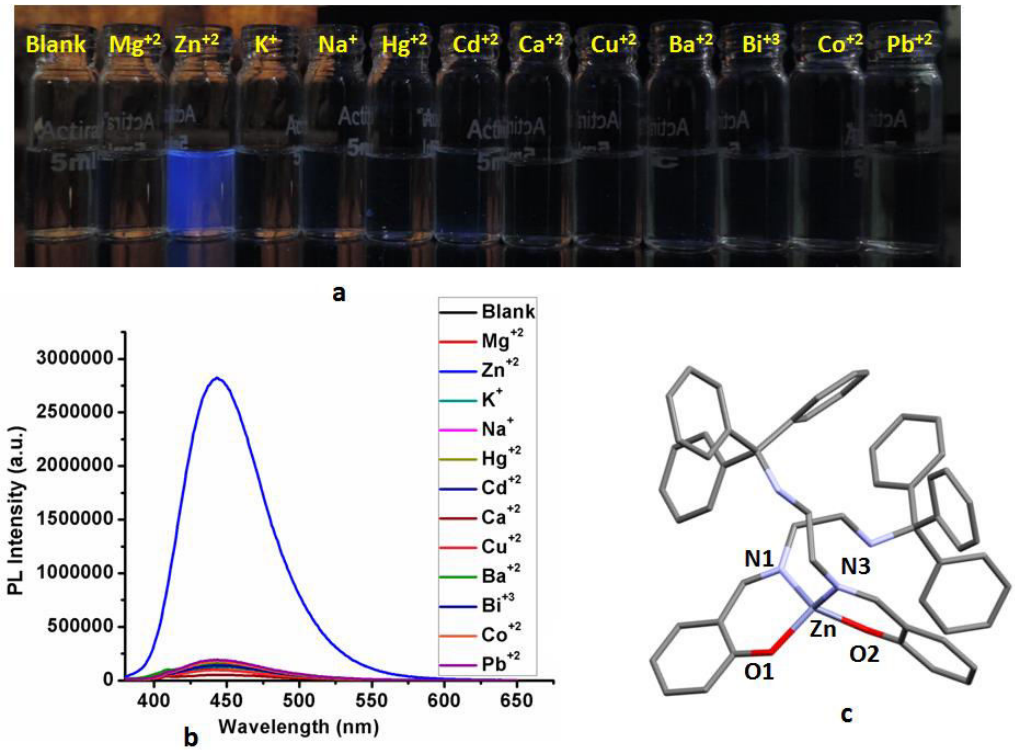

Figure. 15 (a) Luminescent images of **2** in methanol (c, $1X10^{-5}$M) with various metal salts (10 equiv., $\lambda_{exc.}$= 365 nm); (b) Emission spectra of **2** in various salts; (c) Single crystal structure of **2b** with Zn(II).

It is observed that Mg(II) and Cd(II) salts result in green and blue emission, respectively if the reaction mixture is heated at 70°C with stirring for ~15min (Figure 16). But Hg(II) salt doesn't produce any emission even upon heating for longer time. While Zn(II) salt shows the following emission instantaneously on adding of **2** at room temperature. It can be explained based on the general trend of reactivity of Zn(II) which is expected to be higher as compared to its congeners. Furthermore, Hg(II) and Cd(II), being softer can't easily react with the hard ligated donors N and O in **2**.

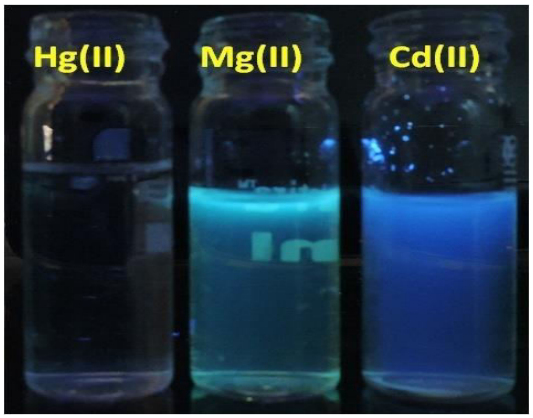

Figure. 16 Luminescent images of **2** in methanol (c, $1x10^{-5}$M) with $HgCl_2$, $Mg(NO_3)_2$ and $Cd(NO_3)_2$ (10 equiv., λ_{exc} = 365 nm) stirred for 15 minutes at 70°C.

The emission intensity was found to ~23 times higher in presence of Zn(II) metal ion as compared to blank solution (other metal ions do not interfere into the emission spectra). The absorption spectra of **2** shows two peaks at 314 and 402nm, which are gradually decreasing and absorption at 352nm is gradually increasing with addition of Zn(II) metal ion (Figure 17), in addition it is observed two isosbestic points at 337nm and 373nm. It indicates Zn(II) metal ion is interacting with **2**.

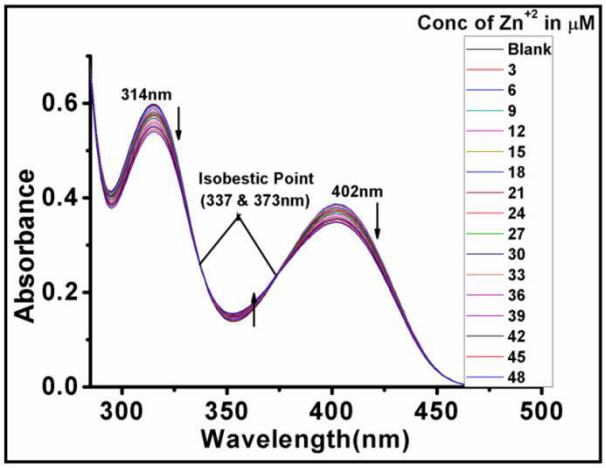

Figure. 17 Absorption spectra of **2** in MeOH (conc. $1x10^{-5}$M) with gradual increasing concentration of $Zn(NO_3)_2$.

Titration experiment was performed by the help of steady state fluorescence spectrophotometer. Gradual addition of Zn(II) metal ion into the methanolic solution of **2**, emission intensity rises up at λ_{max}, 410nm and 446nm (Figure 18). A linear relationship was found between concentration of Zn(II) metal ion (0 to 12μM) with PL intensity of **2** (Figure 18) at 410nm and 446nm, indicating sensitivity of **2** towards Zn(II) metal ion. The detection limit was calculated as ~0.064ppm (0.000064g/kg), with the help of 3σ/m, where σ is a standard deviation of the blank measurements and m is the slope. Furthermore, to evaluate the selectivity for Zn(II), the fluorescence spectra of **2** was recorded in presence of Zn(II) and the various metal ions [Mg(II), Zn(II), K(I), Na(I), Hg(II), Cd(II), Ca(II), Cu(II), Ba(II), Bi(III), Co(II) and Pb(II)] was added and found that there had no detectable change of emission (Figure 19). To grow single crystals, 10 equivalents of Zn(II) salts was added into the methanolic solution of **2** and kept aside for overnight and obtained the single crystals of Zn(II) complex (**2b**).

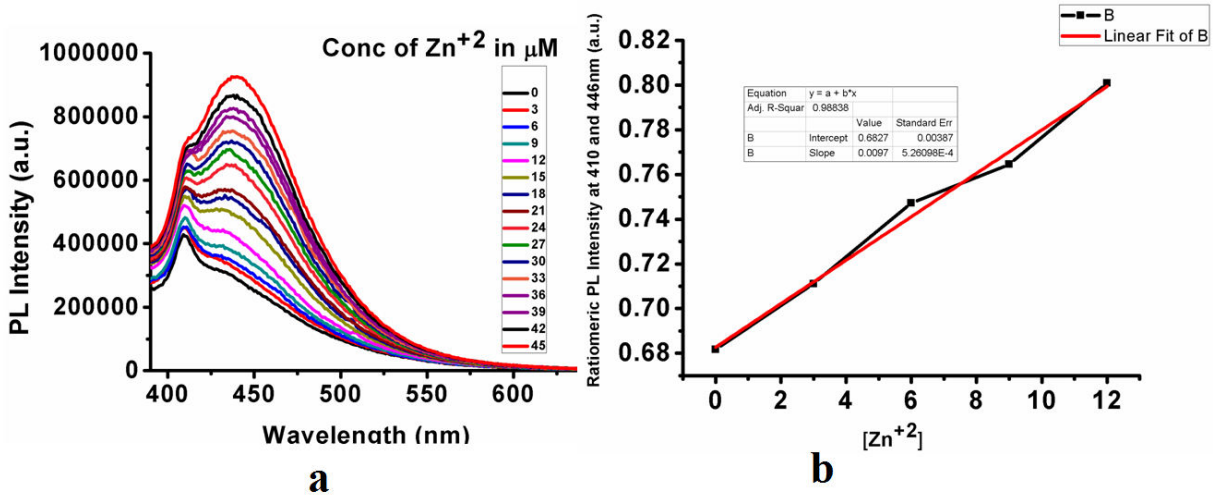

Figure. 18 (a) The luminescent spectral changes of **2**in MeOH with [M] = 10^{-6} mol L^{-1} upon gradual increasing concentration of $Zn(NO_3)_2$; (b) A linear fitting was obtained between concentration range from 0 to 12μM in methanol vs. PL intensity

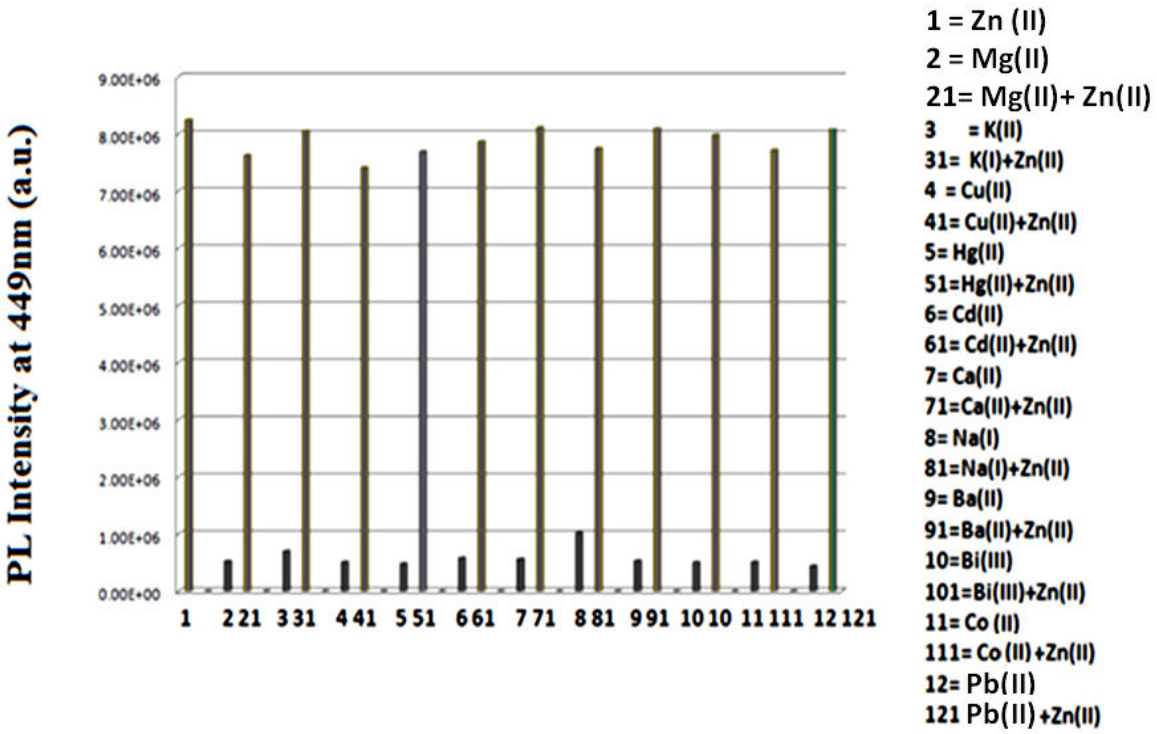

Figure. 19 The comparative fluorescent intensity at 449 nm of mixture of compound **2**with various salt solutions in MeOH (10equiv) and the mixtures with Zn(II) salt (λ_{ex} = 365 nm, λ_{em} = 449 nm).

The analyzed single crystal structure of the complex was found to form bis complex where the ligand is coordinated in chelating mode forming a six-membered ring (Figure 15c & Table 5)

5A.3 Conclusion

It has been strategically designed and synthesized an 'Aggregation Induced Emission' active organic molecule **2**, by following Schiff-base technique. The cause of the AIE property was investigated and identified as 'restricted intramolecular rotation' (RIR). It shows ML property upon grinding which is irreversible in nature. More or less similar emissive colour change can be achieved upon lowering temperature of the sample to liq. N_2 / or putting normal pressure with a hydraulic press. Interestingly, in both cases this change can be reverted by bringing the low temperature back to room temperature / standing for several hours of the ground sample by hydraulic press. The mechanism

behind this property has been rationalized. Furthermore, it selectively senses Zn(II) through turn-on emission signal with detection limit 0.064ppm and the cause behind of it has been rationalized.

5A.4 Experimental Section

General Syntheses of N1-tritylethane-1,2-diamine, **1**(we discussed in earlier chapter)

General Synthesis of [2-(2-(tritylamino)ethylideneamino) methyl phenol], 2. Salicylaldehyde (0.82mmol, 0.1g), N1-tritylethane-1,2-diamine (0.82mmol, 0.247g) and catalytic amount of acetic acid were dissolved in a 5ml of methanol and stirred at room temperature. After 30min of stirring, a light green precipitate was separated out, filtered and dried under vacuum oven for 15 min. The crude product was recrystallized by methanol which produced a solid product. Yield, 90%.

^{1}H NMR (400 MHz, $CDCl_3$) (Figure 20) δ 13.41 (s, 1H), 8.44 (s, 1H), 7.53 – 7.44 (m, 6H), 7.32 (dddd, J = 10.2, 7.9, 5.0, 1.6 Hz, 8H), 7.24 – 7.15 (m, 3H), 6.94 (ddd, J = 17.1, 8.5, 4.6 Hz, 2H), 3.74 (t, J = 5.5 Hz, 2H), 2.54 – 2.45 (t, 2H) : **^{13}C NMR** (101 MHz, CDCl3) (Figure 21) δ 165.88, 161.19, 145.92, 132.26, 131.29, 128.57, 127.91, 126.34, 118.79, 118.57, 117.04, 70.81, 60.40, 44.18.

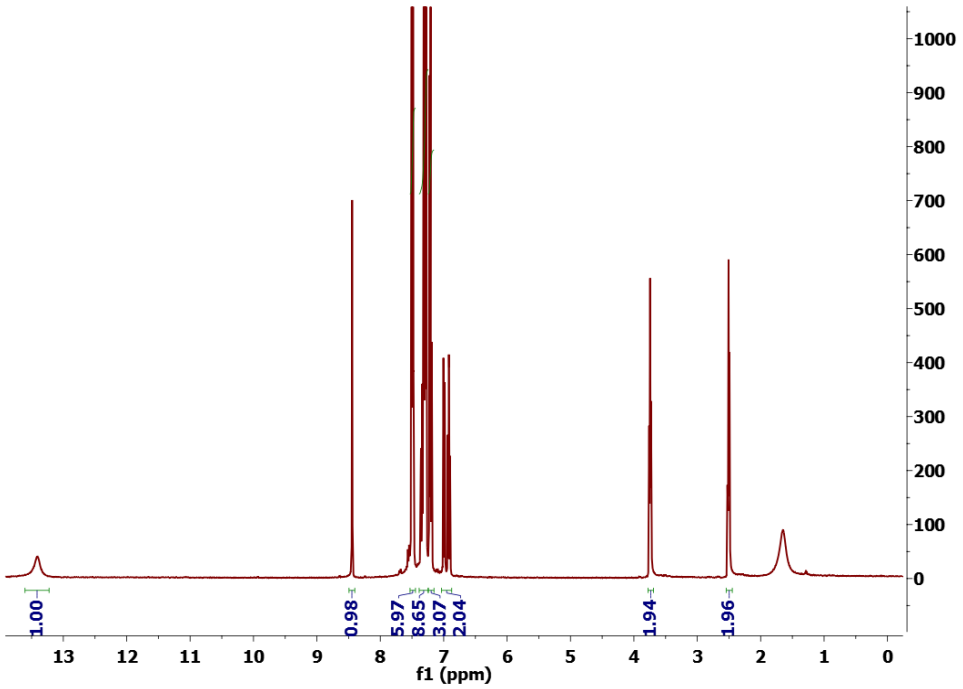

Figure. 20 ^{1}H NMR spectrum of **2**

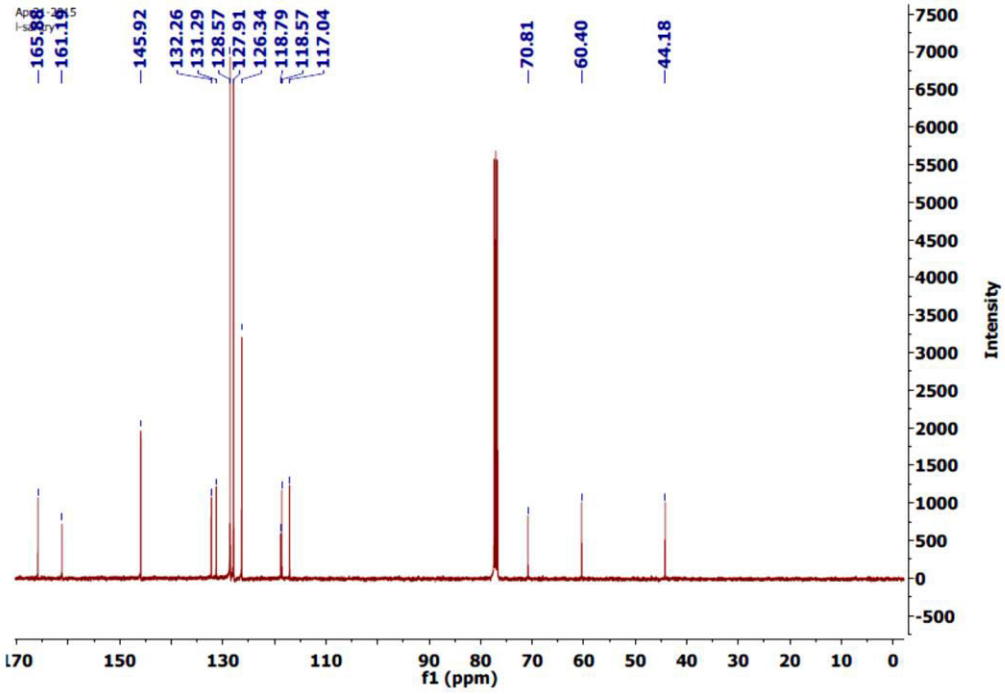

Figure. 21 ^{13}C NMR spectrum of **2**

Table 3 Crystal data and structure refinement for **2** at 293K

Empirical formula	$C_{28}H_{26}N_2O$
Formula weight	406.51
Temperature/K	293
Crystal system	Triclinic
Space group	$P\bar{1}$
a/Å	8.6938(3)
b/Å	9.22050(10)
c/Å	14.9549(13)
α/°	75.860(19)
β/°	85.34(2)
γ/°	67.887(16)
Volume/Å^3	1076.90(18)
Z	2
ρ_{calc}g/cm^3	1.254
μ/mm^{-1}	0.076
F(000)	432.0
Crystal size/mm^3	0.2 × 0.2 × 0.2
Radiation	MoKα (λ = 0.71075)
2Θ range for data collection/°	6.19 to 54.968
Index ranges	$-11 \le h \le 11$, $-11 \le k \le 11$, $-19 \le l \le 19$
Reflections collected	11595
Independent reflections	4902 [R_{int} = 0.0442, R_{sigma} = 0.0458]
Data/restraints/parameters	4902/0/285
Goodness-of-fit on F^2	1.076
Final R indexes [I>=2σ (I)]	R_1 = 0.0494, wR_2 = 0.1290
Final R indexes [all data]	R_1 = 0.0641, wR_2 = 0.1426
Largest diff. peak/hole / e Å^{-3}	0.26/-0.18

Table 4 Crystal data and structure refinement for **2** at 90K

Empirical formula	$C_{28}H_{26}N_2O$
Formula weight	406.51
Temperature/K	90K
Crystal system	Triclinic
Space group	$P\bar{1}$
a/Å	8.652(1)
b/Å	9.2161(6)
c/Å	14.815(2)
α/°	75.93(4)
β/°	85.85(4)
γ/°	68.03(3)
Volume/Å^3	1062.4(4)
Z	2
ρ_{calc}g/cm^3	1.271
μ/mm^{-1}	0.077
F(000)	432.0
Crystal size/mm^3	-
Radiation	MoKα (λ = 0.71075)
2Θ range for data collection/°	-
Index ranges	-
Reflections collected	-
Independent reflections	
Data/restraints/parameters	-
Goodness-of-fit on F^2	-
Final R indexes [I>=2σ (I)]	-
Final R indexes [all data]	-
Largest diff. peak/hole / e Å^{-3}	-

Table 5 Crystal data and structure refinement for **2b** at 293K

Empirical formula	$C_{56}H_{52}N_4O_2Zn$
Formula weight	878.38
Temperature/K	293(2)
Crystal system	Triclinic
Space group	$P\bar{1}$
a/Å	13.339(4)
b/Å	13.342(4)
c/Å	15.359(5)
α/°	95.814(3)
β/°	109.924(7)
γ/°	112.425(9)
Volume/Å^3	2289.8(12)
Z	2
ρ_{calc}g/cm^3	1.274
μ/mm^{-1}	0.583
F(000)	924.0
Crystal size/mm^3	0.1 × 0.1 × 0.1
Radiation	MoKα (λ = 0.71075)
2Θ range for data collection/°	6.166 to 54.976
Index ranges	-17 ≤ h ≤ 17, -17 ≤ k ≤ 17, -19 ≤ l ≤ 19
Reflections collected	25027
Independent reflections	10469 [R_{int} = 0.0908, R_{sigma} = 0.1280]
Data/restraints/parameters	10469/0/568
Goodness-of-fit on F^2	1.054
Final R indexes [I>=2σ (I)]	R_1 = 0.0853, wR_2 = 0.1445
Final R indexes [all data]	R_1 = 0.1796, wR_2 = 0.1919
Largest diff. peak/hole / e Å^{-3}	0.46/-0.38

Procedure of collecting the aggregate

To record the PXRD of **2** at f_h = 50% and f_h = 90% we used centrifuge method. For that we have prepared aggregate of f_h = 50% and f_h = 90% large amount (each case 100 ml). Then at 10000 rotation/minutes for 10minutes centrifuged, then we collected the powder and recorded PXRD.

5A.5. References

[1] D. Amgar, S. Aharon and L. Etgar, *Adv. Funct. Mater*., 2016, **26**, 8576.

[2] A. Paun, N. D. Hadade, C. C. Paraschivescu and M. Matache*, J. Mater. Chem. C*, 2016, **4**, 8596.

[3] L. Gengwei, P. Huiren, C. Long, N. Han, L. Wenwen, L. Yinghao,C. Shuming, H. Rongrong, Q. Anjun, Z. Zujin and B. Z. Tang,*ACS Appl. Mater. Interfaces*, 2016, **8**, 16799.

[4] K. Suzuki, T. Kimura, H. Shinoda, G. Bai, M. J. Daniels,Y. Arai, M. Nakano and T. Naga, *Nat. Commun*., 2016,**7**, 13718.

[5] S. S. Pasha, P. Das, N. P. Rath, D. Bandyopadhyay, N. R. Jana and I. R. Laskar, *Inorg. Chem. Commun*., 2016, **67**, 107.

[6] W. Zhang, Y.-Y. Ren, L.-N. Zhang, X. Fan, H. Fan, Y. Wu, Y. Zhang and G.-C. Kuang, *RSC Adv*., 2016, **6**, 101937.

[7] W. P. Dempsey, S. E. Fraser and P. Pantazis, *BioEssays*, 2014,**34**, 351.

[8] S. S. Pasha, P. Alam, S. Dash, G. Kaur, D. Banerjee, R. Chowdhury, N. Rath, A. R. Choudhury and I. R. Laskar, *RSC Adv*., 2014, **4**, 50549.

[9] Y. Yang, Q. Zhao, W. Feng and F. Li, Chem. Rev., 2013, 113, 192.

[10] Q. Zhan, J. Qian, H. Liang, G. Somesfalean, D. Wang, S. He, Z. Zhang and S. A. Engels, *ACS Nano*, 2011, **5,** 3744.

[11] S. Wang and S. G. Feng, *Langmuir*, 2016, **48**, 725.

[12] W. Ding, G. Zhang, H. Zhang, J. Xu, Y. P. Wen and J. Zhang, *Sens. Actuators, B*, 2016, **237**, 59.

[13] Z. Zece, W. Sheng, W. Danqing and C. Yang, *Biosens. Bioelectron*., 2016, **85**, 792.

[14] X.-Y. Wang, C.-G. Niu, L.-Y. Hu, D.-W. Huang, S.-Q. Wu, L. Zhang and G.-M. Zeng, *Sens. Actuators, B*, 2017, **243**, 1046.

[15] M. Shyamal, P. Mazumdar, S. Maity, G. P. Sahoo, G. Salgado- Moran and A. Misra, *J. Phys. Chem. A*, 2016, **120**, 210.

[16] P. Alam, V. Kachwal and I. R. Laskar, *Sens. Actuators, B*,2016, **228**, 539–550.

[17] H. Liu, Y. Dong, B. Zhang, F. Liu, C. Tan, Y. Tan and Y. Jiang, *Sens. Actuators, B*, 2016, **234**, 616.

[18] X. F. Ma, R. Sun, J. H. Cheng, J. Y. Liu, F. Gou, H. F. Xiang and X. Zhou, J. *Chem. Educ*., 2016, **93**, 345.

[19] W. Z. Yuan, P. Lu, S. C. Jacky, W. Y. Lam, Z. Wang, Y. Liu, H. S. Kwok, Y. Ma and B. Z. Tang, *Adv. Mater*., 2010, **22**, 2159.

[20] J. Luo, Z. Xie, J. W. Y. Lam, L. Cheng, H. Chen, C. F. Qiu, H. S. Kwok, X. Zhan, Y. Liu, D. Zhuc and B. Z. Tang, *Chem. Commun*., 2001, **20**, 1740.

[21] X. Zhang, Z. Chi, Y. Zhang, S. Liu and J. Xu, *J. Mater. Chem. C*, 2013, **1**, 3376.

[22] A. Pucci, F. D. Cuia, F. Signori and G. Ruggeri, *J. Mater. Chem*., 2007, **17**, 783.

[23] Y. Dong, J. W. Y. Lam, A. Qin, J. Liu, Z. Li, B. Z. Tang, J. Sun and H. S. Kwok, *Appl. Phys. Lett*., 2007, **91**, 11111.

[24] B. R. Crenshaw, M. Burnworth, D. Khariwala, A. Hiltner, P. T. Mather, R. Simhaand and C. Weder, *Macromolecules*, 2007, **40**, 2400.

[25] Z. Ning, Z. Chen, Q. Zhang, Y. Yan, S. Qian, Y. Cao andH. Tian, *Adv. Funct. Mater*., 2007, **17**, 3799.

[26] M. Kinami, B. R. Crenshaw and C. Weder, *Chem. Mater*.,2006, **18**, 946.

[27] S. J. Toal, K. A. Jones, D. Magde and W. C. Trogler, *J. Am.Chem. Soc*., 2005, **127**, 11661.

[28] S. Hirata and T. Watanabe, *Adv. Mater*., 2006, **18**, 2725.

[29] S. J. Lim, B. K. An, S. D. Jung, M. A. Chung and S. Y. Park,*Angew. Chem., Int. Ed*., 2004, **43**, 6346.

[30] C. E. Olson, M. J. R. Previte and J. T. Fourkas, *Nat. Mater*.,2002, **1**, 225.

[31] M. Irie, T. Fukaminato, T. Sasaki, N. Tamaiand andT. Kawai, *Nature*, 2002, **420**, 759.

[32] A. Kishimura, T. Yamashita, K. Yamaguchi and T. Aida, *Nat.Mater*., 2005, **4**, 546.

[33]Y. Sagara, S. Yamane, T. Mutai, K. Araki and T. Kato, *Adv.Funct. Mater*., 2009, **19**, 1869.

[34] R. Gawinecki, G. Viscardi, E. Barni and M. A. Hanna, *DyesPigm*., 1993, **23**, 73.

[35] A. K. Srivastava, A. K. Singh, N. Kumari, R. Yadav, A. Gulino,A. Speghini, R. Nagarajan and L. Mishra, *J. Lumin*., 2017,**182**, 274.

[36] S. T. Zhang, T. R. Li, B. D.Wang, Z. Y. Yang, J. Liu, Z. Y.Wangand W. K. Dong, *Dalton Trans*., 2014, **43**, 2713.

[37] K. Ohno, S. Yamaguchi, A. Nagasawa and T. Fujihara, *DaltonTrans*., 2016, **45**, 5492.

[38] T. Han, X. G. Gu, J. W. Y. Lam, A. C. S. Leung, R. T. K. Kwok,T. Y. Han, B. Tong, J. B. Shi, Y. P. Dong and B. Z. Tang,*J. Mater. Chem. C*, 2016, **4**, 10430.

[39] N. Roy, A. Dutta, P. Mondal, P. C. Paul and T. S. Singh, *Sens.Actuators, B*, 2016, **236**, 719.

[40] G. Donadio, R. D. Martino, R. Oliva, L. Petraccone,P. D. Vecchio, B. D. Luccia, E. Ricca, R. Isticato, Al.D. Donato and E. Notomista, *J. Mater. Chem. B*, 2016, **4**,6979.

[41] N. A. Bumagina, E. V. Antina, A. Y. Nikonova, M. B. Berezin,A. A. Ksenofontov, A. I. Vyugin, *J. Fluoresc*., 2016, **26**, 1967.

[42] X. Zhang, H. Li, G. Liu, S. Pu, *J. Photochem. Photobiol., A*, 2016, **330**, 22.

[43] M. Amirnasr, R. S. Erami, S. Meghdadi, *Sens. Actuators, B*, 2016, **233**, 355.

[44] Y. B. Ding, X. Li, T. Li, W. H. Zhu and Y. S. Xie, *J. Org. Chem*., 2013, **78**, 5328.

[45] S. Samanta, U. Manna, T. Ray and G. Das, *Dalton Trans*., 2015, **44**, 18902.

[46] (a) Y. Zhou, H. N. Kim and J. Yoon, *Bioorg. Med. Chem. Lett*., 2010, 1, 125; (b) X. Feng, Y. Q. Feng, J. J. Chen, S. W. Ng, L. Y. Wang and J. Z. Guo, *Dalton Trans*., 2015, **44**, 804.

[47] J. C. Qin, B. D. Wang, Z. Y. Yang and K. C. Yu, *Sens. Actuators, B*, 2016, **224**, 892.

[48] O. V. Dolomanov, L. J. Bourhis, R. J. Gildea, J. A. K. Howard and H. Puschmann, *J. Appl. Crystallogr*., 2009, **42**, 339.

[49] M. Sowmiya, A. K. Tiwari, Sonu and S. K. Saha, *J. Photochem. Photobiol. A*, 2011, **218**, 76.

[50] S. Jana, S. Dalapati and N. Guchhait, *J. Phys. Chem. A*, 2013, **117**, 4367.

[51] Sonu, A. K. Tiwari, A. Sarmah, R. K. Roy and S. K. Saha, *Dyes Pigm*., 2014, **102**, 114.

[52] M. J. Frisch, G. W. Trucks, H. B. Schlegel, G. E. Scuseria, M. A. Robb, G. Cheeseman, V. Barone, B. Mennucci and G. A. Petersson, et al., Gaussian 09, 2010, Revision C. 01, *Gaussian, Inc*., Wallingford, CT, 2010.

[53] A. F. Rausch, H. H. H. Homeier and H. Y. Top, *Organomet. Chem*., 2010, **29**, 193

[54] E. Baranoff, S. Fantacci, F. De Angelis, X. Zhang and R. Scopelliti, *Inorg. Chem*., 2011, **50**, 451

[55] S. Obara, M. Itabashi, S. Tamaki, Y. Tanabe, Y. Ishii, K. Nozaki and M. A. Haga, *Inorg. Chem*., 2006, **45**, 8907.

[56] F. Wurthner, T. E. Kaiser and C. R. Saha-Moller, *Angew. Chem., Int. Ed*., 2011, **50**, 3376.

[57] H. Manzano, L. Esnal, T. M. Matesanz, J. Ban˜uelos, I. L. Arbeloa, M. J. Ortiz, L. Cerdan, A. Costela, I. G. Moreno and J. L. Chiara, *Adv. Funct. Mater*., 2016, **26**, 2756.

Chapter V

PART-B

Strategic Design and Synthesis of Schiff-base based 'Aggregation Induced Emission' Active Molecule: Study of Reversible and Turn on Mechanoluminescent Property

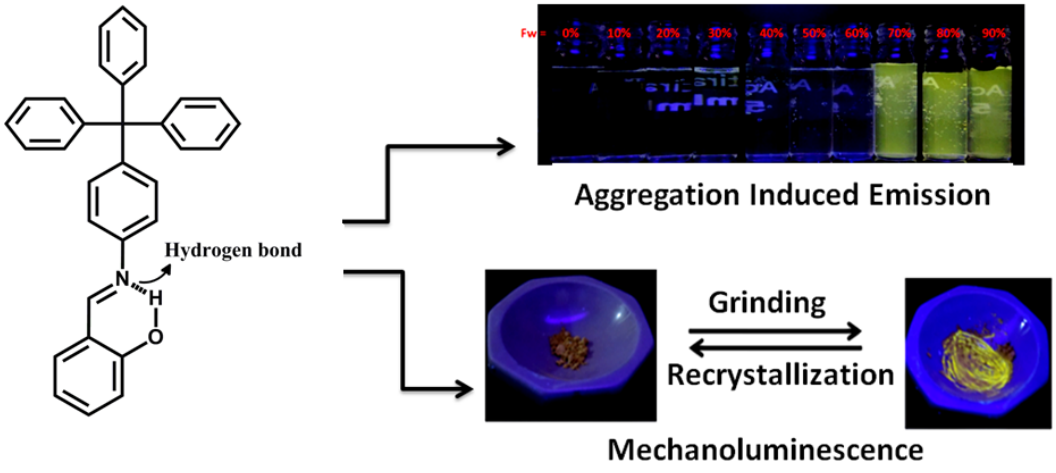

5B.1. Introduction

Luminescent materials are useful in the field of organic light emitting diodes (OLED) [1-3], chemo sensing [4-5], bio imaging [6-7], currency security [8-9] etc. 'Aggregation Caused Quenching' (ACQ) effect is a detrimental effect of luminogens which degrades the performances of solid state devices. 'Aggregation Induced Emission' (AIE) active materials [10-11]] would be useful to resolve these problems (discussed in Chapter 3B).

The syntheses of Schiff-base type of compounds draw special attraction to the scientific communities because these can be prepared in a simple technique with high yield. As an organoluminogens, Schiff-base compounds are widely reported, but few reports are found as AIEgens.

Mechanoluminescence (ML) is an interesting property of the luminescent compounds which shows different emission upon external stimuli like grinding, crushing etc [12]. Several examples of organic materials have been reported to exhibit ML and the prime reason being the change in intermolecular interactions caused by altering the molecular arrangements in the crystalline state by mechanical stress. Conversion of material from crystalline to amorphous state and in some cases from one crystalline form to other crystalline form might be the reason for ML. In some cases, even conversion of planar conjugated molecules (π delocalization) to non conjugated form due to disturbance of planarity arrangement might cause ML [12-14]. ML materials have been used in security papers, luminescent switches etc., [12-14]. Most of the ML active organoluminogens have been suffering from ACQ effect and detectable wavelength difference which limits their potential in solid state applications [14]. To overcome these problems scientists have focused on AIE-based ML materials.

There are many reports published on mechanoluminescence property of various compounds. It would be interesting if ML property can be introduced in AIE based Schiff-based materials. There are only a few reports on ML based AIE active Schiff base compounds. Xiang *et al*. [15] reported a series of noble and simple AIE and ML active salicylaldehyde based Schiff bases, which have a non-conjugated trimethylamine bridge but emit strong blue, green and yellow color. B. Z. Tang and his group also reported two diaminomaleonitrile based Schiff bases with a donor–acceptor structure and AIE-ML feature [16].

In the current work, a simple Schiff base organic molecule was synthesized which showed AIE property and the cause of it was explored. DFT based calculations were performed to investigate the excited state properties and experimental results were compared with the computational calculations. The compound exhibited 'Excited State Intramolecular Proton Transfer' (ESIPT) and ML properties.

5B.2 Results and discussion

5B.2.1 Syntheses and characterizations

The Schiff-base based AIE active compound, **1** has been prepared by reaction of salicylaldehyde with 4-trityl aniline in a simple single step reaction (Yield, 89%, Scheme 1). The compounds, **2** and **3** have also been synthesized by following similar methods. The structure was characterized with the help of ^{1}HNMR, ^{13}CNMR and mass spectrum. In ^{1}HNMR, a peak appeared at δ = 13.35 ppm represents the hydrogen attached to oxygen. CH=N proton appeared at δ = 8.66ppm and rest of the aromatic proton signals appeared in the range of δ = 6.9 -7.42 ppm. The ^{13}CNMR spectrum of **1** displayed one signal at 64.76 ppm which is assigned for sp^3 carbon of trityl group and rest of the carbon signals appeared in between, δ = 117.25-162.42 ppm. The HRMS data showed the major fragmented peak appeared as [M+H] at m/z 440.2036 which is attributed to the monomeric species. Similarly, **2** and **3** have also been synthesized (Scheme 1) and characterized with the help of ^{1}HNMR, ^{13}CNMR and mass spectrum.

Scheme 1 Schematic presentation of the synthetic protocol for **1-3**

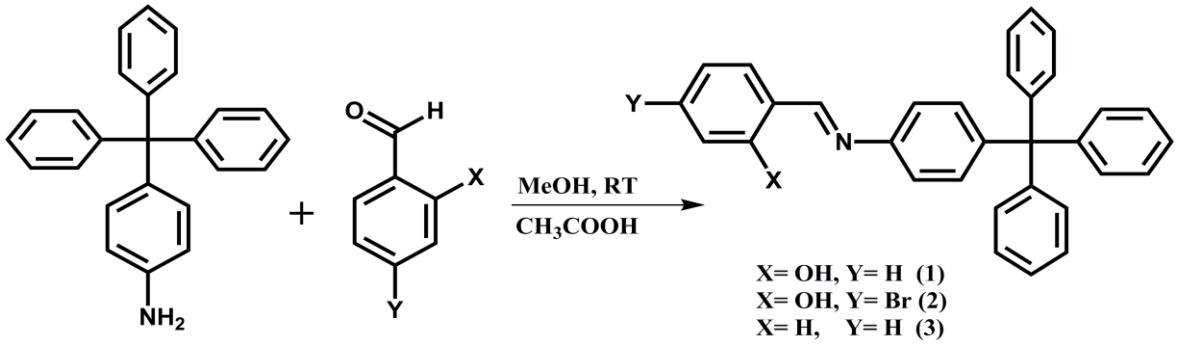

5B 2.2 Study of photophysical property of 1

Excited state intramolecular proton transfer (ESIPT) is one of the frequent cases in salicylaldehyde schiff base luminogens [17-20]. It arises because of proton transfer occurring from enolic form to keto form at the excited state in Schiff base compounds. The absorption and photoluminescence spectra of compound **1** were recorded in polar and non polar solvents at room temperature (Figure 1) to support the ESIPT phenomenon. The recorded absorbance spectra in polar and non polar solvents of **1** showing no significant difference in absorption profile implying the ground state molecule exists in enolic form irrespective of the polarity of the solvent (^{1}HNMR, *vide infra*) (Figure 1a). The absorption spectrum of **1** in cyclohexane showed two absorption peaks observed at 268 nm and 345 nm along with two humps at 307 nm and 323 nm. With addition of slight amount of base to cyclohexane solution of **1**, we observed three peaks in absorption spectra with λ_{max}, 260 nm, 296 nm and 443 nm (Figure 1b). The addition of base is expected to abstract the proton from phenolic -OH group of **1** to form ionic species. The experiment also supports in favor of the existence of enolic form in ground state.

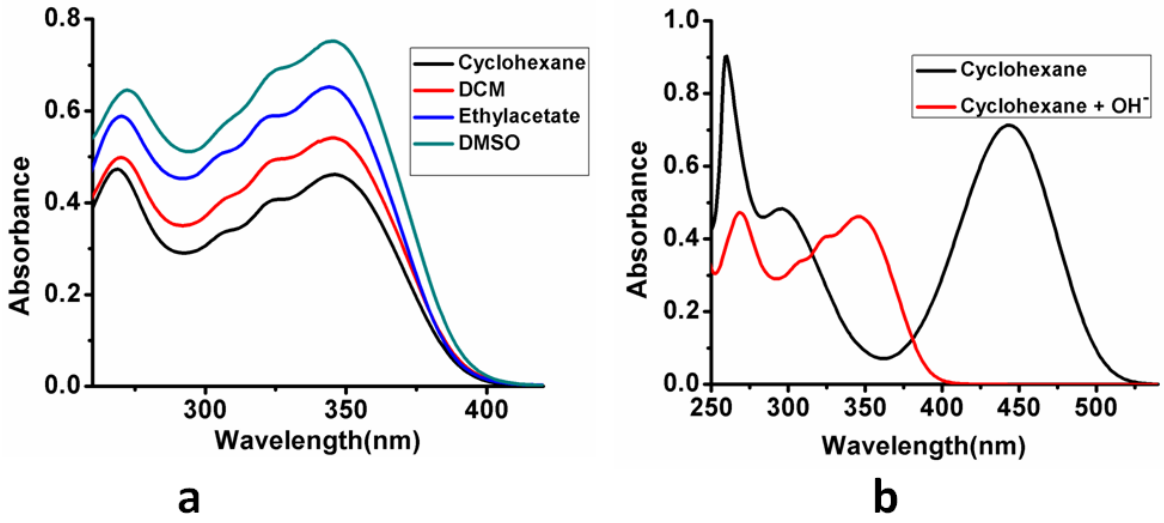

Figure. 1 a) Absorption spectra of **1** in various solvents (c, 1×10^{-6} M); b) Absorption spectra of **1** in cyclohexane and cyclohexane with base (10^{-6} M NaOH in 10µL water) (conc, 1×10^{-6} M in cyclohexane).

We have recorded photoluminescence spectra of **1** in polar and non polar solvents while exciting at 350 nm (Figure 2a). **1** shows two peaks in polar and non polar solvents with λ_{max} 413

nm and 534 nm but with different peak intensities. On recording PL spectra with changing solvent polarity (non-polar → polar), the peak intensity at 413 nm is gradually decreased while the peak intensity at 534 nm is gradually increased. The experimental results hint the possibility to have ESIPT in the present system. To verify it further, we have recorded emission spectra with gradual increasing excitations in the range, 320-380 nm and found that the PL intensity of ~534 nm is steadily increased up to λ_{exc}, 370 nm and it is increased sharply at 380 nm (Figure 2b).

The structural optimization of **1** at ground state was performed with DFT/B3LYP/6-31G(+). The pictorial representations of the theoretically generated HOMO and LUMO for the ground-state geometry of **1** are displayed in Figure 3.

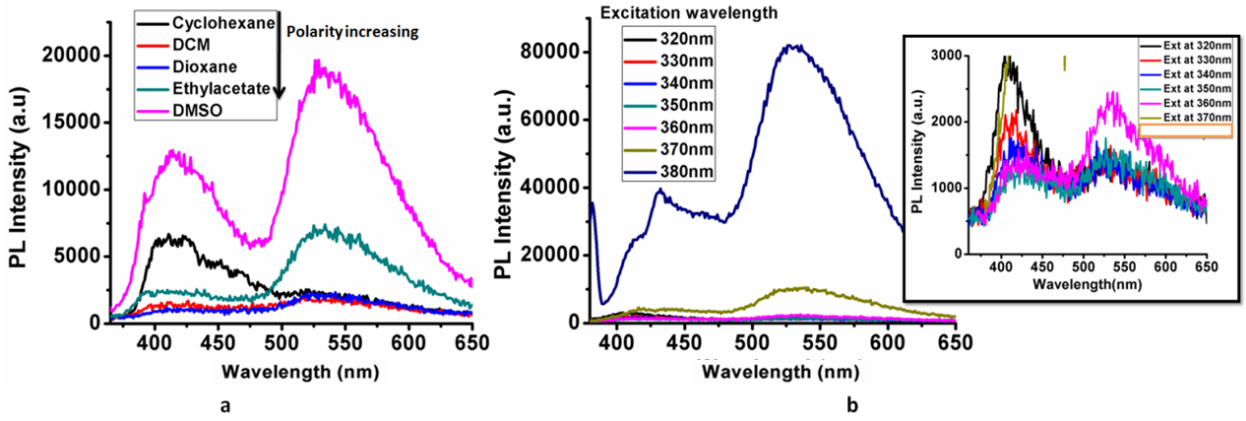

Figure. 2 a) Emission spectra of **1** in various solvents (c, 1×10^{-5}M); b) Photoluminescence spectra of **1** at different excitation wavelengths (conc, 1×10^{-5}M, DMF) (Inset image shows the zoom version of figure 2b).

The DFT based optimized structure showing HOMO and LUMO which are mainly located on phenol, imine and imine attached phenyl part (Figure 3). The approximate calculated HOMO-LUMO energy gap is 3.99eV, which is in good agreement with the experimental value obtained from the absorption band edge, (3.18eV) (Figure 4). Cyclic voltammetry was used to investigate the electrochemical behavior of **1**. It shows one irreversible oxidation peak at – 0.77V (Figure 4). The energy of the HOMO and LUMO was found to be – 5.42eV and – 2.24eV, respectively [Calculations: HOMO (eV) = – (4.65 + E_{onset})] whereas the computationally obtained HOMO and LUMO energy values are – 5.92eV and – 1.93eV, respectively.

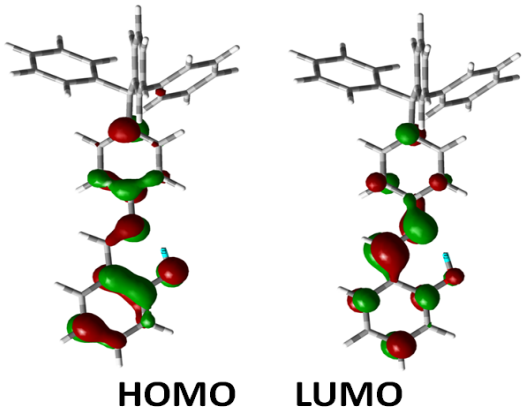

Figure. 3 DFT based calculated ground state optimized HOMO and LUMO orbitals of **1**

The time-dependent DFT calculations of **1** are correlated to the UV−VIS spectroscopic data (Figure 4b). The TD-DFT-based vertical excitation energies and corresponding oscillator strength (OS) values for the compound **1** are presented in Table 1 and Figure 5. On the basis of oscillator strength, the transition occurring from the ground state (S_0) to the first singlet excited state (S_1) (*i.e.*, $S_0 \rightarrow S_1$) is showing the major contribution.

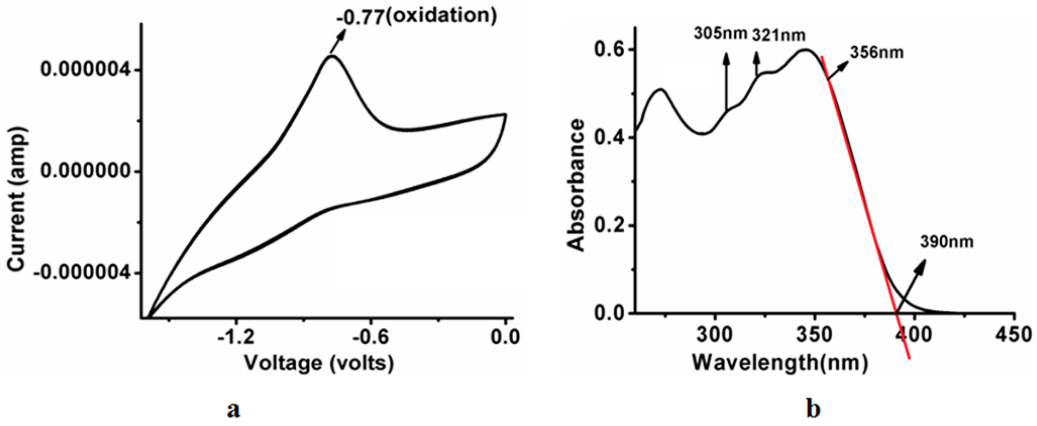

Figure. 4 a) Cyclic voltammogram of **1**, recorded in acetonitrile at a scan rate of 0.05 V s^{-1}; b) UV-VIS absorption spectrum of **1** (c, 1×10^{-5} M, in DCM) (the TD-DFT-based calculated wavelengths are marked in the spectra).

Table. 1 Vertical excitation energies, corresponding orbital contributions, experimental absorption and the corresponding extinction coefficients.

State	ΔE, eV (nm)	Oscillator strength	Assignments and Contribution of transitions	Experimental absorption wavelength (nm) (DCM)	Molar extinction coefficient ($M^{-1}cm^{-1}$)
S_1	3.48(356)	0.7302	HOMO→LUMO, 96.47%	345	60146.1
S_2	3.86(321)	0.1230	HOMO-1→LUMO, 87.9%	323	54908.5
S_3	4.05(305)	0.0170	HOMO-3→LUMO, 97.0%	305	46179.2

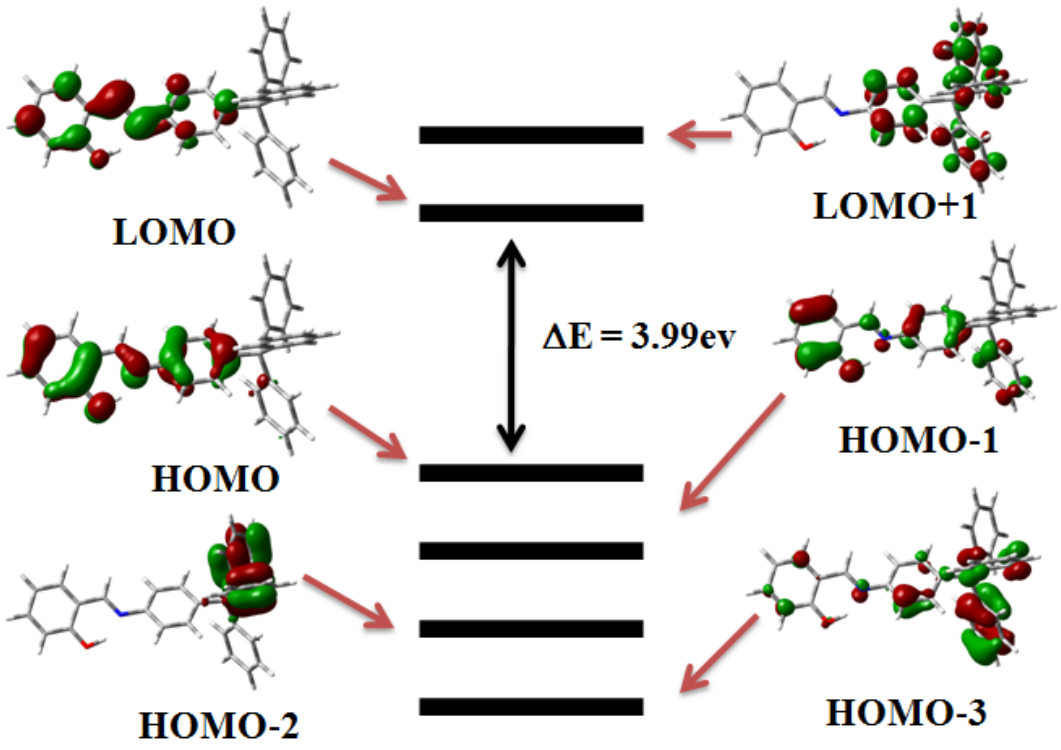

Figure. 5 Molecular orbital diagram showing the highest occupied and lowest unoccupied molecular orbitals of **1**.

5B.2.3. Aggregation Induced Emission (AIE) of 1

1 is soluble in common organic solvents such as dichloromethane (DCM), tetrahydrofuran (THF), dimethyl sulfoxide (DMSO) and dimethylformamide (DMF) but not soluble in water and hexane. To verify AIE activity of **1**, DMF and water solvents were chosen. The emission spectra of **1** were recorded with gradual increase of water in DMF (0-90%). As water serves as a non-solvent for this ligand, **1** gets aggregated at high water concentration. Different amount of water (f_w = 0 – 90%) gradually added to a set of solutions of **1**, keeping the overall concentration of the solution as 10^{-5} M.

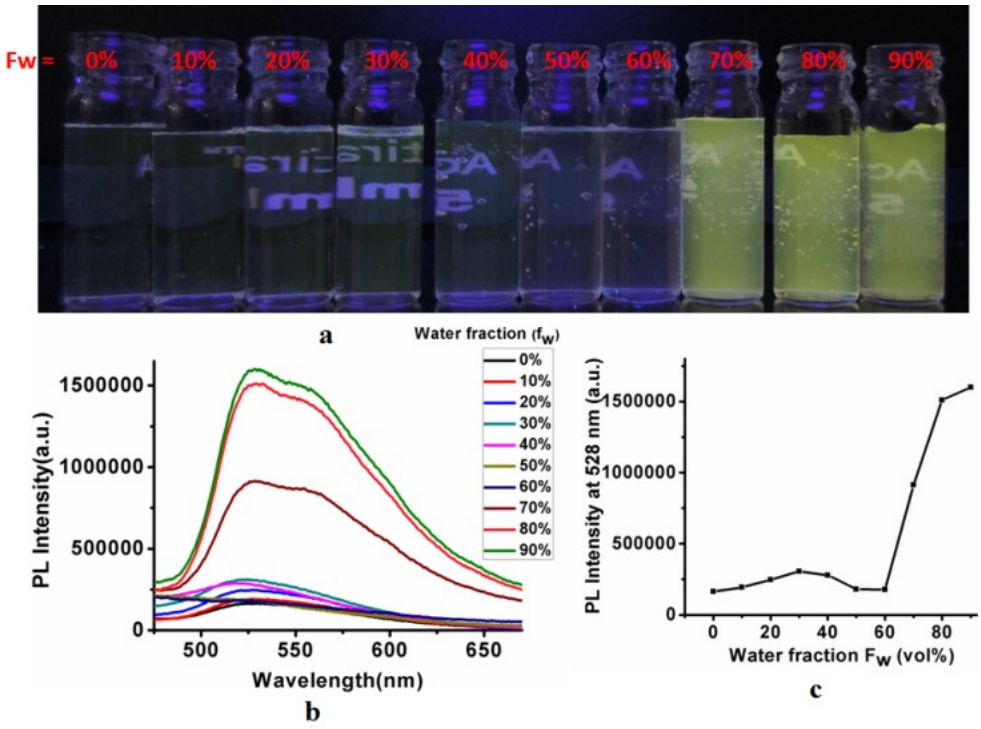

Figure. 6 (a) Luminescent images of compound (irradiated with an ultraviolet light at 365 nm) in water-DMF mixed solvents (c, 2 × 10^{-5} M); (b) PL spectra of **1** in DMF/water mixed solvents with different f_w (λ_{exc}, 365 nm); (c) the changes of PL peak intensity with different f_w (λ_{max} = 529 nm).

The photoluminescence (PL) intensity of **1** increases at a slow rate up to a water concentration of about $f_w \leq 30\%$, then the PL intensity gets decreased upto $f_w \leq 60\%$ and again sharply increased with increasing water content from $f_w = 70\%$ to $f_w = 90\%$. The PL intensity at f_w = 90% showed 9.5 times PL enhancement as compared to pure DMF solution (Figure 6). To

investigate the cause of AIE, we have recorded the emission spectra in PEG-DMF mixture with a different fraction of viscous PEG (0-90%) resulting 7 fold emission enhancement at f_{PEG} = 90% as compared to its pure DMF (0%) solution. Based on the results obtained from this experiment, it is proposed that the occurrence in enhancement of emission from 0% to 90% might be resulting from the restriction of intramolecular rotation by the presence of trityl rotor (Figure 7)

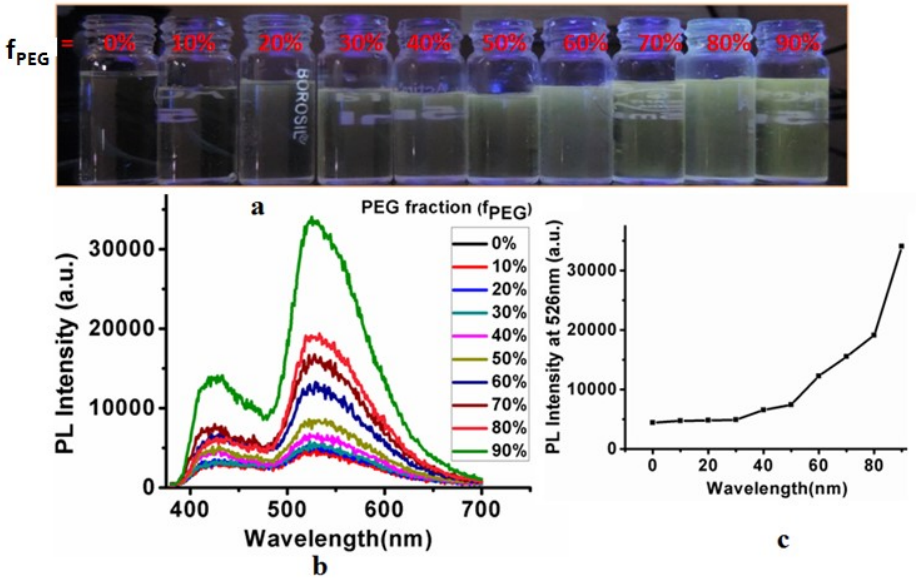

Figure. 7 (a) Luminescent images of **1** (λ_{exc}, 365nm) in PEG-DMF mixed solvents with the concentration kept at 2 × 10^{-5} M; (b) PL spectra of **1** in PEG/DMF mixed solvents with different f_{PEG} with excitation at 365 nm; (c) the changes of PL peak intensity with different f_{PEG} (λ_{max} = 529 nm).

The measured average size at f_w, 90% by dynamic light scattering (DLS) experiment was obtained to ~127 nm . (Figure 8).

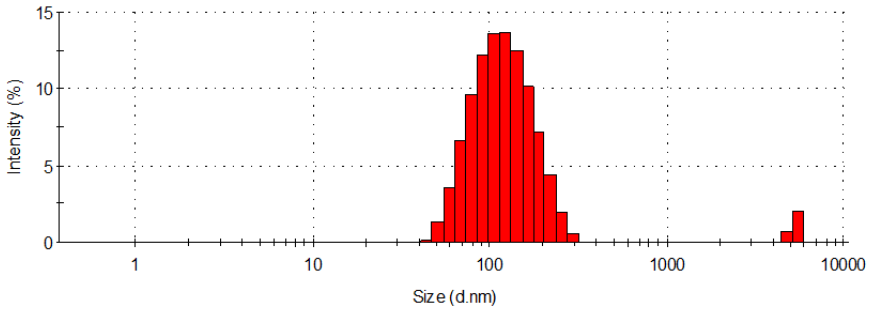

Figure. 8 Average particle size distribution of **1** at 90% f_w in DMF-water.

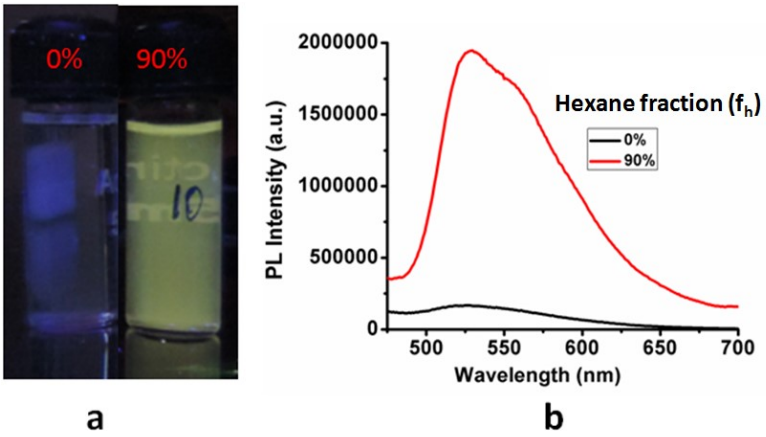

Figure. 9 (a) Luminescent images of **1** (λ_{exc}, 365 nm) in DCM-Hexane mixed solvents (c, 2×10^{-5} M); (b) PL spectra of **1** in DCM-Hexane mixed solvents with different hexane fraction (f_h = 0% and 90%) with excitation at 365 nm, ($\lambda_{max, em}$ = 529 nm).

The obtained high emission intensity in 90% water at the mixture of DMF-water might be occurring because of aggregation not because of solvent polarity/nature. To confirm this fact, we have recorded emission spectra in another solvent mixture, DCM/hexane, with gradually varying the DCM concentration in hexane of **1.** The resultant emission spectra are found to be similar with the 90% (DMF-Water) mixture (Figure 9). The result convinced us that the emission of 90% is resulting from aggregated form. In this case, when the molecules get closer during aggregation, the H-bonding is facilitated in between imine nitrogen and hydroxyl group, thus triggering the ESIPT process.

5B.2.4 Mechanoluminescence (ML) property of 1-3

1 shows almost no emission in solid state whereas upon grinding it turns into yellow emitted compound with λ_{max}, 557 nm (Figure 10). The compound obtained after grinding of **1** is reverted after recrystallization in DCM and observed no significant change in emission intensity with the original compound.

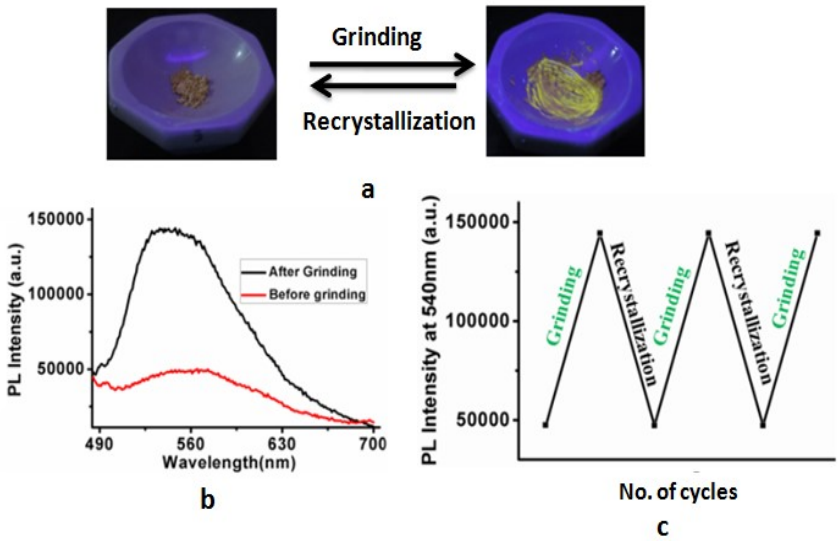

Figure. 10 (a) Luminescent images of pristine and ground sample of **1** (photograph taken under 365 nm UV illumination); (b) Emission spectra of as-synthesized solid and after grinding sample of **1**; (c) Maximum PL intensity changes upon repeated grinding-recrystallization cycles of **1**.

Several experiments have been carried out to explore the mechanism behind the ML property of **1**. Powder XRD of **1** showed intense peaks of the as-synthesized sample while broad and less intense peaks observed for the ground sample (Figure 11). These results confirmed the crystalline nature of both the samples. Compared to ground sample, the as-synthesized sample showing extra peaks at 10° and 15° (2θ) and intensity of peaks from 18° to 27° is relatively higher than the corresponding peaks of ground sample. The observation hints the as-synthesized compound is more crystalline nature as compared to ground sample.

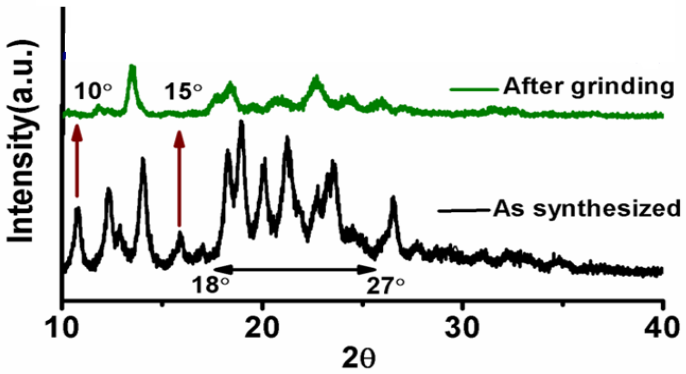

Figure. 11 Powder XRD of as-synthesized **1** and at its after grinding states.

In Differential Scanning Calorimetry (DSC) study, the as-synthesized compound (**1**) was found to melt at 274 °C, whereas the ground sample (**1a**) melts at 263 °C. In addition, **1a** shows crystallization peak at 63 °C (Figure 12). These obtained results support that the as-synthesized compound is highly crystalline naure while **1a** is semicrystalline nature.

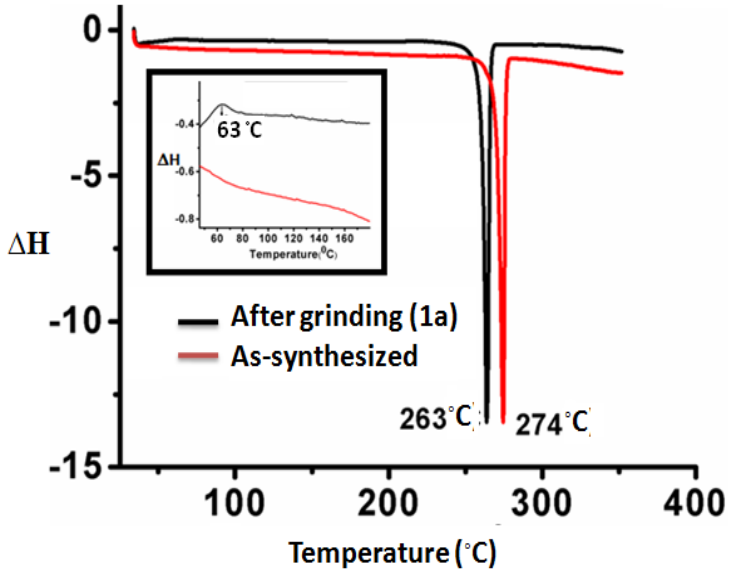

Figure. 12 DSC plots of sample of **1** before and after grinding (Inset image shows the zoom version with the temperature range, 25 °C to 170 °C).

To investigate molecular level mechanism of ML property of **1**, the following compounds, **2** and **3** (**2** with hydroxyl group and **3** without hydroxyl group) have been synthesized. The non-luminescent compound, **3** remains non-luminescent even after grinding (Figure 13). But the yellow emitting, **2** resulting more intense emission after grinding (λ_{max} = 557 nm) (Figure 14). The FTIR spectrum of ground sample of **1** shows a broad peak at 3060-3650 cm^{-1}, whereas as-synthesized compound showing a sharp peak at 3650 cm^{-1} indicating the H of -OH remains free from H-bonding (Figure 15), however the IR spectrum of **2** shows peak at 3115-3667 cm^{-1} before and after grinding. These results hint the role of -OH group present in the molecule to exhibit the ML of **1**.

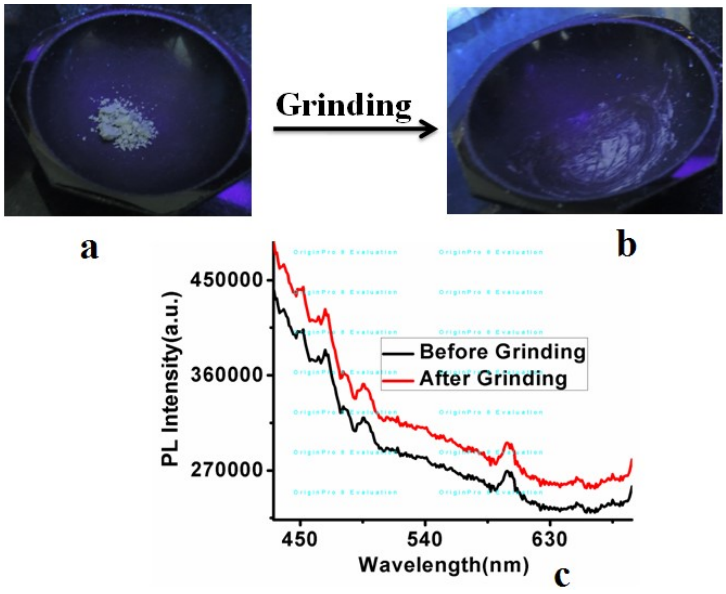

Figure. 13 (a and b) shows luminescent images of pristine and ground sample of **3** (photograph taken under 365 nm UV illumination); (c) Emission spectra of as-synthesized solid, and ground sample of **3.**

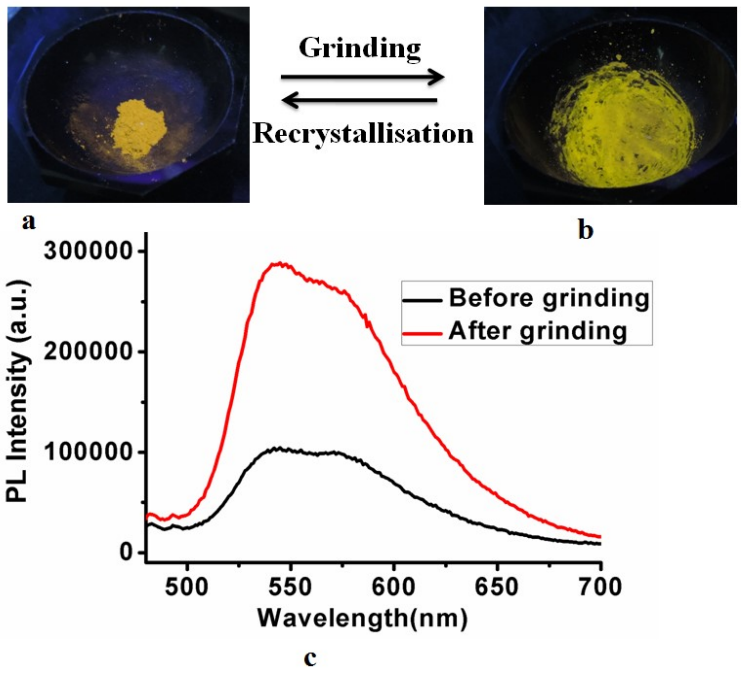

Figure. 14 (a and b) shows luminescent images of pristine and ground sample of **2** (photograph taken under 365 nm UV illumination); (c) Emission spectra of as synthesized solid, and ground sample of **2.**

Scheme. 2 Proposed molecular-level mechanism of ML property of **1**

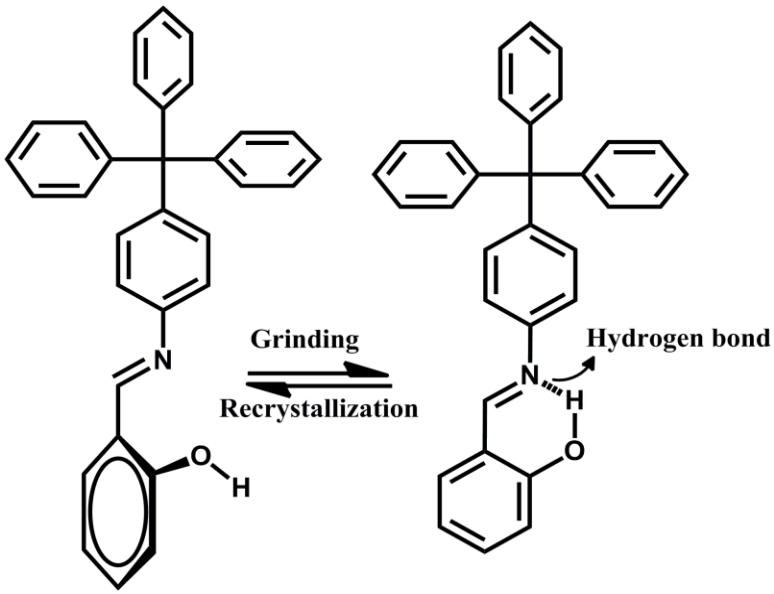

The studied fact supports that there has no H-bonding present in between -OH and nitrogen of imine of **1**. But H-bonding is generated after grinding **1** (Scheme 2), hence ESIPT becomes operative under excitation.

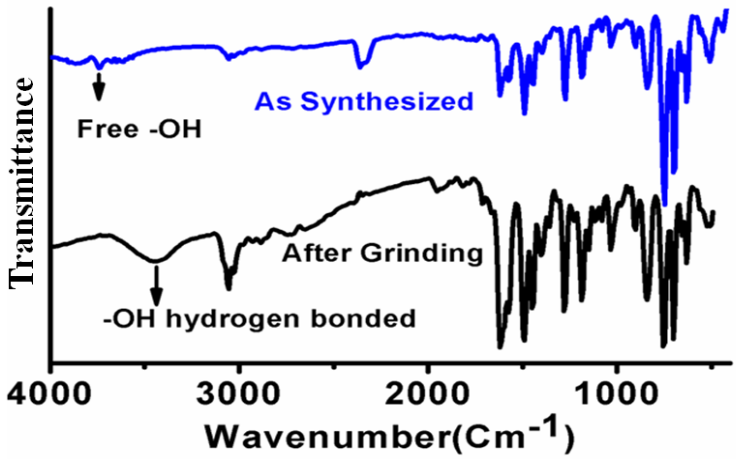

a

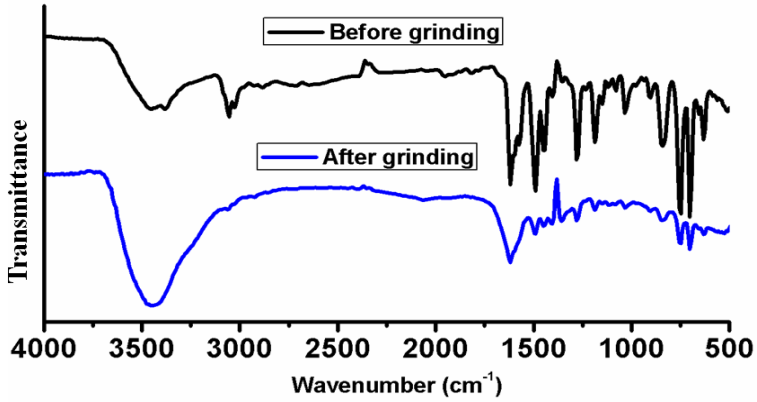

b

Figure. 15 a and b are FTIR spectra of **1** and **2** before and after grinding, respectively.

Most of the reported ML active compounds exhibit irreversibility in the solid phase, but undergoes reversible transformation once the ground sample is dissolved in some solvent [15-16]. Interestingly, the compound **1** shows time dependent reversibility in the solid phase. The recorded time-dependent emission spectra after grinding of **1** support the reversibility of the ground sample in solid phase (Figure 16).

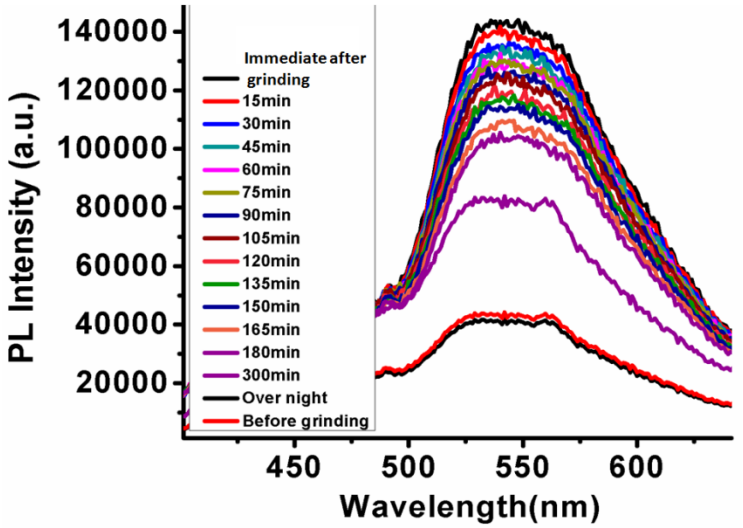

Figure. 16 The recorded time-dependent emission spectra of ground sample and the as-synthesized compound of **1**.

From the experimental results, it is presumed that the hydrogen bonding is generated after grinding **1** that results a strong emission. The presence of bulky trityl group in the vicinity of imine-hydroxyl H-bonding, interrupt the H-bonding through steric interaction, hence transformed the compound into the original form, **1**.

In the original solid state, **1** shows weak emission, probably the -OH functional group will be remaining away from the imine nitrogen (weak or no hydrogen bond) but after grinding / or, at higher fraction f_w (~90%) of DMF-water mixture, -OH and imine groups are reoriented to approach each other at such a distance which make the H-bonding possible. Hence, this H-bonding facilitates a strong emission through ESIPT.

5B.3 Conclusions

We have attempted to design and synthesis of an 'aggregation induced emission' active compound based on a simple Schiff-base technique. Although the compound does not emit any light in its pristine form, it shows bright emission at 90% water in the DMF-water mixture. In addition, the compound, **1** exhibits reversible mechanoluminescence property. The mechanism behind the observed emission in **1** has been explored which is identified as observed through ESIPT process.

5B.4 Experimental Section

General Synthesis of 2-((E)-(4-tritylphenylimino)methyl)phenol (1) (Scheme 1): In a 50 ml round bottom flask, salicylaldehyde and tritylaniline, (1:1 0.59m moles) were dissolved in 20 ml methanol. The mixture was stirred at room temperature for 30 min and powdered solid was obtained. The powdered product was recrystallized in methanol solvent. The yield of the product was ~89%.

^{1}H NMR (400 MHz, CDCl3) δ 13.33 (s, 1H), 8.66 (s, 1H), 7.43 – 7.37 (m, 2H), 7.33 – 7.19 (m, 20H including $CDCl_3$ proton), 7.06 – 7.02 (m, 1H), 6.99 – 6.93 (m, 1H) (Figure 17). **^{13}C NMR** (101 MHz, CDCl3) δ162.42, 161.15, 146.60, 146.09,145.84, 133.09, 132.22, 132.15,131.08, 127.60, 126.05, 120.24, 119.25, 119.05, 117.25, 64.76 (Figure 18). HRMS calculated ([M + H]+) m/z 440.2014, found ([M + H]+)m/z 440.2036 (Figure 19).

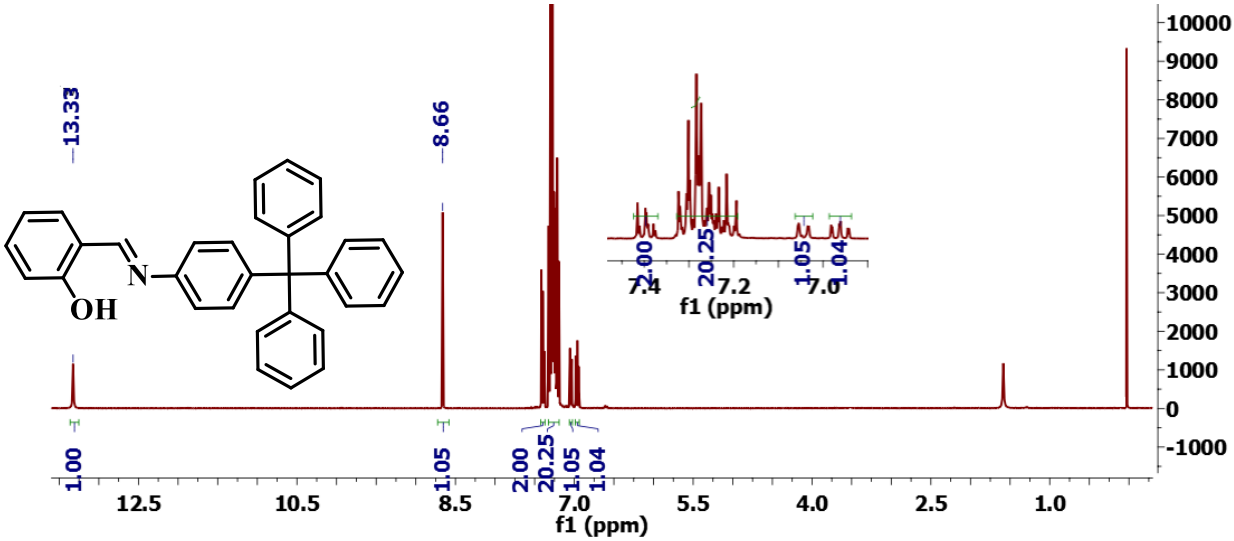

Figure. 17 ^{1}H NMR spectrum of **1**

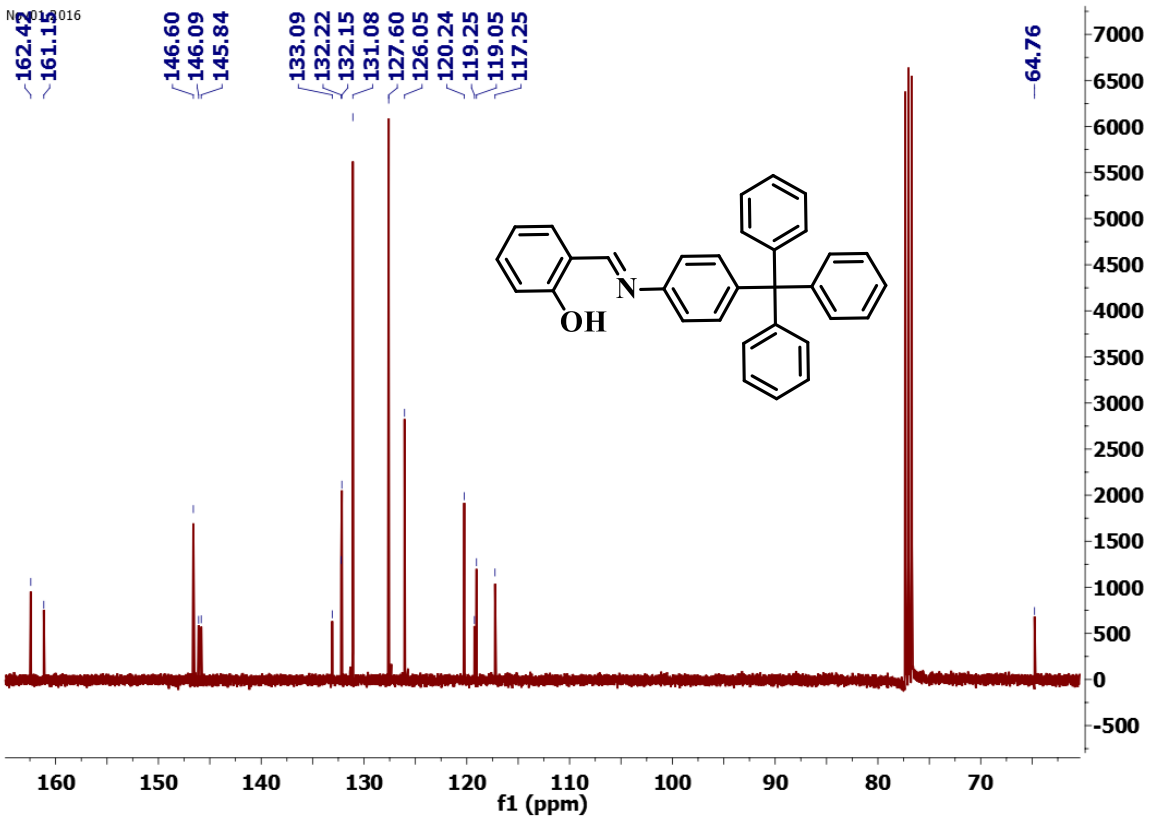

Figure. 18 ^{13}C NMR spectrum of **1**

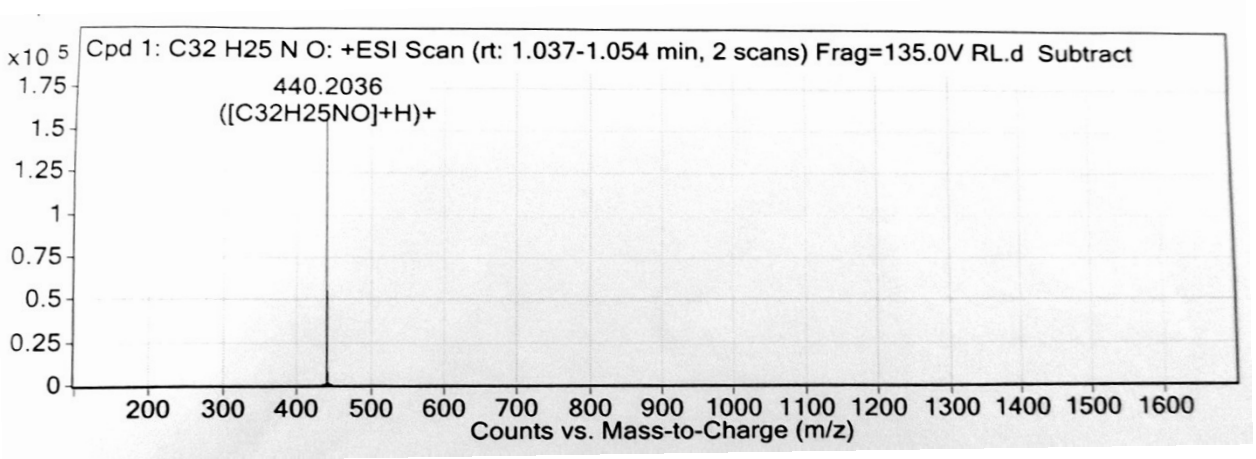

Figure. 19 Mass spectrum of **1**

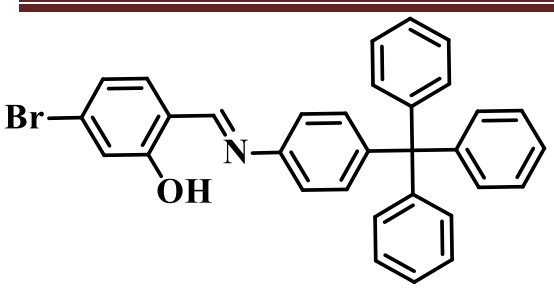

^{1}H NMR (400 MHz, CDCl3) δ 13.36 (s, 1H), 8.59(s, 1H), 7.51 – 7.45 (m, 1H), 7.34 – 7.32 (m, 1H), 7.31 – 7.21 (m, 20H including $CDCl_3$ proton), 7.20 – 7.19 (m, 1H) (Figure 20**)**. **^{13}C NMR** (101 MHz, CDCl3) δ 160.83, 160.18, 146.51, 146.41, 145.46, 135.63, 134.15, 132.23, 131.06, 127.62, 126.09, 120.63, 120.28, 119.27, 110.48, 64.78 (Figure 21**)**. HRMS calculated ([M + H]+) m/z 517.1041, found ([M + H]+)m/z 517.4431.

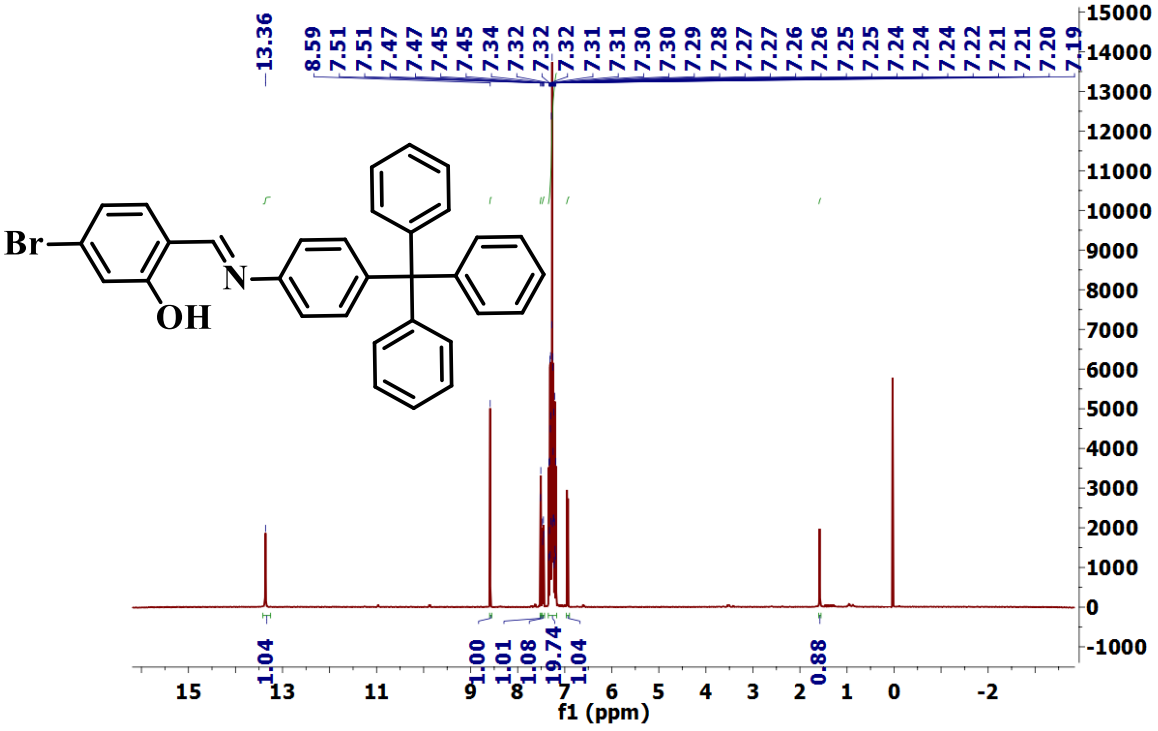

Figure. 20 ^{1}H NMR spectrum of **2**

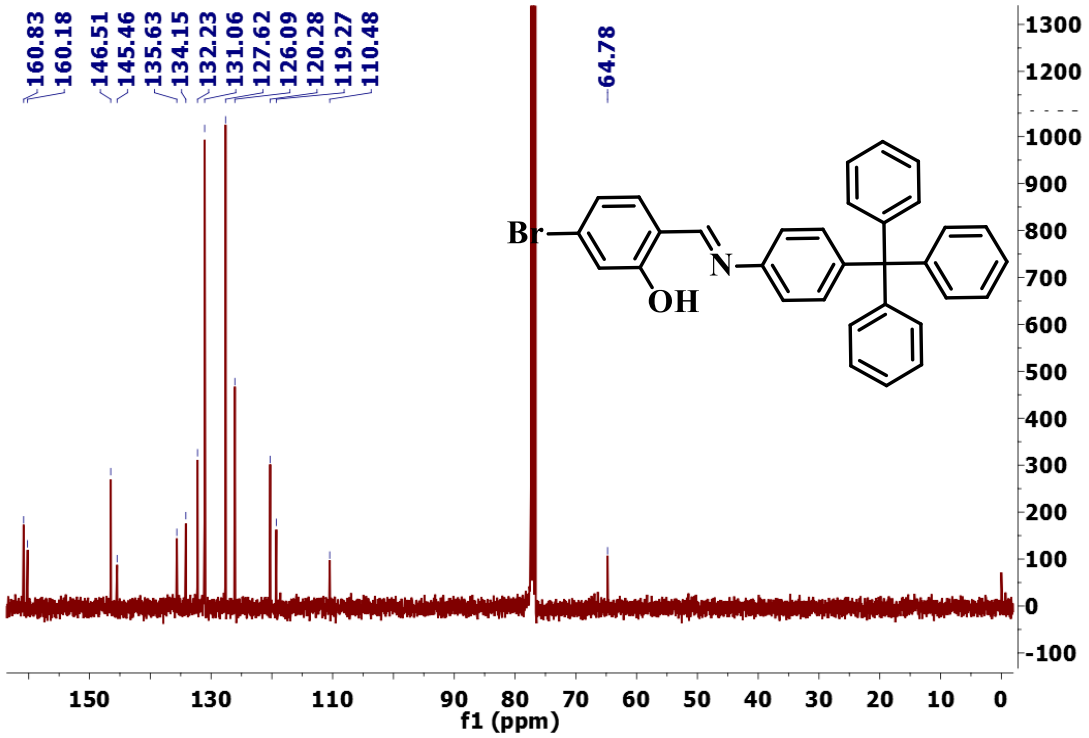

Figure. 21 ^{13}C NMR spectrum of **2**

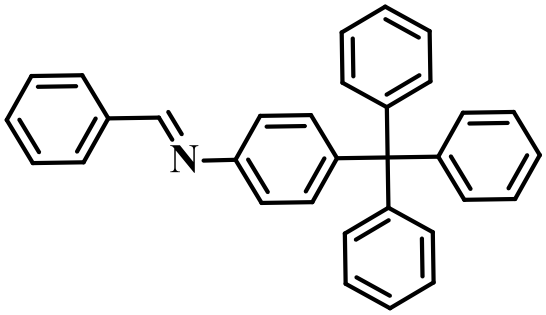

^{1}H NMR (400 MHz, $CDCl_3$) δ 8.51 (s, 1H), 7.94 – 7.87 (m, 2H), 7.53 – 7.44 (m,3H),7.32 – 7.26 (m, 13H), 7.23 (m, 3H), 7.16 – 7.11 (m, 2H) (Figure 22)**.^{13}C NMR** (101 MHz, CDCl3) δ 160.15, 149.63, 146.81, 144.71, 136.29, 131.97, 131.34, 131.16, 128.78, 128.78, 127.51, 125.96, 119.99, 64.72 (Figure 23**)**. HRMS calculated ([M + H]+) m/z 423.1987, found ([M + H]+) m/z 423.5471.

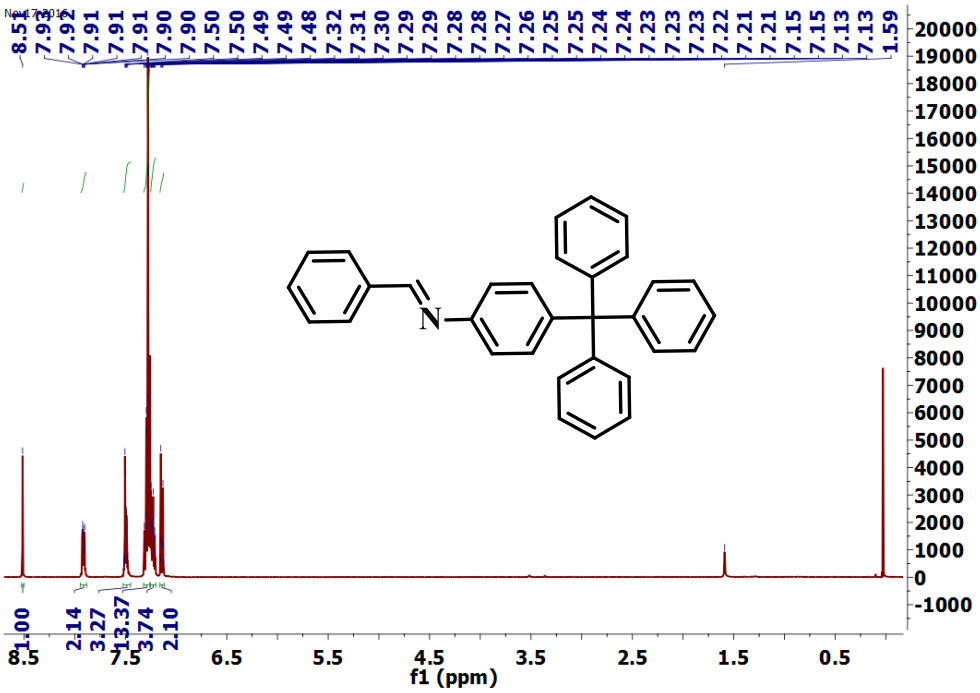

Figure. 22 ^{1}H NMR spectrum of **3**

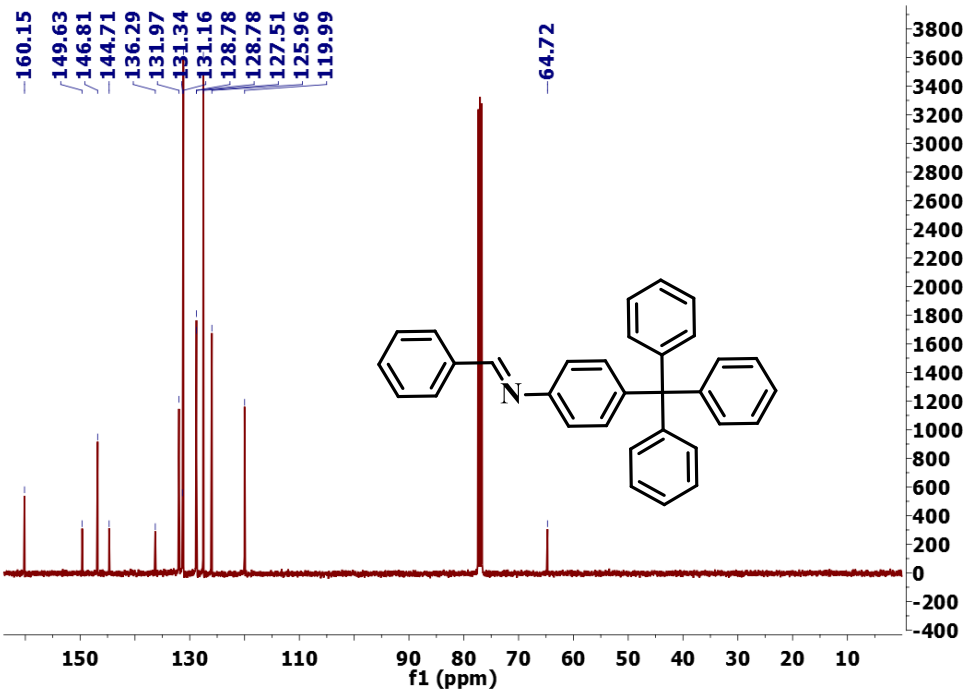

Figure. 23 ^{13}C NMR spectrum o f **3**

5B.5 References

[1] X. T. Tao, H. Suzuki, T. Wada, H. Sasabe and S. Miyata, *Appl. Phys. Lett*., 1999, **75**, 1655.

[2] X. T. Tao, H. Suzuki, T. Wada, S. Miyata and H. Sasabe, *J. Am. Chem. Soc*., 1999, **121**, 9447.

[3] Y. Qiu, Y. Shao, D. Q. Zhang and X. Y. Hong, *J. Appl. Phys*., 2000, **39**, 1151.

[4] D. Ray, P.K. Bharadwaj*, Inorg. Chem*., 2008, **47**, 2252.

[5] J. S. Wu, W.M. Liu, X.Q. Zhuang, F. Wang, P. F. Wang, S. L. Tao, X. H. Zhang, S. K. Wu, S. Tong, *Org. Lett*., 2007, **9**, 33.

[6] A. M. G. Campana, F. A. Barrero and M. R. Ceba, *Analyst*, 1992, **117**, 1189.

[7] N. Chimpalee, D. Chimpalee, B. chayakul and D. T. Burns, *Anal. Chim. Acta*,1993, **182**, 643.

[8] R. L. Renesse (Ed.), *Optical Document Security*, Artec House, MA, 1994.

[9] A. N. Becidyan, *Color Res. Appl*., 1995, **20**, 124.

[10] Y. Hong, W. Jacky, Y. Lam and B. Z. Tang, *Chem. Soc. Rev*., 2011, **40**, 5361.

[11] Z. Yang, Z. Chi, Z. Mao, Y. Zhang, S. Liu, J. Zhao, M. P. Aldred and Z. Chi, *Mater. Chem. Front*., 2018, DOI: 10.1039/c8qm00062j.

[12] Y. Sagara and T. Kato, *Nat. Chem*., 2009, **1**, 605.

[13] Y. Sagara, S. Yamane, M. Mitani, C. Weder and T. Kato, *Adv. Mater*., 2015, **28**, 1073.

[14] Z. Chi, X. Zhang, B. Xu, X. Zhou, C. Ma, Y. Zhang, S. Liu and J. Xu, *Chem. Soc. Rev*., 2012, **41**, 3878.

[15] X. Zhang, J. Shi, G. Shen, F. Gou, J. Cheng, X. Zhou and H. Xiang, *Mater. Chem. Front.,* 2017, **1**, 1041.

[16] T. Han, X. G. Gu, J. W. Y. Lam, A. C. S. Leung, R. T. K. Kwok, T. Y. Han, B. Tong, J. B. Shi, Y. P. Dong and B. Z. Tang, *J. Mater. Chem. C*, 2016, **4**, 10430.

[17] I. Kaur, P. Kaur and K. Singh, *Sens. Actuator B-Chem.*, 2018, **257**, 1083.

[18] M. Tajbakhsh, G. B. Chalmardi, A. Bekhradnia, R. Hosseinzadeh, N. Hasani and M. A. Amiri, *Spectrochim. Acta A,* 2018, **189**, 22.

[19] Y. Wang, Z. Y. Ma, D. L. Zhang, J. L. Deng, X. Chen, C. Z. Xie, X. Qiao, Q. Z. Li and J. Y. Xu, *Spectrochim. Acta A,* 2018, **195**, 157.

[20] L. Q. Yan, R. J. Li, W. Shen and Z. J. Qi, *J. Lumin*., 2018, **194**, 151.

1. Pt(II)-based AIE active complex for Organic Light Emitting Diodes (OLEDs)

Scientists worldwide have focused on the development of organic phosphorescence materials over fluorescence. The way to utilize unused triplet excitons is to employ heavy metals (Ir/Pt/Os etc). Platinum (II) metal complexes is one of the most promising materials for solid state phosphoresce emitter. Cyclometaleted-based platinum (II) materials are becoming increasingly important to scientists with respect to their applications in field of OLED due to their high luminescence quantum yields, color tunability, fair stability and straightforward synthetic routes. Synthesis of AIE-based Pt(II) excimer promise for the development of full-color OLED devices.

2. AIE Stimuli Responsive systems

Mechanochromic luminogens (ML) or Piezoluminogens (PZL) are smart materials which change their emission properties in presence of external stimuli such as pressure, grinding, shearing, rubbing, milling and crushing. The ML materials are falling in the category of fourth generation of materials after natural materials - synthetic polymer materials and artificial design materials. ML materials scientist are using in the field of mechanosensors, security papers, and optical storage. It is obvious that the development of such kind of materials will lead the world to the next generation technologies. These AIEgens have propeller type twisted geometry which result a weak interaction in the crystal packing. The design of new AIE active materials may lead to the production of ML materials which are promising to be applied for various applications.

3. AIE active molecules encapsulated mesoporous silica nano-particles for early detection of cancerous cells

Mesoporous silica nano-particles are interesting in current research world because of their interesting properties like colloidal stability, high surface area, pore volume, tunable pore sizes, and the possibility to conjugate the surface with specific functional groups (e.g., various biomolecules, folic acid etc.,) made the mesoporous silica nanoparticles as a promising matrix for various applications. The encapsulation of AIE platinum(II) complexes into the mesoporous silica pore and their surface functionalization for the target will provide a platform to explore these as promising biomaterials. These can be utilized for selective bioimaging probe specially

to target the tumor tissues. These approaches will be auspicious for early age detection of cancerous cells.

4. Design and syntheses of new AIE active platinumn(II) based complexes for targeted sensitive sensing of different analytes

The selective and sensitive detection of different ions can be done by using signaling unit approach. Syntheses of following complexes (**1** and **2**) may lead to very good results in the field of sensors for fluoride and cyanide.

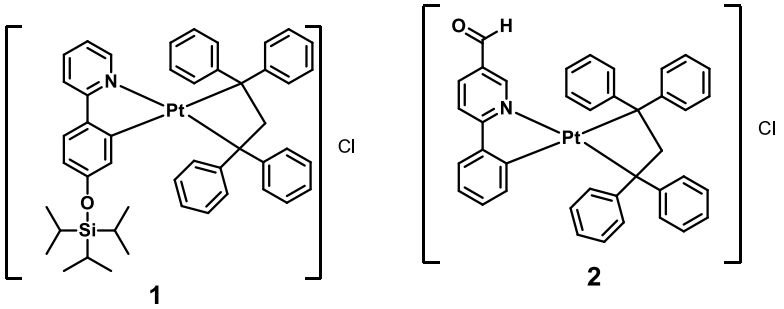

In a similar way the specific imaging of different cell organelle can be achieved by modification of functional groups in the complex.

5. Simple technique to synthesis new AIE system

We have developed several Schiff-base based AIE systems in a very simple technique. We have also synthesized Pt(II) complexes by microwave reactor in a very short time. There has a possibility to develop synthetic methodology in a simple and shorter time. It provides the opportunity to explore the new AIE molecules through incorporation of rotating units in the chromophoric ligands (e.g. L1 and L2). Restricted rotation (due to bulkiness) will minimize the nonradiative energy loss and efficiency would increase in the solid state.

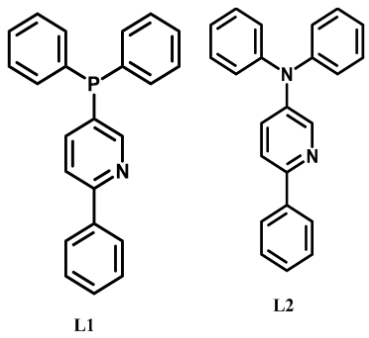

Appendices

List of Publications *[A-1]*

---

1. Parvej Alam, Gurpreet Kaur, Clàudia Climent, **Sheik Saleem Pasha**, David Casanova, Pere Alemany, Angshuman Roy Choudhury and Inamur Rahaman Laskar, 'Aggregation Induced Emission (AIE)' Active Cyclometalated Iridium(III) Based Fluorescent Sensors: High Sensitivity for Mercury(II) Ions, *Dalton Trans*., 2014, 43, 16431.

2. **Sheik Saleem Pasha**, Parvej Alam, Subhra Dash, Gurpreet Kaur, Debashree Banerjee, Rajdeep Chowdhury, Nigam Rath, Angshuman Roy Choudhury and Inamur Rahaman Laskar, Rare Observation of 'Aggregation Induced Emission' in Cyclometalated Platinum(II) Complexes and their Biological Activities, *RSC Adv.*, 2014, 4, 50549.

3. **Sheik Saleem Pasha**, Parvej Alam, AmritSarmah, Ram Kinkar Roy, Inamur Rahaman Laskar, Encapsulation of Multi-Stimuli AIE Active Platinum(II) Complex: A Facile and Dry Approach for Luminescent Mesoporous Silica, *RSC Adv.*, 2016, 90, 87791.

4. **Sheik Saleem Pasha**, Pradip Das, Nigam P. Rath, DebashreeBandyopadhyay, Nikhil R. Jana, Inamur Rahaman Laskar, Water Soluble Luminescent Cyclometalated Platinum(II) Complex - A Suitable Probe for Bio-imaging Applications, *Inorg. Chem. Commun.,*2016, 67, 107.

5. **Sheik Saleem Pasha**, Hare Ram Yadav, Angshuman Roy Choudhury, Inamur Rahaman Laskar, Strategic Design of 'Aggregation Induced Emission (AIE)' Active Salicylaldehyde based Schiff Base: Study of Mechanoluminescence and Sensitive Zn(II) Sensing, *J. Mater. Chem. C*, 2017, 5, 9651.

6. Clàudia Climent, Parvej Alam, **Sheik Saleem Pasha**, Gurpreet Kaur, Angshuman Roy Choudhury, Inamur Rahaman Laskar, David Casanova, Pere Alemany, Dual emission and Multi-Stimuli-Response in Iridium(III) complexes with Aggregation-Induced Enhanced Emission: Application to Quantitative CO₂ Detection, *J. Mater. Chem. C*, 2017, 5, 7784.

7. LeenaFageria, VikramPareek, Ramapuram Dilip, **Sheik Saleem Pasha**, Inamur Rahaman Laskar, Heena Saini, Subhra Dash, Rajdeep Chowdhury, JitendraPanwar, Biosynthesized protein-capped silver nanoparticles induce ROS-dependent pro-apoptotic signals and pro-survival autophagy in cancer cells,*ACS Omega***,** 2017, 2, 1489.

8. Vishal Kachwal, Parvej Alam, Hare Ram Yadav, **Sheik Saleem Pasha**, Angshuman R. Choudhury, Inamur Rahaman Laskar, Simple Ratiometric Push-Pull With 'Aggregation-Induced Emission Enhancement' Active Pyrene Based Organic Molecule: Multifunctional Probe With no Quenching Fluorescent Sensor, *New J. Chem,* 2018, 42, 1133.

9. **Sheik Saleem Pasha**, LeenaFageria, Nigam P. Rath, Rajdeep Chowdhury, Aniruddha Roy and Inamur Rahaman Laskar, Evaluation of a Novel Platinum(II) Based AIE Compound-Encapsulated Mesoporous Silica Nanoparticles for Cancer Theranostic Application, *Dalton Trans*., 2018, 47, 4613.

Research articles under review

10. **Sheik Saleem Pasha**, Rrahulbardwaj and Inamur Rahaman Laskar, Strategic Design and Synthesis of Schiff-base based 'Aggregation Induced Emission' Active Molecule: Study of Reversible and Turn on Mechanolumenescent Property (UnderPreparation)

List of Oral/poster presented in conferences *[A-2]*

---

1. Rare observation of 'aggregation induced emission' in cyclometalated platinum(II) complexes and their biological activities(National Seminar on crystallography(43A) held in IISER Mohali, 28 – 30th March, 2014) (**Poster**)

2. Design and synthesis of 'Aggregation Induced Phosphorescence(AIP)'Active Platinum(II) Complex and a Facile Approach to Phosphorescent Mesoporous Silica (NFM-2014 held in BITS-Pilani, 7-9th November 2014) (**Poster**)

3. Design and synthesis of 'Aggregation Induced Phosphorescence(AIP)'Active Platinum(II) Complex and a Facile Approach to Phosphorescent Mesoporous Silica (CRSI-RSC held in NCL Pune, 4-8th February 2015) (**Poster**)

4. Water Soluble Luminescent Cyclometalated Platinum(II) Complex - A Suitable Probe for Bio-imaging Applications (Nascent Developments in Chemical Sciences: Opportunities for Academia-Industry Collaboration NDCS International Conference (NDCS-2015) held at BITS Pilani, Pilani Campus during October 16-18, 2015) (**Poster**)

5. Strategic Design of 'Aggregation Induced Emission (AIE)'Active Organic Material: Application in Zn(II) Sensing and Mechanofluorochromism (held at BITS Pilani, Pilani Campus during October 29-30, 2016)(**Poster**)

6. Evaluation of a Novel Platinum(II) Based AIE Compound-Encapsulated Mesoporous Silica Nanoparticles for Cancer Theranostic Application (NFM-2017 held in BITS-Pilani, 16-18th November 2017) (**Poster**)

7. Synthesis of 'Aggregation Induced Emission (AIE)' Active Salicylaldehyde Based Schiff Base: Study of Mechanoluminescence and Sensitive Zn(II) Sensing (NFM-2017 held in BITS-Pilani, 16-18th November 2017) (**'Best Oral Presentation'** Award)

BRIEF BIOGRAPHY OF THE CANDIDATE *[A-3]*

Mr. Sheik Saleem Pasha is a Ph.D. student of BITS Pilani, Pilani Campus, Rajasthan, obtained his master degree from Osmania University, HYB (India) in 2011. Then, he joined Neo Quantum junior college as a chemistry lecturer, Hyderabad (India) and worked there for 1 year**.** He qualified GATE-2012, then he has joined CSIR Project as a junior research fellow. He started pursuing Ph.D. at the Department of Chemistry, BITS Pilani in August, 2012. He has been working on the project **"**Syntheses and Studies on Photo-Physical Property of Luminescent complexes of Platinum(II) and Iridium(III) and their Applications in Bioimaging and Sensory**"**. He has published nine research articles in peer reviewed international journals and presented papers in seven conferences/symposiums.

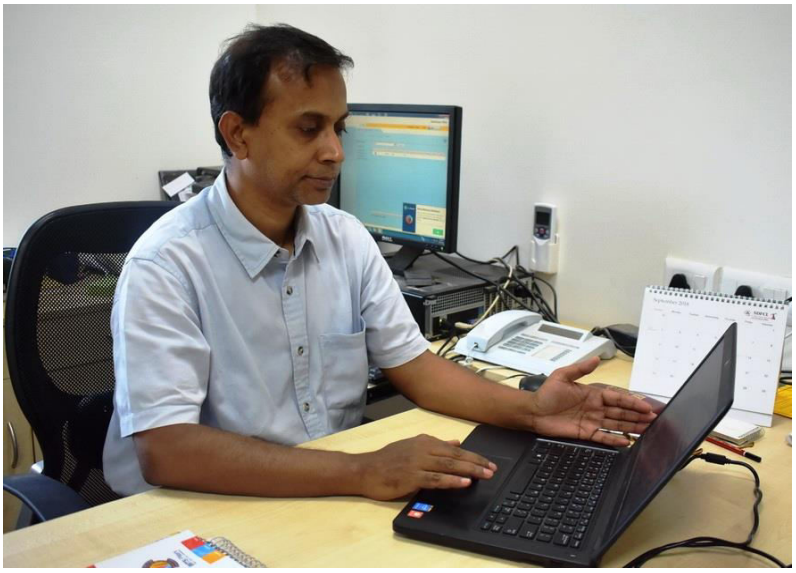

Currently, **Prof. Inamur Rahaman Laskar** has been employed as an Associate Professor at Department of Chemistry, Birla Institute of Technology & Science, Pilani Campus, Pilani, Rajasthan, India. He was awarded Ph. D. degree in Inorganic Chemistry from 'Indian Association for the Cultivation of Science (IACS)', Kolkata, India in 2000. He was working as a Lecturer at Ananda Mohan College (affiliated to University of Calcutta), Kolkata, India during Sept., 1999–July, 2001. He worked as a postdoctoral associate at NCTU Taiwan, during April, 2002–March, 2006 and NTHU Taiwan, during July, 2001–Feb., 2002. Further, he did his Post-doctoral (as JSPS Postdoctoral Fellow) research work at Kochi University, Japan in the period of April, 2006–March, 2008. He joined the Department of Chemistry, BITS Pilani on August, 2008. His current research interest is mainly focused on the design and syntheses of novel luminescent and AIE active luminescent materials, exploring the AIE mechanism, detailed study of luminescent behavior and targeted these materials in various applications such as applications in bio-imaging and cancer therapy, sensing (explosive/toxic analytes from solution and vapor phase), mechanofluorochromic and organic light emitting diodes etc. Modeling of the synthesized luminescent materials to explore the excited state properties and validation into the spectroscopic data of these complexes remains his further interest.